ARTICLE

Conformally bonded molecular interface retarded iodine migration for durable perovskite solar cells

Received 00th January 20xx,
Accepted 00th January 20xx

DOI: 10.1039/x0xx00000x

Ligang Yuan,[1,†] Weiya Zhu,[1,†] Yiheng Zhang,[1] Yuan Li,[1,*] Christopher C. S. Chan,[2] Minchao Qin,[3] Jianhang Qiu,[4] Kaicheng Zhang,[5] Jiaxing Huang,[1] Jiarong Wang,[1] Huiming Luo,[1] Zheng Zhang,[1] Ruipeng Chen,[1] Weixuan Liang,[1] Qi Wei,[1] Kam Sing Wong,[2] Xinhui Lu,[3] Ning Li,[1,*] Christoph J. Brabec,[5, 6] Liming Ding,[7] Keyou Yan[1,*]

State-of-the-art n-i-p perovskite solar cells (PSCs) suffer from stability issues due to ionic interdiffusion. Herein, by enlarging indacenodithiophene π-bridge donor (D') to combine with methoxy triphenylamine donor (D) and benzothiadiazole acceptor (A), three linear molecules termed as L1, L2 and L3 with D-A-D'-A-D structure are developed as dopant-free hole transport materials (HTMs). The π-bridge extension with active sites for coordination leverages the intramolecular dipole effect and intermolecular packing effect, resulting in conformally bonded ultrathin interface with compact and uniform coverage (~60 nm) to retard iodine migration and protect the buried perovskite. The unencapsulated L3-PSC (ITO/SnO_2/Perovskite/L3/MoO_3/Au) achieved an impressive PCE of 22.61% (certified 21.79%, 0.0525 cm^2). Ultrafast laser spectroscopy reveals that L-series molecules have sequential reduction of photoexcited energy disorder to illustrate the structure-performance-stability relationship. L3-PSC maintains over 85% of the initial efficiency after 500-hour at 85°C maximum power point tracking (MPP) and realizes the possibility of using small molecules to stabilize n-i-p PSCs.

Introduction

During the last decade, the power conversion efficiencies (PCEs) of both p-i-n and n-i-p type perovskite solar cells (PSCs) have been boosted to over 25%.[1, 2] However, the device durability is still one of the most challenging obstacles to realize their commercialization. It is encouraging that some reported *p-i-n* (inverted) PSCs have demonstrated superior thermal stability (at 85°C)[3-5] and passed the damp-heat test according to the International Electrotechnical Commission (IEC) 61215:2016 regulations,[2, 6] which was mainly ascribed to the progress in stable dopant-free electron/hole transport layers (ETM/HTM). In contrast, the high efficiency *n-i-p* (conventional) PSCs rely on the lithium bis(trifluoromethanesulfonyl)imide (Li-TFSI) and 4-tert-butyl pyridine (t-BP) additives to improve hole mobility (~10^{-5} cm^2 V^{-1} s^{-1}) and carrier conductivity (10^{-8} S cm^{-1}) of pristine 2,2',7,7'-tetrakis(*N*,*N*-di-*p*-methoxyphenylamine)-9,9'-spirobifluorene (spiro-OMeTAD).[7-9] The ionic interdiffusion between hygroscopic dopants/additives and halide of perovskite can cause device degradation, especially under continuous thermal and illumination conditions.[10, 11] Hence, the currently reported operational lifetime values of state-of-the-art *n-i-p* PSCs according to the ISOS protocols lag much behind the one of *p-i-n* PSCs (Table S1). Therefore, developing stable and efficient HTMs is a necessary strategy to endow n-i-p PSCs with both high PCEs and superior device operation lifetime for their potential commercialization.

The desired HTMs for the *n-i-p* PSCs with high performance should have a well-aligned energy level with perovskite, a sufficiently high hole mobility, superior chemical and photothermal stability, and should passivate the surface trap density at the perovskite/HTL interface as well.[12-17] By now, several types of

[1] School of Environment and Energy, State Key Laboratory of Luminescent Materials and Devices, Institute of Polymer Optoelectronic Materials and Devices, Guangdong Provincial Key Laboratory of Solid Wastes Pollution Control and Recycling, Guangdong Provincial Key Laboratory of Luminescence from Molecular Aggregates, AIE Institute, South China University of Technology, Guangzhou 510000, P. R. China
[2] Department of Physics and William Mong Institute of Nano Science and Technology, The Hong Kong University of Science and Technology, Clearwater Bay, Hong Kong, P. R. China
[3] Department of Physics, The Chinese University of Hong Kong, Shatin 999077, Hong Kong, P. R. China
[4] Shenyang National Laboratory for Materials Science, Institute of Metal Research, Chinese Academy of Sciences, Shenyang, 110016, China
[5] Institute of Materials for Electronics and Energy Technology (i-MEET) Friedrich-Alexander-University Erlangen-Nuremberg Martensstraße 7, Erlangen 91058, Germany
[6] Helmholtz-Institute Erlangen-Nürnberg for Renewable Energy (HI ERN), Forschungszentrum Jülich (FZJ), Erlangen 91058, Germany
[7] Center for Excellence in Nanoscience (CAS), Key Laboratory of Nanosystem and Hierarchical Fabrication (CAS), National Center for Nanoscience and Technology, Beijing 100190 P. R. China
[†] These two authors contributed equally to this work.
[*]Corresponding author: celiy@scut.edu.cn, ningli2022@scut.edu.cn, kyyan@scut.edu.cn
Electronic Supplementary Information (ESI) available: [details of any supplementary information available should be included here]. See DOI: 10.1039/x0xx00000x

dopant-free HTMs have been developed. Inorganic HTMs, such as NiO_x[18] and CuSCN,[19] enable long-term stable PSCs. Organic polymeric HTMs have shown promising stability and film-forming properties.[20-23] Hou and co-workers have introduced a dopant-free PDCBT polymer as the HTM in PSCs. In combination with the tantalum doped tungsten oxide, a bilayer hole extraction contact led to PSCs with negligible hysteresis and a PCE of over 21%.[20, 24] Recently, HTMs based on dopant-free polymer achieved PCEs of over 24% as well.[25-27] Small molecular HTMs can be precisely controlled to yield chemically pure and structurally homogeneous products and are thus a great promise for achieving PSCs with uniform properties and high reproducibility.[13, 14, 28-30]

So far, the reported small molecular HTMs for PSCs can be categorized into donor-π-donor (D-π-D) type, acceptor-D-acceptor (A-D-A) type, D-A-D type and D-A-π-A-D type configurations.[31] As shown in Fig. S1, spiro-OMeTAD as well as its derivative spiro-*m*F, the most famous D-π-D type HTM, exhibited limited hole mobility for dopant-free PSCs, because the rigid orthogonal spirobifluorene hinders the formation of close π-π stacking and the propeller-like triphenylamine induces a large intermolecular distance.[32] In order to improve hole mobility, the linear D-π-D type molecules with enhanced intermolecular π-π interactions have been developed to increase the mobility for dopant-free HTMs (Fig. S1). For example, Tang and co-workers employed dithia[3,2-b:2',3'-d]pyrrole core as π-bridge to synthesize DTPC13-ThTPA and DTP-C6Th, with which dopant-free PSCs achieved a PCE of 20.38% and 21.04%, respectively.[33, 34] Loo and co-workers synthesized the HTM of YZ22 with 1,10-phenanthroline as π-bridge and demonstrated that YZ22 also effectively passivated defects and hence boosted the PCE to 22.4%.[13] The D-A molecular backbone has a high dipole moment to induce intramolecular charge transfer (ICT), though it is regarded that the charge mobility and extraction capability can be further improved,[35] and thus A-D-A type with a large-sized donor and D-A-D type HTM are progressing as dopant-free PSCs (Fig. S1). For example, Yang and co-workers synthesized an A-D-A type DOR3T-TBDT HTM[36] and changed the core unit with an even larger-sized alkylthienyl-substituted benzo[1,2-b:4,5-b']dithiophene donor for DERDTS-TBDT HTM (Fig. S1) for better performance.[37] The incorporation of electron acceptor can not only enhance the performance, but also improve the intrinsic photothermal stability.[30] Moreover, Zhu and co-workers designed a series of quinoxaline-based D-A-D type HTMs (TQ1, TQ2, and TQ3) and extended the π-conjugation with a quinoxaline core to form TQ4. The PCE of PSCs with TQ4 was increased to 21.03%.[30, 38] D-A-D small molecules based on imide-functionalized thiophene (BTTI-C6, BTTI-C8, and BTTI-C12) were also developed and the dopant-free planar PSCs with BTTI-C6 HTL achieved an efficiency of 19.69%.[39] Recently, the D-A-π-A-D type molecule DTB-FL and BDT-DPA-F were employed as dopant-free HTMs in PSCs.[28, 40] However, these small molecules cannot inhibit the ionic interdiffusion and pass the harsh stability test, *e.g.* damp-heat, 85°C maximum power point (MPP) test. There are still plenty of room to engineer the structure units for photothermal stable PSCs.[28, 30, 41] It is meaningful to deliver a compact and tightly-bonded interface to retard the ionic interfusion (e. g. iodine migration) and ameliorate the 85°C MPP stability.

In this work, we employ indacenodithiophene (IDT)-based weak donor (D') derivatives with sequentially extended π-bridge, in combination with methoxy triphenylamine donor and benzothiadiazole acceptor, to synthesize three D-A-D'-A-D type linear molecules (named L1, L2, and L3) (Fig. 1a). IDT has a coplanar symmetrical structure, in which the three aromatic rings are in conjugation, and a bridging atom fixes the coplanarity between the adjacent rings. It is an excellent candidate as the π-bridge, which maximizes the π orbital overlap and hence reduces the photoexcited energetic disorder.[42] We find that expanding the side chain by four 4-hexylphenyl substituents to form L2 from L1 can regulate intermolecular interactions but slightly increase the intramolecular distortion.[43, 44] Extending the backbone with two thieno[3,2-b]thiophene units to form indacenodithieno[3,2-b]thiophene (IDTT in L3) can restore linearity and reduce intramolecular distortion. Through fine tuning of the molecular structure, hole mobility, glass transition temperature (T_g) and intermolecular order are gradually improved.[45] Compared to our recent work, IDT/IDTT-based weak donors possess active sites to coordinate to the perovskite, endowing conformally bonded molecular interface on the perovskite, which is verified by the grazing-incidence wide-angle X-ray scattering (GIWAXS) patterns and is beneficial for retarding iodine migration as well as device stability.[28] L1, L2 and L3 deliver 20.20%, 21.05 % and 21.90% efficiency for dopant-free PSCs, respectively. Through optical optimization, L3-based PSC (L3-PSC) finally achieved a champion PCE of 22.61%, which significantly exceeds the PCE of 15.87% for dopant-free spiro-OMeTAD-based PSCs. Rapid carrier transport, sequentially reduced disorder and improved defect passivation capability of the L-series are also demonstrated by ultrafast laser spectroscopy. Compared with the PSCs with doped spiro-OMeTAD, the unencapsulated L3-PSCs show promising long-term stability under various conditions. It maintains 90% of the initial PCE after 2736 hours stored in an argon-filled glovebox. Owing to the tightly bonded conformal coverage and interaction between L3 and perovskite, L3-PSCs can maintain ~85% initial value after 500-hour at 85°C MPP tracking. This work not only provides important guidelines for the multi-objective optimization of PSCs by independently tuning the energy level, hole mobility, thermal stability, solubility, and film-forming properties of dopant-free HTMs, but also demonstrates the possibility of using small molecules to address the key challenge of harsh 85°C MPP for *n-i-p* PSCs.

Results and discussion

Molecular synthesis and properties

It is important to introduce substantial active sites for coordination onto perovskite to strengthen the interface and thus deliver high photothermal stable properties for molecular film. The molecular design strategy for L1, L2, and L3 is described in Fig. 1a and π-bridge extension with two thieno[3,2-b]thiophene is employed to strengthen coordination bonding (Fig. 1b). The corresponding synthetic steps are presented in the supporting information (see Scheme S1-4). Briefly, L1, L2, and L3 were synthesized via Stille coupling of different IDT tin reagents with the intermediate TPAOMe-BT-Br.[28] We first enlarged the side chain of IDT π-bridge from alkyl to alkylaryl (L1 to L2) and then extended the backbone π-

bridge unit of the IDT by two thieno[3,2-b]thiophene (TT) unit (L2 to L3). The chemical structures for intermediate and target molecules were carefully characterized by ^{1}H- and ^{13}C-nuclear magnetic resonance (NMR) as well as matrix-assisted laser desorption/ionization on a time-of-flight mass spectrometry (MALD-ToFMS) (Figs. S2-S11). The yields of L1, L2, L3 are 85.5%, 90.5% and 83.8%, respectively.

The thermal properties of L1, L2, and L3 were investigated by thermogravimetric analysis (TGA) and differential scanning calorimetry (DSC). The recorded TGA curves in Fig. S12 exhibit a high decomposition temperature (T_d) of 440°C for L1, 449°C for L2, and 449°C for L3 during the heating process at a 5% weight loss. In addition, DSC measurement revealed a high T_g of 105°C for L1 HTM, 120°C for L2 HTM, and 163°C for L3 HTM (see Fig. S13), which are much higher than that of doped spiro-OMeTAD (72°C).[46] Especially, the L3 with a T_g of 163°C higher than that of pristine spiro-OMeTAD (125°C),[47] which is expected to be beneficial to the thermal stability of dopant free HTMs based PSCs.

The geometric structures of L1, L2, and L3 are elucidated using density-functional theory (DFT) calculations. From the optimized geometries in Fig. S14**,** the backbones of three molecules all exhibit a small twisting between the main building blocks. For L1, the torsion angle between benzothiadiazole (A) and the adjacent phenyl (D) is 32.93°/31.41° (left/right sides) and the torsion angle between benzothiadiazole (A) and thiophene (π) is 6.32°/2.90°. For L2 with the increased size of alkylaryl side chain, slightly larger torsion angle values (34.57°/33.61°, 7.46°/5.69°) were found. For L3, the torsion angle values slightly decrease (33.67°/33.9°, 6.54°/4.43°) due to the increased linear structure and are between the ones for L1 and L2. The D-A parts at both sides have larger torsion than the A-π-A parts in the middle due to the more bulky structure of donor.

We performed the electrostatic potential (ESP) analysis for electronic structure from the DFT calculation (Fig. S15). In the ground state, both benzothiadiazole unit (A) and thiophene-spacer of IDT unit (π) present high electron densities, and thus can provide favorable coordination sites for under-coordinated Pb^{2+} in the perovskite film.[28] [48] As shown in Fig. S16, the HOMOs are delocalized throughout triphenylamine moieties, the benzothiadiazole and π-bridge IDT unit, while the LUMOs are concentrated on the benzothiadiazole and partially delocalized to the thiophene. Therefore, there is a good electronic push-pull effect within the molecule leading to a significant dipole moment, which is in favour of charge transport.

Device performance

The PSCs were fabricated with the structure of ITO/SnO_2/perovskite/HTM/MoO_3/Ag, where the perovskite film without post-treatment with PEAI was fabricated by the "two-step" method according to previous work and HTMs were spin-coated for tight anchorage via coordination bonding (Fig. 1b).[49, 50] The systematic optimization of processing conditions for the HTMs is presented in Fig. S17 and Table S3, S4. We found that the dopant-free HTM with a concentration of 12 mg/mL in CB solvent at a speed of 4000 rpm achieved the champion efficiency. As shown in Fig. 1c, L3-PSC reaches a PCE of 21.90% under the AM 1.5 G irradiation at 100 mW/cm^2 with an open-circuit voltage (V_{OC}) of 1.12 V, a short-circuit photocurrent (J_{SC}) of 24.75 mA/cm^2 and a fill factor (FF) of 78.70%. It is higher than that of the best L1-PSC and L2-PSC with a PCE of 20.20% and 21.05%, respectively. The control devices based on spiro-OMeTAD with/without Li-TFSI and tBP have PCE of 21.94% and 15.87% in this work. The detailed photovoltaic parameters are summarized in Table 1.

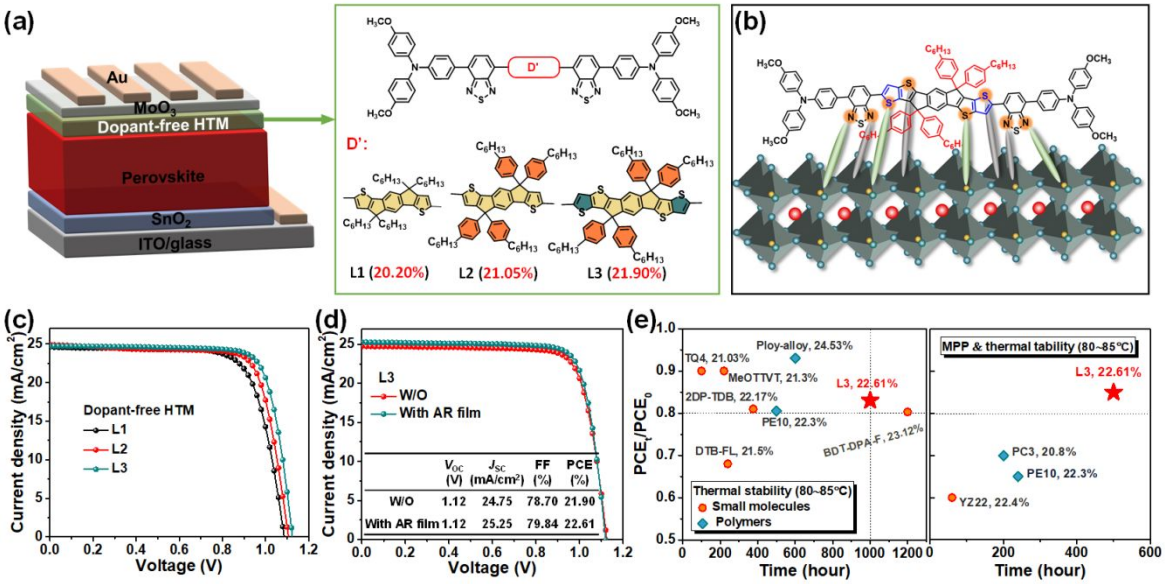

Fig. 1 Conformal bonded interface enhances device performance. (a) The design strategy of HTMs with extended active sites of L-series of HTMs (L1, L2 and L3) and device configuration. (b) Coordination sites between HTM and perovskite. (c) *J-V* curves of L-series PSCs. (d) *J-V* curves of L3-PSC without and with an anti-reflection (AR) film. (e) Summary of the thermal stability (80-85°C), MPP & thermal stability (80-85°C) for *n-i-p* PSCs with dopant-free HTMs (PCEs over 20%, their corresponding detailed parameters were listed in Table S2).

Table 1. Detailed parameters of PSCs with different HTLs.

HTL	V_{OC} (V)	J_{SC} (mA/cm^2)	FF (%)	PCE (%)
L1	1.09	24.91	74.33	20.20
L2	1.11	24.93	76.30	21.05
L3	1.12	24.75	78.70	21.90
Dopant-free spiro-OMeTAD	1.04	24.59	61.82	15.87
Doped spiro-OMeTAD	1.15	24.83	77.01	21.94

The statistics of the detailed photovoltaic parameters are shown in Fig. S18. All three dopant-free HTMs-based PSCs showed high reproducibility. Compared with L1-PSCs and L2-PSCs, the enhanced PCE of L3-PSCs is mainly ascribed to an increased V_{OC} and FF (see Table S5). The similar J_{SC} values are consistent with the absorption profiles of perovskite films coated with different HTMs (Fig. S19). As well, the calculated J_{SC} values from integrating the IPCE spectra in Fig. S20 confirm the photocurrents determined from *J-V* analysis.

Most importantly, the PCE of L3-PSCs can be further enhanced to 22.61% by employing an AR film to reduce light reflection at the glass substrate (Fig. 1d). This performance is comparable with the state-of-the-art PCE with dopant-free small-molecular HTMs recently reported in the literature (Fig. 1e and Table S2) and the doped spiro-OMeTAD PSCs (Fig. S21). As shown in Fig. S22, the L3-PSC achieved a PCE 21.79% certified by China CEPREI Laboratory with a mask area of 0.0525 cm^2.

The cross-sectional SEM images of the overall device are depicted in Fig. S23. The optimal thickness of the dopant free L1/L2/L3 HTM is found to be ~60 nm, which is much lower than the thickness of doped spiro-OMeTAD HTM (~180 nm). It is surprising that the conformal coverage of ultrathin molecular films is sufficient to guarantee efficient hole extraction and electron blocking, leading to the acceptable photovoltage and FF. Hence, we perform a series of experiments to illustrate the performance-structure-stability relationship.

Film microstructure

In order to reveal the microstructure, the molecular packing of L1, L2 and L3 neat films was firstly investigated by GIWAXS. As shown in Figs. 2a-d, all films exhibit two weak and broad scattering peaks centered at q = ~0.36 Å^{-1} and q = ~1.34 Å^{-1}, which can be attributed to the lamellar packing and π-π stacking, respectively. The low film crystallinity indicates that the films are predominantly amorphous due to their relatively twisted backbone.[24] Nonetheless,

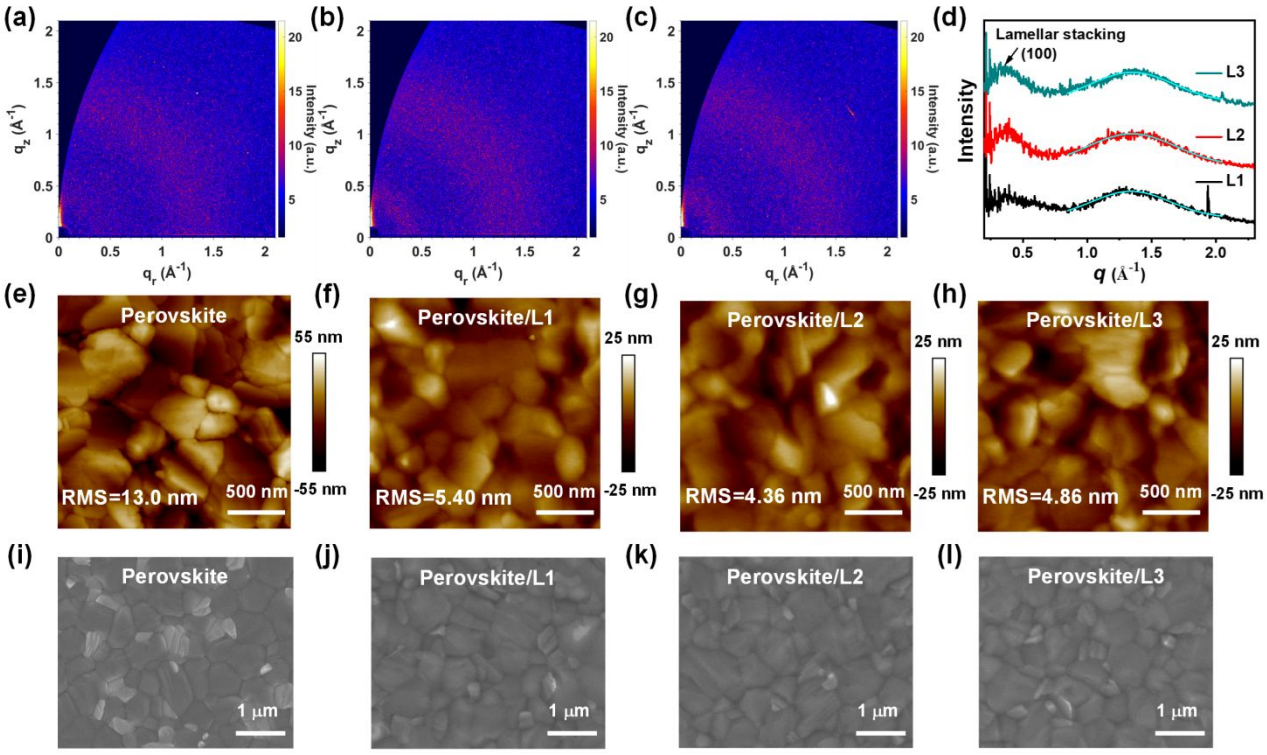

Fig. 2 Film microstructure suggests L-series HTMs have compact molecular packing and conformally bonded coverage with ultrathin thickness on perovskite. GIWAXS patterns of (a) L1, (b) L2, and (c) L3 films. (d) The corresponding GIWAXS intensity profiles. AFM images (e-h) and top-view SEM images (i-l) of the perovskite film, perovskite/L1, perovskite/L2, and perovskite /L3.

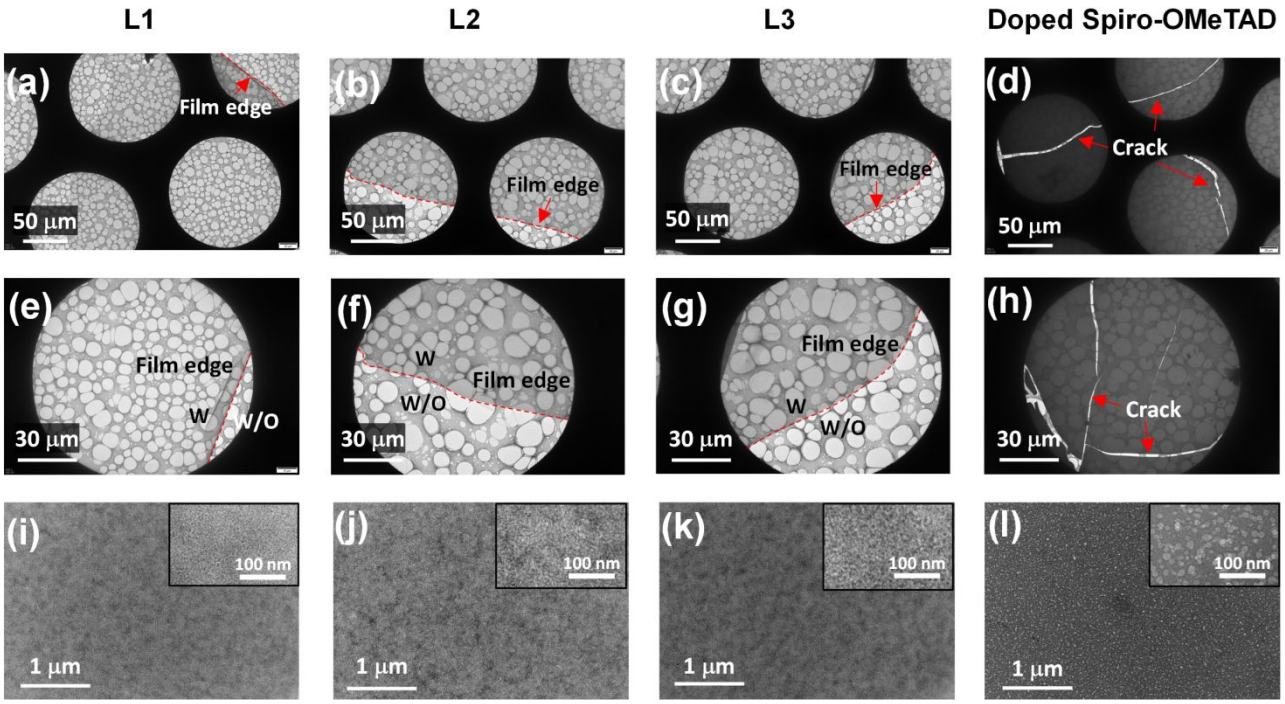

Fig. 3 TEM indicates L-series films are stronger than spiro-OMeTAD film. TEM images of (a) and (e) L1 film, (b) and (f) L2 film, (c) and (g) L3 film, (d) and (h) doped spiro-OMeTAD film. HRTEM images of (i) L1 film, (j) L2 film, (k) L3 film, and (l) doped spiro-OMeTAD film.

we found that the L3 film presents a higher peak position of the π-π stacking at q = 1.350 Å^{-1} than those of the L1 (1.340 Å^{-1}) and L2 (1.347 Å^{-1}) films, suggesting that the L3 molecules are packed more tightly in the film, which is beneficial for intermolecular charge transfer and inhibiting ionic interdiffusion. To some extent, these results are in good agreement with the slightly enhanced hole mobility from L1 to L3.

To further analyse the surface morphology of the HTM layers, atomic force microscopy (AFM) was performed. As shown in Fig. S24 and Figs. 2e-h, the three HTMs coated on perovskite films could provide a continuous and dense coverage that smoothen the perovskite surface. The root mean square (RMS) roughness of perovskite films covered with L1, L2, and L3 HTM are estimated to be 5.40, 4.36, and 4.86 nm, respectively, significantly smaller than that of bare perovskite film (RMS=13.0 nm). Compared with the RMS value of a perovskite film covered with L1 HTM, the decreased RMS values of perovskite layers with L2 and L3 demonstrate that the substitution of alkyl aryl group for alkyl group in the side chain of IDT π-bridge is an effective strategy to improve their film formation capability.

Scan electron microscopy (SEM) supports the microstructure of AFM. There is a typical perovskite film morphology with few bright PbI_2 spots as shown in the SEM images in Fig. 2i.[51] After coating with HTMs of L1/L2/L3 (Figs. 2j-l), we can clearly distinguish the grain pattern of the perovskite, which shows a very similar surface morphology to the bare perovskite. This indicates that the HTMs are uniformly and conformally covered on the surface of the perovskite film like "leotard", which is conducive to the interfacial hole extraction and transport.[48]

The uniform, dense and conformal coverage is further revealed by TEMs (Fig. 3). We prepared the samples with a structure of ITO/PEDOT:PSS/HTM by spin-coating, and then immersed the samples in deionized water to dissolve the bottom PEDOT:PSS film, leaving behind HTM films floating on the water surface (see video in Supporting Information). The films were collected by copper grid for characterization. TEM images confirm L-series have uniform, dense and conformal coverage in amorphous state while doped spiro-OMeTAD film has small grains in crystalline state (Fig. 3). Due to the flexible backbone, L-series HTMs are much more stable than doped spiro-OMeTAD film. Surface tension will make spiro-OMeTAD film cracking into pieces while L-series films retains overall structure after soaking in the water (Figs. 3a-h). The high-resolution TEM (HRTEM) images (Figs. 3i-l) confirm the amorphous state of L-series and crystalline grains in dot structure of spiro-OMeTAD film. The brittleness of spiro-OMeTAD grains will make the film not stable enough. During HRTEM test, sequentially improved membrane quality was observed after using high intensity electron beam for duration test, which is consistent with the sequentially increased T_g as aforementioned. More importantly, it is notable that this pin-hole free and dense film with ultrathin thickness of L-series HTMs will help to suppress the ionic interdiffusion and protect the buried perovskite, which will be discussed in the following section.

All the L-series HTMs exhibit extremely high hydrophobicity. Their water contact angles (θ) are larger than 90°, which is significantly higher than that of the spiro-OMeTAD film (θ = 73.6°, see Fig. S25). Meanwhile, the enlarged water contact angles from L1 to L2 to L3 could be ascribed to the additional aromatic rings of side chains and enlarged fused-rings of main chains.[30, 35] The degradation images of perovskite films in Fig. S26 also suggest that the strong hydrophobicity of the L-series HTMs efficiently protects the perovskite film from the degradation by atmospheric moisture. This result is also consistent with membrane structure judging from TEM images.

Photo-excited energy disorder

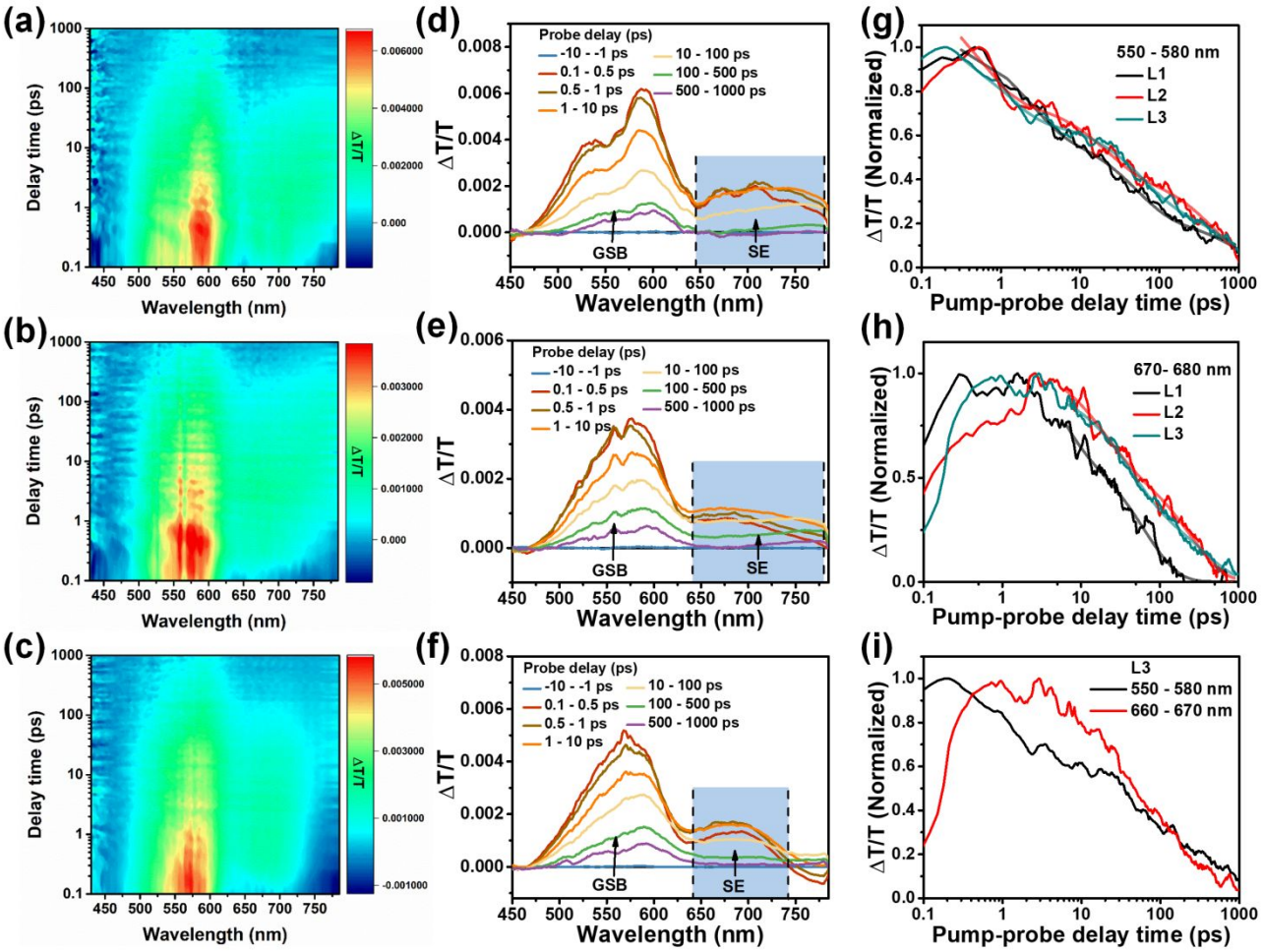

Fig. 4. TAS suggests L-series films have sequentially reduced photoexcited energy disorder. 2D colour plot of TAS of (a) L1, (b) L2, and (c) L3; TAS plots of (d) L1, (e) L2, and (f) L3 HTM films; (g) GSB kinetics at 550-580 nm, and (h) SE kinetics at 660-670 nm; (i) shows the differences in kinetics between GSB and SE. $\tau_{ave} = \sum A_i \cdot \tau_i / \sum A_i$, where A and τ are the fitted amplitudes and the lifetimes of the multi-exponential fitting. The HTM was excited at 400 nm wavelength with an excitation fluence of ~ 5 μJ/cm^2.

To further understand the photo-excited properties of L1-L3 HTMs, the ultrafast transient absorption spectroscopy (TAS) was applied and the sequentially reduced energy disorder was observed. As shown in Figs. 4a-f, all three HTMs exhibit a broad positive signal at 500-650 nm and an additional transient positive signal at 650-720 nm when excited at 400 nm. The feature at 500-650 nm can be assigned to ground state photobleaching (GSB) that coincides with the peak of steady-state absorption spectra (Fig. S27). The positive feature at 650-720 nm coincides with the steady state PL spectrum (Fig. S28), and is assigned to stimulated emission (SE).

The full ground-state recovery of photo-excited HTM films takes over 1 ns. The decay curves were best fit with triexponential functions, indicative of a broad overlap of multiple decay pathways.[52] To compare the GSB decay times, an amplitude average decay time constant of 230, 190, and 250 ps was extracted for L1, L2, and L3, respectively (Fig. 4g). The SE probes the excited state that correlates with the fluorescence in the system. The SE grows in the first few ps as the emissive states are populated. L1 shows a rapid decay that within 100 ps, whereas L2 and L3 takes significantly longer, with L3 having not decayed completely even at

Table 2. Optical, electrochemical, thermal, and charge transport properties of L1, L2 and L3.

	$\lambda_{abs,sol}$ (nm)[a]	$\lambda_{abs,film}$ (nm)	E_g^{opt} (eV)[b]	HOMO (eV)[c]	LUMO (eV)	T_d (°C)	T_g (°C)	μ_h (cm^2 V^{-1} s^{-1})
L1	569	583	1.94	-5.26	-3.32	440	105	2.53×10^{-4}
L2	561	570	1.95	-5.31	-3.36	449	120	3.28×10^{-4}
L3	559	569	1.96	-5.32	-3.36	449	163	3.46×10^{-4}

[a] Measured in CB solution with a concentration; [b] Estimated from the absorption edge in neat film using the equation: $E_g^{opt} = 1240/\lambda_{onset}$ (eV); [c] E_{HOMO}=-(4.8+E_{ox}-0.26) (eV).

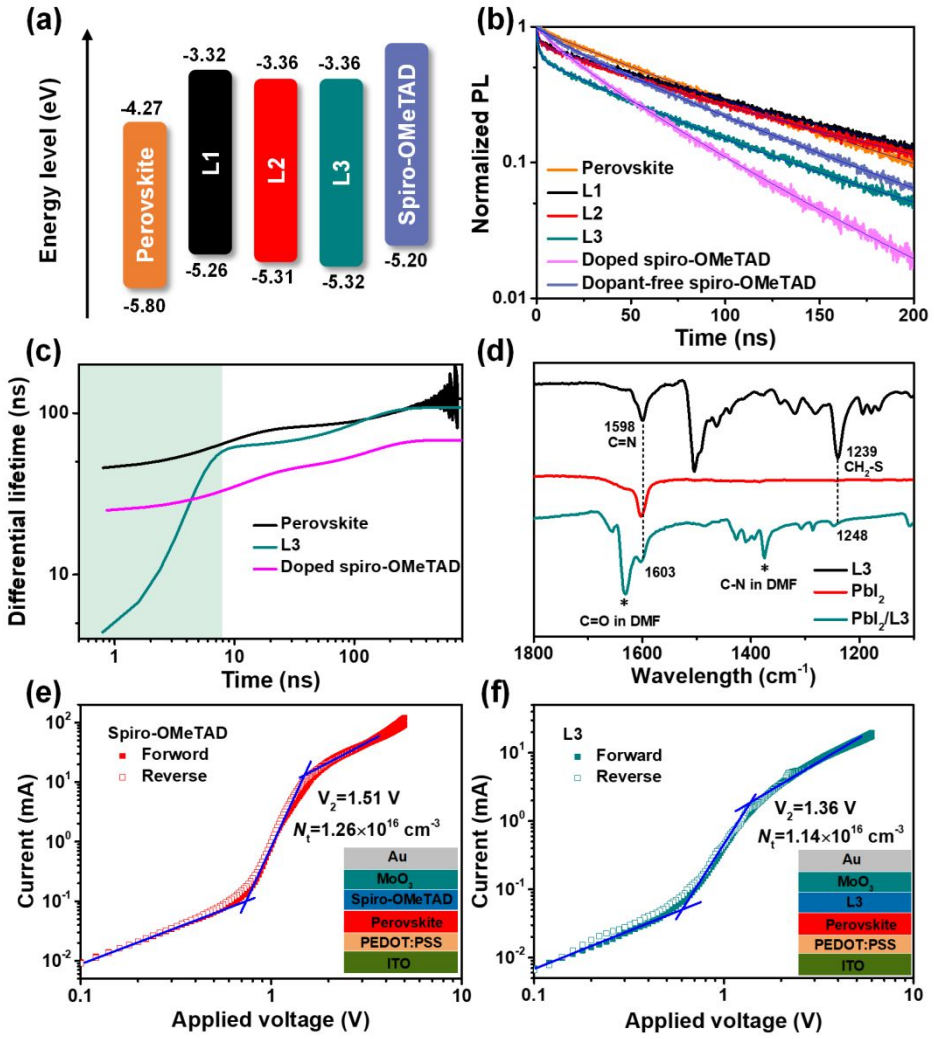

Fig. 5 Charge transfer and passivation effect. (a) Energy level diagram, (b) TRPL and (c) computed differential lifetimes from Fig. 5b for the bare perovskite, L3, and doped spiro-OMeTAD coated perovskites. The shaded areas are a guide marking for charge extraction. (d) FTIR spectra of the powders of L3, PbI_2 and PbI_2/L3 blend. The peak of 1632 cm^{-1} and 1375 cm^{-1} are ascribed to C=O and C-N of DMF, respectively, which form an adduct of PbI_2•xDMF.[60] The forward and reverse SCLC curves of (e, f) hole-only devices.

1 ns (Figs. 4, h and i). The observation of a decay behaviour of the excited state (probed by SE) and the GSB that is independent of each indicates the generation of multiple species following photoexcitation.[52] Interestingly, the extended excited state lifetime of L2 and L3 suggests a reduced recombination rate which is generally regarded as a beneficial quality criterion for electronic materials.

In addition, L1-L3 HTMs exhibit the reduced fold of peaks and a sequentially narrowed GSB and SE width. This is due to better alignment and enhanced π-π stacking as suggested as well from the GIWAXS data and can be indicative of enhanced intermolecular charge transport of L3 HTM (Fig. 2d). This property is not observed by static UV-Vis absorption spectra and PL (Figs. S27 and S28). The narrowing GSB and SE width suggests the reduction of photo-excited energy disorder, which is important for photovoltaics under illumination as well as the photothermal stability under MPP test.

Band alignment and mobility

We in-detail analyse the band alignment. In the film, the main absorption peaks of L1, L2, and L3 are located at 583, 570 and 569 nm (Table 2 and Fig. S27), respectively. Compared with the solution, a red shift of the main peak is observed in the corresponding thin films, which may be attributed to the enhanced intermolecular stacking induced electron delocalization.[53-55] From Tauc plots of L1, L2, and L3 in Fig. S29, the optical band gaps (E_g^{opt}) of L1, L2, and L3 films were determined to be 1.94, 1.95 and 1.96 eV, respectively. The detailed optical and parameters listed in Table 2.

From the oxidation potential of *C-V* curves (Fig. S30), the HOMO energy levels were calculated to be -5.26, -5.31 and -5.32 eV for L1, L2, and L3, respectively.[55] According to the HOMO values from *C-V* curves and the E_g^{opt} from solid film of HTMs, the LUMO levels of L1, L2, and L3 are calculated to be -3.32, -3.36 and 3.36 eV, respectively. The deeper HOMO values of L2 and L3 may better match the VB edge position of the perovskite.[56, 57] The energy level diagram of all three HTMs and the perovskite film are given in Fig. 5a, and one can see that L2 and L3 have a deeper lying HOMO level

and can be expected to provide a better energetic match between the perovskite and the anode interface.

The hole transport behaviour of L1, L2, and L3 films was determined by using the space charge limited current (SCLC) method with a device structure of ITO/ poly(3,4-ethylenedioxythiophene)-poly(styrenesulfonate) (PEDOT:PSS)/HTM/MoO_3/Ag (Fig. S31). All three HTMs exhibited similar hole mobility values of 2.53 × 10^{-4} cm^2 V^{-1} s^{-1} for L1, 3.28 × 10^{-4} cm^2 V^{-1} s^{-1} for L2 and 3.46 × 10^{-4} cm^2 V^{-1} s^{-1} for L3, which are higher than that of the dopant-free spiro-OMeTAD (1.57 × 10^{-4} cm^2 V^{-1} s^{-1}). Although hole mobility is not very high, but it can extract the holes effectively and block the recombination in ultrathin thickness (~60 nm) in this work judging from their performance aforementioned.

Charge extraction, passivation effect and chemical bonding

The PCE of PSCs with dopant-free spiro-OMeTAD HTM is 15.87%, which is lower than that of L3-PSC, mainly due to low V_{OC} and FF (see Fig. S32 and Table 1). Compared with the PCE of 21.94% for doped spiro-OMeTAD PSC, L3-PSC also exhibits a comparable efficiency of 21.90%, but as well shows a higher and more stable output efficiency at maximum power point (MPP) within 120 s (Figs. S32 and S33). In our case, we do not deposit PEAI on the perovskite surface to passivate surface defects but we find that the photovoltage is acceptable. Therefore, the charge transfer and passivation effect of L-series HTM are further identified. The steady-state photoluminescence (PL) spectra were measured on glass/perovskite/HTM samples (Fig. S34). After covering the perovskite film with HTM, the PL intensity is obviously quenched, especially when it is covered by L3 HTM, indicating that the three HTMs have strong hole extraction and transfer capabilities.[56]

The time resolved PL (TRPL) of the perovskite films with different HTMs were further preformed, as shown in Fig. S35a. It is evident from the magnified spectra in Fig. S35b that the PL decay consists of a fast component followed by a long-lived component in the perovskite films covered with HTMs. The TRPL were fitted with tri-exponential decays, as shown in Fig. S36, and the fitted corresponding parameters are summarized in Table S6. Tri-exponential decays give better fit than traditional bi-exponential decays, which is due probably to the charge extraction/transport (τ_1), radiative recombination (τ_2) and passivation effect events (τ_3), presumably corresponding to the quenching process of photogeneration of free carriers of perovskite through charge transfer (including charge extraction from perovskite to HTL and charge transport in HTL), radiative recombination in the perovskite film, and passivation effects by functional group, respectively. As listed in Table S6, the average lifetimes of L-series perovskite films were incredibly improved compared with bare perovskite film. This indicated the passivation effect of L-series HTM on the perovskite film. Furthermore, differential lifetime was modelled by fitting the TRPL spectra (Fig. 5b) with the equation of $t = -(d\ln(\varphi(t))/dt)^{-1}$,[58, 59] where $\varphi(t)$ is the time-dependent PL photon flux. As shown in Fig. 5c, the processes that reduce the PL counts over time are separable, and the lifetime t is directly readable at each time point.[59]

The perovskite films with L-series HTMs exhibit faster charge extraction process than that of doped spiro-OMeTAD HTM. A readily charge extraction process from the perovskite film to L3 HTM was observed within 10 ns (green region in Figure 5c), which can be mainly ascribed to the extended backbone of the IDTT π-bridge with deep HOMO energy level and high mobility.[44] While the doped spiro-OMeTAD has a faster transport due to its higher mobility. Compared with 21.94% efficiency of the doped spiro-OMeTAD PSCs, L3 PSCs also have a comparable efficiency of 21.9%. This performance is also consistent with TRPL data.

Fourier transform infrared spectroscopy (FTIR) measurement was carried out to confirm chemically-bonded passivation of perovskite surface by L3 HTM. As shown in Fig S37 and Fig. 5d, the CH_2-S peak in thiophene moiety in L3 slightly shifted after mixing with PbI_2, from 1240 cm^{-1} to 1248 cm^{-1}, respectively. The C=N stretch peak in benzothiadiazole moiety of 1598 cm^{-1} also shifted to 1603 cm^{-1}. These results indicate that chemically bonding between PbI_2 and the benzothiadiazole and thiophene moieties of L3 occurred with lone pair electrons. X-ray photoelectron spectroscopy (XPS) measurement was further performed, as shown in Fig. S38. Compared to the bare perovskite film, a shift of the Pb^{2+} 4f towards lower binding energy was observed for the perovskite film covered with L3 HTM, indicating the functional groups in L3 could donate the lone pair electrons to the empty 6p orbital of Pb^{2+} via the coordination interactions and effectively passivate the defects and suppressed the defect-assisted recombination at the interface between the perovskite film and HTMs.[28, 48] The I $3d_{3/2}$ and $3d_{5/2}$ signals for perovskite/L3 to shift to lower binding energy compared to those in the XPS spectrum of bare perovskite film. We believe this shift stems from L3 donating electrons to Pb^{2+}, which perturbs the static interactions between Pb^{2+} and I^- at the interface.[13] A small shift of *N* 1s and *S* 2p also occurs in the perovskite film coated with L3 HTM and the peak of O 1s do not shifts. These results are in good agreement with the FTIR measurement, which demonstrate chemically bonding passivation between PbI_2 and the benzothiadiazole and thiophene moieties of L3 HTM.

The trap density was further quantified by the SCLC method. The dark *J-V* curves of hole-only devices with a configuration of ITO/PEDOT:PSS/perovskite/HTM/MoO_3/Ag. We evaluated the trap-state density via the trap-filled limit voltage (V_{TFL}), obtained from $n_t = q\varepsilon\varepsilon_0 V_{TFL}/(qL^2)$,[61-63] where q is the elementary charge, ε relative dielectric constant, ε_0 vacuum permittivity, L thickness of the perovskite film, and V_{TFL} trap-filling limit voltage. As shown in Fig. 5, e and f, V_2 gives the most accurate value for the trap density due to the mixed ionic and electronic nature of perovskites.[63] The trap densities were calculated to be 1.26 × 10^{16} and 1.14 × 10^{16} cm^{-3} by V_2 for the devices with doped spiro-OMeTAD and L3 HTL, respectively, with similar values to each other. For the standard spiro-OMeTAD, the dopants can not only enhance the conductivity (Li-salt), but can passivate perovskite film by the pyridine group.[64] For L3 HTL, the low trap states may be attributed to the reduced energy disorder of L3 and passivation effect on the perovskite film.[40] L3 HTL has much thinner thickness (~60 nm) than doped spiro-HTL to block the charge recombination event at the interface, due to close packing, coordination interaction and conformal coverage. Therefore, L3 PSC has similar PV performance to the doped spiro-OMeTAD PSC in our system.

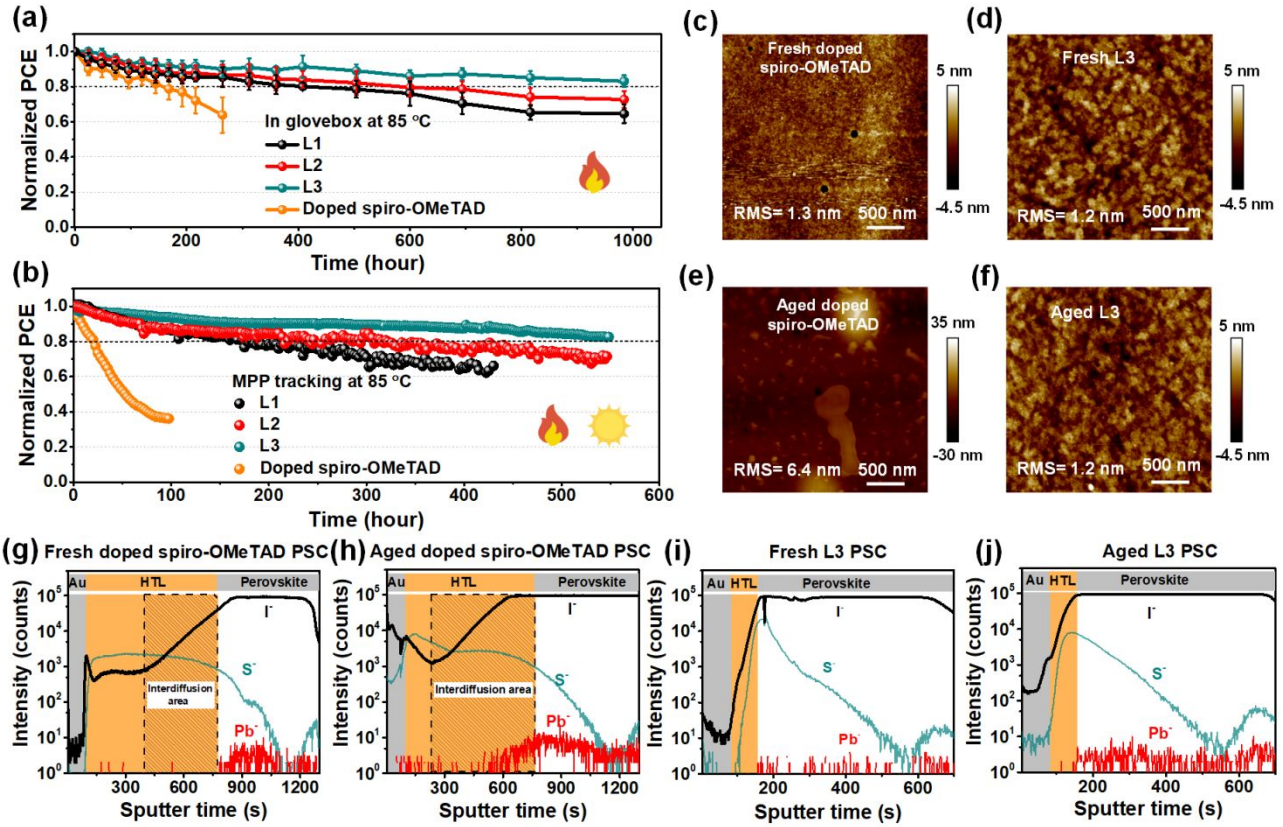

Fig. 6 Long-term stability tests suggest L3 can endure 85°C MPP test**.** (a) 85°C thermal stability, and (b) 85°C MPP tracking stability for unencapsulated doped spiro-OMeTAD and dopant-free L-series PSCs. AFM images of HTMs on ITO substrates, the aging condition is 100°C for 10 hours on the hotplate in N_2-filled glovebox, (c) fresh doped spiro-OMeTAD film, (d) fresh L3 film, (e) aged spiro-OMeTAD film, and (f) aged L3 film. ToF-SIMS of depth profiles of anion distribution within full PSCs: (g) fresh doped spiro-OMeTAD PSC, (h) doped spiro-OMeTAD PSCs with 85°C aging for 10 days in argon, (i) fresh L3 PSC, (j) L3 PSC with 85°C aging for 10 days in argon.

Stability

We have tested the stability of L-series PSCs and control devices with doped spiro-OMeTAD HTM. Firstly, the unencapsulated devices were stored in a glovebox filled with argon under the dark condition. Over 2700 hours, L3-PSC retained 90% of its initial value and the control device had 85% (Fig. S39). This result indicates that dopant free HTM in PSCs can avoid ionic interdiffusion to degrade the perovskite film and prolong the long-term storage stability of PSCs. Secondly, the 85°C thermal stability measurement under argon atmosphere was performed. As shown in Fig. 6a, the PCE of PSCs with doped spiro-OMeTAD HTM quickly decayed to 70% of their initial values within 200 hours, whereas the L3-PSC maintained ~83% of their initial PCE after ~1000 hours. Finally, stability at 85°C and MPP tracking was performed to evaluate the photothermal stability of the unencapsulated devices under white LEDs at one-sun intensity. As shown in Fig. 6b, the L3-PSC could maintain 85% of its initial efficiency after over 500 hours, while the control PSC was dropped rapidly within 100 hours. This is the best photothermal stability of the PSCs with dopant-free organic small molecule HTMs (Fig. 1d and Table S2).

The promising thermal stability of L3-PSCs reveals that dopant-free L3 HTM with a high T_g of 163°C exhibits a more stable molecular configuration than that of doped spiro-OMeTAD HTM with a T_g of ~72°C.[46] From the XRD patterns of perovskite film in Fig. S41, the low PbI_2 peak diffraction and strong (001) perovskite peaks in the aged perovskite film with L3 HTM confirm the improved stability for perovskite covered with L3 HTM. Moreover, as shown in Fig. S41, both the doped spiro-OMeTAD and L3 HTMs-covered perovskite films were found to exhibit red-shifted absorption edges in the UV-vis absorption spectra for aged perovskite film, indicating that the perovskite itself inevitably degrades through the loss of chloride component under heating conditions.[65, 66] This may be one of the reasons for the slightly decreased efficiency of L3-PSC under the 85°C thermal aging test. Although the colour of the perovskite film does not change significantly (see the images in Fig. S42a), degradation spots appeared on the surface of the spiro-OMeTAD film after aging under 85°C for 10 days as shown in Fig. S42b. These degradational spots at the interface between spiro-OMeTAD HTL and metal electrode will further impair the efficiency of the PSCs.

In order to further analyse the influence of the HTM morphology on device efficiency under heating conditions, we used AFM to characterize the morphology of bare HTM before and after heating. As shown in Figs. 6c-f, the morphology of doped spiro-OMeTAD film shows an obvious agglomeration after aging at 100°C for 10 hours accompanied by an increase in surface roughness. On the contrary, negligible changes in the morphology of L3 film could be detected before and after 10 hours aging. Moreover, when the heating time even prolongs to 100 hours, L3 film can still maintain the dense and smooth morphology (Fig. S43), strongly suggesting the excellent thermal stability of L3 HTM.

Furthermore, the ToF-SIMS of depth profiles of iodine anion (I^-) distribution was carried out to analyses ion migration within complete PSCs. As shown in Figs. 6g-j, substantial iodine was detected in spiro-OMeTAD layer for the fresh and aged control device based on doped spiro-OMeTAD due to ionic interdiffusion between Li-salt and iodide ions. The ionic interdiffusion in the fresh control device occurs during the spin-coating process. The additive species can penetrate into perovskite and iodine can diffuse into HTL layer, resulting in iodine gradient area. As shown in Figs. 6g, h, this interdiffusion area was enlarged in spiro-OMeTAD layer after thermal aging process. The iodine migration is the major reason for performance degradation for traditional *n-i-p* PSCs. In contrast, iodine is flatly distributed inside the whole perovskite layer in L3-PSC. After thermal annealing at 85°C for 10 days, the diffusion of I^- ions from the perovskite layer to the Au anion electrode could be significantly suppressed in L3-PSC compared to the control device based on doped spiro-OMeTAD, by a factor of ~100. This again underlines that the dense and conformal film coverage of L3 HTM at 85°C can prevent the iodine migration, leading to ionic fixation and enhanced photothermal stability of L3-PSCs. Therefore, in dopant-free condition, the ionic interdiffusion is greatly suppressed by L3 because of the conformal bonding with perovskite surface.

Conclusions

We reported photothermal stable conventional PSCs with high efficiency based on dopant-free small molecule HTMs with a D-A-D'-A-D configuration. By engineering the IDT π-bridge, the four 4-hexylphenyl side chains and two TT units in IDT π-bridge main chain make L3 HTM possess good film formation quality and proper energy levels, ensuring the efficient charge transport performance. Meanwhile, surface passivation effects by the functional group in HTM also endow the L3 layer with great benefits in charge transport and extraction property at the perovskite/HTM interface with reduced interfacial recombination loss and suppressed ionic interdiffusion. As a result, PSCs with three HTMs (L1, L2 and L3) all showed PCEs more than 20%, especially the PSCs with L3 HTM delivered a champion PCE of 22.61% with an antireflection film. More importantly, due to the high mobility and T_g of L-series HTMs, the dopant-free L3 HTM could avoid the negative effect of additives on perovskite layer and maintain high quality morphology of HTL. As a result, the PSCs with the dopant-free L3 HTM exhibited a great photothermal and operational stability under 85°C, which maintained 83% of initial PCE after ~1000 hours at the dark, and 85% of initial PCE after 500 hours with continuous illumination measured at MPP in the argon-filled glovebox. We demonstrated that conformally bonded ultrathin interface with compact and uniform coverage (~60 nm) to retard iodine migration and protect the buried perovskite. Ultrafast spectroscopy spectra revealed that L-series molecules have sequential reduction of photoexcited energy disorder to illustrate the structure-performance-stability relationship. This work provides a strategy to design high mobility and T_g HTM and shows a promising application prospect of small molecular HTM with the D-A-D'-A-D configuration in conventional *n-i-p* PSCs.

Author Contributions

K.Y.Y. and Y.L. conceived the idea and supervised the overall project. K.Y.Y., Y.L., N.L., C.J.B., L.M.D. and L.G.Y. designed the experiments. Y.L. designed the L1, L2, L3 HTMs. W.Y.Z., Y.H.Z., J.X.H., Q.W. and Y.L. synthesized the L1, L2, L3 HTMs. L.G.Y. fabricated and characterized perovskite thin film and devices. K.C.Z., J.R.W. and H.M.L. helped on the device fabrication and characterization. W.Y.Z., Y.H.Z., J.X.H., R. P.C., W. X. L., Q.W. and Y.L. characterized their structure of HTMs. C.C.S.C. and K.S.W. contributed TRPL and fs-TA measurements and corresponding data analysis. M.C.Q. and X.H.L. carried out the GIWAXs measurements and corresponding data analysis. Z.Z. performed DTF calculation. J.H.Q. helped on ToF-SIMS measurements. K.Y.Y. and L.G.Y. drafted the manuscript and all authors were involved in discussion and revision.

Conflicts of interest

There are no conflicts of interest to declare.

Acknowledgements

This work was in part supported by National Key Research and Development Program of China (2022YFB3803300) and Start-up funds from Central Organization Department and South China University of Technology, as well as funds from the National Natural Science Foundation of China (U2001217) Guangdong Science and Technology Program (Grant Nos: 2020B121201003, 2019ZT08L075, 2019QN01L118), and the Program for Introducing Overseas High-level Talents of Shanxi (Hundred Talents Plan). Y.L. acknowledges funding from the National Natural Science Foundation of China (No. 51973063), the Tip-top Scientific and Technical Innovative Youth Talents of Guangdong Special Support Program (No. 2019TQ05C890), and the 111 Project (No. BP0618009). C.C.S.C. and K.S.W. acknowledge the support from Research Grants Council of Hong Kong (grant number C7035-20G) and William Mong Institute of Nano Science and Technology (grant number WMINST19SC04). N.L. acknowledges the financial support by State Key Lab of Luminescent Materials and Devices, South China University of Technology (Skllmd-2022-03).

References

1. M. Kim, J. Jeong, H. Lu, K. Lee Tae, T. Eickemeyer Felix, Y. Liu, W. Choi In, J. Choi Seung, Y. Jo, H.-B. Kim, S.-I. Mo, Y.-K. Kim, H. Lee, G. An Na, S. Cho, R. Tress Wolfgang, M. Zakeeruddin Shaik, A. Hagfeldt, Y. Kim Jin, M. Grätzel and S. Kim Dong, *Science*, 2022, **375**, 302-306.
2. Z. Li, B. Li, X. Wu, A. Sheppard Stephanie, S. Zhang, D. Gao, J. Long Nicholas and Z. Zhu, *Science*, 2022, **376**, 416-420.
3. X. Zheng, Y. Hou, C. Bao, J. Yin, F. Yuan, Z. Huang, K. Song, J. Liu, J. Troughton, N. Gasparini, C. Zhou, Y. Lin, D.-J. Xue, B. Chen, A. K. Johnston, N. Wei, M. N. Hedhili, M. Wei, A. Y. Alsalloum, P. Maity, B. Turedi, C. Yang, D. Baran, T. D. Anthopoulos, Y. Han, Z.-H. Lu, O. F. Mohammed, F. Gao, E. H. Sargent and O. M. Bakr, *Nat. Energy*, 2020, **5**, 131-140.
4. Y.-H. Lin, N. Sakai, P. Da, J. Wu, H. C. Sansom, A. J. Ramadan, S. Mahesh, J. Liu, R. D. J. Oliver, J. Lim, L. Aspitarte, K. Sharma, P. K. Madhu, A. B. Morales-Vilches, P. K. Nayak, S. Bai, F. Gao, C. R. M. Grovenor, M. B. Johnston, J. G. Labram, J. R. Durrant, J. M.

Ball, B. Wenger, B. Stannowski and H. J. Snaith, *Science*, 2020, **369**, 96.
5. R. Chen, S. Liu, X. Xu, F. Ren, J. Zhou, X. Tian, Z. Yang, X. Guanz, Z. Liu, S. Zhang, Y. Zhang, Y. Wu, L. Han, Y. Qi and W. Chen, *Energy Environ. Sci.*, 2022, **15**, 2567-2580.
6. R. Azmi, E. Ugur, A. Seitkhan, F. Aljamaan, A. S. Subbiah, J. Liu, G. T. Harrison, M. I. Nugraha, M. K. Eswaran, M. Babics, Y. Chen, F. Xu, T. G. Allen, A. U. Rehman, C. L. Wang, T. D. Anthopoulos, U. Schwingenschlogl, M. De Bastiani, E. Aydin and S. De Wolf, *Science*, 2022, **376**, 73-77.
7. J. J. Yoo, G. Seo, M. R. Chua, T. G. Park, Y. Lu, F. Rotermund, Y. K. Kim, C. S. Moon, N. J. Jeon, J. P. Correa-Baena, V. Bulovic, S. S. Shin, M. G. Bawendi and J. Seo, *Nature*, 2021, **590**, 587-593.
8. G. Kim, H. Min, K. S. Lee, D. Y. Lee, S. M. Yoon and S. I. Seok, *Science*, 2020, **370**, 108-112.
9. J. Jeong, M. Kim, J. Seo, H. Lu, P. Ahlawat, A. Mishra, Y. Yang, M. A. Hope, F. T. Eickemeyer, M. Kim, Y. J. Yoon, I. W. Choi, B. P. Darwich, S. J. Choi, Y. Jo, J. H. Lee, B. Walker, S. M. Zakeeruddin, L. Emsley, U. Rothlisberger, A. Hagfeldt, D. S. Kim, M. Gratzel and J. Y. Kim, *Nature*, 2021, **592**, 381-385.
10. Z. Li, C. Xiao, Y. Yang, S. P. Harvey, D. H. Kim, J. A. Christians, M. Yang, P. Schulz, S. U. Nanayakkara, C.-S. Jiang, J. M. Luther, J. J. Berry, M. C. Beard, M. M. Al-Jassim and K. Zhu, *Energy Environ. Sci.*, 2017, **10**, 1234-1242.
11. T. Zhang, F. Wang, H.-B. Kim, I.-W. Choi, C. Wang, E. Cho, R. Konefal, Y. Puttisong, K. Terado, L. Kobera, M. Chen, M. Yang, S. Bai, B. Yang, J. Suo, S.-C. Yang, X. Liu, F. Fu, H. Yoshida, W. M. Chen, J. Brus, V. Coropceanu, A. Hagfeldt, J.-L. Brédas, M. Fahlman, D. S. Kim, Z. Hu and F. Gao, Science, 2022, **377**, 495-501.
12. Z. J. Li, J. Park, H. Park, J. Lee, Y. Kang, T. K. Ahn, B. G. Kim and H. J. Park, *Nano Energy*, 2020, **78**, 105159.
13. B. X. M. Zhao, C. Yao, K. C. Gu, T. R. Liu, Y. Xia and Y. L. Loo, *Energy Environ. Sci.*, 2020, **13**, 4334-4343.
14. X. X. Yin, Z. N. Song, Z. F. Li and W. H. Tang, *Energy Environ.Sci.*, 2020, **13**, 4057-4086.
15. X. L. Sun, X. Y. Yu and Z. A. Li, *ACS Appl. Energy Mater.*, 2020, **3**, 10282-10302.
16. E. Rezaee, X. Liu, Q. Hu, L. Dong, Q. Chen, J.-H. Pan and Z.-X. Xu, *Solar RRL*, 2018, **2**, 1800200.
17. K. Yang, Q. Liao, J. Huang, Z. Zhang, M. Su, Z. Chen, Z. Wu, D. Wang, Z. Lai, H. Y. Woo, Y. Cao, P. Gao and X. Guo, *Angew. Chem. Int. Ed.,* 2022, **61**, e202113749.
18. Z. Zhu, Y. Bai, T. Zhang, Z. Liu, X. Long, Z. Wei, Z. Wang, L. Zhang, J. Wang, F. Yan and S. Yang, *Angew. Chem. Int. Ed.,* 2014, **53**, 12571-12575.
19. N. Arora, M. I. Dar, A. Hinderhofer, N. Pellet, F. Schreiber, S. M. Zakeeruddin and M. Gratzel, *Science*, 2017, **358**, 768-771.
20. Y. Hou, X. Du, S. Scheiner, D. P. McMeekin, Z. Wang, N. Li, M. S. Killian, H. Chen, M. Richter, I. Levchuk, N. Schrenker, E. Spiecker, T. Stubhan, N. A. Luechinger, A. Hirsch, P. Schmuki, H. P. Steinruck, R. H. Fink, M. Halik, H. J. Snaith and C. J. Brabec, *Science*, 2017, **358**, 1192-1197.
21. X. Q. Li, W. J. Chen, S. H. Wang, G. Y. Xu, S. Liu, Y. W. Li and Y. F. Li, *Adv. Funct. Mater.*, 2021, **31**, 2010696.
22. Z. W. Wang, Q. Q. Dong, Y. J. Xia, H. Yu, K. C. Zhang, X. D. Liu, X. Guo, Y. Zhou, M. J. Zhang and B. Song, *Org. Electron.*, 2016, **33**, 142-149.
23. H. Guo, C.-Y. Yang, X. Zhang, A. Motta, K. Feng, Y. Xia, Y. Shi, Z. Wu, K. Yang, J. Chen, Q. Liao, Y. Tang, H. Sun, H. Y. Woo, S. Fabiano, A. Facchetti and X. Guo, *Nature*, 2021, **599**, 67-73.
24. Y. Zhao, T. Heumueller, J. Zhang, J. Luo, O. Kasian, S. Langner, C. Kupfer, B. Liu, Y. Zhong, J. Elia, A. Osvet, J. Wu, C. Liu, Z. Wan, C. Jia, N. Li, J. Hauch and C. J. Brabec, *Nat. Energy*, 2021, **7**, 144-152.
25. Q. Fu, X. Tang, H. Liu, R. Wang, T. Liu, Z. Wu, H. Y. Woo, T. Zhou, X. Wan, Y. Chen and Y. Liu, *J. Am. Chem. Soc.*, 2022, **144**, 9500-9509.
26. Q. Fu, H. Liu, S. Li, T. Zhou, M. Chen, Y. Yang, J. Wang, R. Wang, Y. Chen and Y. Liu, *Angew. Chem. Int. Ed.,* 2022, e202210356.
27. M. J. Jeong, K. M. Yeom, S. J. Kim, E. H. Jung and J. H. Noh, *Energy Environ. Sci.*, 2021, **14**, 2419-2428.
28. T. Niu, W. Zhu, Y. Zhang, Q. Xue, X. Jiao, Z. Wang, Y.-M. Xie, P. Li, R. Chen, F. Huang, Y. Li, H.-L. Yip and Y. Cao, *Joule*, 2021, **5**, 249-269.
29. H. Zhu, Z. Shen, L. Pan, J. Han, F. T. Eickemeyer, Y. Ren, X. Li, S. Wang, H. Liu, X. Dong, S. M. Zakeeruddin, A. Hagfeldt, Y. Liu and M. Grätzel, *ACS Energy Lett.*, 2020, **6**, 208-215.
30. H. Guo, H. Zhang, C. Shen, D. Zhang, S. Liu, Y. Wu and W. H. Zhu, *Angew. Chem. Int. Ed.,* 2021, **60**, 2674-2679.
31. Y.-H. Zhang and Y. Li, *Rare Metals*, 2021, **40**, 2993-3018.
32. M. Jeong, W. Choi In, M. Go Eun, Y. Cho, M. Kim, B. Lee, S. Jeong, Y. Jo, W. Choi Hye, J. Lee, J.-H. Bae, K. Kwak Sang, S. Kim Dong and C. Yang, *Science*, 2020, **369**, 1615-1620.
33. X. Yin, J. Zhou, Z. Song, Z. Dong, Q. Bao, N. Shrestha, S. S. Bista, R. J. Ellingson, Y. Yan and W. Tang, *Adv. Funct. Mater.*, 2019, **29**, 1904300.
34. J. Zhou, X. Yin, Z. Dong, A. Ali, Z. Song, N. Shrestha, S. S. Bista, Q. Bao, R. J. Ellingson, Y. Yan and W. Tang, *Angew. Chem. Int. Ed.*, 2019, **58**, 13717-13721.
35. Y. Wang, W. Chen, L. Wang, B. Tu, T. Chen, B. Liu, K. Yang, C. W. Koh, X. Zhang, H. Sun, G. Chen, X. Feng, H. Y. Woo, A. B. Djurisic, Z. He and X. Guo, *Adv. Mater.*, 2019, **31**, e1902781.
36. Y. Liu, Q. Chen, H.-S. Duan, H. Zhou, Y. Yang, H. Chen, S. Luo, T.-B. Song, L. Dou, Z. Hong and Y. Yang, *J. Mater. Chem. A*, 2015, **3**, 11940-11947.
37. Y. Liu, Z. Hong, Q. Chen, H. Chen, W.-H. Chang, Y. Yang, T.-B. Song and Y. Yang, *Adv. Mater.*, 2016, **28**, 440-446.
38. H. Zhang, Y. Wu, W. Zhang, E. Li, C. Shen, H. Jiang, H. Tian and W.-H. Zhu, *Chem. Sci.*, 2018, **9**, 5919-5928.
39. B. Tu, Y. Wang, W. Chen, B. Liu, X. Feng, Y. Zhu, K. Yang, Z. Zhang, Y. Shi, X. Guo, H. F. Li, Z. Tang, A. B. Djurisic and Z. He, *ACS Appl. Mater. Interfaces*, 2019, **11**, 48556-48563.
40. Q. Cheng, H. Chen, F. Yang, Z. Chen, W. Chen, H. Yang, Y. Shen, X. M. Ou, Y. Wu, Y. Li and Y. Li, *Angew. Chem. Int. Ed.,* 2022, **61**, e202210613.
41. P. Y. Yan, D. B. Yang, H. Q. Wang, S. C. Yang and Z. Y. Ge, Energy Environ. Sci., 2022, 15, 3630-3669.
42. I. McCulloch, R. S. Ashraf, L. Biniek, H. Bronstein, C. Combe, J. E. Donaghey, D. I. James, C. B. Nielsen, B. C. Schroeder and W. Zhang, *Acc. Chem. Res.,* 2012, **45**, 714-722.
43. X. Liu, Q. D. Li, Y. C. Li, X. Gong, S. J. Su and Y. Cao, *J. Mater. Chem. A*, 2014, **2**, 4004-4013.
44. S. Feng, C. Zhang, Y. Liu, Z. Bi, Z. Zhang, X. Xu, W. Ma and Z. Bo, *Adv. Mater.*, 2017, **29**, 1703527.
45. Y. H. Cai, X. L. Zhang, X. N. Xue, D. H. Wei, L. J. Huo and Y. M. Sun, *J. Mater. Chem. C*, 2017, **5**, 7777-7783.
46. T. Malinauskas, D. Tomkute-Luksiene, R. Sens, M. Daskeviciene, R. Send, H. Wonneberger, V. Jankauskas, I. Bruder and V. Getautis, *ACS Appl. Mater. Interfaces*, 2015, **7**, 11107-11116.
47. V. A. Chiykowski, Y. Cao, H. Tan, D. P. Tabor, E. H. Sargent, A. Aspuru-Guzik and C. P. Berlinguette, *Angewandte Chemie International Edition*, 2018, **57**, 1552 9-15533.
48. S. Wang, H. Chen, J. Zhang, G. Xu, W. Chen, R. Xue, M. Zhang, Y. Li and Y. Li, *Adv. Mater.*, 2019, **31**, e1903691.
49. M. Qin, H. Xue, H. Zhang, H. Hu, K. Liu, Y. Li, Z. Qin, J. Ma, H. Zhu, K. Yan, G. Fang, G. Li, U. S. Jeng, G. Brocks, S. Tao and X. Lu, *Adv. Mater.*, 2020, **32**, e2004630.
50. J. Wang, L. Yuan, H. Luo, C. Duan, B. Zhou, Q. Wen and K. Yan, *Chem. Eng. J.*, 2022, **446**, 136968.
51. L. Yuan, H. Luo, J. Wang, Z. Xu, J. Li, Q. Jiang and K. Yan, *J. Mater. Chem. A*, 2021, **9**, 4781-4788.
52. Z. Li, Z. Zhu, C. C. Chueh, S. B. Jo, J. Luo, S. H. Jang and A. K. Jen, *J. Am. Chem. Soc.*, 2016, **138**, 11833-11839.
53. Q. Fan, W. Su, X. Guo, B. Guo, W. Li, Y. Zhang, K. Wang, M. Zhang and Y. Li, *Adv. Energy Mater.*, 2016, **6**, 1600430.

54. R. Wang, L. Lüer, S. Langner, T. Heumueller, K. Forberich, H. Zhang, J. Hauch, N. Li and C. J. Brabec, *ChemSusChem*, 2021, **14**, 3590-3598.
55. L. Yuan, J. Li, Z. W. Wang, P. Huang, K. C. Zhang, Y. Liu, K. Zhu, Z. Li, T. Cao, B. Dong, Y. Zhou, M. Zhou, B. Song and Y. Li, *ACS Appl. Mater. Interfaces*, 2017, **9**, 42961-42968.
56. P. Huang, Q. Chen, K. Zhan g, L. Yuan, Y. Zhou, B. Song and Y. Li, *J. Mater. Chem. A*, 2019, **7**, 6213-6219.
57. Q. Jiang, L. Zhang, H. Wang, X. Yang, J. Meng, H. Liu, Z. Yin, J. Wu, X. Zhang and J. You, *Nat. Energy*, 2016, **2**, 16177.
58. A. Al-Ashouri, E. Köhnen, B. Li, A. Magomedov, H. Hempel, P. Caprioglio, J. A. Márquez, A. B. Morales Vilches, E. Kasparavicius, J. A. Smith, N. Phung, D. Menzel, M. Grischek, L. Kegelmann, D. Skroblin, C. Gollwitzer, T. Malinauskas, M. Jošt, G. Matič, B. Rech, R. Schlatmann, M. Topič, L. Korte, A. Abate, B. Stannowski, D. Neher, M. Stolterfoht, T. Unold, V. Getautis and S. Albrecht, *Science*, 2020, **370**, 1300.
59. B. Krogmeier, F. Staub, D. Grabowski, U. Rau and T. Kirchartz, *Sustain. Energy Fuels*, 2018, **2**, 1027-1034.
60. X. B. Cao, Y. H. Li, F. Fang, X. Cui, Y. W. Yao and J. Q. Wei, *RSC Advances*, 2016, **6**, 70925-70931.
61. Q. Dong, Y. Fang, Y. Shao, P. Mulligan, J. Qiu, L. Cao and J. Huang, *Science*, 2015, **347**, 967-970.
62. D. Shi, V. Adinolfi, R. Comin, M. Yuan, E. Alarousu, A. Buin, Y. Chen, S. Hoogland, A. Rothenberger, K. Katsiev, Y. Losovyj, X. Zhang, P. A. Dowben, O. F. Mohammed, E. H. Sargent and O. M. Bakr, *Science*, 2015, **347**, 519-522.
63. V. M. Le Corre, E. A. Duijnstee, O. El Tambouli, J. M. Ball, H. J. Snaith, J. Lim and L. J. A. Koster, *ACS Energy Lett.*, 2021, **6**, 1087-1094.
64. J. Xie, K. Yan, H. Zhu, G. Li, H. Wang, H. Zhu, P. Hang, S. Zhao, W. Guo, D. Ye, L. Shao, X. Guan, T. Ngai, X. Yu and J. Xu, *Science Bulletin*, 2020, **65**, 1726-1734.
65. H. Yu, F. Wang, F. Xie, W. Li, J. Chen and N. Zhao, *Adv. Funct. Mater.*, 2014, **24**, 7102-7108.
66. C. Li, Q. Guo, H. Zhang, Y. Bai, F. Wang, L. Liu, T. Hayat, A. Alsaedi and Z. Tan, *Nano Energy*, 2017, **40**, 248-257.

Supplementary Materials

Conformally bonded molecular interface retarded iodine migration for durable perovskite solar cells

Ligang Yuan,[1,†] Weiya Zhu,[1,†] Yiheng Zhang,[1] Yuan Li,[1,*] Christopher C. S. Chan,[2] Minchao Qin,[3] Jianhang Qiu,[4] Kaicheng Zhang,[5] Jiaxing Huang,[1] Jiarong Wang,[1] Huiming Luo,[1] Zheng Zhang,[1] Ruipeng Chen,[1] Weixuan Liang,[1] Qi Wei,[1] Kam Sing Wong,[2] Xinhui Lu,[3] Ning Li,[1,*] Christoph J. Brabec,[5, 6] Liming Ding,[7] Keyou Yan[1,*]

[1] School of Environment and Energy, State Key Laboratory of Luminescent Materials and Devices, Institute of Polymer Optoelectronic Materials and Devices, Guangdong Provincial Key Laboratory of Solid Wastes Pollution Control and Recycling, Guangdong Provincial Key Laboratory of Luminescence from Molecular Aggregates, AIE Institute, South China University of Technology, Guangzhou 510000, P. R. China

[2] Department of Physics and William Mong Institute of Nano Science and Technology, The Hong Kong University of Science and Technology, Clearwater Bay, Hong Kong, P. R. China

[3] Department of Physics, The Chinese University of Hong Kong, Shatin 999077, Hong Kong, P. R. China

[4] Shenyang National Laboratory for Materials Science, Institute of Metal Research, Chinese Academy of Sciences, Shenyang, 110016, China

[5] Institute of Materials for Electronics and Energy Technology (i-MEET) Friedrich-Alexander-University Erlangen-Nuremberg Martensstraße 7, Erlangen 91058, Germany

[6] Helmholtz-Institute Erlangen-Nürnberg for Renewable Energy (HI ERN), Forschungszentrum Jülich (FZJ), Erlangen 91058, Germany

[7] Center for Excellence in Nanoscience (CAS), Key Laboratory of Nanosystem and Hierarchical Fabrication (CAS), National Center for Nanoscience and Technology, Beijing 100190 P. R. China

[†] These two authors contributed equally to this work.

*Corresponding author: celiy@scut.edu.cn, ningli2022@scut.edu.cn, kyyan@scut.edu.cn

Materials and Methods

Materials: Methylammonium bromide (MABr, 99.5%), Methylammonium chloride (MACl, 99.5%), Lead iodide (PbI_2, 99.99%), lithium bistrifluoromethane-sulfonimidate (LiTFSI, 99.95%) and 4-tert-butylpyridine (tBP) were purchased from Xi'an polymer light technology Corp. Formamidinium iodide (FAI) and Guanidinium iodide (GAI) were purchased from Greatcell Solar. Ltd. Spiro-OMeTAD (99.86%) purchased from Advanced Election Technology Co., Ltd. The SnO_2 colloid precursor (tin(IV) oxide, 15% in H_2O colloidal dispersion) were acquired from Alfa Aesar.

Isopropanol (IPA, 99.5%), *N,N*-dimethylformamide (DMF, anhydrous, 99.8%), dimethyl sulfoxide (DMSO, anhydrous, 99.8%), chlorobenzene (CB, anhydrous, 99.8%) and acetonitrile (anhydrous, 99.9%) were acquired from Sigma-Aldrich and used as received without further purification. Commercially available reagents and chemicals were purchased from Suzhou Nakai Technology or Energy chemical and used without further purification.

Synthesis for dopant-free HTMs

Synthesis of TPAOMe-BT-Br

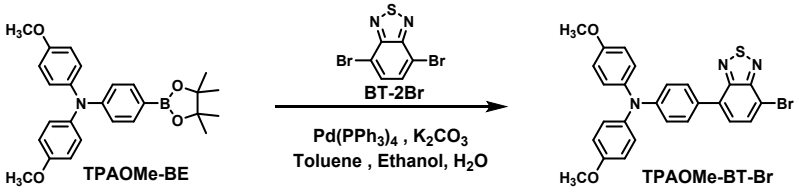

Scheme S1. Synthetic routes of **TPAOMe-BT-Br**.

TPAOMe-BE (3.448 g, 8.00 mmol, purchased from Suzhou Nakai Technology), **BT-2Br** (3.516 g, 12.00 mmol), $Pd(PPh_3)_4$ (30 mg, 0.026 mmol), potassium carbonate (K_2CO_3) aqueous solution (2 mol/L, 20 mL), ethanol (20 mL) and toluene (50 mL) were mixed and stirred under nitrogen atmosphere, and then heated to 100 °C and soaked for 12 h. After the reaction was completed, the mixture was cooled to room temperature and extracted three times with dichloromethane. The crude product was purified by column chromatography (silica gel, petroleum ether/dichloromethane, v/v, 3:1) to afford **TPAOMe-BT-Br** as a red solid compound (3.774 g, 91.0%). **^{1}H NMR (400 MHz, $CDCl_3$) δ 7.88 (d, J = 7.6 Hz, 1H), 7.75 (d, J = 8.5 Hz, 2H), 7.51 (d, J = 7.6 Hz, 1H), 7.13 (d, J = 7.3 Hz, 4H), 7.03 (d, J = 7.5 Hz, 2H), 6.87 (d, J = 8.9 Hz, 4H), 3.81 (s, 6H).**

Synthesis of L1

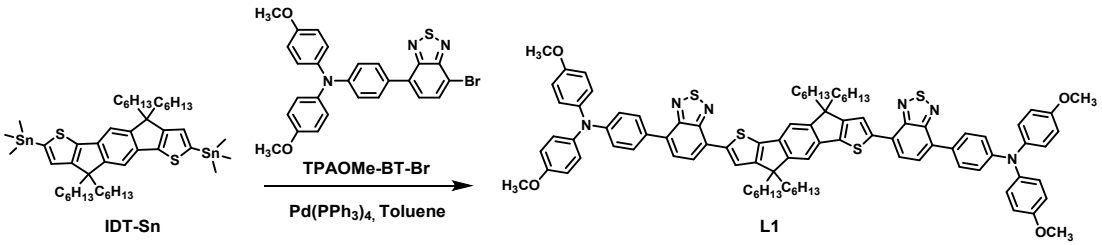

Scheme S2. Synthetic routes of **L1**.

TPAOMe-BT-Br (0.319 g, 0.62 mmol), **IDT-Sn** (0.260 g, 0.28 mmol), $Pd(PPh_3)_4$ (0.013 g, 0.011 mmol) and toluene (15 mL) were mixed and stirred under nitrogen atmosphere, and then heated to 110 °C and soaked for 4 h. After the reaction was completed, the mixture was cooled to room temperature and extracted three times with dichloromethane. The crude product was purified by column chromatography (silica gel, petroleum ether/dichloromethane, v/v, 2:1) to afford **L1** as a black solid compound (0.354 g, 85.5%). **^{1}H NMR (400 MHz, $CDCl_3$) δ 8.06 (s, 2H), 7.97 (d, J = 7.5 Hz, 2H), 7.85 (d, J = 8.6 Hz, 4H), 7.70 (d, J = 7.6 Hz, 2H), 7.39 (s, 2H), 7.15 (d, J = 8.7 Hz, 8H), 7.07 (d, J = 8.5 Hz, 4H), 6.88 (d, J = 8.8 Hz, 8H), 3.82 (s, 12H), 2.14 – 2.06 (m, 4H), 1.96 (t, J = 10.2 Hz, 4H), 1.13 (s, 24H), 0.98 (s, 4H), 0.90 (s, 4H), 0.77 (t, J = 6.6 Hz, 12H). ^{13}C NMR (126 MHz, $CDCl_3$) δ 156.20, 129.70, 127.07, 119.80, 114.79, 113.42, 55.54, 54.23, 39.30, 31.63, 29.78, 24.26, 22.61, 14.05.**

Synthesis of L2

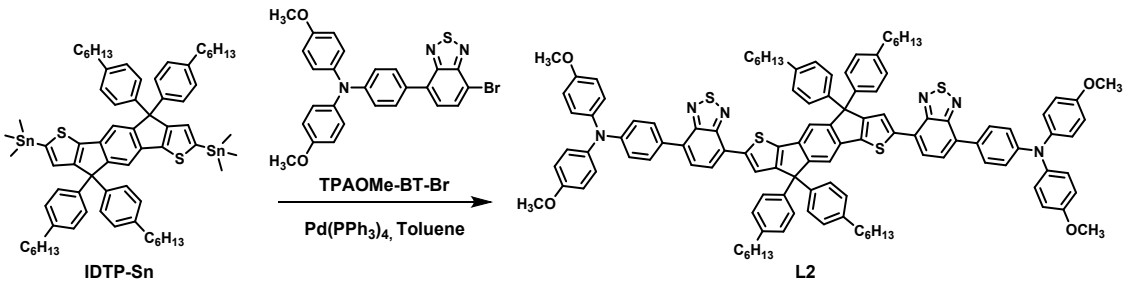

Scheme S3. Synthetic routes of **L2**.

TPAOMe-BT-Br (0.259 g, 0.499 mmol), **IDTP-Sn** (0.280 g, 0.227 mmol, purchased from Suzhou Nakai Technology), $Pd(PPh_3)_4$ (0.010 g, 0.009 mmol) and toluene (15 mL) were mixed and stirred under nitrogen atmosphere, and then heated to 110 °C and soaked for 4 h. After the reaction was completed, the mixture was cooled to room

temperature and extracted three times with dichloromethane. The crude product was purified by column chromatography (silica gel, petroleum ether/dichloromethane, v/v, 2:1) to afford **L2** as a black solid compound (0.366 g, 90.5%). **^{1}H NMR (400 MHz, $CDCl_3$) δ 8.01 (s, 2H), 7.95 – 7.71 (m, 6H), 7.53 (s, 6H), 7.28 (s, 2H), 7.26 – 7.17 (m, 4H), 7.10 (d, J = 8.1 Hz, 14H), 6.88 (s, 12H), 3.82 (s, 12H), 2.60 – 2.54 (m, 8H), 1.59 (p, J = 7.6 Hz, 8H), 1.34 (d, J = 7.6 Hz, 6H), 1.28 (d, J = 14.2 Hz, 18H), 0.86 (t, J = 6.5 Hz, 12H). ^{13}C NMR (126 MHz, $CDCl_3$) δ 141.91, 141.53, 128.42, 128.01, 55.51, 35.61, 31.74, 31.37, 29.18, 22.61, 14.12.**

Synthesis of L3

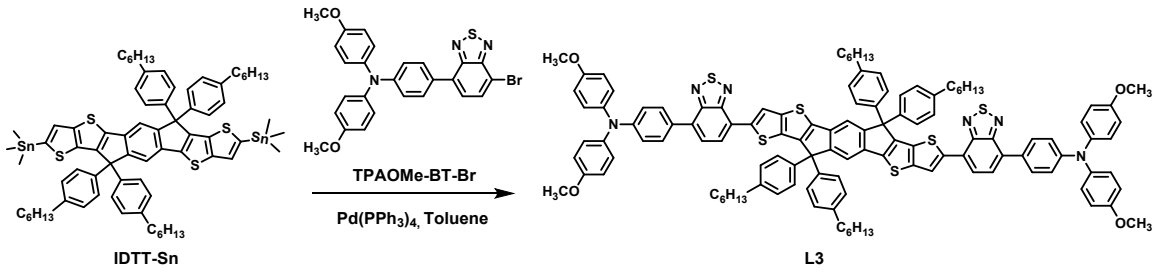

Scheme S4. Synthetic routes of **L3**.

TPAOMe-BT-Br (0.241 g, 0.466 mmol), **IDTT-Sn** (0.285 g, 0.211 mmol, purchased from Suzhou Nakai Technology), $Pd(PPh_3)_4$ (0.010 g, 0.009 mmol) and toluene (15 mL) were mixed and stirred under nitrogen atmosphere, and then heated to 110 °C and soaked for 4 h. After the reaction was completed, the mixture was cooled to room temperature and extracted three times with dichloromethane. The crude product was purified by column chromatography (silica gel, petroleum ether/dichloromethane, v/v, 2:1) to afford **L3** as a black solid compound (0.336 g, 83.8%). **^{1}H NMR (400 MHz, $CDCl_3$) δ 8.54 (s, 2H), 8.09 – 7.79 (m, 6H), 7.56 (s, 6H), 7.28 (s, 2H), 7.28 – 7.27 (m, 2H), 7.25 – 7.10 (m, 12H), 7.04 (s, 8H), 6.92 (s, 10H), 3.87 (s, 12H), 2.61 – 2.55 (m, 8H), 1.62 (d, J = 14.5 Hz, 8H), 1.39 – 1.27 (m, 24H), 0.86 (s, 12H). ^{13}C NMR (126 MHz, $CDCl_3$) δ 141.85, 140.19, 128.55, 128.13, 55.52, 35.63, 31.72, 31.28, 29.20, 22.61, 14.10.**

Fabrication of devices: ITO glass substrates (Advanced Election Technology Co., Ltd.) were cleaned sequentially by sonication in detergent, deionized water, acetone,

ethanol and isopropanol, twice for each liquid and 15 min for each time, followed by ultraviolet-ozone treatment for 30 min. The SnO_2 electron transport layer was coated onto the ITO substrate with diluted SnO_2 nanoparticles solution (2.67%) in ambient air, and then annealed at 150 °C for 30 min. After being cooled to room temperature, the substrate was treated with UV-ozone for 30 min before spin-coating of perovskite solution. The perovskite layer was deposited by a two-step spin coating method; first, 360 mg PbI_2 and 10.2 mg CsI in 600 μL dissolved in mixed solvent (DMF:DMSO (v/v=95:5)) followed by stirring at 70 °C for 4 h, then the PbI_2 solution was spin coated onto the SnO_2 ETL at 2500 rpm for 50 s, during this process, the mixture organic amino solution of FAI:MABr:MACl:GAI (60 mg:6 mg:6 mg:4 mg in 1 mL isopropanol) was adding before the end of 30 s, and then the perovskite film was annealed in at 150 °C for 11 min. For the doped spiro-OMeTAD-based devices, 72.3 mg/mL spiro-OMeTAD with 28.8 μL tBP and 17.5 μL Li-TFSI (520 mg/mL in Acetonitrile) in CB was deposited by spin-coating at 4000 rpm for 30 s. For dopant-free HTM devices, different concentrations in CB solution with different speeds were spin coating on the perovskite film. Finally, MoO_3 blocking layer (6 nm) and metal electrode (80 nm) were eventually deposited by vacuum thermal evaporation (pressure < 2×10^{-4} Pa). The overlapping area between the cathode and anode defined a pixel size of 0.08 cm^{-2}.

HTMs characterizations:

^{1}H-NMR spectra were recorded by DRX-400 spectrometer (400 and 500 MHz ^{1}H-NMR frequency, Bruker Co., Ettlingen, Germany) in $CDCl_3$ at room temperature. ^{13}C NMR spectra were collected using the same instrument at 126 MHz. The mass spectra were recorded on MALDI-TOF/TOF 5800 system (AB SCIEX). Cyclic voltammetry (CV) tests were performed in CH_2Cl_2 solution with 0.1 M tetrabutylammonium hexafluorophosphate (Bu_4NPF_6) as the electrolyte at a scan rate of 50 mV/s, a $Hg/HgCl_2$ (Saturated KCl solution) electrode as the reference electrode, a carbon-glass electrode as the working electrode, a Pt line electrode as the counter electrode

and ferrocene/ferrocenium (Fc/Fc^+) as an internal reference on electrochemistry workstation (CHI660E, China). XPS results were acquired on a photoelectron spectrometer (ESCALAB 250Xi, Thermo Fisher Scientific). Thermogravimetric analysis (TGA) was performed on a thermogravimetric analyzer (TA Instruments) at a scan rate of 20 K/min in the nitrogen atmosphere. Differential scanning calorimetry (DSC) was recorded on a DSC201F2 differential scanning calorimeter under the protection of nitrogen at a heating rate of 10 K/min.

DFT calculation: The neutral and charged molecular geometries are optimized by the DFT method with the Lee-Yang-Parr (B3LYP) hybrid functional and 6-31G(d,p) basis set implemented in the Gaussian 09 package.

Film characterizations measurements:

The absorption spectrum of HTMs and perovskite films were tested using a Cary Series UV-Vis-NIR Spectrophotometer.

Contact angle measurements were conducted on ZJ-7000 with a drop of ultrapure water (0.002 mL). The photographs were taken 1 second after water dripping.

The perovskite film and HTMs surface morphology were characterized by atomic force microscope (AFM, Bruker, Santa Barbara, CA).

Fourier transform infrared spectra were obtained on a CCR-1 instrument (Thermo Nicolet). PbI_2 and L3 are the pure powders. The PbI_2/L3 sample was mixed PbI_2 solution and L3 solution directly, then the powder was dried at 80 °C for eight hours. For the ART FTIR measurements, the perovskite film covered L3 film by spin-coating 1mg/mL L3 CB solution with a speed of 3000 rpm 30s.

The top-view and cross-sectional SEM images of the samples were characterized using a high-resolution scanning electron microscope (Zeiss Merlin). An electron beam accelerated to 5 kV was used with an InLens detector.

Transmission electron microscope (TEM, JEOL JEM-2100 Plus) measurements were performed under 200 kV. We exfoliated the films from the substrates by floating

technique with orthogonal solvent. The substrates with a structure of ITO/PEDOT:PSS/HTM prepared by spin-coating, then deionized water were employed to dissolve the bottom PEDOT:PSS film, leaving behind HTM film on the surface. The films were collected by copper grid for characterization.

The GIWAXS measurements were performed with a Xeuss 2.0 SAXS/WAXS laboratory beam line using a Cu X-ray source (8.05 keV, 1.54 Å) and a Pilatus3R 300K detector. The incidence angle was 0.2º.

Time resolved photoluminescence (TRPL) was performed on encapsulated films of glass substrate/perovskite/HTM. The samples were excited from the top surface with a 640 nm sub-100ps diode laser (Edinburgh Instruments EPL640). The PL was collected and diverted into a monochromator transmitting the peak PL wavelength and collected by a single photon counter to carry out time correlated single photon counting with a Becker and Hickl system. The time resolution is <500 ps.

Transient absorption spectroscopy was carried out on encapsulated pure HTM films to minimize photooxidation and environmental degradation during the measurement. A Ti:Sapphire regenerative laser amplifier (Coherent Legend) provided 800 nm fundamental pulses with pulse width of 100 fs at 1 kHz. Excitation pump pulses at 400 nm was generated by splitting the fundamental pulse into an optical parametric amplifier (Opera Solo). The probe beam is set on a mechanical delay stage and focused onto a YAG crystal to generate a stable supercontinuum for broadband absorption probe. The pump and probe beams are spatially overlapped on the sample surface and the transmission is collected by a spectrometer (Acton SpectraPro 275) equipped with a line array CCD.

Device characterizations measurements:

J–V characteristics of photovoltaic cells were taken using a Keithley 2400 source measurement unit under a simulated AM 1.5G spectrum. With a SS-F5-3A solar

simulator (Enli Technology CO., Ltd.), the light intensity was calibrated by standard KG3 reference silicon solar cells.

The Mott-Schottky plot measurements were measured by an IM6 electrochemical workstation (Zahner Zennium, Germany) at room temperature in ambient conditions. IPCE measurements also were performed on a Zahner system, using a TLS03 light source (300 HZ, 100 counts) at mixed mode.

Mobility and trap state density measurements:

Hole-only devices (ITO/PEDOT:PSS/HTL/MoO_x/Ag) were fabricated to calculate the hole mobility. The dark *J-V* characteristics of the hole-only devices were measured by a Keithley 2400 source.

The mobility of L-series HTLs is extracted by fitting the *J-V* curves by the Mott-Gurney equation of $J = 9\varepsilon_r\varepsilon_0 V^2/(8L^3)$.

The trap state density of perovskite film was determined by the trap-filled limit voltage using the equation of $n_t = 2\varepsilon\varepsilon_0 V_{TFL}/(qL^2)$ with a structure of ITO/PEDOT:PSS/perovskite/HTL/MoO_x/Ag.

Stability measurements: For the long-term storage stability, the unencapsulated PSCs with Ag top electrode were stored at argon filled glovebox under dark condition.

For thermal stability measurement (85°C), Ag electrode was replaced by Au and the PSCs were heated on a hotplate under dark condition, and the temperature was cooled down to room temperature before 30 min of PCE test.

For photo-thermal stability measurement (MPP & 85°C), The illumination was provided by white light-emitting diode lamp in a Lifetime Test equipment (Guangzhou Crysco Equipment Co.Ltd, P3000), and the radiation intensity is adjusted according the J_{SC}, which is equal to the J_{SC} under solar simulator. The temperature of

PSCs was provided an electric resistance heater and control by a temperature controller, and the temperature error is 0.2°C. In this study, our temperature was set to 85°C in argon filled glovebox.

For the XRD and optical images teats for thermal aged perovskite film covered with HTMs, the prepared ITO/SnO_2/perovskite/HTM samples were heated on the hotplate with a temperature of 85°C in argon filled glovebox.

For the AFM and optical microscope image for thermal aged HTM measurements, the 15mg/mL HTMs were spin-coated on the SnO_2/ITO glass substrates and heated on the hotplate with a temperature of 100°C in nitrogen filled glovebox.

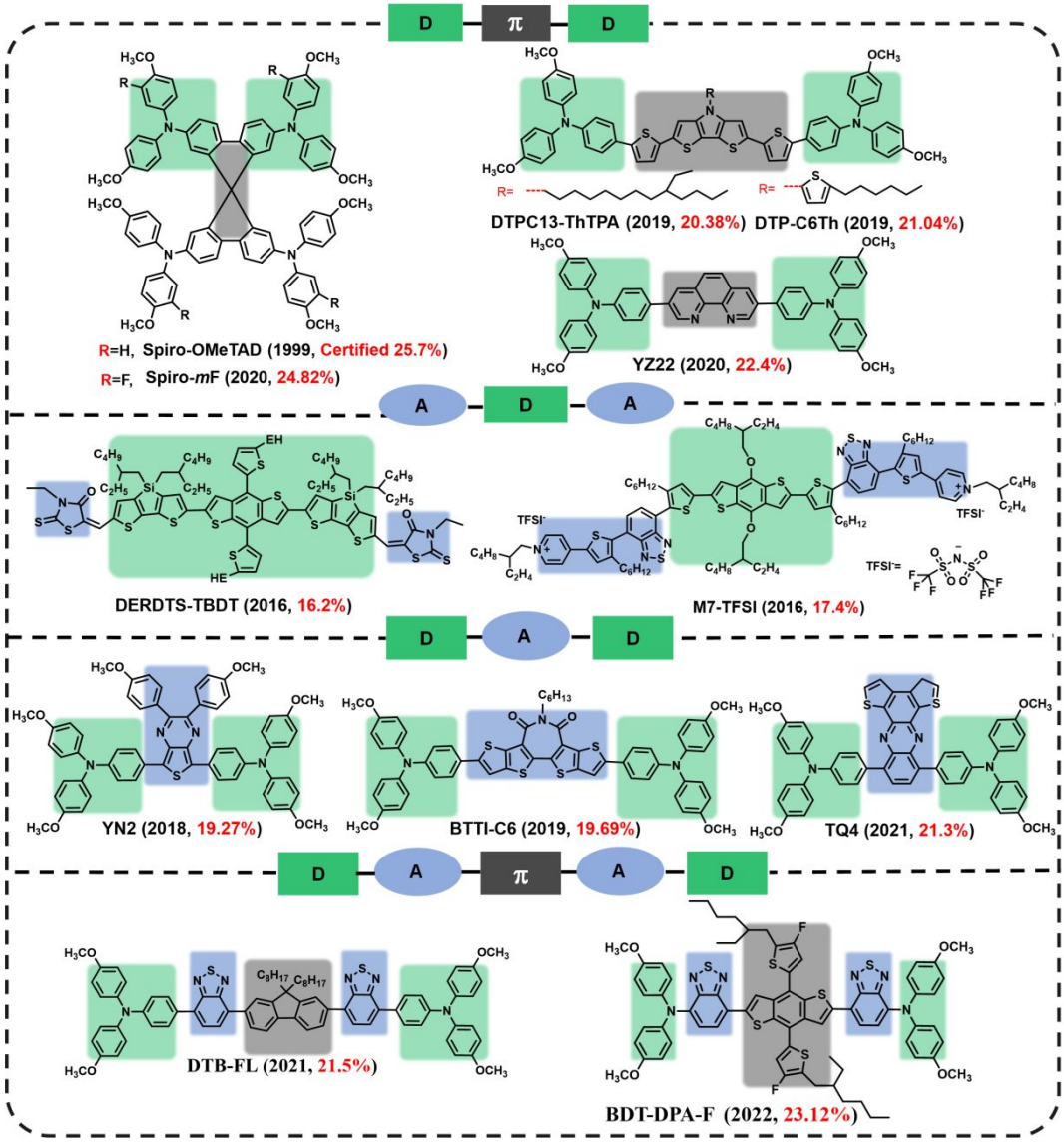

Fig. S1. Some established molecular structures of D-π-D, A-D-A and D-A-D HTMs for PSCs.[1-12]

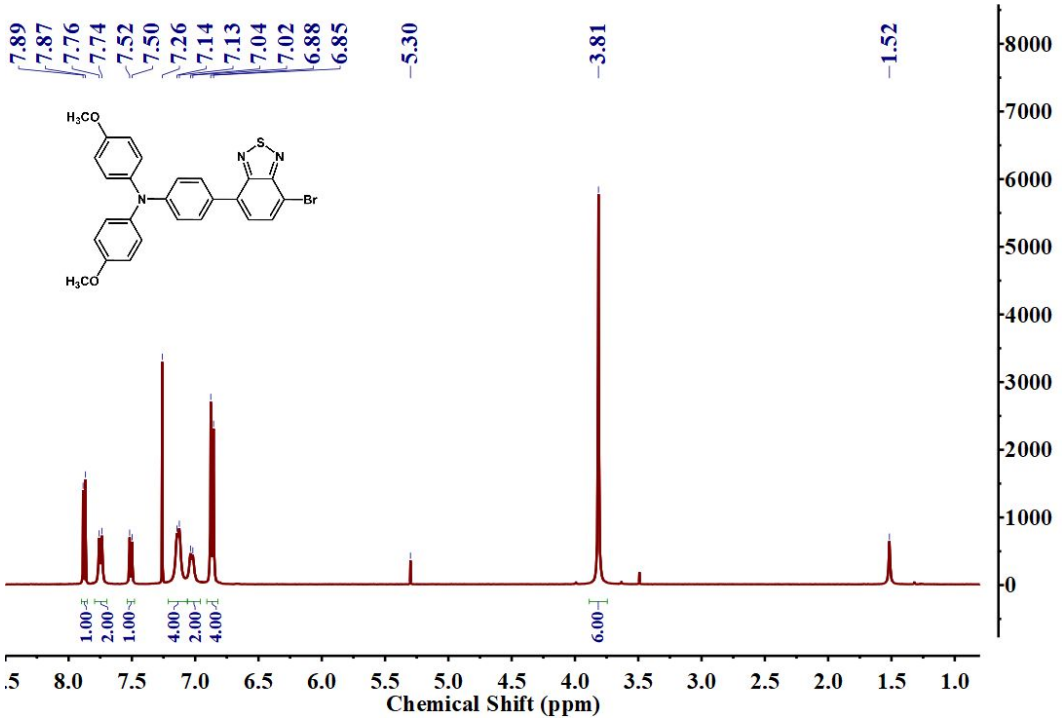

Fig. S2. **^{1}H NMR** spectrum of **TPAOMe-BT-Br**.

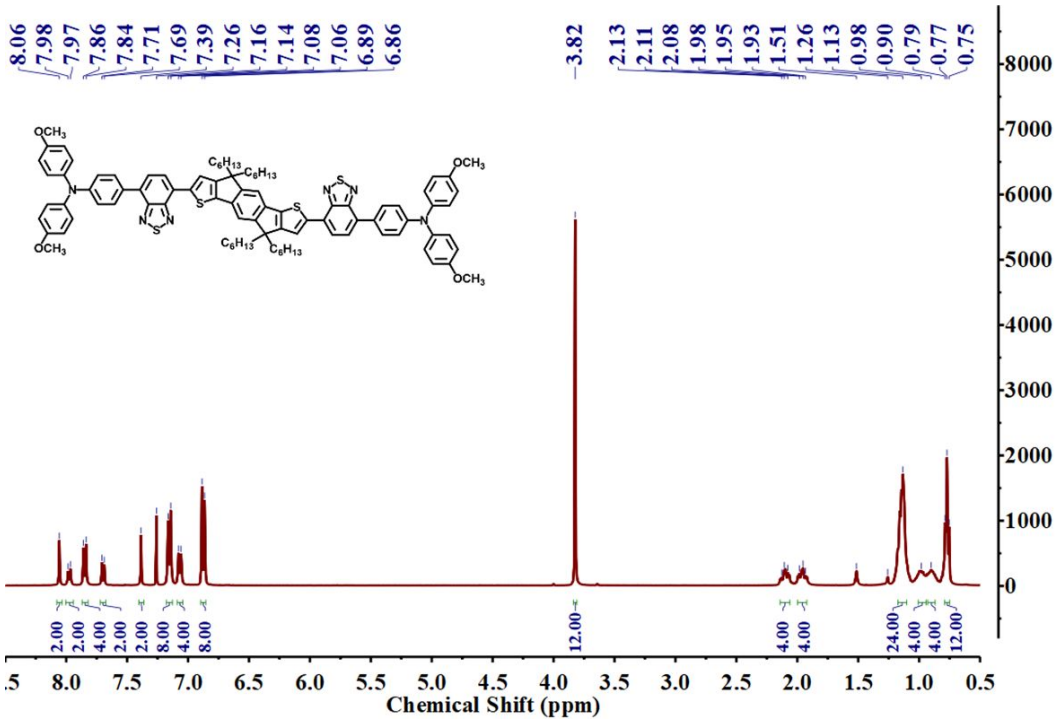

Fig. S3. **^{1}H NMR** spectrum of **L1**.

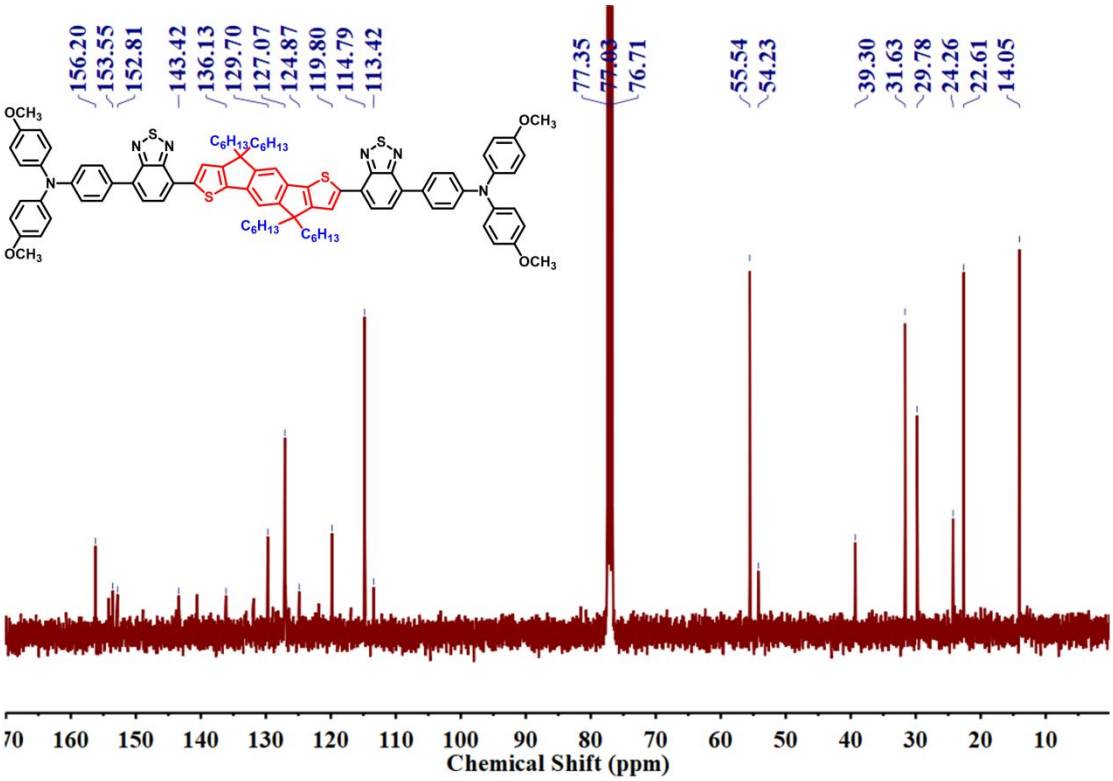

Fig. S4. **^{13}C NMR** spectrum **L1**.

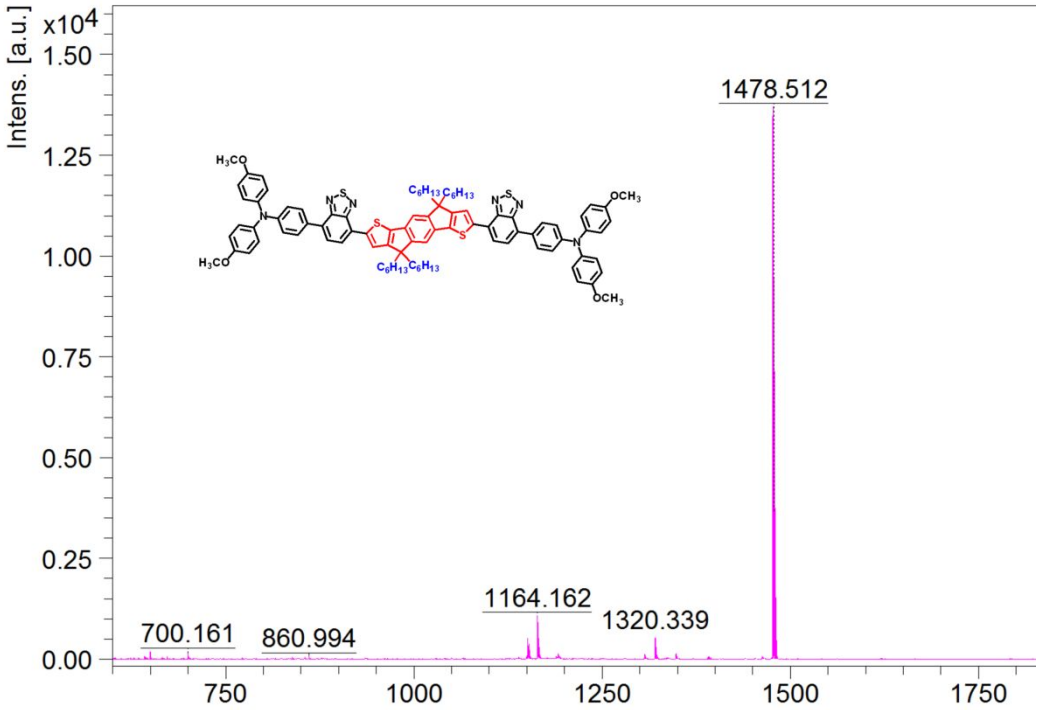

Fig. S5. MALDI-TOF-MS (m/z) spectrometry of **L1**: calcd. for $C_{92}H_{96}N_6O_4S_4$, 1478.06; found: 1478.516.

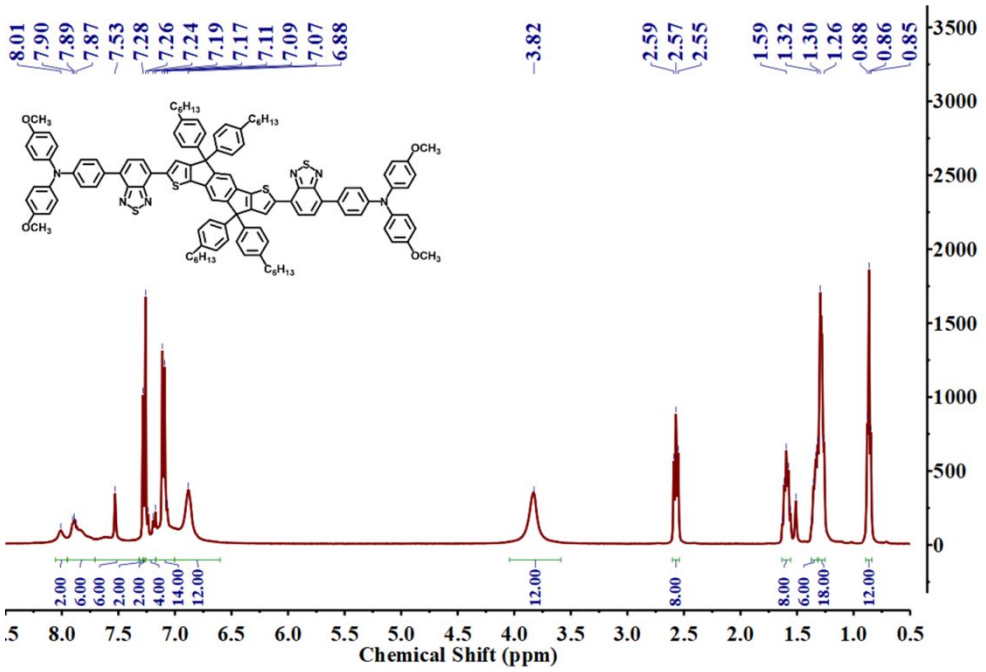

Fig. S6. ^{1}**H NMR** spectrum of **L2**.

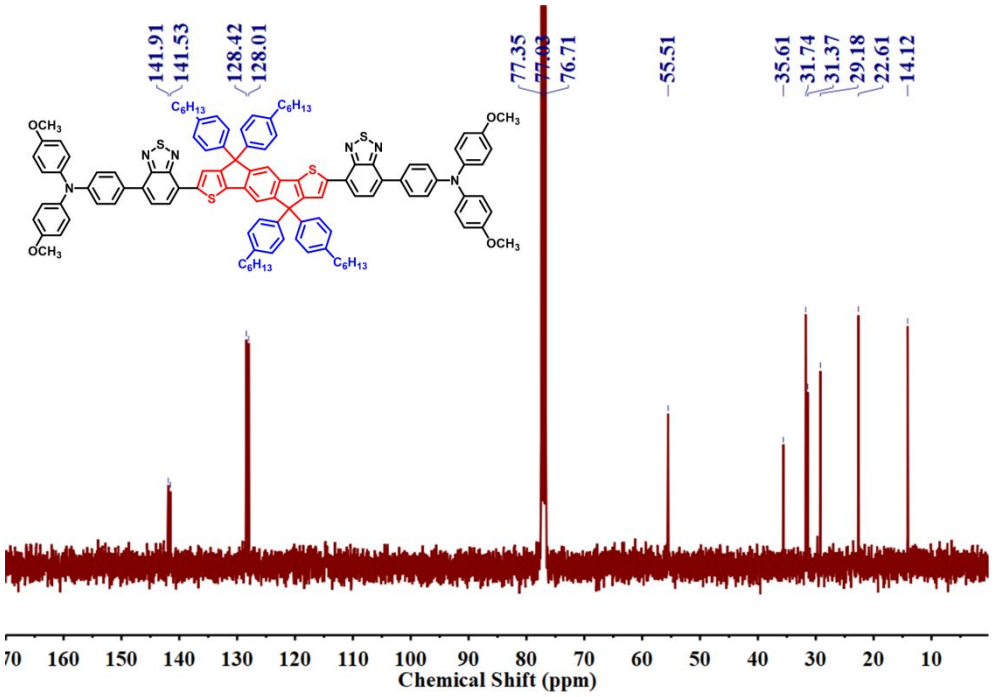

Fig. S7. ^{13}**C NMR** spectrum **L2**.

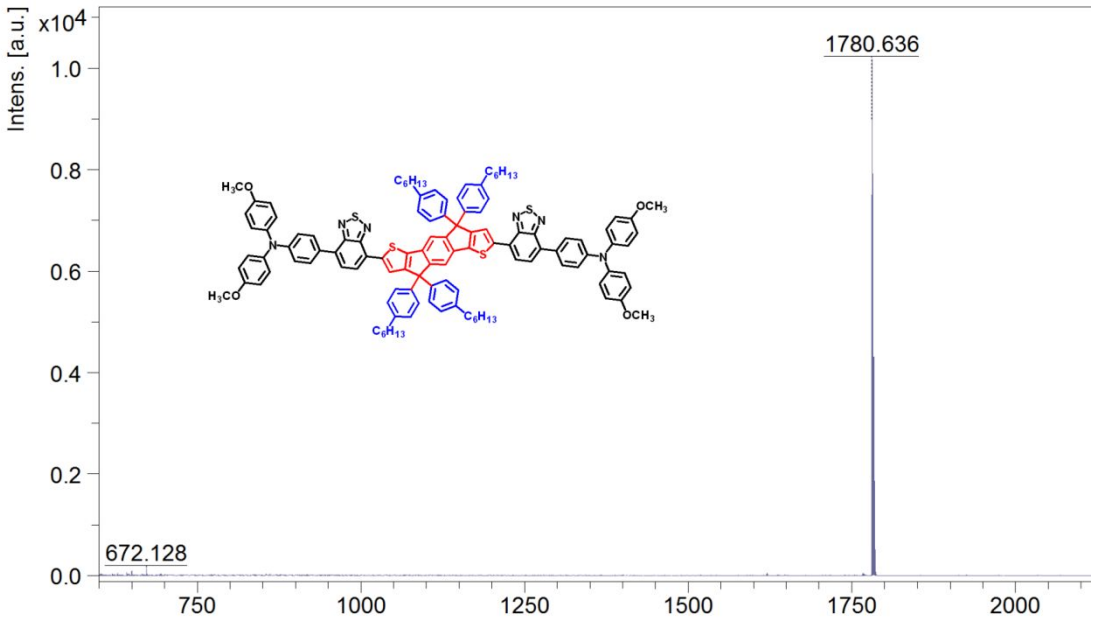

Fig. S8. MALDI-TOF-MS (m/z) spectrometry of **L2**: calcd. for $C_{116}H_{112}N_6O_4S_4$, 1782.45; found: 1780.636.

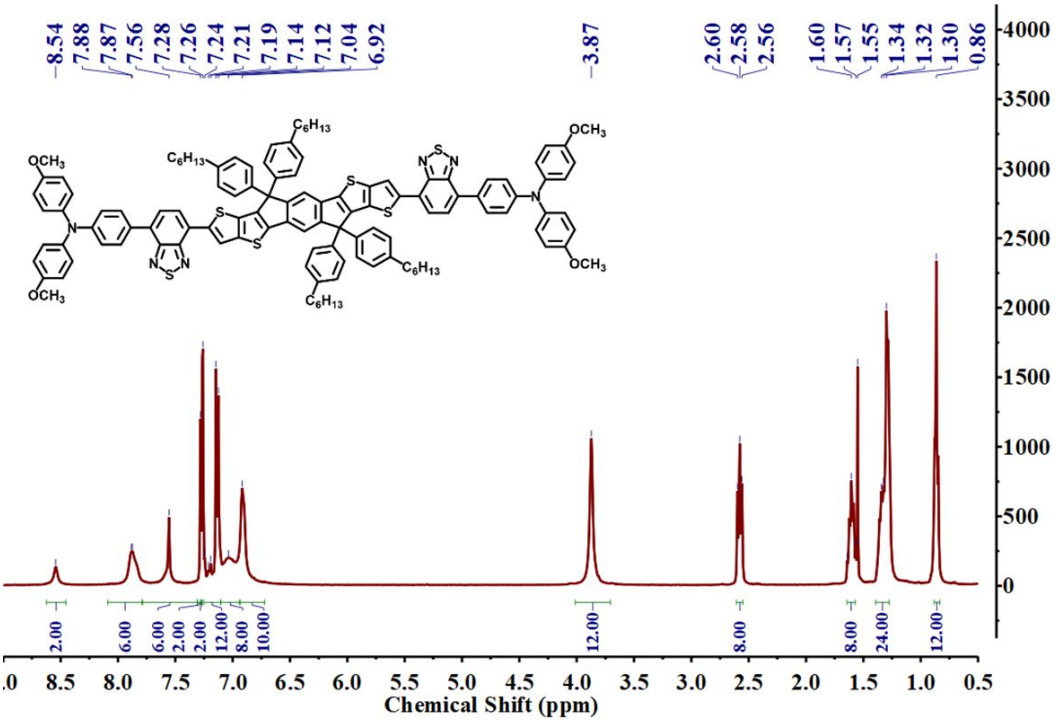

Fig. S9. ^{1}**H NMR** spectrum of **L3**.

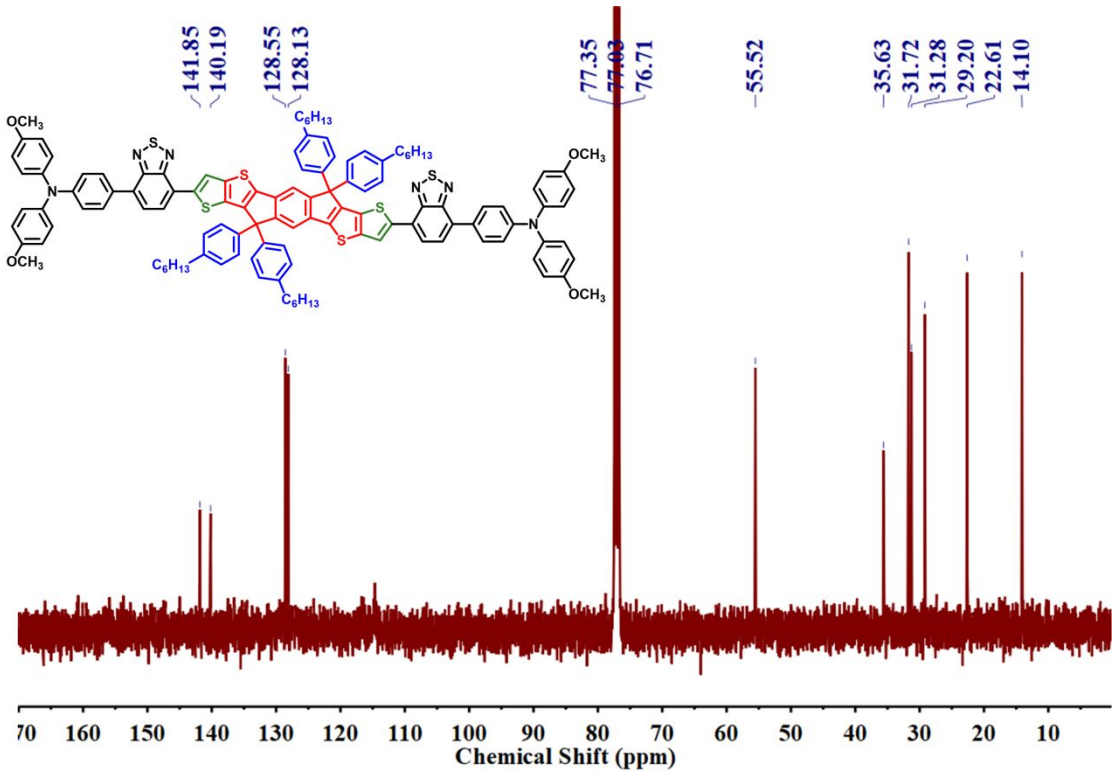

Fig. S10. ^{13}**C NMR** spectrum **L3**.

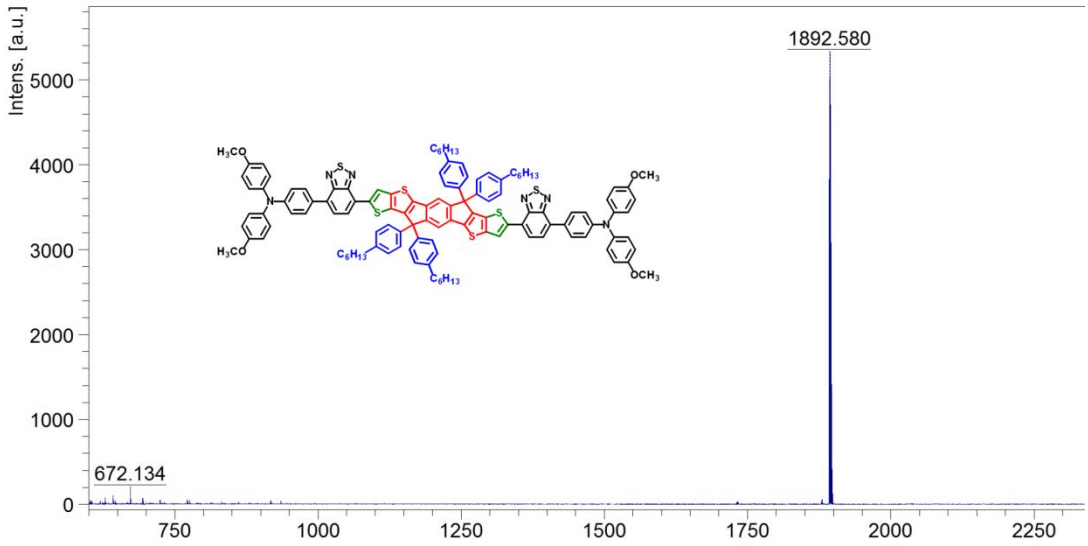

Fig. S11. MALDI-TOF-MS (m/z) spectrometry of **L3**: calcd. for $C_{120}H_{112}N_6O_4S_6$, 1894.61; found: 1892.580.

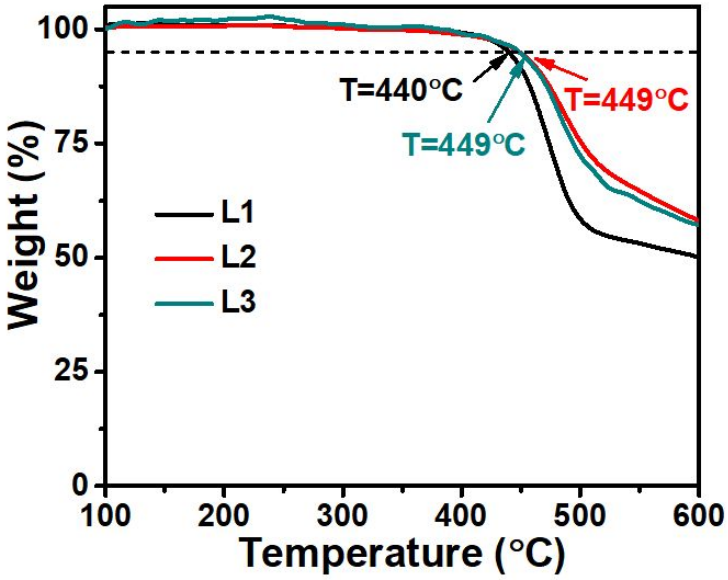

Fig. S12. TGA curves of **L1**, **L2**, and **L3** HTMs. Thermogravimetric analysis (TGA) was performed on a NETZSCH TG 209. Under nitrogen protection, the percentage of sample mass loss was collected at a heating rate of 10 °C/min, and the temperature corresponding to 5% sample mass loss was calculated.

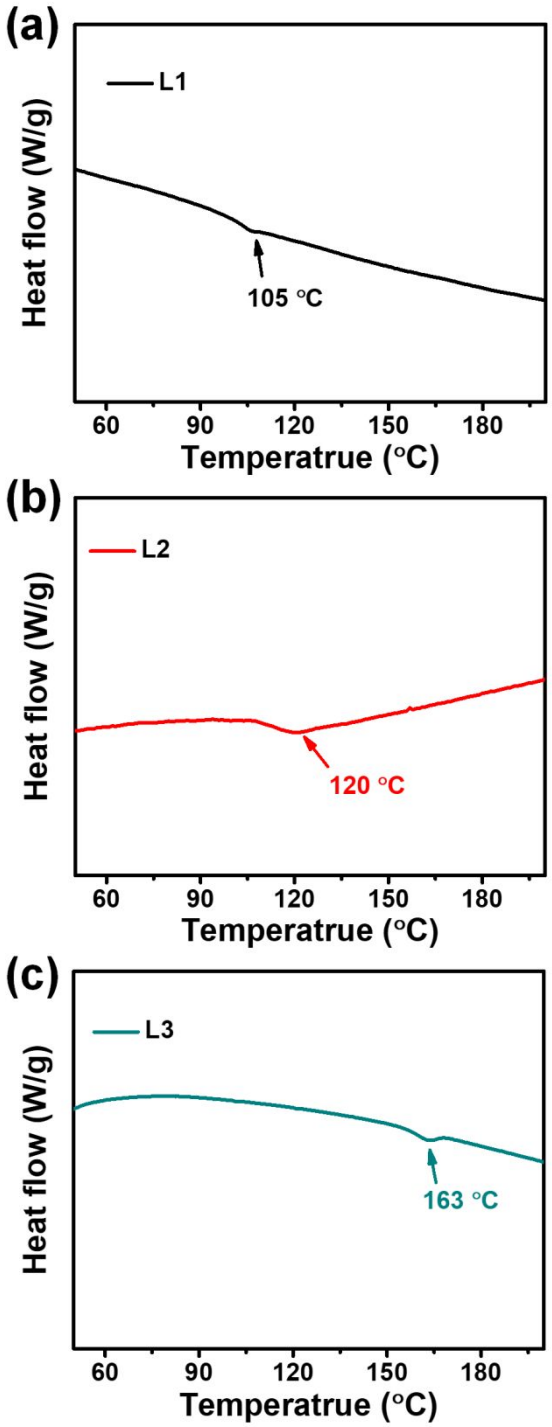

Fig. S13. Differential scanning calorimetry (DSC) curves of (a) **L1**, (b) **L2** and (c) **L3** HTMs. DSC was performed on a Netzsch DSC 200F3 under nitrogen at a heating rate of 10 °C/min to record the heat absorbed or released by the sample, and calculate the melting point of each material. The glass transition temperatures (T_g) of the three molecules are marked in the figure.

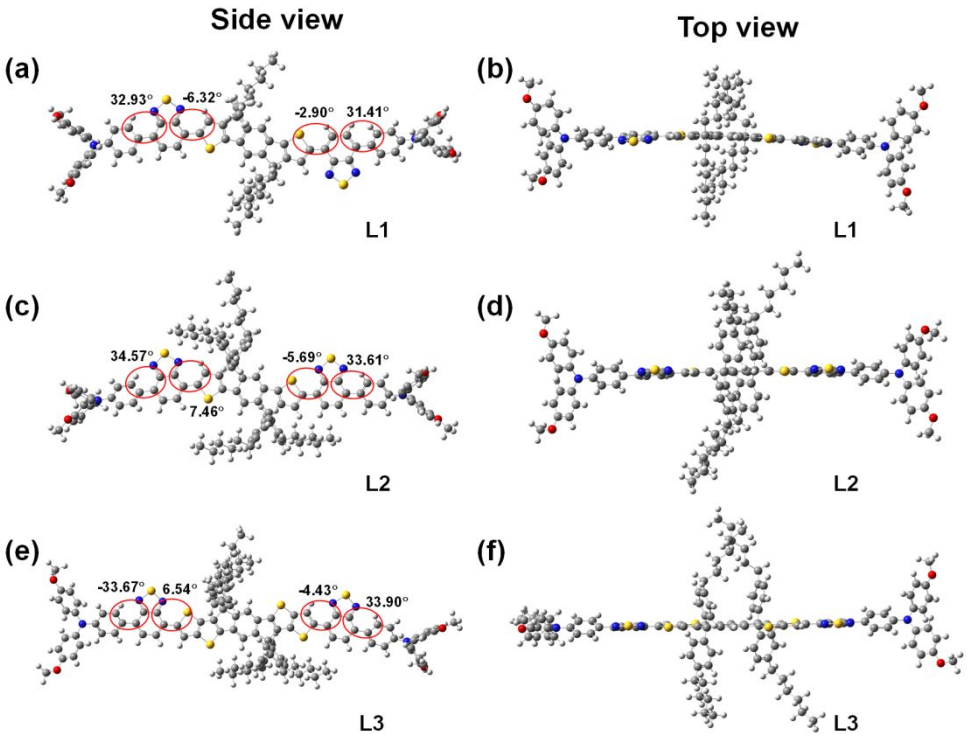

Fig. S14. DFT calculated optimized molecular conformations of **L1**, **L2** and **L3**, respectively. Compared with the **L2**, the torsion angle between the planes of the structural units in the **L3** is smaller, and the shape of **L3** is closer to the plane.

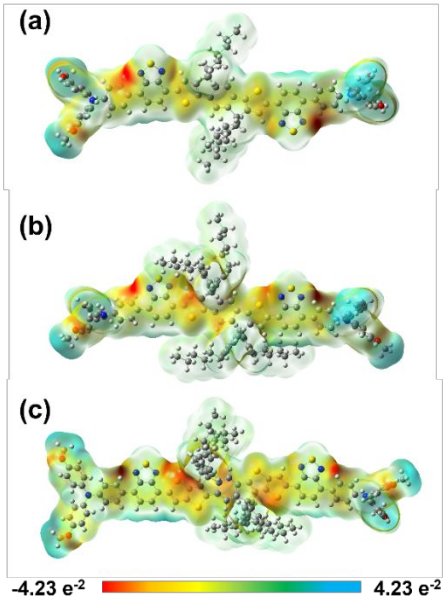

Fig. S15. Electrostatic surface (ESP) potential of (a) **L1**, (b) **L2**, and (c) **L3** molecules. The red and blue colors indicate negative and positive potentials, respectively.

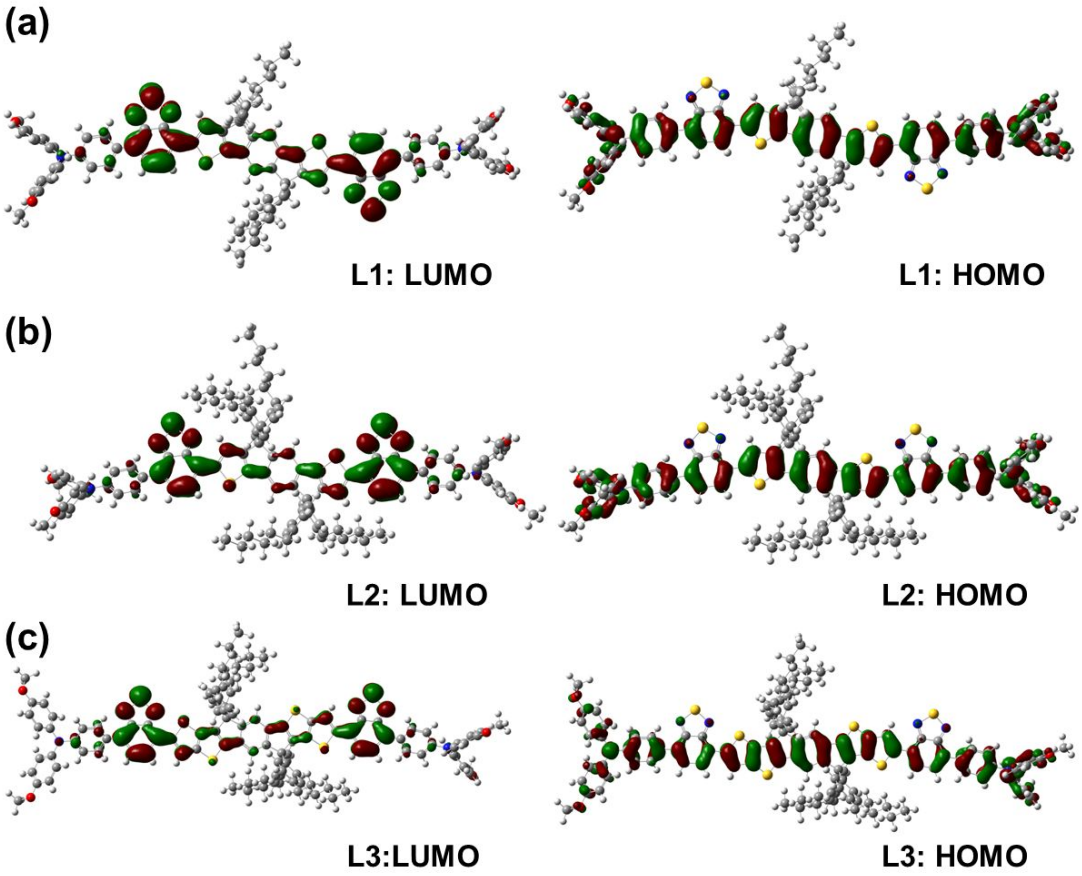

Fig. S16. DFT calculated molecular frontier orbitals of the LUMO and HOMO levels of (a) **L1**, (b) **L2**, and (c) **L3** molecules.

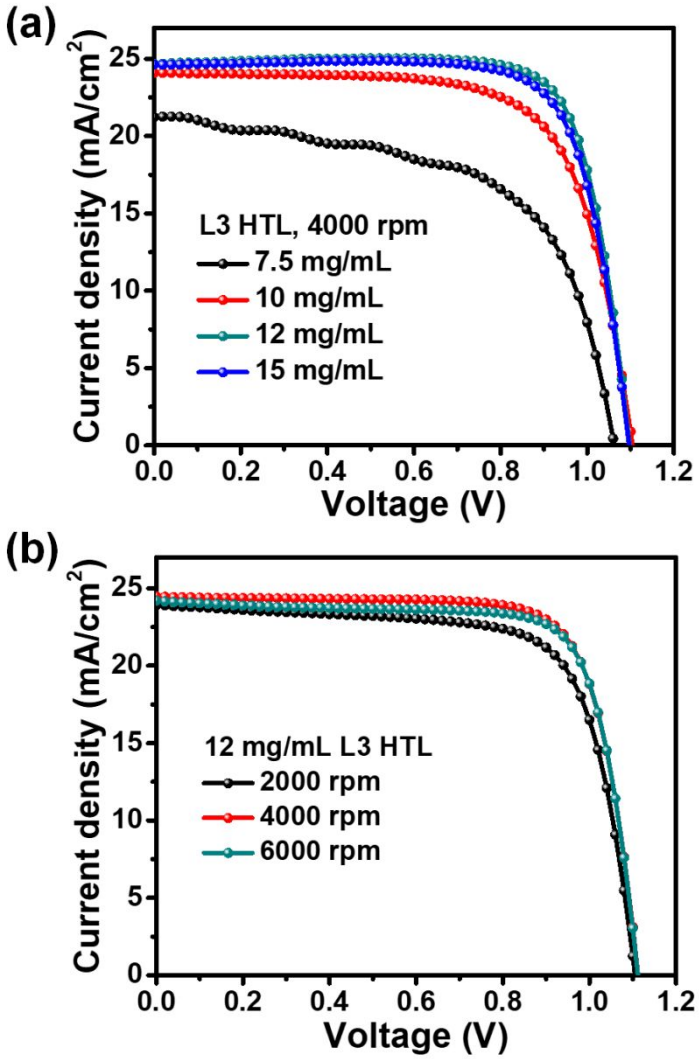

Fig. S17. *J-V* curves of PSCs. (a) different concentration of **L3**, (b) 12 mg/mL **L3** with different speed of spin-coating.

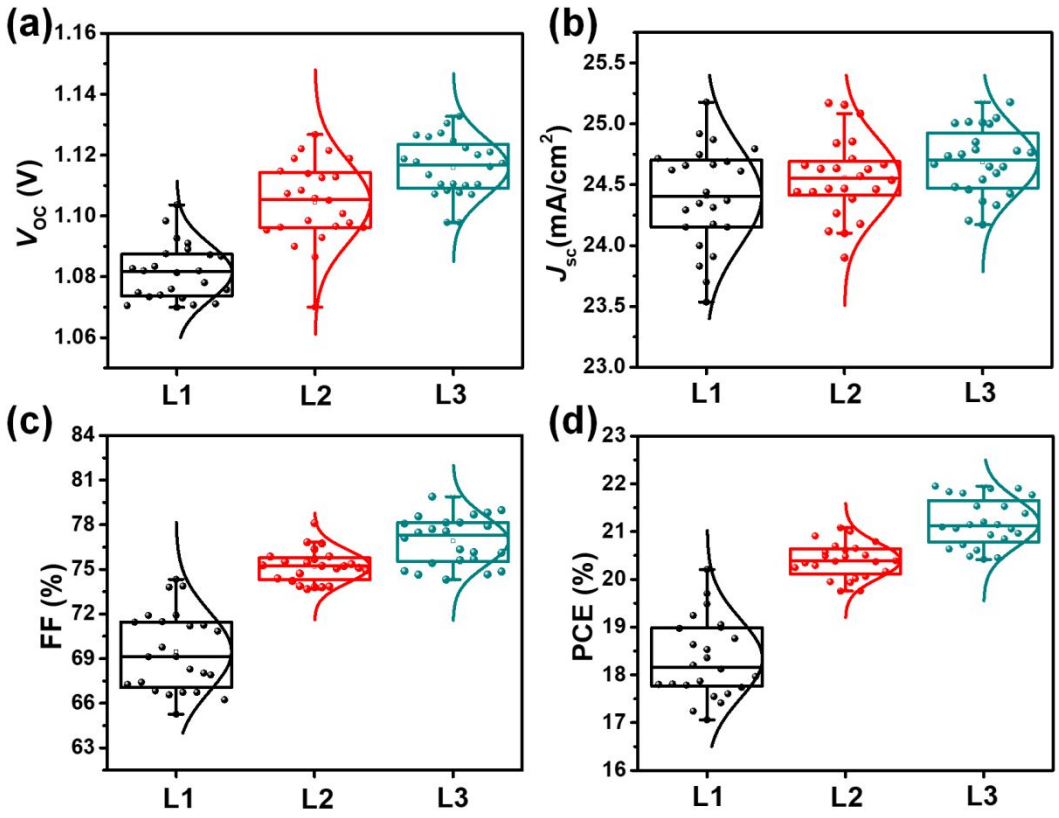

Fig. S18. Histogram of the PSCs with dopant-free HTMs of **L1**, **L2** and **L3**, analyzed from 24 cells. (a) V_{OC}, (b) J_{SC}, (c) FF, and (d) PCE.

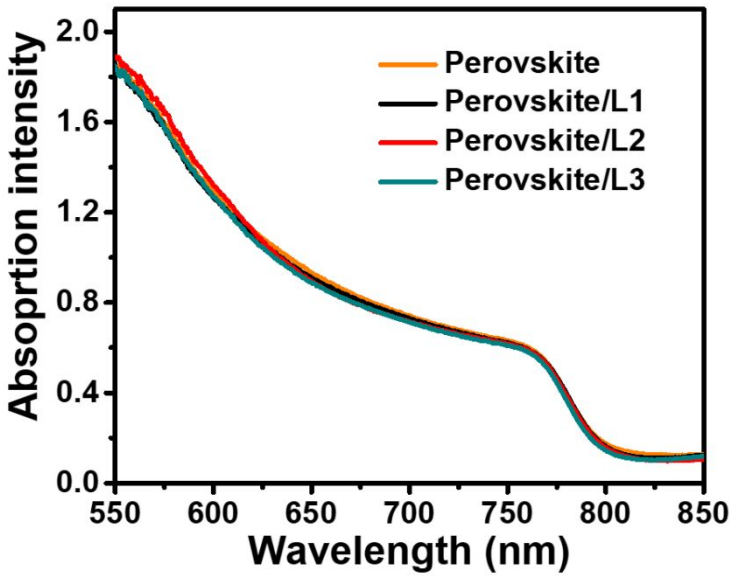

Fig. S19. The absorption spectra of perovskite and perovskite film cover with **L1**, **L2** and **L3** HTL, respectively.

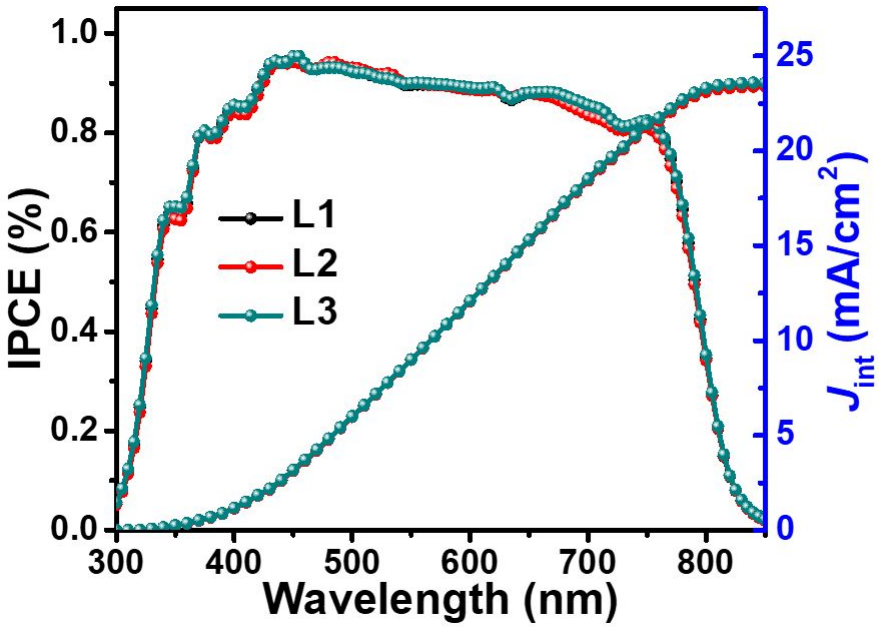

Fig. S20. IPCE curves and integrated J_{SC} of the best PSC with **L1**, **L2**, and **L3**, respectively.

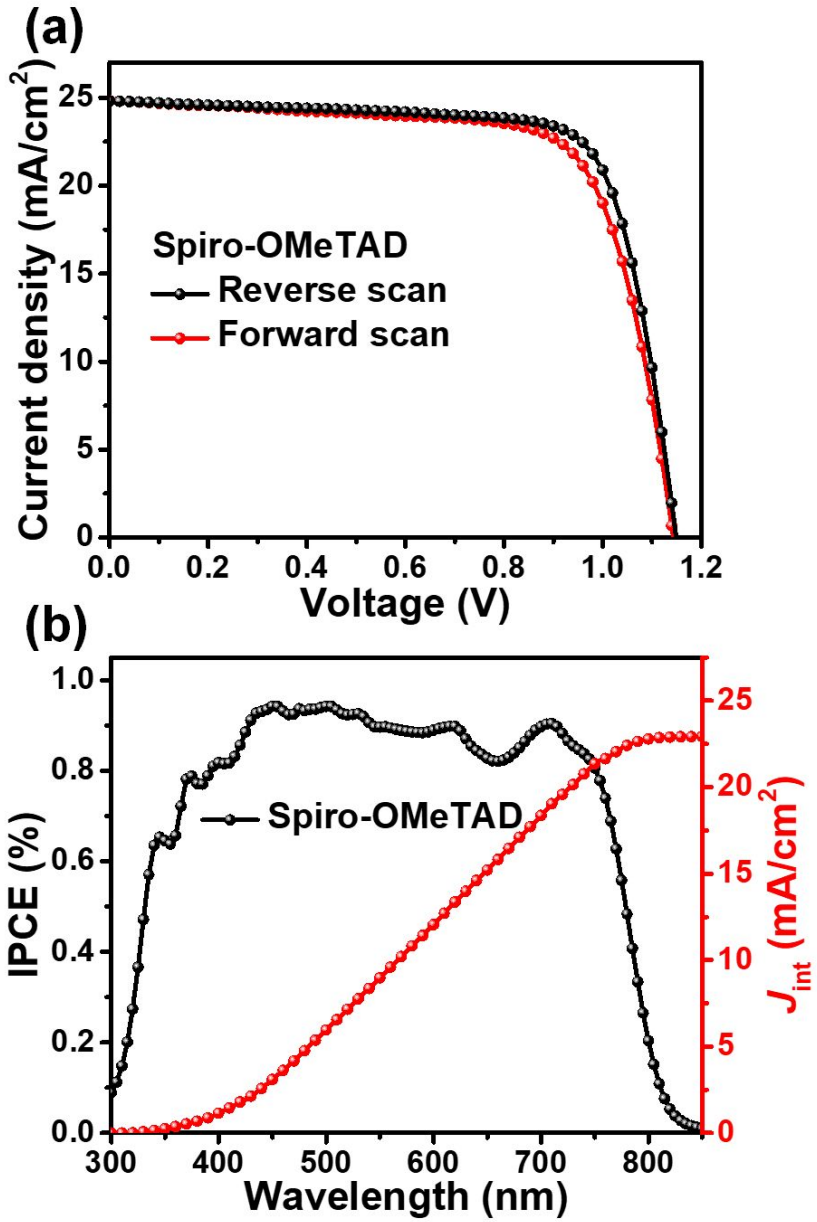

Fig. S21. (a) *J-V* curves and (b) IPCE spectra of PSC with doped **spiro-OMeTAD** HTL

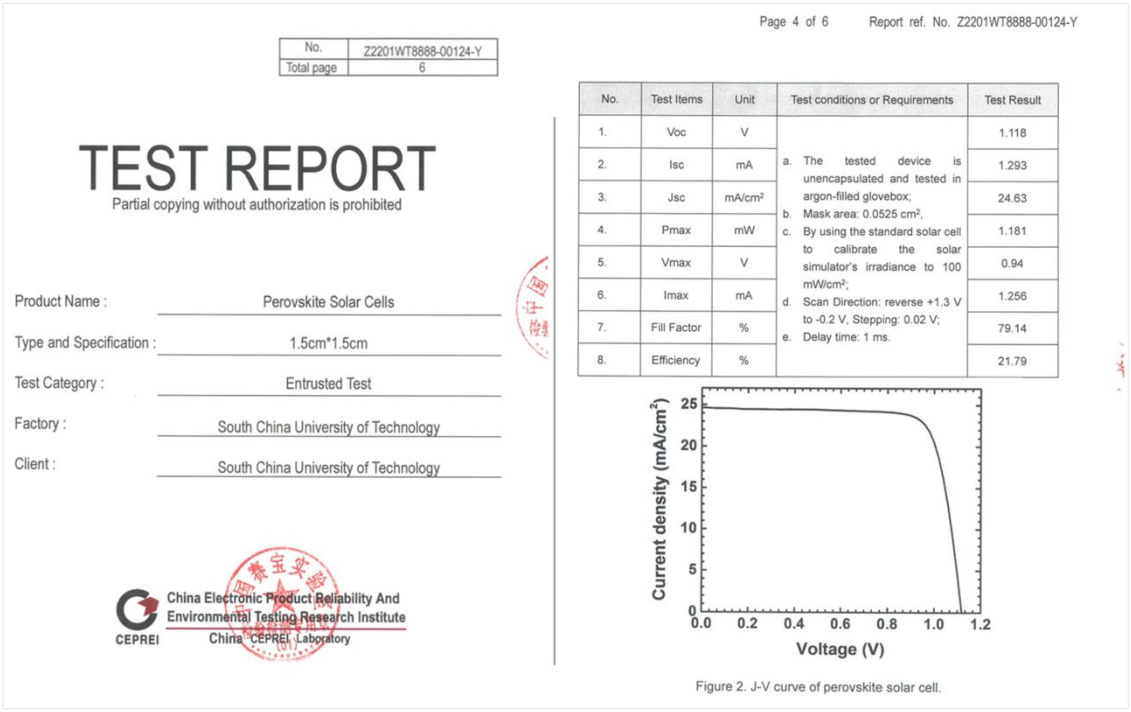

Page 4 of 6 Report ref. No. Z2201WT8888-00124-Y

No.	Z2201WT8888-00124-Y
Total page	6

TEST REPORT

Partial copying without authorization is prohibited

Product Name : Perovskite Solar Cells

Type and Specification : 1.5cm*1.5cm

Test Category : Entrusted Test

Factory : South China University of Technology

Client : South China University of Technology

China Electronic Product Reliability And Environmental Testing Research Institute

CEPREI China CEPREI Laboratory

No.	Test Items	Unit	Test conditions or Requirements	Test Result
1.	Voc	V	a. The tested device is unencapsulated and tested in argon-filled glovebox; b. Mask area: 0.0525 cm², c. By using the standard solar cell to calibrate the solar simulator's irradiance to 100 mW/cm²; d. Scan Direction: reverse +1.3 V to -0.2 V, Stepping: 0.02 V; e. Delay time: 1 ms.	1.118
2.	Isc	mA		1.293
3.	Jsc	mA/cm²		24.63
4.	Pmax	mW		1.181
5.	Vmax	V		0.94
6.	Imax	mA		1.256
7.	Fill Factor	%		79.14
8.	Efficiency	%		21.79

Figure 2. J-V curve of perovskite solar cell.

Fig. S22. The certified result of a perovskite solar cell measured by China CEPREI Laboratory. The device achieved V_{OC} of 1.12 V, a J_{SC} of 24.63 mA/cm^2 and an FF of 79.14% and a PCE of 21.79% with a mask area of 0.0525 cm^2.

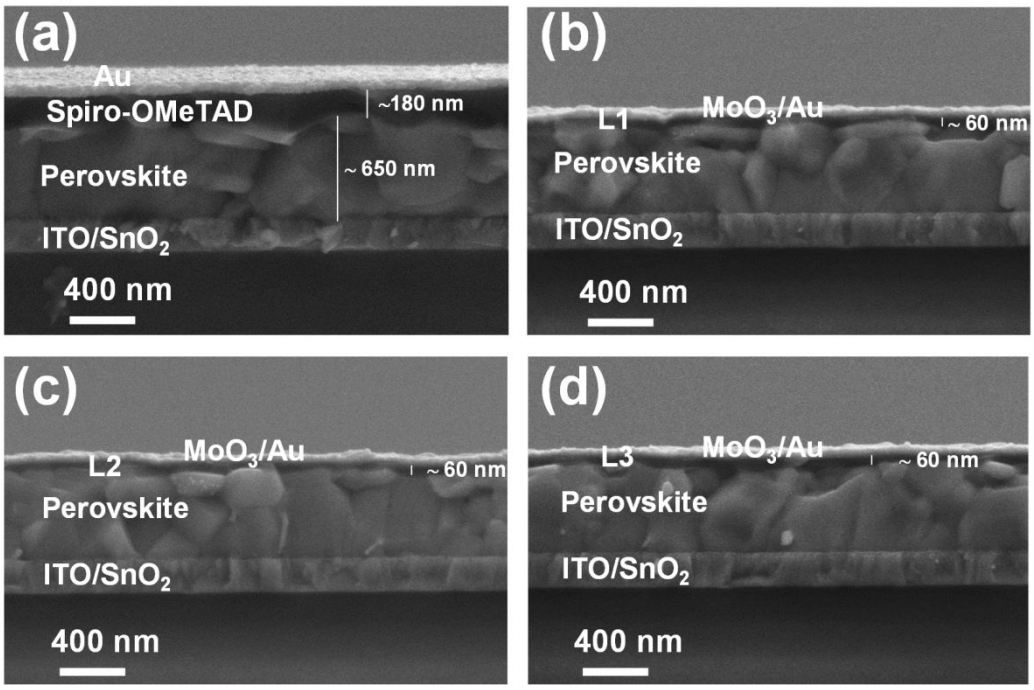

Fig. S23. Across-section SEM images of full PSCs. (a) PSC with doped **spiro-OMeTAD** HTM, (b) PSC with **L1** HTM, (c) PSC with **L2** HTM, and (d) PSC with **L3** HTM.

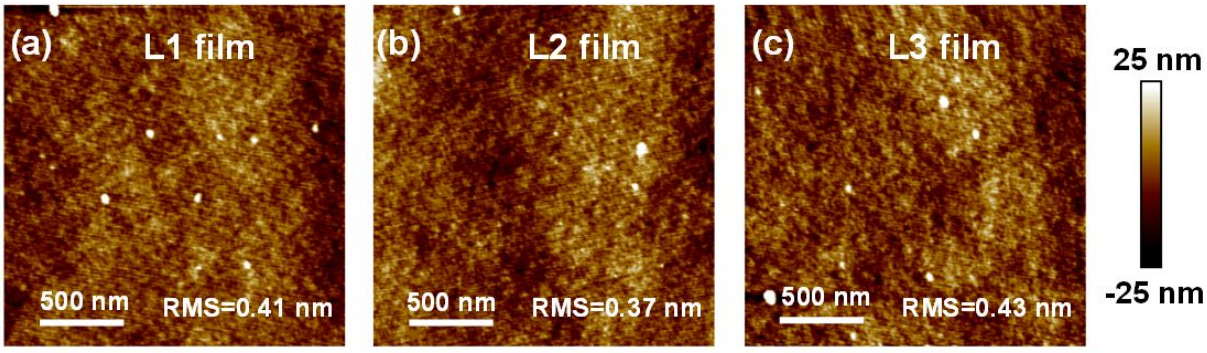

Fig. S24. AFM images of (a) **L1** film, (b) **L2** film and (c) **L3** film. All the HTM films were deposited on silicon wafer substrate.

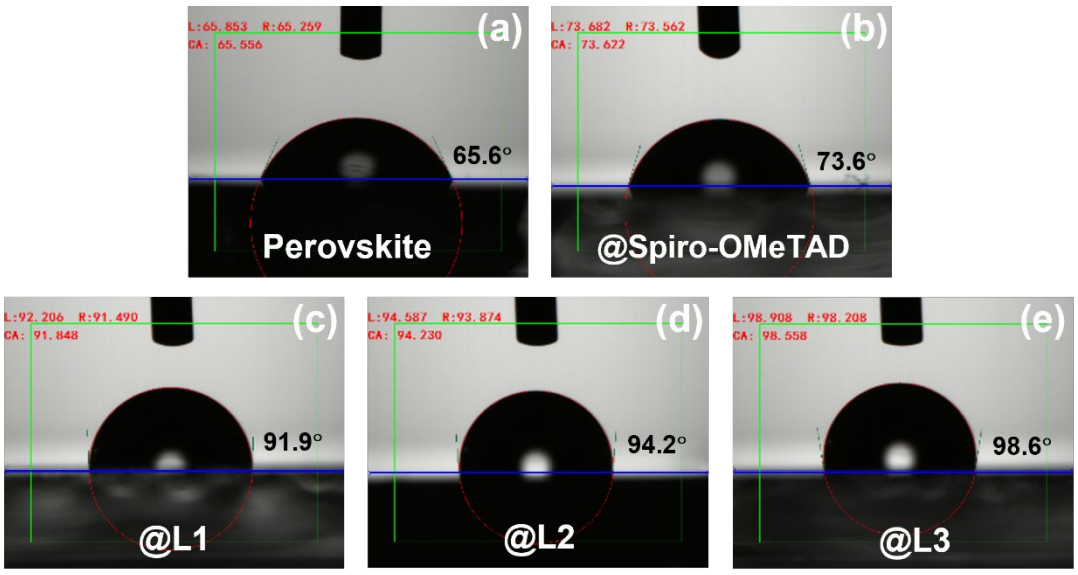

Fig. S25. The images of water contact angle of various surfaces: (a) perovskite film, (b) perovskite film with doped **spiro-OMeTAD** HTL (c) perovskite film with **L1** HTL, (d) perovskite film with **L2** HTL, and (e) perovskite film with **L3** HTL.

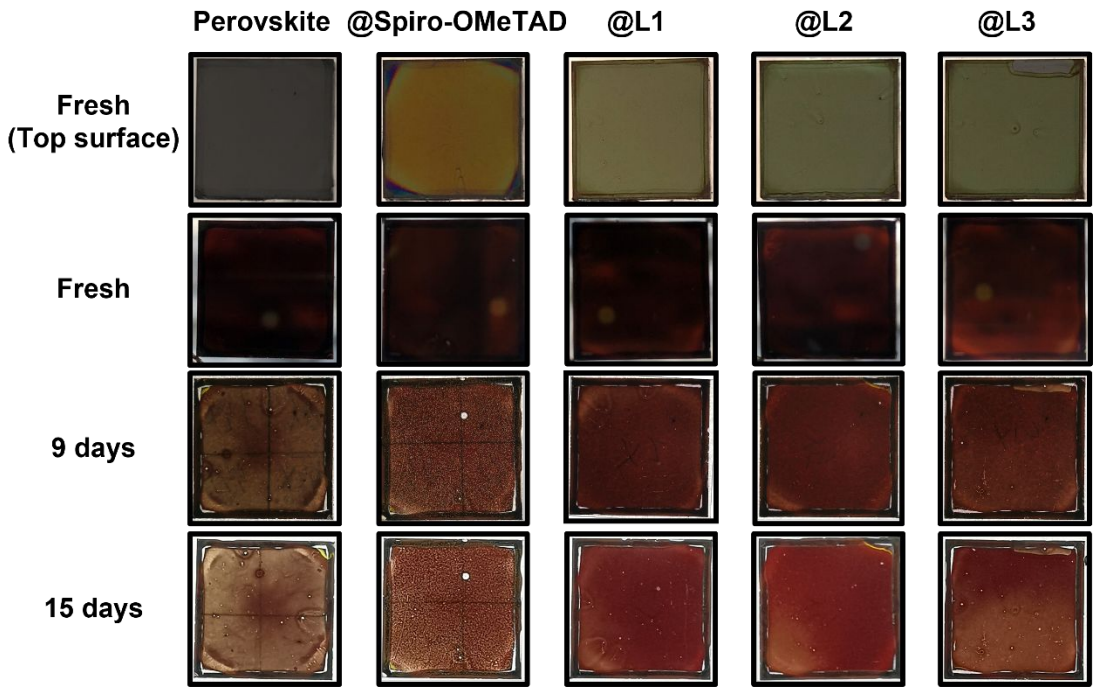

Fig. S26. The degradation images of the perovskite film with different HTL (glass/ITO/SnO_2/perovskite/HTM) under ambient atmosphere with RH=50-60%.

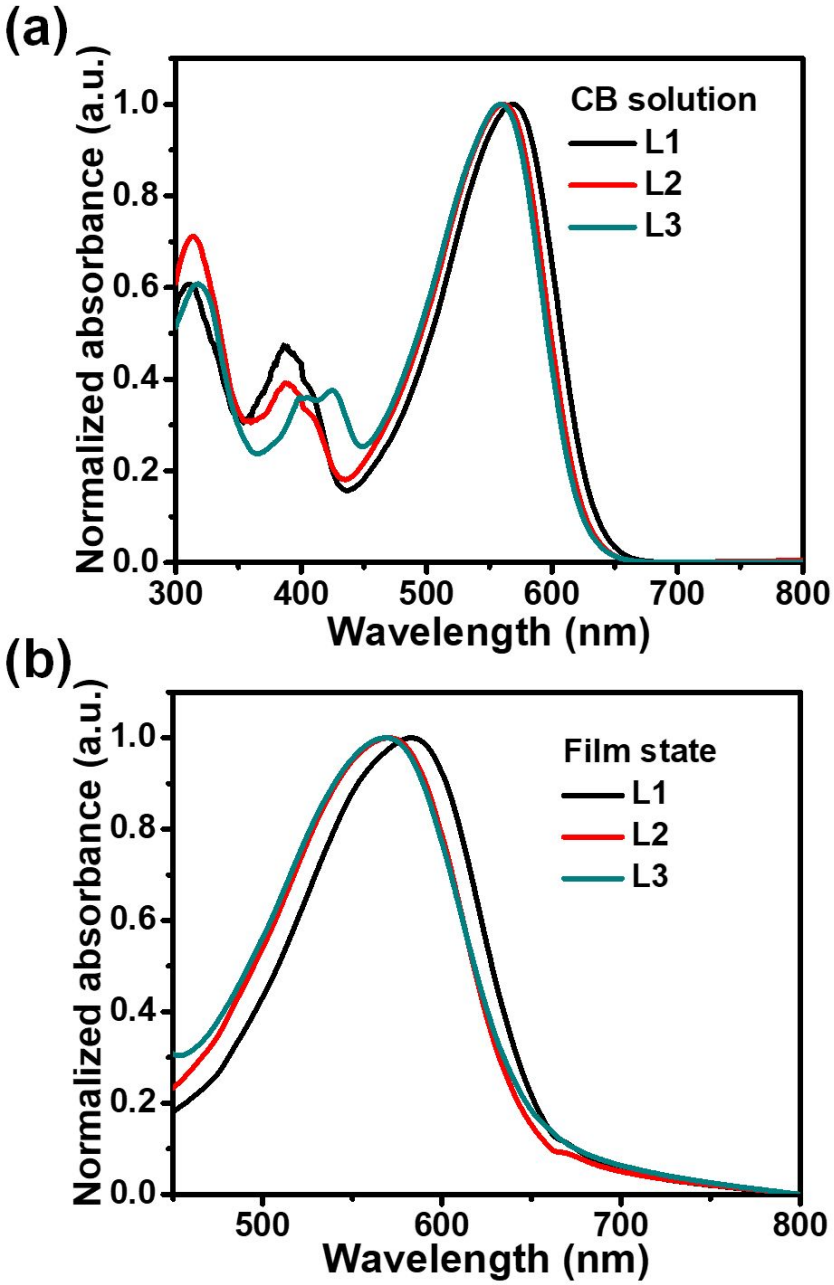

Fig. S27 Normalized UV-Vis absorption spectra of the HTMs in (a) CB solution and (b) film state.

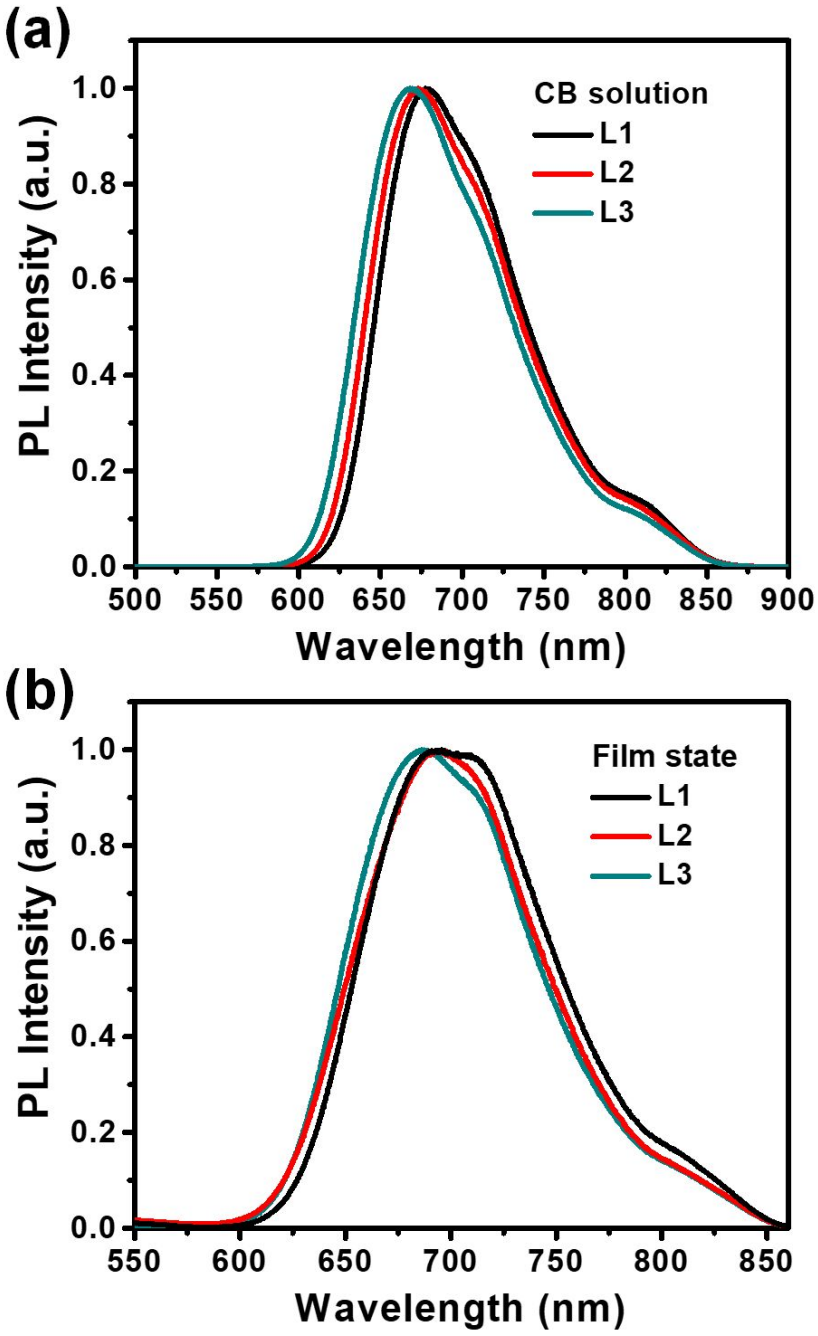

Fig. S28 Steady-state PL of **L1**, **L2** and **L3** HTMs. (a) solution state and (b) film state.

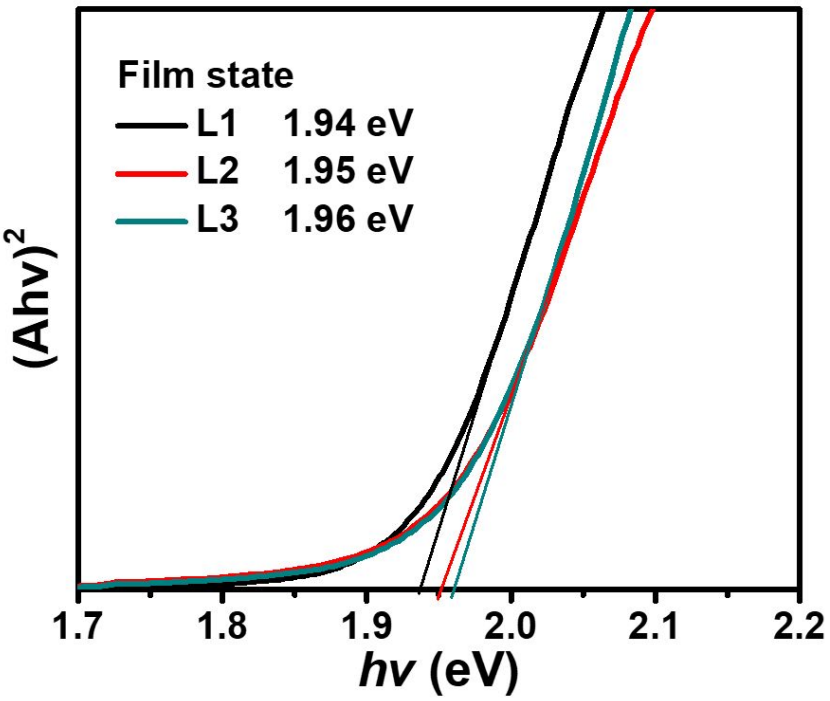

Fig. S29 Tauc plots of **L1**, **L2** and **L3** film.

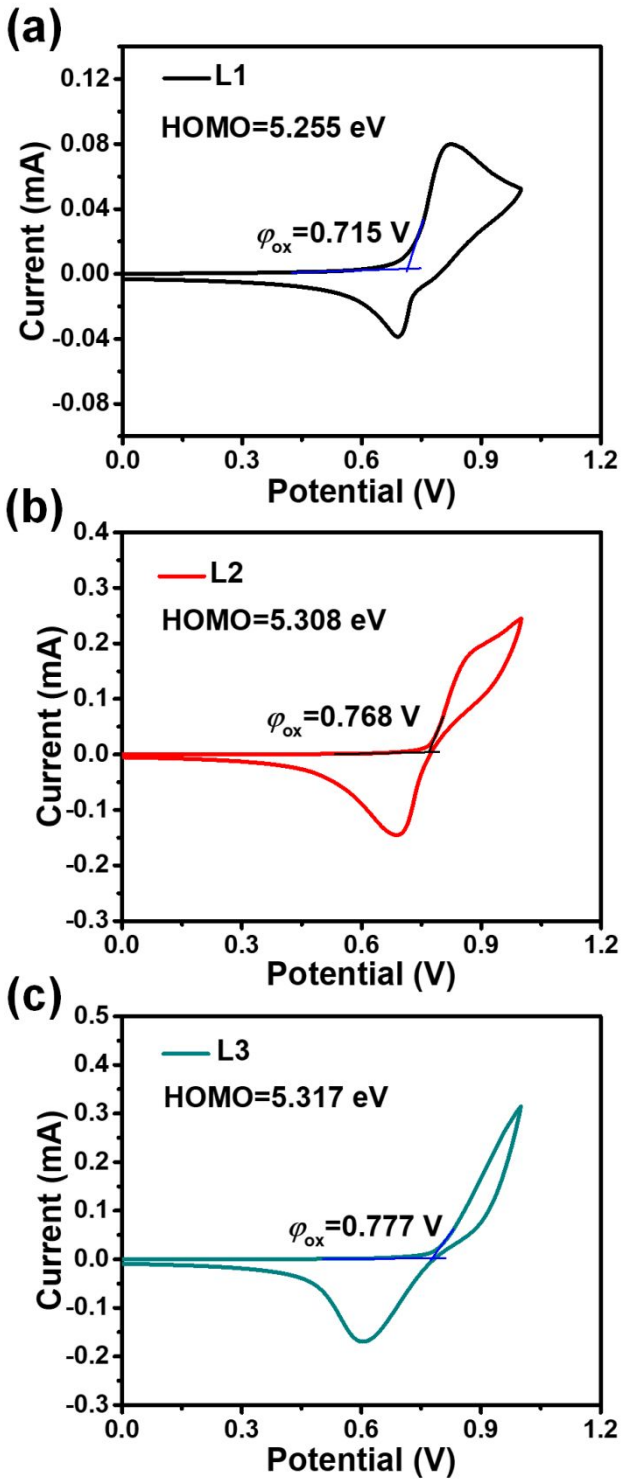

Fig. S30 Cyclic voltammograms of (a) **L1**, (b) **L2** and (c) **L3** film. With the saturated calomel electrode (SCE) as the reference electrode, the energy level of the molecules was calculated according to the equation: E_{HOMO}=-(4.8+E_{ox}-E_f) (eV), where E_{ox} is the initial oxidation potential, E_f is 0.26. The calculated HOMO levels of **L1**, **L2** and **L3** are -5.255, -5.308 and -5.317 eV, respectively.

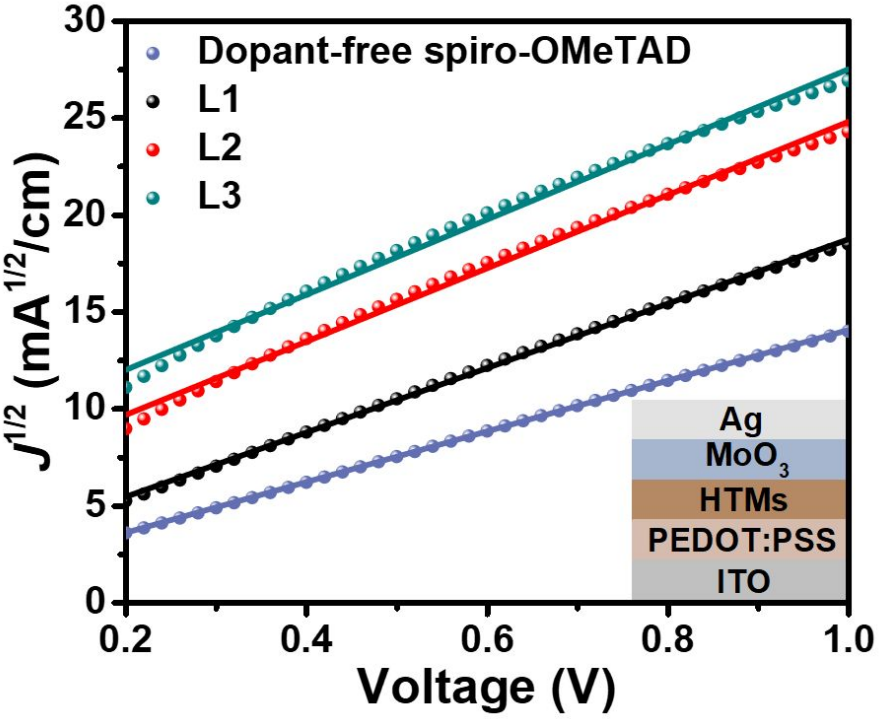

Fig. S31 *J-V* curves of hole-only ITO/PEDOT:PSS/HTM/MoO_3/Ag devices.

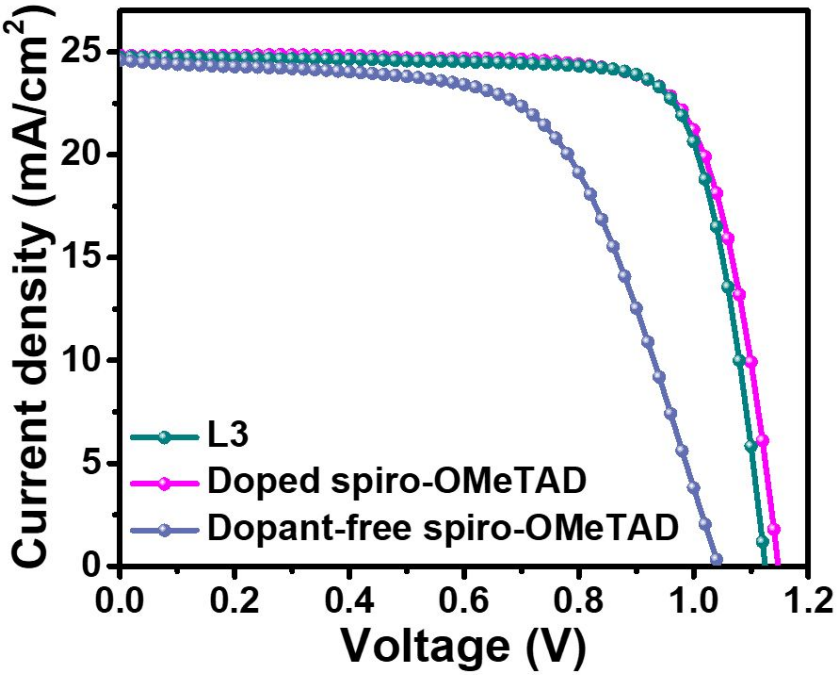

Fig. S32 *J-V* curves of PSCs with doped **spiro-OMeTAD**, dopant-free **spiro-OMeTAD** and **L3** HTM.

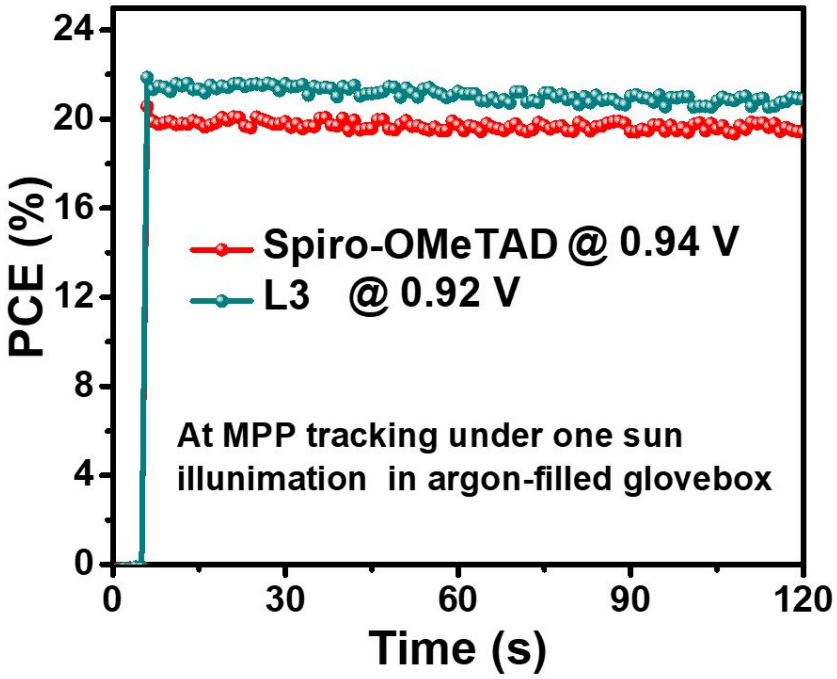

Fig. S33 Stable power output of the best devices with doped **spiro-OMeTAD** and dopant-free **L3** HTL.

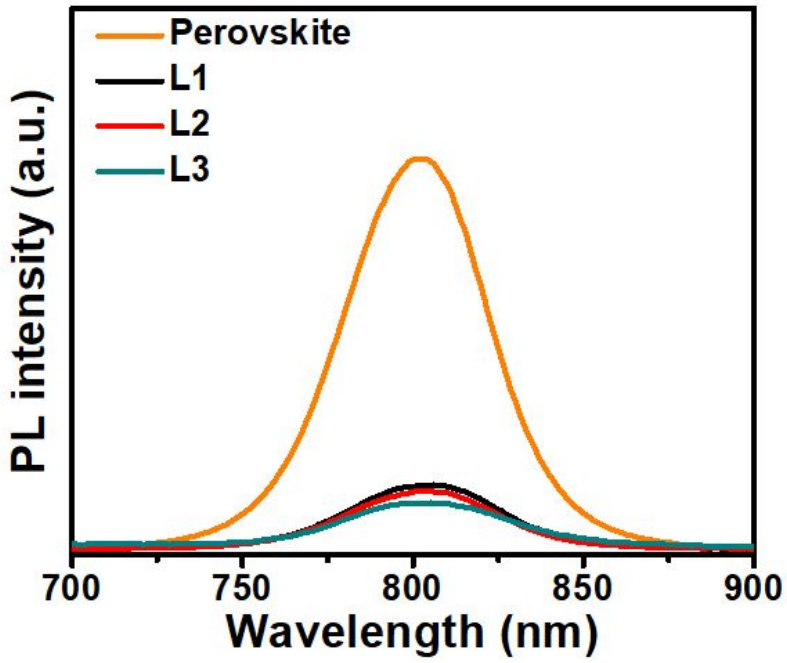

Fig. S34 Steady-state PL of perovskite film and perovskite film covered with **L1**, **L2** and **L3**, respectively.

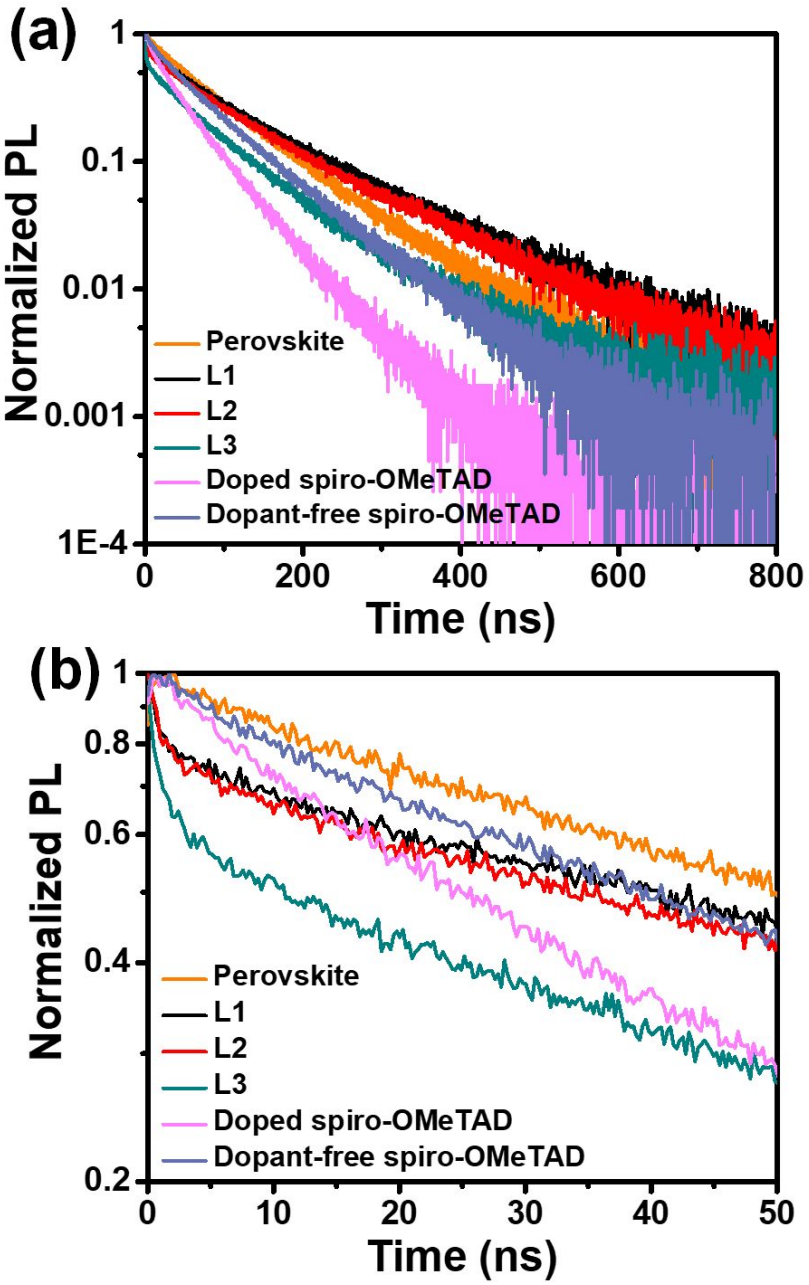

Fig. S35 (a) Time-resolved PL of the perovskite film cover with doped **spiro-OMeTAD**, dopant-free **spiro-OMeTAD** and **L1-3** HTM. (b) Zoom-in to Fig. S36a.

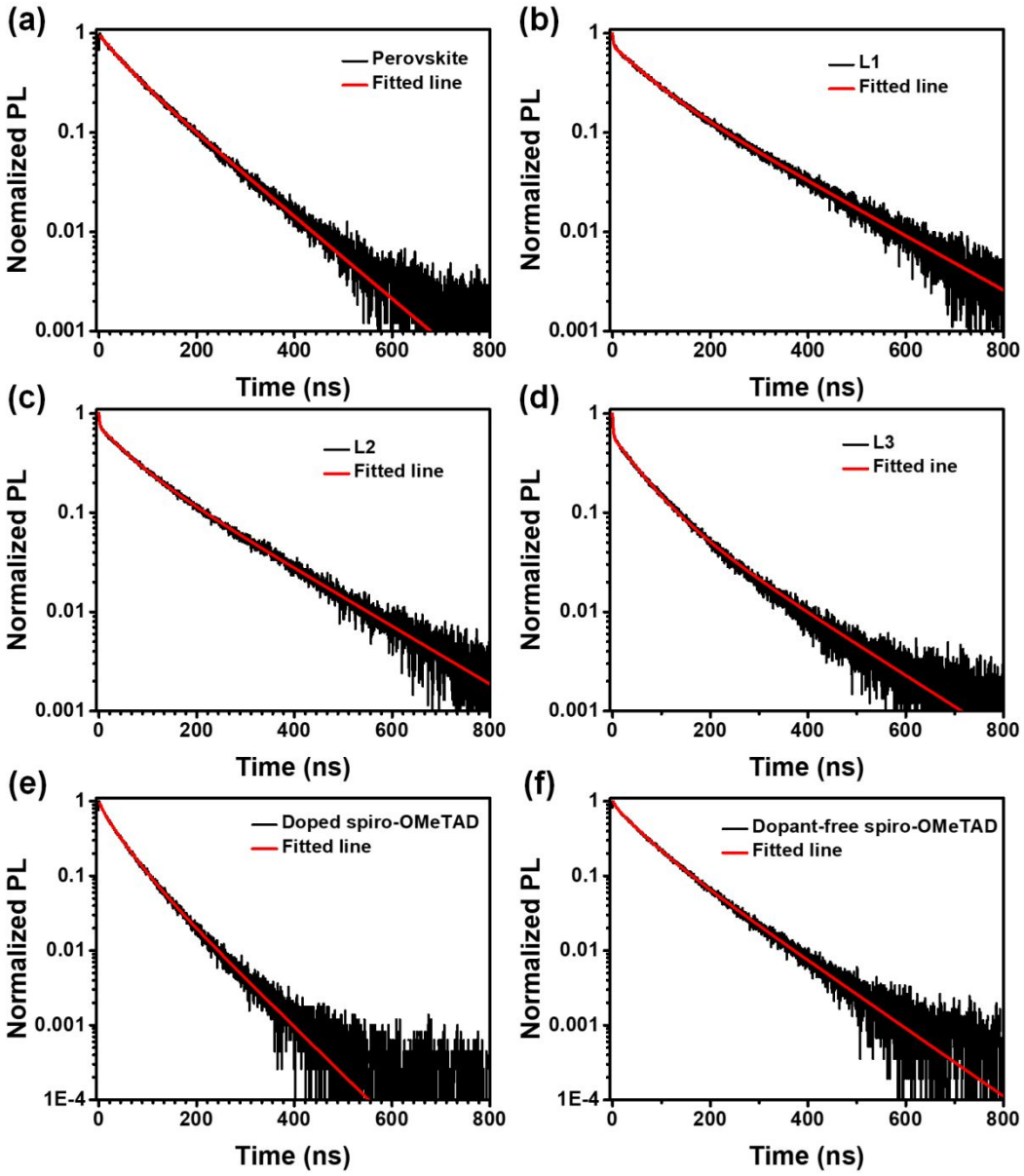

Fig. S36 (a) Time-resolved PL of the perovskite film cover with doped **spiro-OMeTAD**, dopant-free **spiro-OMeTAD** and **L1-3** HTM. (a) bare perovskite film, (b) perovskite film with **L1** HTM, (c) perovskite film with **L2** HTM, (d) perovskite film with **L3** HTM, (e) perovskite film with doped **spiro-OMeTAD** HTM, (f) perovskite film with dopant-free **spiro-OMeTAD** HTM. The corresponding TRPL curves were also fitted by triple-exponential functions (no physical model before, arbitrary choice to better fit the data to help with the differential lifetime evaluation), which includes a fast component (lifetime τ_1, and weight fraction A_1) and an intermediate component (lifetime τ_2, and weight fraction A_2), an slow component (lifetime τ_3, and weight

fraction A_3), presumably corresponding to the quenching process of photogeneration of free carriers of perovskite through charge extraction from the perovskite to the HTLs, radiative recombination in the perovskite film, and passivation effects by functional group, respectively for L-series films. The fit for perovskite film is directly transformed to bi-exponential function due to convergence. The additional decay of spiro-based film may be assigned to trap-mediate recombination.

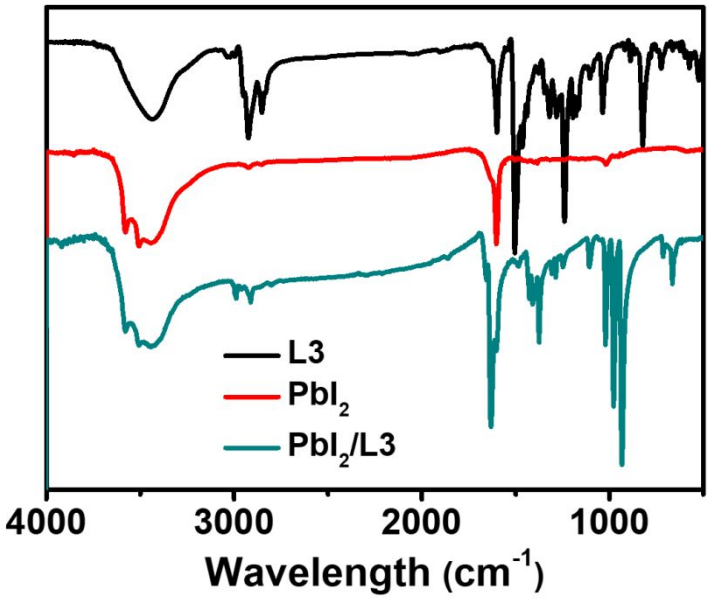

Fig. S37 Full FTIR spectra of the powders of L3, PbI_2 and PbI_2/L3 blend. The PbI_2/L3 sample was mixed PbI_2 solution and L3 solution directly, then the powder was dried at 80 °C for eight hours.

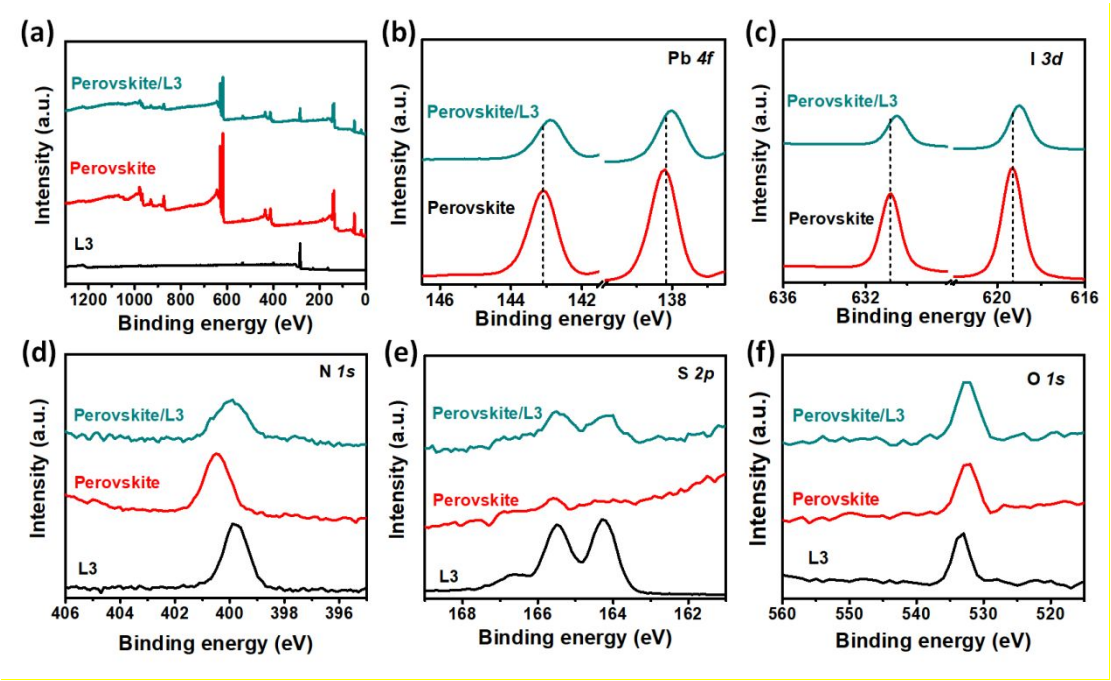

Fig. S38 The XPS spectrum of the perovskite film, L3 film, and perovskite/L3 film. (a) full spectrum, (b) Pb 4f, (c) I 3d (d) N 1s (e) S 2p and (f) O 1s.

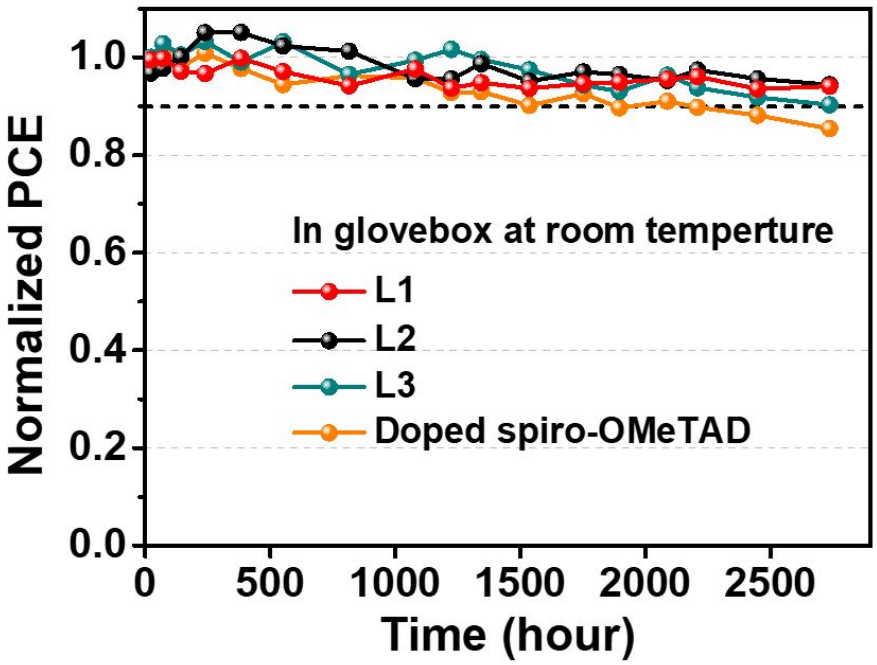

Fig. S39 Long-term stability of unencapsulated control PSC (doped spiro-OMeTAD) and dopant-free L-series PSC stored at argon-filled glovebox.

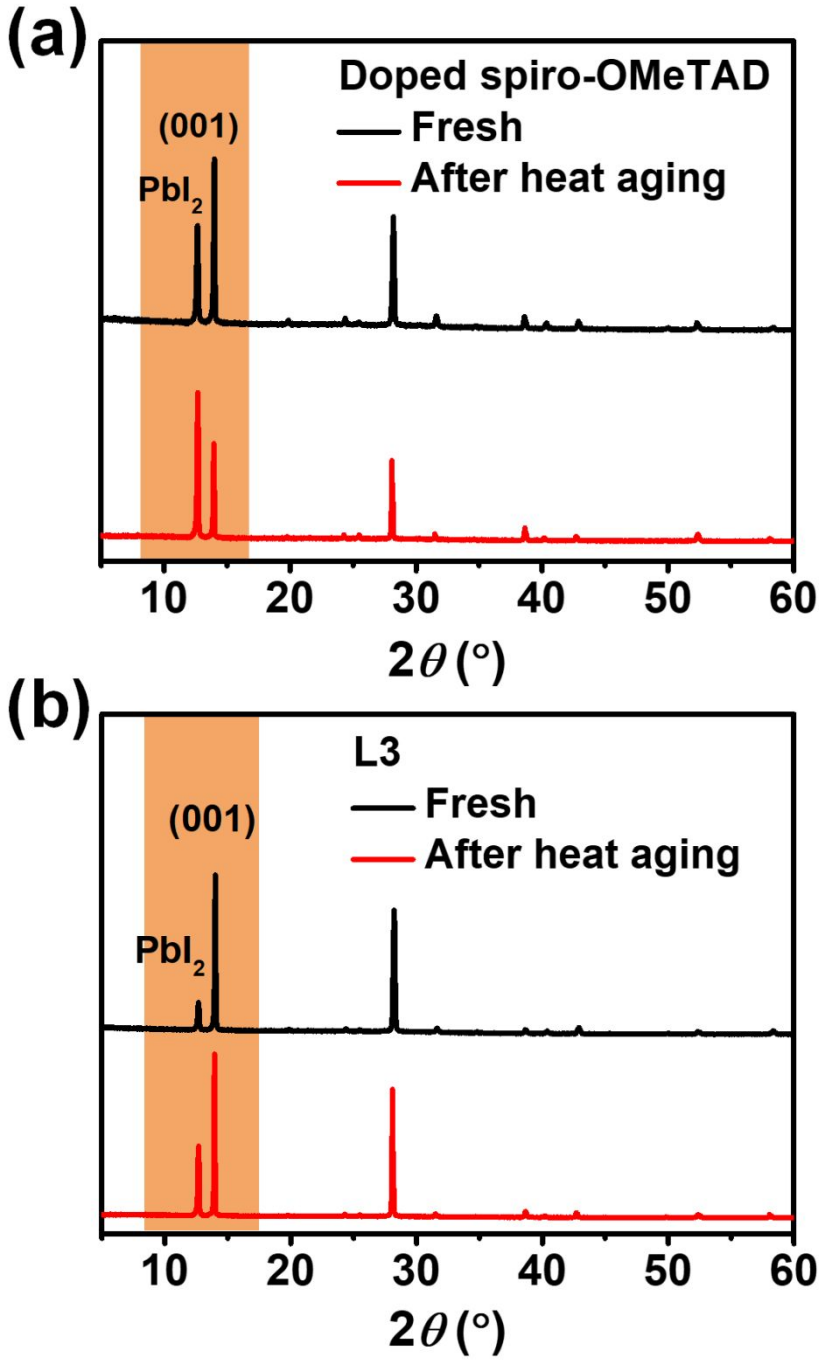

Fig. S40 XRD patterns for doped spiro-OMeTAD perovskite film and L3-perovskite film before and after 85°C aging for 10 days in the argon.

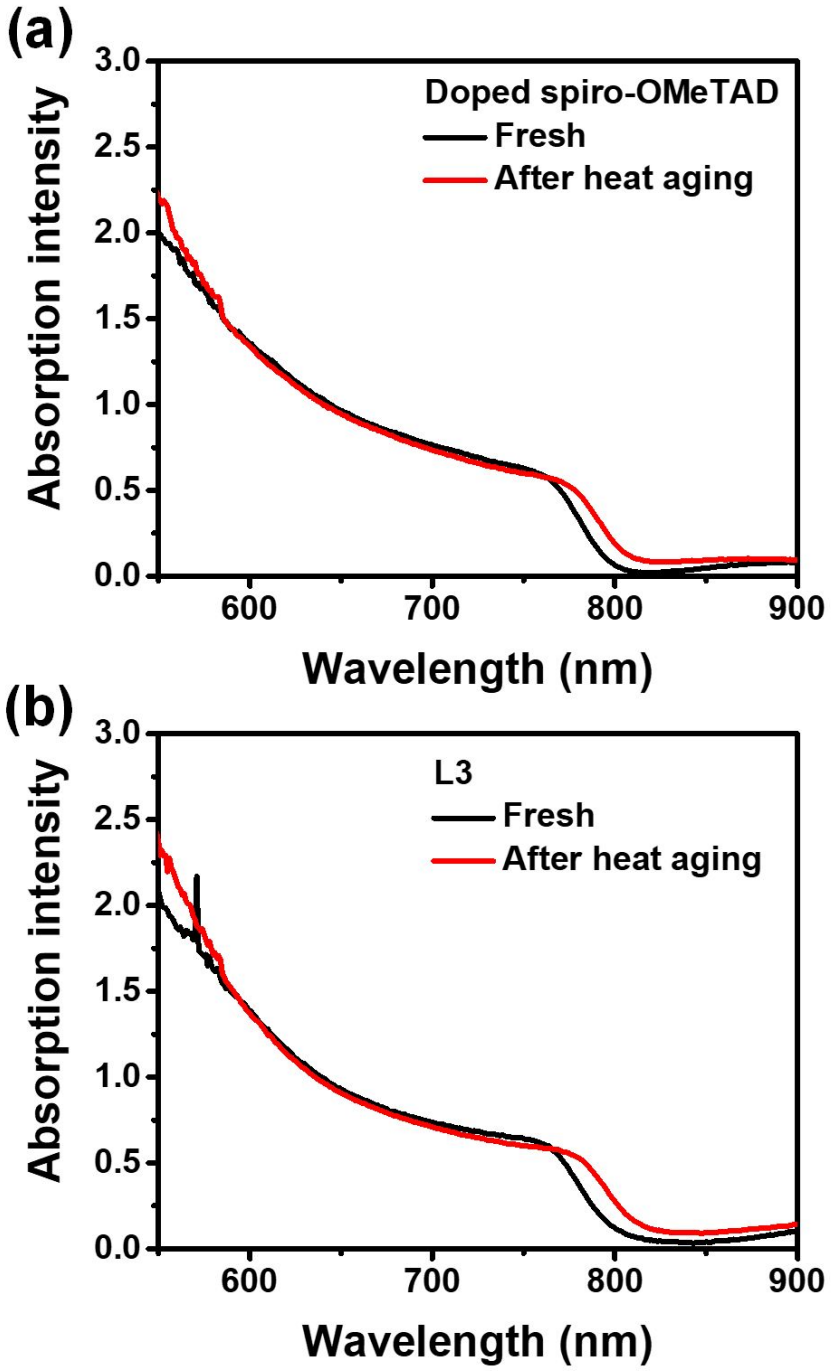

Fig. S41 The absorption spectra of perovskite film coved with doped spiro-OMeTAD and L3 HTL before and after 85°C aging for 10 days in the argon. (a) doped spiro-OMeTAD HTL, (b) L3 HTL.

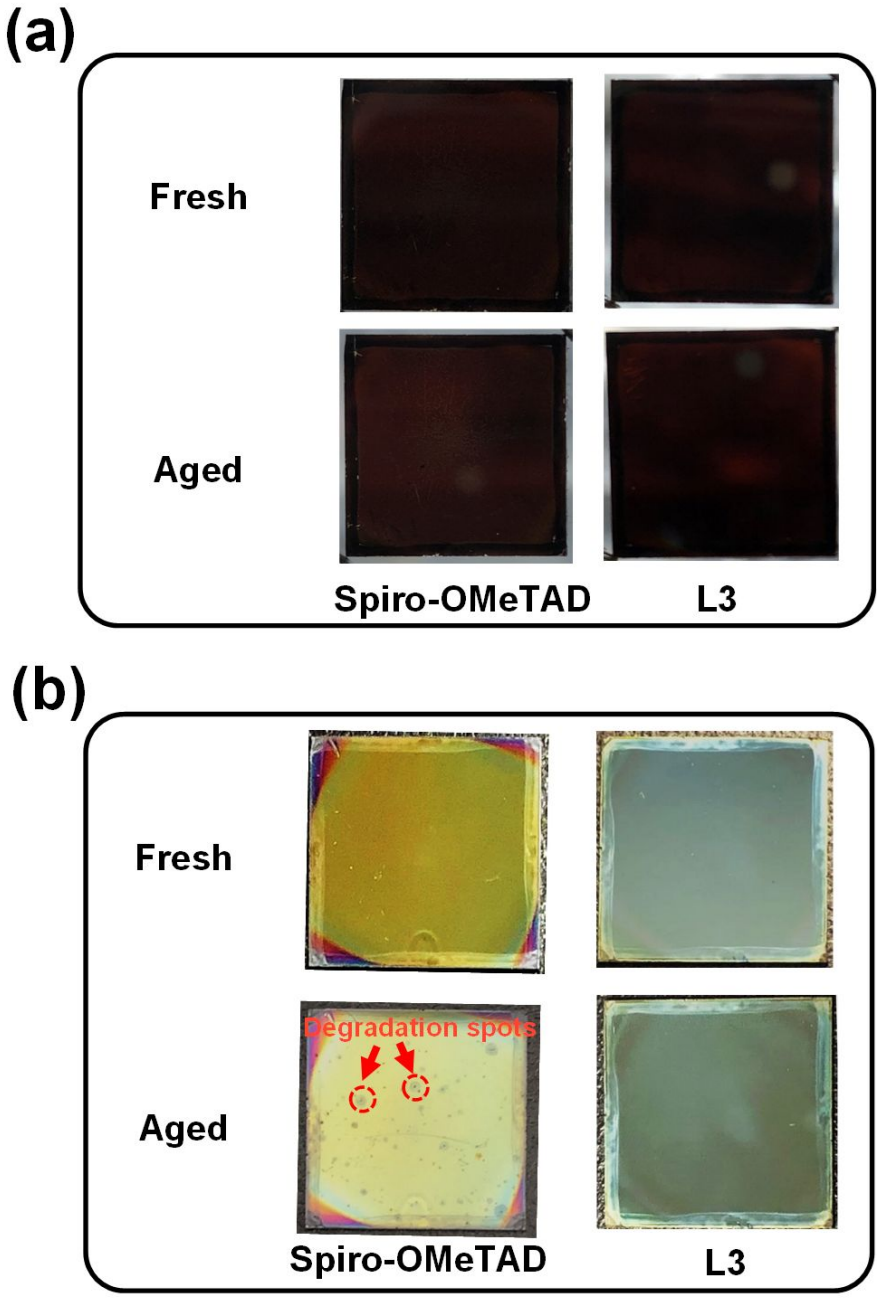

Fig. S42 Photo images for perovskite film with doped spiro-OMeTAD HTL and L3 HTL before and after 85°C aging for 10 days in the argon. (a) glass side, (b) top side.

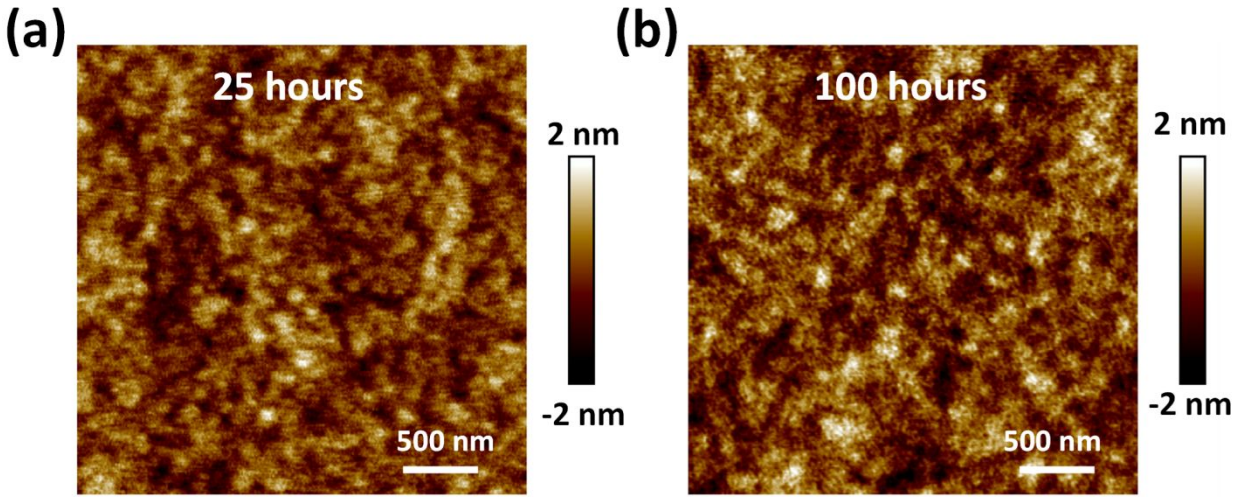

Fig. S43 AFM images of L3 HTMs on ITO substrates, the aging condition is 100°C for (a) 25 hours and (b) 100 hours on the hotplate in N_2-filled glovebox.

Table S1. Summary of thermal stability (at 85°C or MPP tracking at over 70°C) of the state-of-the-art p-i-n and n-i-p PSCs.

Journal	Structure	Stability	Ref.
p-i-n PSCs			
Science	FTO/poly-TPD/$Cs_{0.17}FA_{0.83}Pb(I_{1-x}Br_x)_3$/PCBM/BCP/Cr/Cu	Under full-spectrum sunlight **at 85°C** in ambient air, encapsulated, T_{95}=1200 h.	13
Nat. Energy	ITO/PTAA/perovskite/C_{60}/BCP/Cu	**T=85°C**, T_{90}=1020 h	14
Science	ITO/P3CT-N/$(FAPbI_3)_{0.95}(MAPbBr_3)_{0.05}$/PCBM/$C_{60}$/TPBi/Cu	**T=85°C,** maintained 91.8% for >2200 h.	15
Energy Environ. Sci.	ITO/p-PY/perovskite/PCBM/BCP/Ag	**T=85°C**, maintained over 94% for 500 h, **T=120°C,** maintained over 81% for 200 h.	16
Science	ITO/PTAA/perovskite/C_{60}/BCP/Ag	**Damp heat test (85°C/85%)**, T_{95}>1000 h,	17
Science	ITO/2PACz/3D-perovskite/2D-perovskite/C_{60}/BCP/Ag	**Damp heat test (85°C/85%)**, T_{95}>1200 h.	18
Nature	FTO/NiO/perovskite/PCBM/BCP/Cr/Cr_2O_3/Au	Full spectrum sunlight at **70 to 75°C,** encapsulated, T_{95}=1800 h.	19
n-i-p PSCs			
Joule	FTO/TiO_2/ZrO_2/5AVA$_X$MAPbI$_{1-3}$/carbon	**Damp heat test (85°C/85%**), 1100 h without decay; T=55°C, 9,000 h operational tracking without obvious decay	20
Nat. Energy	FTO/SnO_2/3D:SIG-2D/P3HT/Au	**Damp heat test (85°C/85%),** T_{95}=1056 h	21
Science	ITO/c-TiO_2/TiO_2 nanorods/PMMA:PCBM/$Cs_{0.05}FA_{0.88}MA_{0.07}PbI_{2.56}Br_{0.44}$/PMMA/P3HT:CuPc/Au	**Damp heat test (85°C/85%)**, retained ~95.3% of for >260 h.	22
Science	ITO/SnO_2/3D Perovskite/2D perovskite /spiro-OMeTAD/Au	**T=85°C**, T_{80}=500 h	23
Science	FTO/compact-TiO_2/ mp-TiO_2/perovskite/Spiro-OMeTAD/Au	**T=85°C**, RH=15-25%, T_{80}=1300 h	24

Table S2. Summary of recent developments of doping-free molecule HTMs in *n-i-p* PSCs.

HTM	Perovskite	V_{oc} (V)	J_{sc} (mA/cm^2)	FF (%)	PCE (%)	*Tg* (°C)	Atmosphere	Thermal stability	Publish data	Ref.
Polymer HTMs										
asy-PBTBDT	$Cs_{0.05}FA_{0.81}MA_{0.14}PbI_{2.55}Br_{0.45}$	1.11	22.4	73.2	**18.3**	/		/	2017.08	25
PTEG	Cs-perovskite	1.14	22.5	77.0	**19.8**	/		/	2017.09	26
P3HT	$(FAPbI_3)_{0.95}(MAPbBr_3)_{0.05}$	1.152	24.88	81.4	**23.3**	/		/	2019.03	27
PTB1-C	CsFAMAGA mixed perovskite	1.05	22.37	81.2	**19.06**	/		/	2019.09	28
P3	$MAPbI_3$	1.11	22.8	80.0	**20.3**	/		/	2019.11	29
PBDTT	Cs-perovskite	1.12	23.64	76.67	**20.28**	/		/	2019.12	30
PBTT-T	CsFAMA mixed perovskite	1.14	21.68	76.79	**19.02**	/		/	2020.11	31
alkoxy-PTEG	$Cs_{0.06}FA_{0.78}MA_{0.16}Pb_{0.94}I_{2.4}Br_{0.48}$	23.2	1.14	79.8	**21.2**	/		/	2020.01	32
PBTFO	$Cs_{0.05}(FA_{0.85}MA_{0.15})_{0.95}Pb$ ($I_{0.85}Br_{0.15})_3$	1.21	23.3	75.1	**22.10**	/	N_2	*T*=65°C, unencapsulated, after 500 hours maintains 97%	2020.01	33

PBDT-N20	$(FAPbI_3)_{0.85}(MAPbBr_3)_{0.15}$	1.08	23.4	75.0	**18.9**	/	Glovebox	*T*=80 °C, after 1500 h maintains over 95%	2020.09	34
PC3	$MAPbI_3$	23.5	1.11	80.0	**20.8**	/	/	*T*=85°C, under 1 sun illumination after 200 h maintains 70%	2020.09	35
PE10	$FA_{0.85}MA_{0.15}PbI_3$	1.16	24.1	79.8	**22.3**			T = 85°C, in dark, after 500 h with 45−85% RH maintains 80.5% *T*=85°C, under 1 sun illumination after 240 h maintains 65%	2022.03	36
Ploy-alloy (PM6/PMSe)	$MA_{0.16}FA_{0.84}PbI_3$	1.19	25.07	82.17	**24.53**		N_2	T = 80 °C, in dark, after 600 h maintains 93%	2022.05	37
PM6	$MA_{0.16}FA_{0.84}PbI_3$	1.19	24.55	82.22	**24.04**			/	2022.08	38
PFBTI	$Cs_{0.05}FA_{0.95}PbI_3$	1.16	24.6	80.8	**23.1**			/	2022.10	39
Small molecule HTMs										
2DP-TDB	$FA_{0.85}MA_{0.15}PbI_3$	1.16	24.02	79.57	**22.17**		N_2	*T*=80°C, unencapsulated, in dark, after 376 h maintains 81%	2021.03	40
Z26	$(FAPbI_3)_{0.85}(MAPbBr_3)_{0.15}$	1.132	23.59	75.0	**20.1**	**98**	40% RH	*T*=65°C, unencapsulated, in dark after 120 h maintains ~85%	2017.09	41
TQ2	$MAPbI_3$	1.12	22.55	77.67	**19.62**	**113**		/	2018.07	42
TTE-2	$(FAPbI_3)_{0.95}(MAPbBr_3)_{0.05}$	1.11	23.26	77.52	**20.04**	**158**		/	2019.01	43
YN3	$(FAPbI_3)_{0.85}(MAPbBr_3)_{0.15}$	1.12	22.43	75	**18.84**	/		/	2019.02	44
DTPC13-ThTPA	$MA_{0.7}FA_{0.3}PbI_{2.85}Br_{0.15}$	1.135	22.82	78.7	**20.38**	/		/	2019.07	4
M129	$Cs_{0.05}(FA_{0.83}MA_{0.17})_{0.95}Pb(Br_{0.17}I_{0.83})_3$	1.08	22.50	72.0	**17.50**	**170**	N_2	*T*=60 °C, after 72 h maintains 90%	2019.09	45
BTTI-C6	CsFAMA perovskite	1.10	24.00	74.6	**19.69**	**224**	N_2	*T*=100 °C, unencapsulated, after 60 h maintains 70%	2019.12	3
DTP-C6Th	$MA_{0.7}FA_{0.3}Pb(I_{0.925}Br_{0.075})_3$	1.157	22.76	79.9	**21.04**	**84.5**		/	2019.07	5
YZ22	$Cs_{0.1}FA_{0.9}PbI_3$	1.10	25.1	81.0	**22.4**	**108**	Air	*T*=85°C, encapsulated, MPP (1.1 sun) tracking after 60 h maintains 60%	2020.09	7
TQ4	$Cs_{0.05}FA_{0.85}MA_{0.1}Pb(I_{0.97}Br_{0.03})_3$	1.124	23.78	79.0	**21.03**	**131**	N_2	*T*=85°C, in dark, after100 h maintains 90%	2020.10	8
DTB-FL	$Cs_{0.05}FA_{0.95}PbI_3$	1.14	23.8	77.4	**21.50**	**87**	N_2	*T*=80°C, after 240 h maintains 68%	2020.12	11
MeOTTVT	$Cs_{0.05}FA_{0.85}MA_{0.10}Pb(I_{0.97}Br_{0.03})_3$	1.11	23.89	80.3	**21.30**	**137.1**	/	*T*=80°C, in dark, after 220 h maintains 90%	2020.12	46
SFDT-TDM	$Cs_xFA_{1-x}PbI_3$	1.13	24.1	79.5	**21.7**	/		/	2021.06	47
CB	$MAPbI_3$	1.15	23.60	77.7	**21.09**			/	2021.08	48
BDT-DPA-F	$FAMAPbI_3$	1.18	24.66	79.57	**23.12**	/		*T*=85°C, in dark, after 1200 h maintains 80.3%	2022.09	12
L3	(Cs/GA) doped $(FAPbI_3)_{0.95}(MAPbBr_3)_{0.05}$	1.12	25.25	79.84	**22.61**	**163**	**Argon**	***T*=85°C, in dark, after 1000 h maintains 83%** ***T*=85°C, MPP tracking after 500 h maintains >85%**	/	This work

Table S3. Summary of device performance of PSCs with L3 HTL fabricated by different concentration at a speed 4000 rpm. The thicknesses of L3 film on ITO glass were determined using by using a Profilometer (Ambios Tech. XP-2).

Concentration	Thickness (nm)	V_{OC} (V)	J_{SC} (mA/cm²)	FF (%)	PCE (%)
7.5 mg/mL	~33	1.06	21.22	58.77	13.25
10 mg/mL	~45	1.10	24.08	70.02	18.63
12 mg/mL	~54	1.10	24.65	78.15	21.15
15 mg/mL	~61	1.10	24.62	75.87	20.49

Table S4. Summary of device performance of PSCs with L3 HTL fabricated by different speed of spin-coating with a precursor of 12 mg/mL in CB.

12 mg/mL L3 HTL	V_{OC} (V)	J_{SC} (mA/cm^2)	FF (%)	PCE (%)
2K	1.11	23.91	72.11	19.06
4K	1.11	24.48	76.33	20.78
6K	1.11	24.22	76.45	20.57

Table S5. Summary of the performance of PSCs with different HTMs.

HTL	V_{OC} (V)	J_{SC} (mA/cm^2)	FF (%)	PCE (%)
L1	1.08 ± 0.01	24.41± 0.41	69.53 ± 2.61	18.39 ± 0.81
L2	1.10 ± 0.01	24.66 ± 0.32	74.89 ± 1.08	20.37 ± 0.36
L3	1.11 ± 0.01	24.77 ± 0.27	76.42 ± 1.60	21.11 ± 0.49

Table S6. Lifetimes and weighted fractions fitted by triple-exponential functions from the time-resolved PL.

	A_1	τ_1 (ns)	A_2	τ_2 (ns)	A_3	τ_3 (ns)	τ_{avg} (ns)
Pristine	0.34	44.51	0.66	104.91			94.08
L1	0.22	1.60	0.37	63.48	0.41	158.89	133.08
L2	0.24	1.60	0.34	56.55	0.42	149.00	126.68
L3	0.37	1.39	0.45	53.95	0.18	138.81	96
Dopant-free spiro-OMeTAD	0.13	5.66	0.41	46.26	0.46	95.60	79.86
Doped spiro-OMeTAD	0.16	6.59	0.50	34.48	0.34	67.56	52.18

$$\tau_{avg} = \frac{\sum f_i \tau_i^2}{\sum f_i \tau_i}$$

Reference

1. M. Jeong, W. Choi In, M. Go Eun, Y. Cho, M. Kim, B. Lee, S. Jeong, Y. Jo, W. Choi Hye, J. Lee, J.-H. Bae, K. Kwak Sang, S. Kim Dong and C. Yang, *Science*, 2020, **369**, 1615-1620.
2. Y. Liu, Q. Chen, H.-S. Duan, H. Zhou, Y. Yang, H. Chen, S. Luo, T.-B. Song, L. Dou, Z. Hong and Y. Yang, *J. Mater. Chem. A*, 2015, **3**, 11940-11947.
3. B. Tu, Y. Wang, W. Chen, B. Liu, X. Feng, Y. Zhu, K. Yang, Z. Zhang, Y. Shi, X. Guo, H. F. Li, Z. Tang, A. B. Djurisic and Z. He, *ACS Appl. Mater. Interfaces*, 2019, **11**, 48556-48563.
4. J. Zhou, X. Yin, Z. Dong, A. Ali, Z. Song, N. Shrestha, S. S. Bista, Q. Bao, R. J. Ellingson, Y. Yan and W. Tang, *Angew. Chem. Int. Ed.*, 2019, **58**, 13717-13721.
5. X. Yin, J. Zhou, Z. Song, Z. Dong, Q. Bao, N. Shrestha, S. S. Bista, R. J. Ellingson, Y. Yan and W. Tang, *Adv. Funct. Mater.*, 2019, **29**, 1904300.
6. Y. Liu, Z. Hong, Q. Chen, H. Chen, W.-H. Chang, Y. Yang, T.-B. Song and Y. Yang, *Adv. Mater.*, 2016, **28**, 440-446.
7. B. X. M. Zhao, C. Yao, K. C. Gu, T. R. Liu, Y. Xia and Y. L. Loo, *Energy Environ. Sci.*, 2020, **13**, 4334-4343.
8. H. Guo, H. Zhang, C. Shen, D. Zhang, S. Liu, Y. Wu and W. H. Zhu, *Angew. Chem. Int. Ed.*, 2021, **60**, 2674-2679.
9. M. Cheng, K. Aitola, C. Chen, F. Zhang, P. Liu, K. Sveinbjörnsson, Y. Hua, L. Kloo, G. Boschloo and L. Sun, *Nano Energy*, 2016, **30**, 387-397.
10. P. Xu, P. Liu, Y. Li, B. Xu, L. Kloo, L. Sun and Y. Hua, *ACS Appl. Mater. Interfaces*, 2018, **10**, 19697-19703.
11. T. Niu, W. Zhu, Y. Zhang, Q. Xue, X. Jiao, Z. Wang, Y.-M. Xie, P. Li, R. Chen, F. Huang, Y. Li, H.-L. Yip and Y. Cao, *Joule*, 2021, **5**, 249-269.
12. Q. Cheng, H. Chen, F. Yang, Z. Chen, W. Chen, H. Yang, Y. Shen, X. M. Ou, Y. Wu, Y. Li and Y. Li, *Angew. Chem. Int. Ed.*, 2022, **61**, e202210613.
13. Y.-H. Lin, N. Sakai, P. Da, J. Wu, H. C. Sansom, A. J. Ramadan, S. Mahesh, J. Liu, R. D. J. Oliver, J. Lim, L. Aspitarte, K. Sharma, P. K. Madhu, A. B. Morales-Vilches, P. K. Nayak, S. Bai, F. Gao, C. R. M. Grovenor, M. B. Johnston, J. G. Labram, J. R. Durrant, J. M. Ball, B. Wenger, B. Stannowski and H. J. Snaith, *Science*, 2020, **369**, 96.
14. X. Zheng, Y. Hou, C. Bao, J. Yin, F. Yuan, Z. Huang, K. Song, J. Liu, J. Troughton, N. Gasparini, C. Zhou, Y. Lin, D.-J. Xue, B. Chen, A. K. Johnston, N. Wei, M. N. Hedhili, M. Wei, A. Y. Alsalloum, P. Maity, B. Turedi, C. Yang, D. Baran, T. D. Anthopoulos, Y. Han, Z.-H. Lu, O. F. Mohammed, F. Gao, E. H. Sargent and O. M. Bakr, *Nat. Energy*, 2020, **5**, 131-140.
15. X. Li, W. Zhang, X. Guo, C. Lu, J. Wei and J. Fang, *Science*, 2022, **375**, 434-437.
16. R. Chen, S. Liu, X. Xu, F. Ren, J. Zhou, X. Tian, Z. Yang, X. Guanz, Z. Liu, S. Zhang, Y. Zhang, Y. Wu, L. Han, Y. Qi and W. Chen, *Energy Environ. Sci.*, 2022, **15**, 2567-2580.
17. Z. Li, B. Li, X. Wu, A. Sheppard Stephanie, S. Zhang, D. Gao, J. Long Nicholas and Z. Zhu, *Science*, 2022, **376**, 416-420.

18. R. Azmi, E. Ugur, A. Seitkhan, F. Aljamaan, A. S. Subbiah, J. Liu, G. T. Harrison, M. I. Nugraha, M. K. Eswaran, M. Babics, Y. Chen, F. Xu, T. G. Allen, A. U. Rehman, C. L. Wang, T. D. Anthopoulos, U. Schwingenschlogl, M. De Bastiani, E. Aydin and S. De Wolf, *Science*, 2022, **376**, 73-77.
19. S. Bai, P. Da, C. Li, Z. Wang, Z. Yuan, F. Fu, M. Kawecki, X. Liu, N. Sakai, J. T.-W. Wang, S. Huettner, S. Buecheler, M. Fahlman, F. Gao and H. J. Snaith, *Nature*, 2019, **571**, 245-250.
20. A. Mei, Y. Sheng, Y. Ming, Y. Hu, Y. Rong, W. Zhang, S. Luo, G. Na, C. Tian, X. Hou, Y. Xiong, Z. Zhang, S. Liu, S. Uchida, T.-W. Kim, Y. Yuan, L. Zhang, Y. Zhou and H. Han, *Joule*, 2020, **4**, 2646-2660.
21. Y.-W. Jang, S. Lee, K. M. Yeom, K. Jeong, K. Choi, M. Choi and J. H. Noh, *Nat. Energy*, 2021, **6**, 63-71.
22. J. Peng, D. Walter, Y. Ren, M. Tebyetekerwa, Y. Wu, T. Duong, Q. Lin, J. Li, T. Lu, M. A. Mahmud, O. L. C. Lem, S. Zhao, W. Liu, Y. Liu, H. Shen, L. Li, F. Kremer, H. T. Nguyen, D.-Y. Choi, K. J. Weber, K. R. Catchpole and T. P. White, *Science*, 2021, **371**, 390.
23. T. Bu, J. Li, H. Li, C. Tian, J. Su, G. Tong, L. K. Ono, C. Wang, Z. Lin, N. Chai, X.-L. Zhang, J. Chang, J. Lu, J. Zhong, W. Huang, Y. Qi, Y.-B. Cheng and F. Huang, *Science*, 2021, **372**, 1327.
24. G. Kim, H. Min, K. S. Lee, D. Y. Lee, S. M. Yoon and S. I. Seok, *Science*, 2020, **370**, 108-112.
25. J. Lee, M. Malekshahi Byranvand, G. Kang, S. Y. Son, S. Song, G. W. Kim and T. Park, *J. Am. Chem. Soc.*, 2017, **139**, 12175-12181.
26. G.-W. Kim, J. Lee, G. Kang, T. Kim and T. Park, *Adv. Energy Mater.*, 2018, **8**, 1701935.
27. E. H. Jung, N. J. Jeon, E. Y. Park, C. S. Moon, T. J. Shin, T. Y. Yang, J. H. Noh and J. Seo, *Nature*, 2019, **567**, 511-515.
28. F. Qi, X. Deng, X. Wu, L. J. Huo, Y. Q. Xiao, X. H. Lu, Z. L. Zhu and A. K. Y. Jen, *Adv. Energy Mater.*, 2019, **9**, 1902600.
29. F. Zhang, Z. Yao, Y. Guo, Y. Li, J. Bergstrand, C. J. Brett, B. Cai, A. Hajian, Y. Guo, X. Yang, J. M. Gardner, J. Widengren, S. V. Roth, L. Kloo and L. Sun, *J. Am. Chem. Soc.*, 2019, **141**, 19700-19707.
30. G. You, Q. Zhuang, L. Wang, X. Lin, D. Zou, Z. Lin, H. Zhen, W. Zhuang and Q. Ling, *Adva. Energy Mater.*, 2019, **10**, 1903146.
31. L. Wang, Q. Zhuang, G. You, X. Lin, K. Li, Z. Lin, H. Zhen and Q. Ling, *ACS Appl. Energy Mater.*, 2020, **3**, 12475-12483.
32. J. Lee, G. W. Kim, M. Kim, S. A. Park and T. Park, *Adv. Energy Mater.*, 2020, **10**, 1902662.
33. Z. J. Li, J. Park, H. Park, J. Lee, Y. Kang, T. K. Ahn, B. G. Kim and H. J. Park, *Nano Energy*, 2020, **78**, 105159.
34. X. Q. Jiang, X. Liu, J. F. Zhang, S. Ahmad, D. D. Tu, W. Qin, T. G. Jiu, S. P. Pang, X. Guo and C. Li, *J. Mater. Chem. A*, 2020, **8**, 21036-21043.
35. Z. Yao, F. Zhang, Y. Guo, H. Wu, L. He, Z. Liu, B. Cai, Y. Guo, C. J. Brett, Y. Li, C. V. Srambickal, X. Yang, G. Chen, J. Widengren, D. Liu, J. M. Gardner, L. Kloo

and L. Sun, *J. Am. Chem. Soc.*, 2020, **142**, 17681-17692.
36. Z. Yao, F. Zhang, L. He, X. Bi, Y. Guo, Y. Guo, L. Wang, X. Wan, Y. Chen and L. Sun, *Angew. Chem. Int. Ed.*, 2022, **61**, e202201847.
37. Q. Fu, X. Tang, H. Liu, R. Wang, T. Liu, Z. Wu, H. Y. Woo, T. Zhou, X. Wan, Y. Chen and Y. Liu, *J. Am. Chem. Soc.*, 2022, **144**, 9500-9509.
38. Q. Fu, H. Liu, S. Li, T. Zhou, M. Chen, Y. Yang, J. Wang, R. Wang, Y. Chen and Y. Liu, *Angew. Chem. Int. Ed.*, 2022, **n/a**, e202210356.
39. Y. Bai, Z. Zhou, Q. Xue, C. Liu, N. Li, H. Tang, J. Zhang, X. Xia, J. Zhang, X. Lu, C. J. Brabec and F. Huang, *Adv. Mater.*, 2022, 2110587.
40. Q. Fu, Z. Y. Xu, X. C. Tang, T. T. Liu, X. Y. Dong, X. D. Zhang, N. Zheng, Z. Q. Xie and Y. S. Liu, *Acs Energy Lett.*, 2021, **6**, 1521-1532.
41. F. Zhang, Z. Q. Wang, H. W. Zhu, N. Pellet, J. S. Luo, C. Y. Yi, X. C. Liu, H. L. Liu, S. R. Wang, X. G. Li, Y. Xiao, S. M. Zakeeruddin, D. Q. Bi and M. Gratzel, *Nano Energy*, 2017, **41**, 469-475.
42. H. Zhang, Y. Wu, W. Zhang, E. Li, C. Shen, H. Jiang, H. Tian and W.-H. Zhu, *Chem. Sci.*, 2018, **9**, 5919-5928.
43. C. Shen, Y. Wu, H. Zhang, E. Li, W. Zhang, X. Xu, W. Wu, H. Tian and W. H. Zhu, *Angew. Chem. Int. Ed.*, 2019, **58**, 3784-3789.
44. D. Zhang, P. Xu, T. Wu, Y. Ou, X. Yang, A. Sun, B. Cui, H. Sun and Y. Hua, *J. Mater. Chem. A*, 2019, **7**, 5221-5226.
45. J. Wang, H. Zhang, B. Wu, Z. Wang, Z. Sun, S. Xue, Y. Wu, A. Hagfeldt and M. Liang, *Angew. Chem. Int. Ed.*, 2019, **58**, 15721-15725.
46. H. Zhu, Z. Shen, L. Pan, J. Han, F. T. Eickemeyer, Y. Ren, X. Li, S. Wang, H. Liu, X. Dong, S. M. Zakeeruddin, A. Hagfeldt, Y. Liu and M. Grätzel, *ACS Energy Lett.*, 2020, **6**, 208-215.
47. J. Wang, X. Wu, Y. Z. Liu, T. Qin, K. C. Zhang, N. Li, J. Zhao, R. Q. Ye, Z. X. Fan, Z. G. Chi and Z. L. Zhu, *Adva. Energy Mater.*, 2021, **11**, 2100967.
48. K.-M. Lee, W.-H. Chiu, Y.-H. Tsai, C.-S. Wang, Y.-T. Tao and Y.-D. Lin, *Chem. Eng. J.*, 2022, **427**, 131609.

Table of contents

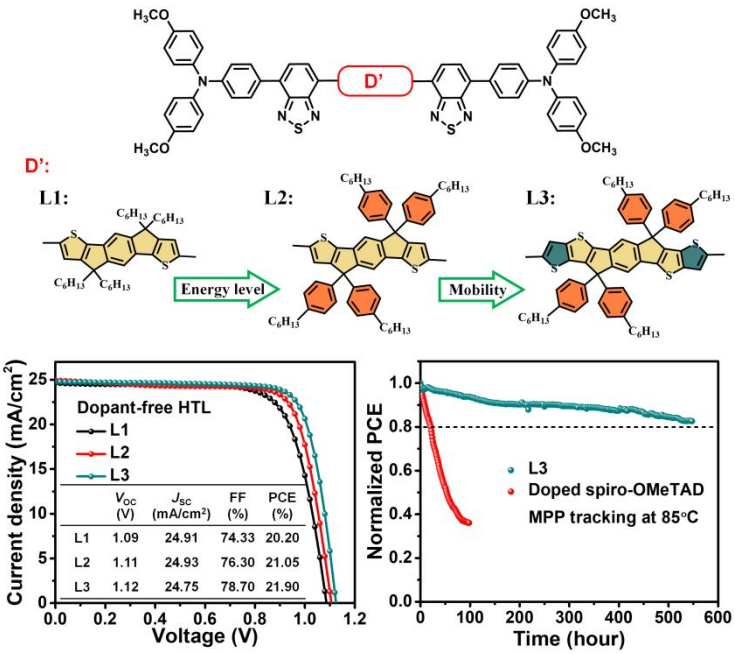

	V_{OC} (V)	J_{SC} (mA/cm²)	FF (%)	PCE (%)
L1	1.09	24.91	74.33	20.20
L2	1.11	24.93	76.30	21.05
L3	1.12	24.75	78.70	21.90

Molecular hole transport material retards the iodine migration and delivers high stability in harsh 85°C MPP test.

Perovskite solar cells (PSCs) have ionic interdiffusion to hamper the stability. Herein, three linear molecules termed as L1, L2 and L3 with D-A-D'-A-D structure are developed as dopant-free hole transport materials (HTMs). The π-bridge extension with active sites for coordination leverages the intramolecular dipole effect and intermolecular packing effect, resulting in conformally bonded ultrathin interface with compact and uniform coverage (~60 nm) to retard iodine migration and protect the buried perovskite. L3-PSC maintains over 85% of the initial efficiency after 500-hour at 85˚C maximum power point tracking (MPP) and realizes the possibility of using small molecules to stabilize n-i-p PSCs. It provides an effective strategy to address the intractable problem of PSC towards commercialization

REVIEWER REPORT(S):

Referee: 1

Recommendation: Minor Revisions

Comments to the Author

The authors designed and synthesized a new series of linear molecules (L-series) for dopant-free hole-transporting materials of D-A-D'-A-D structure for realizing the high performance and stable n-i-p perovskite solar cells (PSCs). L-series have reduced disorder and improved defect passivation capability by changing the bridge extension. Compared to previous works, this paper also delivers a breakthrough result related to the harsh 85°C MPP test with small molecules. There is still no report that small molecular HTM can endure the harsh 85°C MPP test. It demonstrates that the strengthened interface between HTM and perovskite allows PSC with small molecules to endure 85°C MPP. This is a considerable insight into structure design for dopant-free HTMs and a new design concept for highly stable PSCs.

The paper is well presented. It also demonstrates the structure-performance-stability relationship through a series of tests. The π-bridge extension with active sites for coordination leverages the intramolecular dipole effect and intermolecular packing effect, resulting in a conformally bonded ultrathin interface with compact and uniform coverage (~60 nm) to retard iodine migration and protect the buried perovskite. Ultrafast spectroscopy reveals that L-series molecules have a sequential reduction of photoexcited energy disorder to illustrate the structure-performance-stability relationship. Therefore, I suggest publication in Energy & Environmental Science.

Minor points need to be addressed.

Response: We gratefully thank the reviewer for the constructive comments to the manuscript and have made a major revision to address all the reviewers' concerns. We hope the revised version can meet the high standard for publication in Energy & Environmental Science.

(1) Could the performance of the device be further improved by doping in the L3 HTM?

Response: Many thanks to the reviewer for the kind comment! According to comment, additives, such as TBP and Li-TFSI, were added with different concentration in L3 HTM solution. However, the efficiency of PSCs was decreased obviously. We find that the introduction of additives affects the tight packing of L3 molecules and hampers the contact between perovskite and HTM based on the reduced parameters.

Table R1. Summary of device performance of PSCs with doped and dopant-free L3 HTL.

L3	V_{OC} (V)	J_{SC} (mA/cm^2)	FF (%)	PCE (%)
Dopant-free	1.10	24.34	79.33	21.19
Doped	1.12	24.29	59.43	16.14

(2) The authors mention that 'we do not deposit PEAI on the perovskite surface to passivate surface defects but we find that the photovoltage is acceptable'. Whether PEAI was deposited onto perovskite films for the highest efficiency devices should be clear, as this would affect the passivation of perovskite films by HTLs.

Response: We thank the reviewer for the suggestion. Actually, we have fabricated the L-series PSCs with PEAI passivation layer. The results suggested that PEAI passivation could improve the V_{OC} but decrease the PCE of L-series PSCs due to reduced FF. Surface passivation with PEAI with long chains will reduce the chemical bonding between L3 and PbI_2-rich surface of perovskite. The PbI_2-rich surface will enhance the interface charge transfer and stability. Therefore, the coordination interaction between HTL and perovskite is important for the photothermal stability, which is also the novelty of this work. PEAI will interrupt chemical bonding between PbI_2-terminated perovskite and HTL.

Table R2. Summary of device performance of L3-PSCs with different passivated perovskite film.

	V_{OC} (V)	J_{SC} (mA/cm^2)	FF (%)	PCE (%)
Control	1.10	24.34	79.33	21.19
PEAI	1.12	23.81	72.53	19.34

(3) In Figure 6g and h, substantial iodine was detected in the spiro-OMeTAD layer for the fresh and aged control device based on doped spiro-OMeTAD due to ionic interdiffusion between Li-salt and iodide ions. And the interdiffusion area was enlarged in the spiro-OMeTAD HTL of aged device. The areas marked in Figure 6 h may not be accurate, according the iodide ions accumulation and the position where Pb- signal appeared. The author needs further confirmation.

Response: We gratefully thank the reviewer for the kind suggestion. For the gradient longitudinal distribution of iodine ions and lead ions appearing at the interface between perovskite film and spiro-OMeTAD layer with aged doped spiro-OMeTAD PSC, we have careful checked our ToF-SIMS results and assigned the position for the different layers more accurately in the revised manuscript. We fully agree with the reviewer that the “interdiffusion area” can enlarge to the whole spiro-OMeTAD layer in aged spiro-OMeTAD PSCs after 85°C aging for 10 days in the argon. However, according to the curve of iodine ions, we confirm the position of the diffusion boundary.

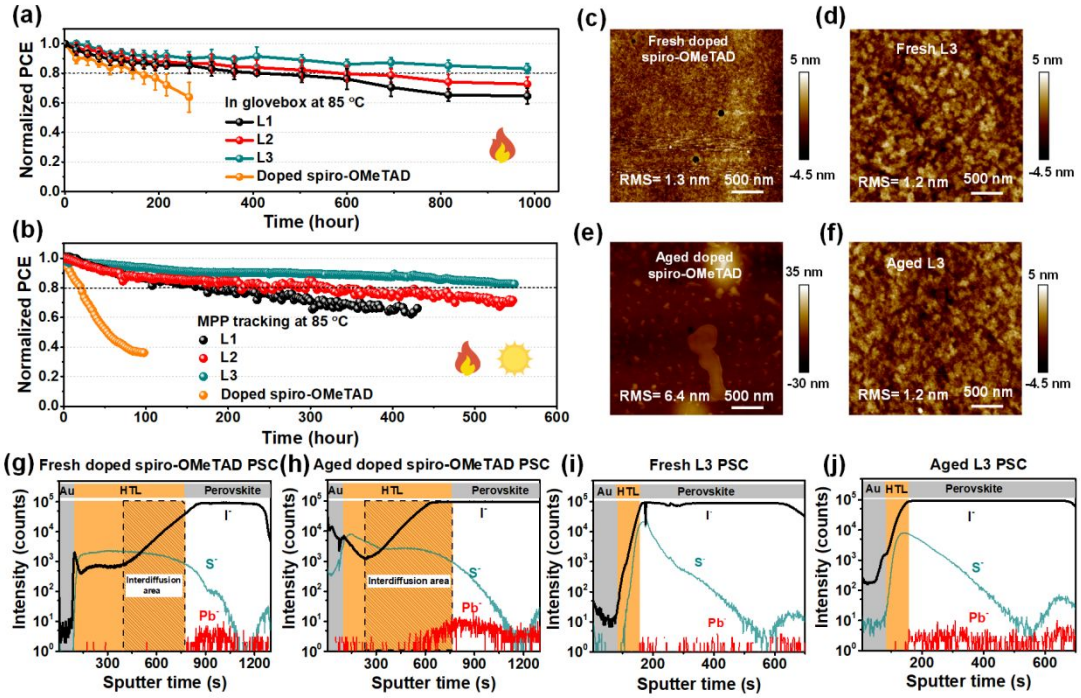

Figure 6. ToF-SIMS of depth profiles of anion distribution within full PSCs, (A) fresh doped spiro-OMeTAD PSC, (B) fresh L3 PSC, (C) doped spiro-OMeTAD PSCs with 85°C aging for 10 days in the argon, (D) L3 PSC with 85°C aging for 10 days in the argon.

(4) Proper references should be added. On page 9, the authors argued that 'Moreover, as shown in Fig. S42, both the doped spiro-OMeTAD and L3 HTMs-covered perovskite films were found to exhibit red-shifted absorption edges in the UV-vis absorption spectra for aged perovskite film, indicating that the perovskite itself inevitably degrades through the loss of chloride component under heating conditions'. I suggest adding the proper references to this statement to make their argument more reliable. I also suggest that authors update the recent state-of-the-art HTL-relevant papers

Response: Many thanks to the reviewer for the kind suggestions! As suggested, we have added the references (*Adv. Funct. Mater.*, 2014, **24**, 7102-7108. *Nano Energy*, 2017, **40**, 248-257.) in the revised manuscript to help the understanding of corresponding statements. We also updated the recently published literatures (Ref. 11,

41) about HTMs in revised manuscript.

The modified statements in the revised manuscript are listed as follows:

In page 1 of revised manuscript

The ionic interdiffusion between hygroscopic dopants/additives and halide of perovskite can cause device degradation, especially under continuous thermal and illumination conditions.[10, 11]

In page 2 of revised manuscript

There are still plenty of room to engineer the structure units for photothermal stable PSCs.[28, 30, 41]

In page 9 of revised manuscript

Moreover, as shown in Fig. S41, both the doped spiro-OMeTAD and L3 HTMs-covered perovskite films were found to exhibit red-shifted absorption edges in the UV-vis absorption spectra for aged perovskite film, indicating that the perovskite itself inevitably degrades through the loss of chloride component under heating conditions.[65.66]

(5) In Figures 5 e and f, the inserted device structure does not match the structure described in the corresponding text.

Response: Thank the reviewer. As suggested, it has been corrected in the revised manuscript.

The modified Figure 5 in the revised manuscript was shown in the following.

In page 7 of revised manuscript.

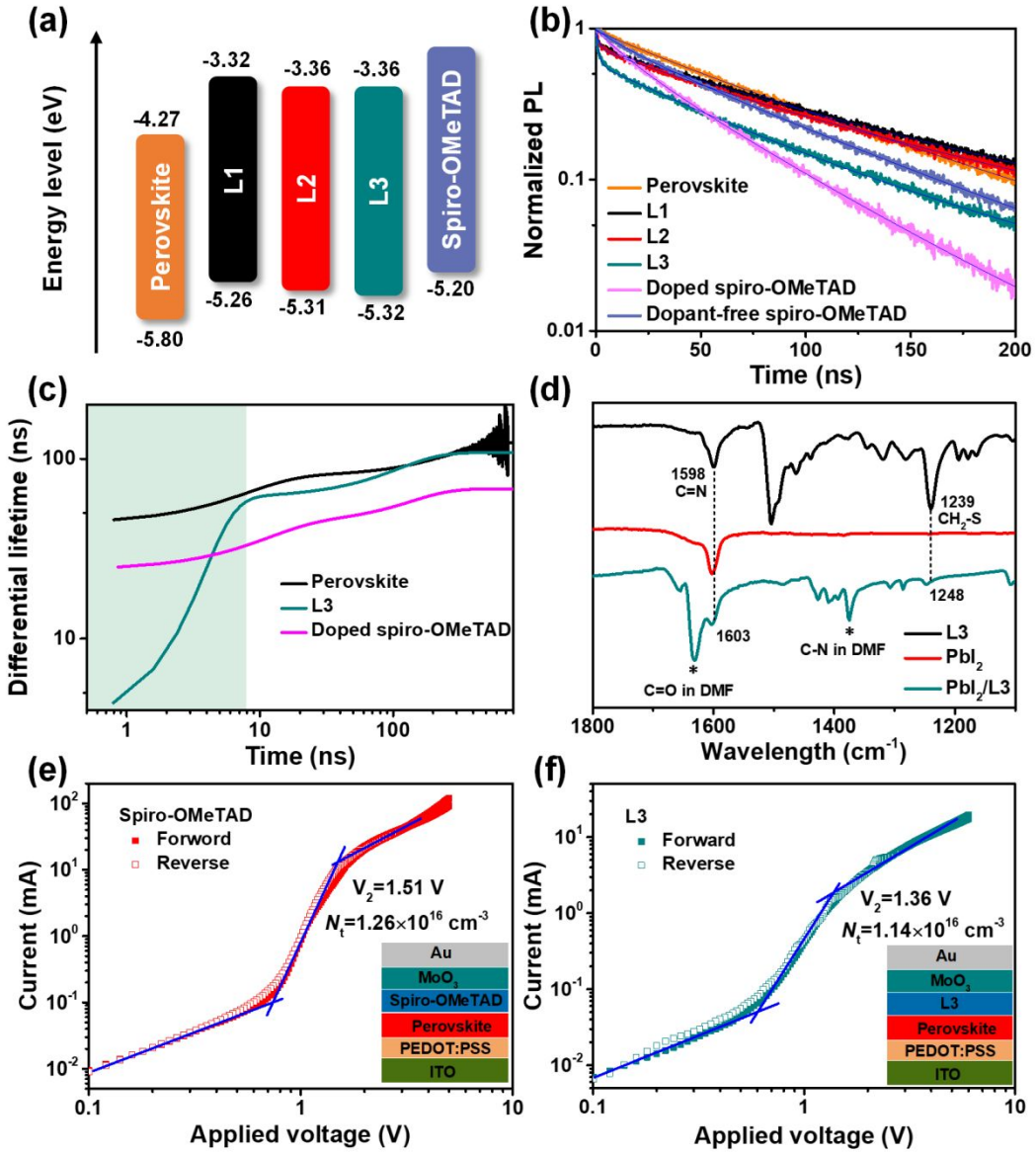

Fig. 5 Charge transfer and passivation effect. (a) Energy level diagram, (b) TRPL and (c) computed differential lifetimes from Fig. 5b for the bare perovskite, L3, and doped spiro-OMeTAD coated perovskites. The shaded areas are a guide marking for charge transfer. (d) FTIR spectra of the powders of L3, PbI_2 and PbI_2/L3 blend. The peak of 1632 cm^{-1} and 1375 cm^{-1} are ascribed to C=O and C-N of DMF, respectively, which form an adduct of PbI_2•xDMF.[58] The forward and reverse SCLC curves of (e, f) hole-only devices.

Referee: 2

Recommendation: Reject & Transfer

Comments to the Author

This work with the title "Conformally bonded molecular interface retarded iodine migration for durable perovskite solar cells" synthesized three IDT-based hole transport materials (HTMs), and the perovskite solar cells (PSCs) based on L3 obtained a champion PCE of 22.61% with AR film and displayed good stability.

However, the so-called "retarded iodine migration" in the title is mainly obtained by the ToF-SIMS test compared with doped spiro-OMeTAD. It is well-known that ion migration in doped spiro-OMeTAD is easy for the volatile TBP and Li-TFSI migration and provides the channel for iodine migration. Thus, it is not so evident that retarded iodine migration for L3 HTM only.

Response: We gratefully thank the reviewer for precious time and the constructive comments on our manuscript, especially on the device physics and related techniques, which are helpful for enhancing the scientific quality of our work. We fully agree with the reviewer that the retarded iodine migration is indeed not only related to L3 HTM. As it is well known, the volatile TBP and Li-TFSI dopants are employed to improve the PCE due to the increased V_{OC} and FF. However, the dopants will aggravate the iodine migration and thus degrade the performance (*ACS Energy Letters*, **2018**, *3*, 1677-1682). Therefore, there is a great trade-off between PCE and stability for doped spiro-OMeTAD. This greatly limits the use of spiro-OMeTAD in the future perovskite mass production, and is also our strong motivation for the design of new dopant-free L-series HTMs.

Compared to doped spiro-OMeTAD, The L3-PSCs has T80 of 85°C thermal stability over 1000 hours and T85 of MPP 85°C thermal stability over 500 hours. Although the retarded iodine migration is not only related to L3 HTM, our results suggest the highest achievable comprehensive performance in terms of efficiency and stability (see Figure 1 and Table 1). Especially, our work demonstrates the

breakthrough result related to harsh 85°C MPP test. There is still no report that small molecular HTM can endure these harsh aging conditions. This molecule design of L3 demonstrates the possibility of using small molecules to realize harsh 85°C MPP for *n-i-p* PSCs.

Table 1. Detailed parameters of PSCs with different HTLs.

HTL	V_{OC} (V)	J_{SC} (mA/cm^2)	FF (%)	PCE (%)
L1	1.09	24.91	74.33	20.20
L2	1.11	24.93	76.30	21.05
L3	1.12	24.75	78.70	21.90
Dopant-free spiro-OMeTAD	1.04	24.59	61.82	15.87
Doped spiro-OMeTAD	1.15	24.83	77.01	21.94

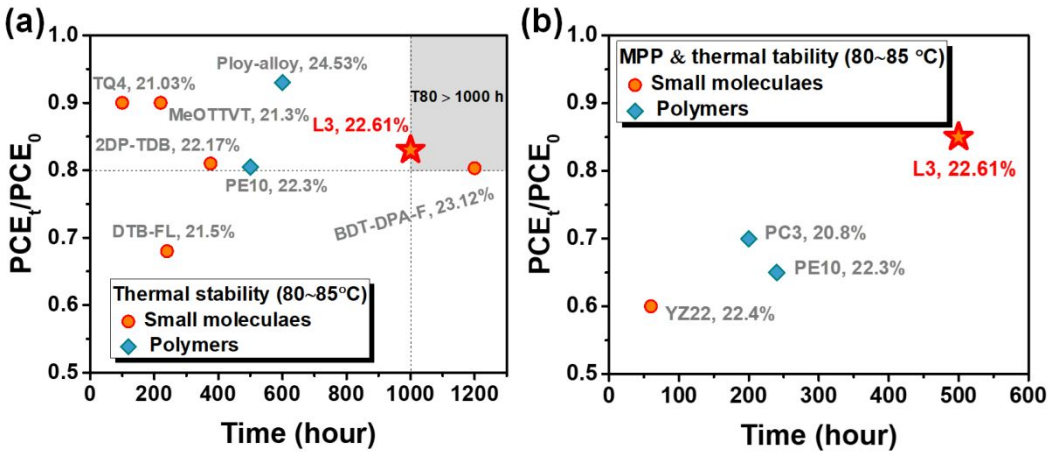

Fig. R1 Summary of the thermal stability PCEs for *n-i-p* PSCs with dopant-free HTMs. (a) thermal stability at 80-85°C, (b) MPP and thermal stability at 80-85°C.

In our design for L-series, the π-bridge extension with active sites for coordination leverages the intramolecular dipole effect and intermolecular packing effect, resulting in conformally bonded ultrathin interface with compact and uniform coverage (~60 nm) to retard iodine migration and protect the buried perovskite. Microstructure analysis (SEM, TEM, AFM) reveals compact and uniform film is conformally bonded on perovskite surface, leading to retarded iodine migration. Rapid carrier transport, sequentially reduced disorder and improved defect passivation capability of the L-series are also demonstrated by ultrafast laser spectroscopy.

Based on the result of ToF-SIMS test, we found that the diffusion of iodine ions

is very obvious in spiro-OMeTAD HTL after thermal aging, while the diffusion of iodine ions in L3 HTL is greatly suppressed. Thus, we can reasonably infer that the reason for the improvement of the thermal stability of L3-based device is that the L3 HTL reduces the migration of iodine ions.

Thus, we demonstrate the molecular packing and interface binding afford the L3 to delivers the high MPP thermal stability and related characterizations help to understand the molecular packing, reduced disorder, transport/recombination dynamics and degradation mechanisms. We made a major revision according to the reviewer's comments, which greatly improves the scientific quality of our manuscript. As such, we hope we have successfully addressed all the concerns raised by the reviewer, and our work could be reconsidered for publication in Energy & Environmental Science.

There are some other concerns:

1. The highlights of this work, "Rapid carrier transport, sequentially reduced disorder, and improved defect passivation capability of the L-series are also demonstrated by ultrafast transient absorption spectroscopy." The manuscript only showed reduced disorder of L3, no rapid carrier transport, and improved defect passivation capability in ultrafast transient absorption spectroscopy.

Response: We gratefully thank the reviewer for the insightful comments on our manuscript! We feel sorry for the misleading of the summaries in the highlights. Actually, we try to emphasize that rapid carrier transport, and improved defect passivation capability of the L-series are demonstrated by ultrafast laser spectroscopy, including TRPL and TAS, as shown in the previous manuscript and SI. The reduced disorder of L3 is demonstrated by TAS on bare L-series films. The rapid transport and defect passivation are revealed by TRPL. We also have carefully checked our revised manuscript and modified the related text.

2. Passivation effect demonstrated by the XPS, the XPS of N, S, and O should be provided.

Response: We appreciate the reviewer for the suggestions! As suggested, we have added the XPS full spectrum, *N* 1s spectrum, *S* 2p spectrum and *O* 1s spectrum in the revised SI. We find the small shift of *N* 1s and *S* 2p also occurs in the perovskite film coated with L3 HTM and the peak of *O* 1s do not shifts. These results are in good agreement with the FTIR measurement, which demonstrate chemically bonding passivation between PbI_2 and the benzothiadiazole and thiophene moieties of L3 HTM.

The corresponding discussion and figures were updated in the revised manuscript and supporting information, respectively.

The modified statements in the revised manuscript were listed in the following:

In page 8 of revised manuscript

"A small shift of *N* 1s and *S* 2p also occurs in the perovskite film coated with L3 HTM and the peak of O 1s do not shifts. These results are in good agreement with the FTIR measurement, which demonstrate chemically bonding passivation between PbI_2 and the benzothiadiazole and thiophene moieties of L3 HTM."

In page 35 of revised supporting information, we modified the Fig. S38.

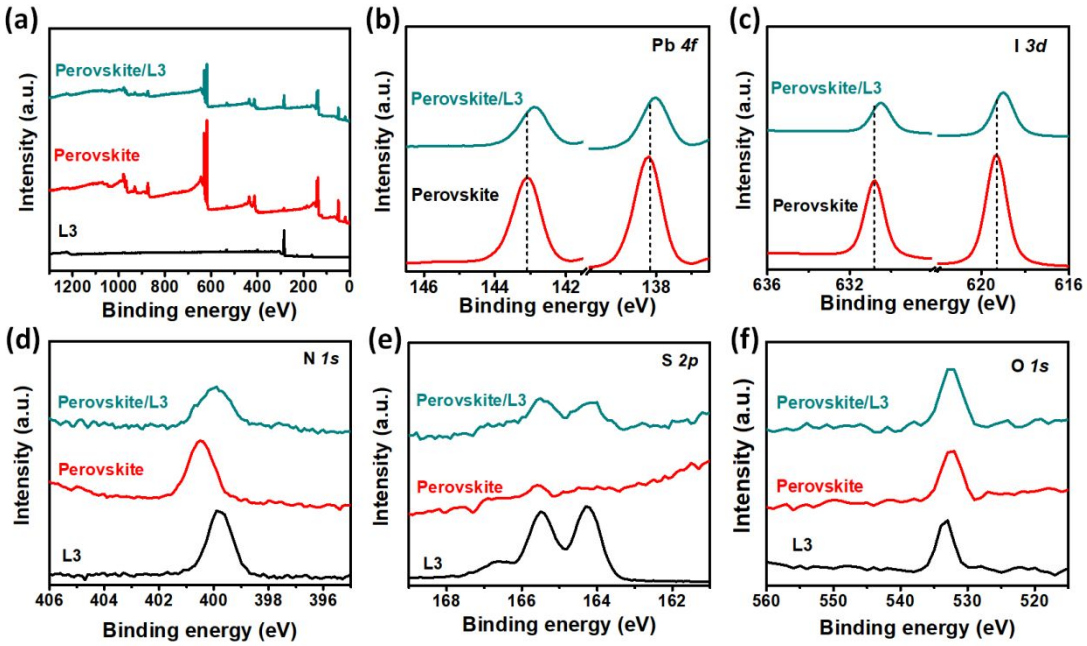

Fig. S38. The XPS spectrum of the perovskite film, L3 film, and perovskite/L3 film. (a) full spectrum, (b) Pb 4f, (c) *I* 3d (d) *N* 1s (e) *S* 2p and (f) *O* 1s.

3. It is not scientific to estimate the passivation effect of perovskite films in the presence of HTMs by the SCLC method, in this work since the HTMs themselves also have traps. You can not differentiate between these defects.

Response: We gratefully thank the reviewer for the kind comments! We fully agree with the reviewer that it is not scientific to directly estimate the passivation effect of perovskite films in the presence of HTMs by the SCLC method. According to the literature, the SCLC test cannot accurately calculate the reduction value of defects in the perovskite film. Actually, the overall estimation for perovskite-HTM is also useful for the device performance. To avoid this misunderstanding, we have modified the corresponding parts in the revised manuscript to describe the decreased overall trap states ascribed to both of perovskite film and L3 HTL.

Besides, we use different characterizations to differentiate them.

First of all, for HTL, we used GIWAX and ultrafast transient absorption spectra to estimate the orientation/arrangement and photoexcited carrier disorder of L-series

HTL. It is found that the better orientation of L3 makes it have fewer carrier disorders, which is conducive to the carrier transfer/transport. This result is also consistent with the device performance results.

Then, for the passivation of L3 on the perovskite thin film, we have used FTIR to explain the interaction between the benzothiadiazole and thiophene moieties in the L3 molecule and the lead iodide in the perovskite. The XPS test further confirmed these interactions between L3 HTM and perovskite film. Based on above results, we believe that L3 has a passivation effect on the perovskite thin film, which can effectively reduce the density of defect states of the perovskite thin film. At the same time, L3 connected with the perovskite film by chemical bonding, which is more conducive to carrier transfer and improves the power conversion efficiency of the corresponding PSCs.

Finally, we quantified the defect density of the hole-only device by the SCLC method, and found that L3-based hole-only device with similar defects to doped spiro-OMeTAD hole-only device. This may be caused by the overall decline of defects in the perovskite layer and HTL. Therefore, in terms of reduced defects in the device, L3 hole-only device has similar performance to that of spiro-OMeTAD hole-only devices, which is also consistent with the similar device performance of standard doped spiro-OMeTAD PSC.

To avoid this misunderstanding, we have modified the corresponding parts in the revised manuscript to describe the decreased trap states ascribed to the both of perovskite film and L3 HTL.

The modified statements in the revised manuscript were listed in the following:

In page 8 of revised manuscript

"The trap density was further quantified by the SCLC method. The dark *J-V* curves of hole-only devices with a configuration of ITO/PEDOT:PSS/perovskite/HTM/MoO_3/Ag. We evaluated the trap-state density via the trap-filled limit voltage (V_{TFL}), obtained from $n_t = q\varepsilon\varepsilon_0 V_{TFL}/(qL^2)$,[61-63] where q is the elementary charge, ε relative dielectric constant, ε_0 vacuum permittivity, L

thickness of the perovskite film, and V_{TFL} trap-filling limit voltage. As shown in Fig. 5, e and f, V_2 gives the most accurate value for the trap density due to the mixed ionic and electronic nature of perovskites.[63] The trap densities were calculated to be 1.26×10^{16} and 1.14×10^{16} cm^{-3} by V_2 for the devices with doped spiro-OMeTAD and L3 HTL, respectively, with similar values to each other. For the standard spiro-OMeTAD, the dopants can not only enhance the conductivity (Li-salt), but can passivate perovskite film by the pyridine group.[64] For L3 HTL, the low trap states may be attributed to the reduced energy disorder of L3 and passivation effect on the perovskite film.[40] L3 HTL has much thinner thickness (~60 nm) than doped spiro-HTL to block the charge recombination event at the interface, due to close packing, coordination interaction and conformal coverage. Therefore, L3 PSC has similar PV performance to the doped spiro-OMeTAD PSC in our system."

4. In time-resolved PL (TRPL), the authors said, "Triexponential decays give a better fit than traditional bi-exponential decays, which is probably due to the charge transfer, radiative recombination, and passivation effect events." The radiative recombination and passivation effect events for t2 and t3 were not mentioned. Moreover, in Fig. 5c, the perovskite films with L-series HTMs exhibit a faster charge transfer process than that of doped spiro-OMeTAD HTM. How to explain the doped spiro-OMeTAD (21.94%) have better performance than all the L-series HTMs.

Response: We gratefully thank the reviewer for the precious time and comments! Especially, the comments related to TRPL are indeed helpful to understand the device physics and give more accurate illustration on structure-property-performance correlation. Therefore, we carefully checked the data and provided more reasonable discussions in the revised manuscript.

For TRPL, we have given specific instructions in the caption of Figure S36 in supporting information and mentioned the passivation effects can be judged from the slowest component of TRPL after comparing with spiro-OMeTAD samples (Figure S35b) (related to $\tau_{1, 2, 3}$). To directly describe the lifetime of τ_2 and τ_3, we have also

added the corresponding statements about the lifetime of τ_2 and τ_3 in the page 8 of revised manuscript. There are two points that need to be noticed.

a) First, we reconsider the assignment of $\tau_{1, 2, 3}$ and make some revisions on the τ_1 based on the matter of fact that the charge transfer process (τ_1) includes the process of carrier extraction from the perovskite film to HTL and charge transport inside HTL. If we consider the two events for TRPL, we find that it makes sense to structure-property-performance correlation. In Fig. 5c, differential lifetime was modeled by fitting the TRPL spectra (Fig. 5b) with the equation of $t = -(d\ln(\varphi(t))/dt)^{-1}$, the processes that reduce the PL counts over time are separable, and the lifetime *t* is directly readable at each time point. We just compare L3 and doped spiro-HTL (Fig. R2), we can easily distinguish the dynamics of carrier recombination events in L3 and doped spiro-OMeTAD samples. See Fig. R2, for L3, the chemical interaction contacts between perovskite and HTL will accelerate the charge extraction, but the poor conductivity will constrain the charge transport. For doped spiro-HTL, although charge extraction occurs a little latter, the dopants greatly improve the charge transport to improve the whole charge transfer. Therefore, there is intersection point at ~4 ns. We have modified the corresponding parts about charge extraction process in the revised manuscript.

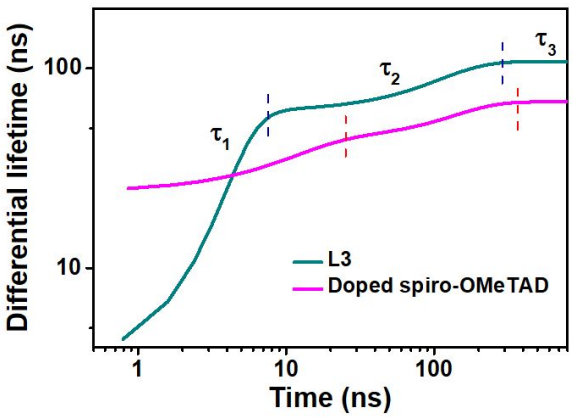

Fig. R2 Computed differential lifetimes from TRPL spectra for the L3, and doped spiro-OMeTAD coated perovskites.

b) Second, we add the discussion on radiative recombination (τ_2) and passivation effect (τ_3) events. Obviously, L-series have better passivation effects, leading to improved lifetimes. As well known, there is trade-off between carrier transport process and perovskite passivation process, leading to different charge collection efficiencies. It is difficult to judge the effect on device efficiency from one of these processes. Although doped spiro-OMeTAD does not have a fast carrier extraction process, the rapid carrier transfer from perovskite also makes it high efficiency. If without dopants, the efficiency is the lowest.

Therefore, according to the TRPL spectra, L3 and doped spiro-OMeTAD exhibit different dynamics in the carrier quenching process. L3 has a fast extraction process and passivation effect on perovskite film, while the doped spiro-OMeTAD has a faster transport due to its higher mobility. Compared with 21.94% efficiency of the doped spiro-OMeTAD PSCs, L3 PSCs also achieve a comparable efficiency of 21.9%, which is consistent with the TRPL data.

The modified statements, Figure and table in the revised manuscript were listed in the following:

In page 8 of revised manuscript

"Tri-exponential decays give better fit than traditional bi-exponential decays, which is due probably to the charge extraction/transport (τ_1), radiative recombination (τ_2) and passivation effect events (τ_3), presumably corresponding to the quenching process of photogeneration of free carriers of perovskite through charge transfer (including charge extraction from perovskite to HTL and charge transport in HTL), radiative recombination in the perovskite film, and passivation effects by functional group, respectively. As listed in Table S6, the average lifetimes of L-series perovskite films were incredibly improved compared with bare perovskite film. This indicated the passivation effect of L-series HTM on the perovskite film."

"The perovskite films with L-series HTMs exhibit faster charge extraction process than that of doped spiro-OMeTAD HTM. A readily charge extraction process from the perovskite film to L3 HTM was observed within 10 ns (green region in Figure 5c), which can be mainly ascribed to the

extended backbone of the IDTT π-bridge with deep HOMO energy level and high mobility.[42] while the doped spiro-OMeTAD has a faster transport due to its higher mobility. Compared with 21.94% efficiency of the doped spiro-OMeTAD PSCs, L3 PSCs also have a comparable efficiency of 21.9%. This performance is also consistent with TRPL data."

In page 7 of revised manuscript

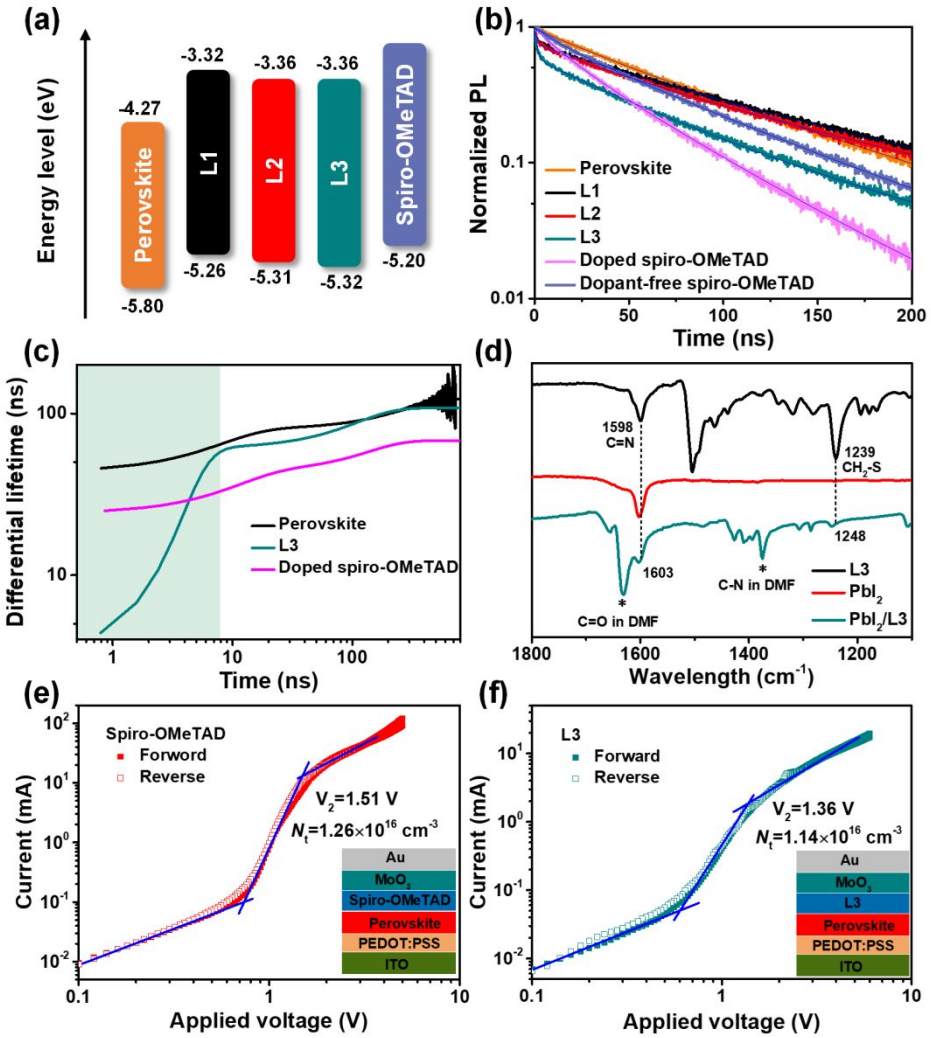

Fig. 5 Charge transfer and passivation effect. (a) Energy level diagram, (b) TRPL and (c) computed differential lifetimes from Fig. 5b for the bare perovskite, L3, and doped spiro-OMeTAD coated perovskites. The shaded areas are a guide marking for charge extraction. (d) FTIR spectra of the powders of L3, PbI_2 and PbI_2/L3 blend. The peak of 1632 cm^{-1} and 1375 cm^{-1} are ascribed to C=O and C-N of DMF, respectively, which form an adduct of PbI_2•xDMF.[58] The forward and reverse SCLC curves of (e, f) hole-only devices.

In page 42 of revised supporting information

Table S6. Lifetimes and weighted fractions fitted by triple-exponential functions from the time-resolved PL.

	A_1	τ_1 (ns)	A_2	τ_2 (ns)	A_3	τ_3 (ns)	τ_{avg} (ns)
Pristine	0.34	44.51	0.66	104.91			94.08
L1	0.22	1.60	0.37	63.48	0.41	158.89	133.08
L2	0.24	1.60	0.34	56.55	0.42	149.00	126.68
L3	0.37	1.39	0.45	53.95	0.18	138.81	96
Dopant-free spiro-OMeTAD	0.13	5.66	0.41	46.26	0.46	95.60	79.86
Doped spiro-OMeTAD	0.16	6.59	0.50	34.48	0.34	67.56	52.18

$\tau_{avg} = \frac{\Sigma f_i \tau_i^2}{\Sigma f_i \tau_i}$

5. There are some mistakes, such as 770 nm λabs, film for L2, the LUMO levels of L3, 3.36 eV.

Response: Thank the reviewer for pointing out the careless mistake! As suggested, it has been corrected in the revised manuscript.

In page 6 of revised manuscript.

Table 2. Optical, electrochemical, thermal, and charge transport properties of L1, L2 and L3.

	$\lambda_{abs,sol}$ (nm)[a]	$\lambda_{abs,film}$ (nm)	E_g^{opt} (eV)[b]	HOMO (eV)[c]	LUMO (eV)	T_d (°C)	T_g (°C)	μ_h (cm^2 V^{-1} s^{-1})
L1	569	583	1.94	-5.26	-3.32	440	105	2.53×10^{-4}
L2	561	570	1.95	-5.31	-3.36	449	120	3.28×10^{-4}
L3	559	569	1.96	-5.32	-3.36	449	163	3.46×10^{-4}

[a] Measured in CB solution with a concentration; [b] Estimated from the absorption edge in neat film using the equation: $E_g^{opt} = 1240/\lambda_{onset}$ (eV); [c] E_{HOMO}=-(4.8+E_{ox}-0.26) (eV).

Referee: 3

Recommendation: Minor Revisions

Comments to the Author
In this manuscript, Yuan et al. design several dopant-free small molecules based HTMs with a D-A-D'-A-D configuration. By systematic investigation using diverse characterizations, the authors found that newly synthesized molecules showed enhanced thermal and photothermal stabilities after forming a conformal layer with coordination interaction with PbI_2-rich surface and the suppressed ionic diffusion is realized by the molecular interface. The highest power conversion efficiency is 22.61%, and this paper delivers a breakthrough result related to devices photothermal stability under harsh 85°C MPP conditions. The molecular design related to coordination strength is thus useful for the interface between HTM and perovskite. Hence, this paper is meaningful to suggest the efficient synthetic approach for dopant-free HTMs of high performance and stabilities in PSCs. Also, various characterizations fully supported the logics and results of studies in this paper.
Based on the breakthrough results in terms of stability for small molecular HTM, I suggest publish in Energy & Environmental Science, with some minor issues suggested to enhance the paper quality.
Response: We would like to thank the reviewer for the constructive comments to the manuscript.

1.The authors mentioned that "The PSCs were fabricated with the structure of ITO/SnO2/perovskite/HTM/MoO3/Ag, where the perovskite film without post-treatment with PEAI was fabricated by the "two-step" method" in Page 3 of manuscript. Have the authors tried other types of surface passivators, such as PMMA, or even additives in HTMs, to further improve the conversion efficiency of the devices? HTM or introducing a passivation layer between the perovskite and the HTL?

Response: Many thanks to the reviewer for the kind comments and suggestions!

a) We have fabricated the L-series PSCs with PEAI passivation layer. The results found that PEAI passivation decreased the PCE of L3-PSCs. Surface PEAI passivation layer will reduce the chemical bonding between L3 and perovskite. Therefore, we mentioned the coordination interaction between HTL and perovskite is important for the photothermal stability, which is also the novelty of

this work. PEAI will interrupt chemical bonding between perovskite and hole transport layer. PMMA also introduced on the perovskite film to further demonstrate this result. The detailed parameters of PSCs with different passivation layer were listed in the following Table R1.

b) Actually, Additives, such as TBP and Li-TFSI, were added with different concentration in L3 HTM solution. However, the efficiency of PSCs was decreased obviously. The detailed photovoltage parameters are listed in the following Table R2. We infer that this is mainly due to the introduction of additives that affect the tight packing of L3 molecules.

Table R1. Summary of device performance of L3-PSCs with different passivated perovskite film.

	V_{OC} (V)	J_{SC} (mA/cm^2)	FF (%)	PCE (%)
Control	1.10	24.34	79.33	21.19
PEAI	1.12	23.81	72.53	19.34
PMMA	1.05	23.97	69.03	17.24

Table R2. Summary of device performance of PSCs with doped and dopant-free L3 HTL.

	V_{OC} (V)	J_{SC} (mA/cm^2)	FF (%)	PCE (%)
Dopant-free	1.10	24.34	79.33	21.19
Doped	1.12	24.29	59.43	16.14

2.There are some typos: a), In Table 2, the absorption edge of the L2 HTM film (770 nm) is inconsistent with Figure S28 (570 nm). b), In Figures 4d and e, two mislabels (GBS) are marked for the ground state photobleaching region (GSB, 500-650 nm). The author must correct these errors in the revised manuscript.

Response: Thank the reviewer for pointing out the careless mistakes! As suggested, they have been corrected in the revised manuscript.

The revised Table 2 and Figure 4 in the revised manuscript were listed in the following.

In page 6 of revised manuscript.

Table 2. Optical, electrochemical, thermal, and charge transport properties of L1, L2 and L3.

	$\lambda_{abs,sol}$ (nm)[a]	$\lambda_{abs,film}$ (nm)	E_g^{opt} (eV)[b]	HOMO (eV)[c]	LUMO (eV)	T_d (°C)	T_g (°C)	μ_h (cm^2 V^{-1} s^{-1})
L1	569	583	1.94	-5.26	-3.32	440	105	2.53×10^{-4}
L2	561	570	1.95	-5.31	-3.36	449	120	3.28×10^{-4}
L3	559	569	1.96	-5.32	-3.36	449	163	3.46×10^{-4}

[a] Measured in CB solution with a concentration; [b] Estimated from the absorption edge in neat film using the equation: $E_g^{opt} = 1240/\lambda_{onset}$ (eV); [c] E_{HOMO}=-(4.8+E_{ox}-0.26) (eV).

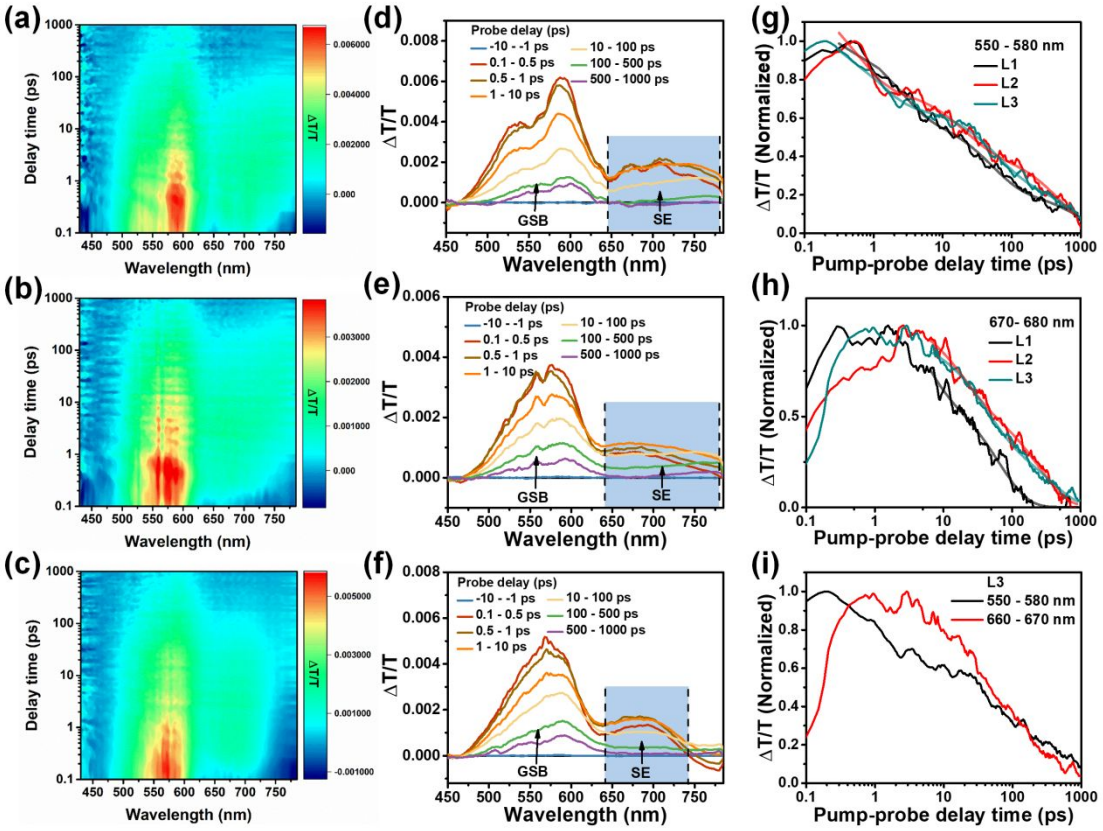

Fig. 4. TAS suggests L-series films have sequentially reduced photoexcited energy disorder. 2D colour plot of

TAS of (a) L1, (b) L2, and (c) L3; TAS plots of (d) L1, (e) L2, and (f) L3 HTM films; (g) GSB kinetics at 550-580 nm, and (h) SE kinetics at 660-670 nm; (i) shows the differences in kinetics between GSB and SE. $\tau_{ave} = \sum A_i \cdot \tau_i / \sum A_i$, where A and τ are the fitted amplitudes and the lifetimes of the multi-exponential fitting. The HTM was excited at 400 nm wavelength with an excitation fluence of ~ 5 μJ/cm^2.

3.In Figures 5e and f, the inserted device structure is inconsistent with the structure described in the corresponding text. And the authors calculated the trap density of V2 based on the J-V curve. To avoid misunderstandings, the V1 value should be removed from the revised manuscript.

Many thanks to the reviewer for the kind comments and suggestions! As suggested, we have revised the Figure 5 in the revised manuscript to avoid misunderstandings of corresponding statements.

The revised Figure 5 in the revised manuscript was listed in the following.

In page 7 of revised manuscript.

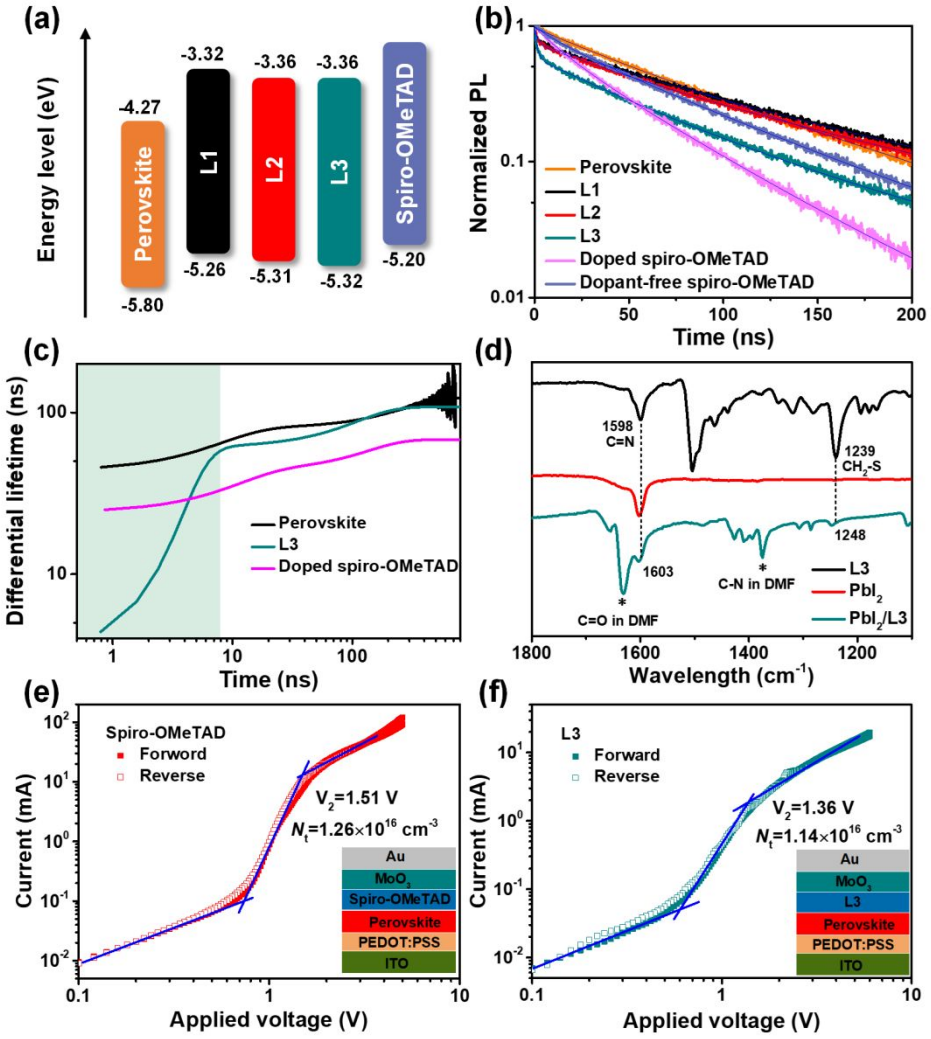

Fig. 5 Charge transfer and passivation effect. (a) Energy level diagram, (b) TRPL and (c) computed differential lifetimes from Fig. 5b for the bare perovskite, L3, and doped spiro-OMeTAD coated perovskites. The shaded areas are a guide marking for charge extraction. (d) FTIR spectra of the powders of L3, PbI_2 and PbI_2/L3 blend. The peak of 1632 cm^{-1} and 1375 cm^{-1} are ascribed to C=O and C-N of DMF, respectively, which form an adduct of PbI_2•xDMF.[58] The forward and reverse SCLC curves of (e, f) hole-only devices.

4.What about the synthetic cost of L1-L3 HTMs, and whether it will be lower than spiro-OMeTAD HTL?

Response: We thank the reviewer for the constructive suggestion! We have calculated the synthetic cost for the L1, L2 and L3 molecule. As listed in the following Table R3, The cost of L1 is ~509 ¥/g (~70 $/g), L2 is ~533 ¥/g (~73 $/g), and L3 is ~620 ¥/g (~85 $/g). These costs are slightly lower or equal to the commercial spirochete-OMeTAD HTM. At the same time, the optimal concentration of L3 was 12

mg/mL, which was lower than the 72.3 mg/mL of spiro-OMeTAD. Therefore, we believe that in future commercial products, the cost of L3 in PSC is lower than that of spiro-OMeTAD HTM.

Table R3. Summaries of synthetic cost for the L1, L2 and L3 molecule.

Chemical name	raw material	Weigth/Volume	Price of material	Cost of material
TPAOMe-BT-Br (3.774 g)	TPAOMe-BE	3.448 g	70 ¥/g	240 ¥
	BT-2Br	3.516 g	6 ¥/g	21 ¥
	$Pd(PPh_3)_4$	0.03 g	60 ¥/g	1.8 ¥
	K_2CO_3	5.52 g	0.04 ¥/g	0.22 ¥
	Ethanol	20 mL	10 ¥/L	0.2 ¥
	Toluene	50 mL	20 ¥/L	1 ¥
	Petroleum ether	300 mL	15 ¥/L	4.5 ¥
	Dichloromethane	150 mL	12 ¥/L	1.8 ¥
	Silica gel	80 g	25 ¥/kg	2 ¥
	Total	≈72 ¥/g （10 $/g）		
L1 (0.354 g)	IDT-Sn	0.260 g	570 ¥/g	148 ¥
	TPAOMe-BT-Br	0.319	72 ¥/g	23 ¥
	$Pd(PPh_3)_4$	0.013g	60 ¥/g	0.78 ¥
	Toluene	15 mL	20 ¥/L	0.3 ¥
	Petroleum ether	300 mL	15 ¥/L	4.5 ¥
	Dichloromethane	150 mL	12 ¥/L	1.8 ¥
	Silica gel	80 g	25 ¥/kg	2 ¥
	Total	≈509 ¥/g （70 $/g）		
L2 (0.366 g)	IDTP-Sn	0.280 g	600 ¥/g	168 ¥
	TPAOMe-BT-Br	0.259 g	72 ¥/g	18 ¥
	$Pd(PPh_3)_4$	0.010 g	60 ¥/g	0.6 ¥
	Toluene	15 mL	20 ¥/L	0.3 ¥
	Petroleum ether	300 mL	15 ¥/L	4.5 ¥

	Dichloromethane	150 mL	12 ¥/L	1.8 ¥
	Silica gel	80 g	25 ¥/kg	2 ¥
	Total	≈533 ¥/g (73 $/g)		
L3 **(0.336 g)**	IDTT-Sn	0.285 g	640 ¥/g	182 ¥
	TPAOMe-BT-Br	0.241 g	72 ¥/g	17 ¥
	$Pd(PPh_3)_4$	0.010 g	60 ¥/g	0.6 ¥
	Toluene	15 mL	20 ¥/L	0.3 ¥
	Petroleum ether	300 mL	15 ¥/L	4.5 ¥
	Dichloromethane	150 mL	12 ¥/L	1.8 ¥
	Silica gel	80 g	25 ¥/kg	2 ¥
	Total	≈620 ¥/g (85 $/g)		

ARTICLE

Conformally bonded molecular interface retarded iodine migration for durable perovskite solar cells

Received 00th January 20xx,
Accepted 00th January 20xx

DOI: 10.1039/x0xx00000x

Ligang Yuan,[1,†] Weiya Zhu,[1,†] Yiheng Zhang,[1] Yuan Li,[1,*] Christopher C. S. Chan,[2] Minchao Qin,[3] Jianhang Qiu,[4] Kaicheng Zhang,[5] Jiaxing Huang,[1] Jiarong Wang,[1] Huiming Luo,[1] Zheng Zhang,[1] Ruipeng Chen,[1] Weixuan Liang,[1] Qi Wei,[1] Kam Sing Wong,[2] Xinhui Lu,[3] Ning Li,[1,*] Christoph J. Brabec,[5, 6] Liming Ding,[7] Keyou Yan[1,*]

State-of-the-art n-i-p perovskite solar cells (PSCs) suffer from stability issues due to ionic interdiffusion. Herein, by enlarging indacenodithiophene π-bridge donor (D') to combine with methoxy triphenylamine donor (D) and benzothiadiazole acceptor (A), three linear molecules termed as L1, L2 and L3 with D-A-D'-A-D structure are developed as dopant-free hole transport materials (HTMs). The π-bridge extension with active sites for coordination leverages the intramolecular dipole effect and intermolecular packing effect, resulting in conformally bonded ultrathin interface with compact and uniform coverage (~60 nm) to retard iodine migration and protect the buried perovskite. The unencapsulated L3-PSC (ITO/SnO_2/Perovskite/L3/MoO_3/Au) achieved an impressive PCE of 22.61% (certified 21.79%, 0.0525 cm^2). Ultrafast laser spectroscopy reveals that L-series molecules have sequential reduction of photoexcited energy disorder to illustrate the structure-performance-stability relationship. L3-PSC maintains over 85% of the initial efficiency after 500-hour at 85°C maximum power point tracking (MPP) and realizes the possibility of using small molecules to stabilize n-i-p PSCs.

Introduction

During the last decade, the power conversion efficiencies (PCEs) of both p-i-n and n-i-p type perovskite solar cells (PSCs) have been boosted to over 25%.[1, 2] However, the device durability is still one of the most challenging obstacles to realize their commercialization. It is encouraging that some reported *p-i-n* (inverted) PSCs have demonstrated superior thermal stability (at 85°C)[3-5] and passed the damp-heat test according to the International Electrotechnical Commission (IEC) 61215:2016 regulations,[2, 6] which was mainly ascribed to the progress in stable dopant-free electron/hole transport layers (ETM/HTM). In contrast, the high efficiency *n-i-p* (conventional) PSCs rely on the lithium bis(trifluoromethanesulfonyl)imide (Li-TFSI) and 4-tert-butyl pyridine (t-BP) additives to improve hole mobility (~10^{-5} cm^2 V^{-1} s^{-1}) and carrier conductivity (10^{-8} S cm^{-1}) of pristine 2,2',7,7'-tetrakis(*N*,*N*-di-*p*-methoxyphenylamine)-9,9'-spirobifluorene (spiro-OMeTAD).[7-9] The ionic interdiffusion between hygroscopic dopants/additives and halide of perovskite can cause device degradation, especially under continuous thermal and illumination conditions.[10, 11] Hence, the currently reported operational lifetime values of state-of-the-art *n-i-p* PSCs according to the ISOS protocols lag much behind the one of *p-i-n* PSCs (Table S1). Therefore, developing stable and efficient HTMs is a necessary strategy to endow n-i-p PSCs with both high PCEs and superior device operation lifetime for their potential commercialization.

The desired HTMs for the *n-i-p* PSCs with high performance should have a well-aligned energy level with perovskite, a sufficiently high hole mobility, superior chemical and photothermal stability, and should passivate the surface trap density at the perovskite/HTL interface as well.[12-17] By now, several types of

[1] School of Environment and Energy, State Key Laboratory of Luminescent Materials and Devices, Institute of Polymer Optoelectronic Materials and Devices, Guangdong Provincial Key Laboratory of Solid Wastes Pollution Control and Recycling, Guangdong Provincial Key Laboratory of Luminescence from Molecular Aggregates, AIE Institute, South China University of Technology, Guangzhou 510000, P. R. China
[2] Department of Physics and William Mong Institute of Nano Science and Technology, The Hong Kong University of Science and Technology, Clearwater Bay, Hong Kong, P. R. China
[3] Department of Physics, The Chinese University of Hong Kong, Shatin 999077, Hong Kong, P. R. China
[4] Shenyang National Laboratory for Materials Science, Institute of Metal Research, Chinese Academy of Sciences, Shenyang, 110016, China
[5] Institute of Materials for Electronics and Energy Technology (i-MEET) Friedrich-Alexander-University Erlangen-Nuremberg Martensstraße 7, Erlangen 91058, Germany
[6] Helmholtz-Institute Erlangen-Nürnberg for Renewable Energy (HI ERN), Forschungszentrum Jülich (FZJ), Erlangen 91058, Germany
[7] Center for Excellence in Nanoscience (CAS), Key Laboratory of Nanosystem and Hierarchical Fabrication (CAS), National Center for Nanoscience and Technology, Beijing 100190 P. R. China
[†] These two authors contributed equally to this work.
[*]Corresponding author: celiy@scut.edu.cn, ningli2022@scut.edu.cn, kyyan@scut.edu.cn
Electronic Supplementary Information (ESI) available: [details of any supplementary information available should be included here]. See DOI: 10.1039/x0xx00000x

dopant-free HTMs have been developed. Inorganic HTMs, such as NiO_x[18] and CuSCN,[19] enable long-term stable PSCs. Organic polymeric HTMs have shown promising stability and film-forming properties.[20-23] Hou and co-workers have introduced a dopant-free PDCBT polymer as the HTM in PSCs. In combination with the tantalum doped tungsten oxide, a bilayer hole extraction contact led to PSCs with negligible hysteresis and a PCE of over 21%.[20, 24] Recently, HTMs based on dopant-free polymer achieved PCEs of over 24% as well.[25-27] Small molecular HTMs can be precisely controlled to yield chemically pure and structurally homogeneous products and are thus a great promise for achieving PSCs with uniform properties and high reproducibility.[13, 14, 28-30]

So far, the reported small molecular HTMs for PSCs can be categorized into donor-π-donor (D-π-D) type, acceptor-D-acceptor (A-D-A) type, D-A-D type and D-A-π-A-D type configurations.[31] As shown in Fig. S1, spiro-OMeTAD as well as its derivative spiro-*m*F, the most famous D-π-D type HTM, exhibited limited hole mobility for dopant-free PSCs, because the rigid orthogonal spirobifluorene hinders the formation of close π-π stacking and the propeller-like triphenylamine induces a large intermolecular distance.[32] In order to improve hole mobility, the linear D-π-D type molecules with enhanced intermolecular π-π interactions have been developed to increase the mobility for dopant-free HTMs (Fig. S1). For example, Tang and co-workers employed dithia[3,2-b:2',3'-d]pyrrole core as π-bridge to synthesize DTPC13-ThTPA and DTP-C6Th, with which dopant-free PSCs achieved a PCE of 20.38% and 21.04%, respectively.[33, 34] Loo and co-workers synthesized the HTM of YZ22 with 1,10-phenanthroline as π-bridge and demonstrated that YZ22 also effectively passivated defects and hence boosted the PCE to 22.4%.[13] The D-A molecular backbone has a high dipole moment to induce intramolecular charge transfer (ICT), though it is regarded that the charge mobility and extraction capability can be further improved,[35] and thus A-D-A type with a large-sized donor and D-A-D type HTM are progressing as dopant-free PSCs (Fig. S1). For example, Yang and co-workers synthesized an A-D-A type DOR3T-TBDT HTM[36] and changed the core unit with an even larger-sized alkylthienyl-substituted benzo[1,2-b:4,5-b']dithiophene donor for DERDTS-TBDT HTM (Fig. S1) for better performance.[37] The incorporation of electron acceptor can not only enhance the performance, but also improve the intrinsic photothermal stability.[30] Moreover, Zhu and co-workers designed a series of quinoxaline-based D-A-D type HTMs (TQ1, TQ2, and TQ3) and extended the π-conjugation with a quinoxaline core to form TQ4. The PCE of PSCs with TQ4 was increased to 21.03%.[30, 38] D-A-D small molecules based on imide-functionalized thiophene (BTTI-C6, BTTI-C8, and BTTI-C12) were also developed and the dopant-free planar PSCs with BTTI-C6 HTL achieved an efficiency of 19.69%.[39] Recently, the D-A-π-A-D type molecule DTB-FL and BDT-DPA-F were employed as dopant-free HTMs in PSCs.[28, 40] However, these small molecules cannot inhibit the ionic interdiffusion and pass the harsh stability test, *e.g.* damp-heat, 85°C maximum power point (MPP) test. There are still plenty of room to engineer the structure units for photothermal stable PSCs.[28, 30, 41] It is meaningful to deliver a compact and tightly-bonded interface to retard the ionic interfusion (e. g. iodine migration) and ameliorate the 85°C MPP stability.

In this work, we employ indacenodithiophene (IDT)-based weak donor (D') derivatives with sequentially extended π-bridge, in combination with methoxy triphenylamine donor and benzothiadiazole acceptor, to synthesize three D-A-D'-A-D type linear molecules (named L1, L2, and L3) (Fig. 1a). IDT has a coplanar symmetrical structure, in which the three aromatic rings are in conjugation, and a bridging atom fixes the coplanarity between the adjacent rings. It is an excellent candidate as the π-bridge, which maximizes the π orbital overlap and hence reduces the photoexcited energetic disorder.[42] We find that expanding the side chain by four 4-hexylphenyl substituents to form L2 from L1 can regulate intermolecular interactions but slightly increase the intramolecular distortion.[43, 44] Extending the backbone with two thieno[3,2-b]thiophene units to form indacenodithieno[3,2-b]thiophene (IDTT in L3) can restore linearity and reduce intramolecular distortion. Through fine tuning of the molecular structure, hole mobility, glass transition temperature (T_g) and intermolecular order are gradually improved.[45] Compared to our recent work, IDT/IDTT-based weak donors possess active sites to coordinate to the perovskite, endowing conformally bonded molecular interface on the perovskite, which is verified by the grazing-incidence wide-angle X-ray scattering (GIWAXS) patterns and is beneficial for retarding iodine migration as well as device stability.[28] L1, L2 and L3 deliver 20.20%, 21.05 % and 21.90% efficiency for dopant-free PSCs, respectively. Through optical optimization, L3-based PSC (L3-PSC) finally achieved a champion PCE of 22.61%, which significantly exceeds the PCE of 15.87% for dopant-free spiro-OMeTAD-based PSCs. Rapid carrier transport, sequentially reduced disorder and improved defect passivation capability of the L-series are also demonstrated by ultrafast laser spectroscopy. Compared with the PSCs with doped spiro-OMeTAD, the unencapsulated L3-PSCs show promising long-term stability under various conditions. It maintains 90% of the initial PCE after 2736 hours stored in an argon-filled glovebox. Owing to the tightly bonded conformal coverage and interaction between L3 and perovskite, L3-PSCs can maintain ~85% initial value after 500-hour at 85°C MPP tracking. This work not only provides important guidelines for the multi-objective optimization of PSCs by independently tuning the energy level, hole mobility, thermal stability, solubility, and film-forming properties of dopant-free HTMs, but also demonstrates the possibility of using small molecules to address the key challenge of harsh 85°C MPP for *n-i-p* PSCs.

Results and discussion

Molecular synthesis and properties

It is important to introduce substantial active sites for coordination onto perovskite to strengthen the interface and thus deliver high photothermal stable properties for molecular film. The molecular design strategy for L1, L2, and L3 is described in Fig. 1a and π-bridge extension with two thieno[3,2-b]thiophene is employed to strengthen coordination bonding (Fig. 1b). The corresponding synthetic steps are presented in the supporting information (see Scheme S1-4). Briefly, L1, L2, and L3 were synthesized via Stille coupling of different IDT tin reagents with the intermediate TPAOMe-BT-Br.[28] We first enlarged the side chain of IDT π-bridge from alkyl to alkylaryl (L1 to L2) and then extended the backbone π-

bridge unit of the IDT by two thieno[3,2-b]thiophene (TT) unit (L2 to L3). The chemical structures for intermediate and target molecules were carefully characterized by ^{1}H- and ^{13}C-nuclear magnetic resonance (NMR) as well as matrix-assisted laser desorption/ionization on a time-of-flight mass spectrometry (MALD-ToFMS) (Figs. S2-S11). The yields of L1, L2, L3 are 85.5%, 90.5% and 83.8%, respectively.

The thermal properties of L1, L2, and L3 were investigated by thermogravimetric analysis (TGA) and differential scanning calorimetry (DSC). The recorded TGA curves in Fig. S12 exhibit a high decomposition temperature (T_d) of 440°C for L1, 449°C for L2, and 449°C for L3 during the heating process at a 5% weight loss. In addition, DSC measurement revealed a high T_g of 105°C for L1 HTM, 120°C for L2 HTM, and 163°C for L3 HTM (see Fig. S13), which are much higher than that of doped spiro-OMeTAD (72°C).[46] Especially, the L3 with a T_g of 163°C higher than that of pristine spiro-OMeTAD (125°C),[47] which is expected to be beneficial to the thermal stability of dopant free HTMs based PSCs.

The geometric structures of L1, L2, and L3 are elucidated using density-functional theory (DFT) calculations. From the optimized geometries in Fig. S14**,** the backbones of three molecules all exhibit a small twisting between the main building blocks. For L1, the torsion angle between benzothiadiazole (A) and the adjacent phenyl (D) is 32.93°/31.41° (left/right sides) and the torsion angle between benzothiadiazole (A) and thiophene (π) is 6.32°/2.90°. For L2 with the increased size of alkylaryl side chain, slightly larger torsion angle values (34.57°/33.61°, 7.46°/5.69°) were found. For L3, the torsion angle values slightly decrease (33.67°/33.9°, 6.54°/4.43°) due to the increased linear structure and are between the ones for L1 and L2. The D-A parts at both sides have larger torsion than the A-π-A parts in the middle due to the more bulky structure of donor.

We performed the electrostatic potential (ESP) analysis for electronic structure from the DFT calculation (Fig. S15). In the ground state, both benzothiadiazole unit (A) and thiophene-spacer of IDT unit (π) present high electron densities, and thus can provide favorable coordination sites for under-coordinated Pb^{2+} in the perovskite film.[28] [48] As shown in Fig. S16, the HOMOs are delocalized throughout triphenylamine moieties, the benzothiadiazole and π-bridge IDT unit, while the LUMOs are concentrated on the benzothiadiazole and partially delocalized to the thiophene. Therefore, there is a good electronic push-pull effect within the molecule leading to a significant dipole moment, which is in favour of charge transport.

Device performance

The PSCs were fabricated with the structure of ITO/SnO_2/perovskite/HTM/MoO_3/Ag, where the perovskite film without post-treatment with PEAI was fabricated by the "two-step" method according to previous work and HTMs were spin-coated for tight anchorage via coordination bonding (Fig. 1b).[49, 50] The systematic optimization of processing conditions for the HTMs is presented in Fig. S17 and Table S3, S4. We found that the dopant-free HTM with a concentration of 12 mg/mL in CB solvent at a speed of 4000 rpm achieved the champion efficiency. As shown in Fig. 1c, L3-PSC reaches a PCE of 21.90% under the AM 1.5 G irradiation at 100 mW/cm^2 with an open-circuit voltage (V_{OC}) of 1.12 V, a short-circuit photocurrent (J_{SC}) of 24.75 mA/cm^2 and a fill factor (FF) of 78.70%. It is higher than that of the best L1-PSC and L2-PSC with a PCE of 20.20% and 21.05%, respectively. The control devices based on spiro-OMeTAD with/without Li-TFSI and tBP have PCE of 21.94% and 15.87% in this work. The detailed photovoltaic parameters are summarized in Table 1.

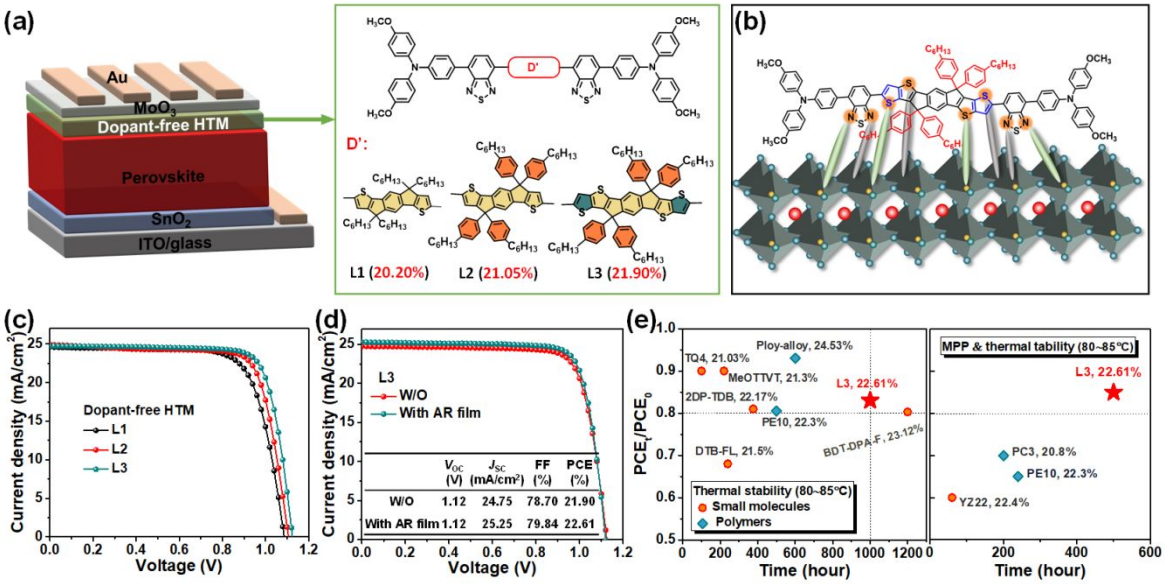

Fig. 1 Conformal bonded interface enhances device performance. (a) The design strategy of HTMs with extended active sites of L-series of HTMs (L1, L2 and L3) and device configuration. (b) Coordination sites between HTM and perovskite. (c) *J-V* curves of L-series PSCs. (d) *J-V* curves of L3-PSC without and with an anti-reflection (AR) film. (e) Summary of the thermal stability (80-85°C), MPP & thermal stability (80-85°C) for *n-i-p* PSCs with dopant-free HTMs (PCEs over 20%, their corresponding detailed parameters were listed in Table S2).

Table 1. Detailed parameters of PSCs with different HTLs.

HTL	V_{OC} (V)	J_{SC} (mA/cm^2)	FF (%)	PCE (%)
L1	1.09	24.91	74.33	20.20
L2	1.11	24.93	76.30	21.05
L3	1.12	24.75	78.70	21.90
Dopant-free spiro-OMeTAD	1.04	24.59	61.82	15.87
Doped spiro-OMeTAD	1.15	24.83	77.01	21.94

The statistics of the detailed photovoltaic parameters are shown in Fig. S18. All three dopant-free HTMs-based PSCs showed high reproducibility. Compared with L1-PSCs and L2-PSCs, the enhanced PCE of L3-PSCs is mainly ascribed to an increased V_{OC} and FF (see Table S5). The similar J_{SC} values are consistent with the absorption profiles of perovskite films coated with different HTMs (Fig. S19). As well, the calculated J_{SC} values from integrating the IPCE spectra in Fig. S20 confirm the photocurrents determined from *J-V* analysis.

Most importantly, the PCE of L3-PSCs can be further enhanced to 22.61% by employing an AR film to reduce light reflection at the glass substrate (Fig. 1d). This performance is comparable with the state-of-the-art PCE with dopant-free small-molecular HTMs recently reported in the literature (Fig. 1e and Table S2) and the doped spiro-OMeTAD PSCs (Fig. S21). As shown in Fig. S22, the L3-PSC achieved a PCE 21.79% certified by China CEPREI Laboratory with a mask area of 0.0525 cm^2.

The cross-sectional SEM images of the overall device are depicted in Fig. S23. The optimal thickness of the dopant free L1/L2/L3 HTM is found to be ~60 nm, which is much lower than the thickness of doped spiro-OMeTAD HTM (~180 nm). It is surprising that the conformal coverage of ultrathin molecular films is sufficient to guarantee efficient hole extraction and electron blocking, leading to the acceptable photovoltage and FF. Hence, we perform a series of experiments to illustrate the performance-structure-stability relationship.

Film microstructure

In order to reveal the microstructure, the molecular packing of L1, L2 and L3 neat films was firstly investigated by GIWAXS. As shown in Figs. 2a-d, all films exhibit two weak and broad scattering peaks centered at q = ~0.36 Å^{-1} and q = ~1.34 Å^{-1}, which can be attributed to the lamellar packing and π-π stacking, respectively. The low film crystallinity indicates that the films are predominantly amorphous due to their relatively twisted backbone.[24] Nonetheless,

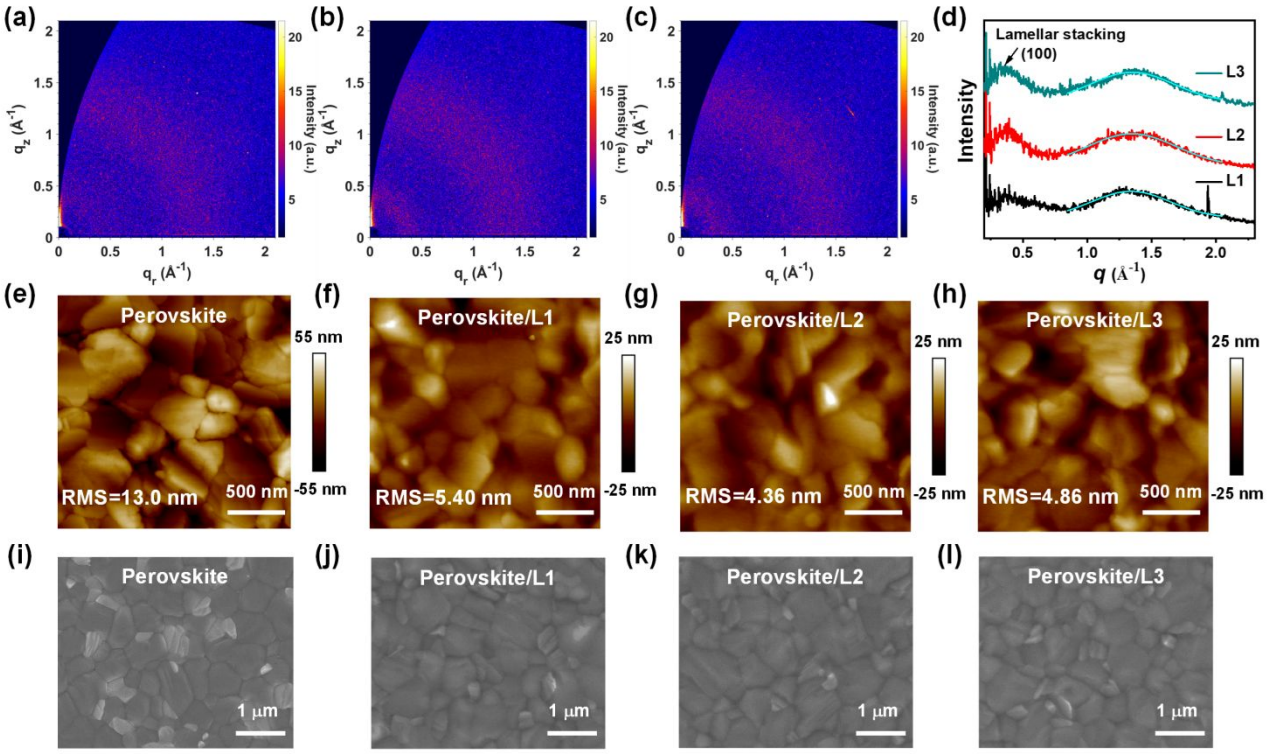

Fig. 2 Film microstructure suggests L-series HTMs have compact molecular packing and conformally bonded coverage with ultrathin thickness on perovskite. GIWAXS patterns of (a) L1, (b) L2, and (c) L3 films. (d) The corresponding GIWAXS intensity profiles. AFM images (e-h) and top-view SEM images (i-l) of the perovskite film, perovskite/L1, perovskite/L2, and perovskite /L3.

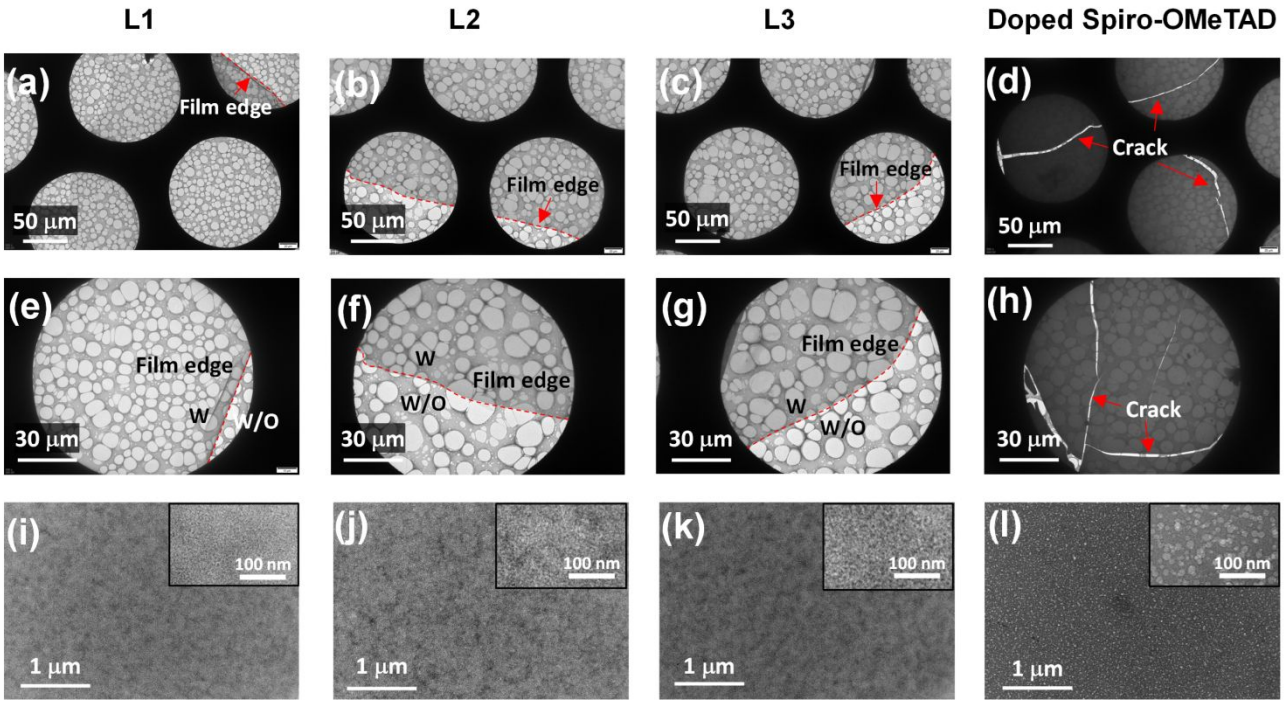

Fig. 3 TEM indicates L-series films are stronger than spiro-OMeTAD film. TEM images of (a) and (e) L1 film, (b) and (f) L2 film, (c) and (g) L3 film, (d) and (h) doped spiro-OMeTAD film. HRTEM images of (i) L1 film, (j) L2 film, (k) L3 film, and (l) doped spiro-OMeTAD film.

we found that the L3 film presents a higher peak position of the π-π stacking at q = 1.350 Å^{-1} than those of the L1 (1.340 Å^{-1}) and L2 (1.347 Å^{-1}) films, suggesting that the L3 molecules are packed more tightly in the film, which is beneficial for intermolecular charge transfer and inhibiting ionic interdiffusion. To some extent, these results are in good agreement with the slightly enhanced hole mobility from L1 to L3.

To further analyse the surface morphology of the HTM layers, atomic force microscopy (AFM) was performed. As shown in Fig. S24 and Figs. 2e-h, the three HTMs coated on perovskite films could provide a continuous and dense coverage that smoothen the perovskite surface. The root mean square (RMS) roughness of perovskite films covered with L1, L2, and L3 HTM are estimated to be 5.40, 4.36, and 4.86 nm, respectively, significantly smaller than that of bare perovskite film (RMS=13.0 nm). Compared with the RMS value of a perovskite film covered with L1 HTM, the decreased RMS values of perovskite layers with L2 and L3 demonstrate that the substitution of alkyl aryl group for alkyl group in the side chain of IDT π-bridge is an effective strategy to improve their film formation capability.

Scan electron microscopy (SEM) supports the microstructure of AFM. There is a typical perovskite film morphology with few bright PbI_2 spots as shown in the SEM images in Fig. 2i.[51] After coating with HTMs of L1/L2/L3 (Figs. 2j-l), we can clearly distinguish the grain pattern of the perovskite, which shows a very similar surface morphology to the bare perovskite. This indicates that the HTMs are uniformly and conformally covered on the surface of the perovskite film like "leotard", which is conducive to the interfacial hole extraction and transport.[48]

The uniform, dense and conformal coverage is further revealed by TEMs (Fig. 3). We prepared the samples with a structure of ITO/PEDOT:PSS/HTM by spin-coating, and then immersed the samples in deionized water to dissolve the bottom PEDOT:PSS film, leaving behind HTM films floating on the water surface (see video in Supporting Information). The films were collected by copper grid for characterization. TEM images confirm L-series have uniform, dense and conformal coverage in amorphous state while doped spiro-OMeTAD film has small grains in crystalline state (Fig. 3). Due to the flexible backbone, L-series HTMs are much more stable than doped spiro-OMeTAD film. Surface tension will make spiro-OMeTAD film cracking into pieces while L-series films retains overall structure after soaking in the water (Figs. 3a-h). The high-resolution TEM (HRTEM) images (Figs. 3i-l) confirm the amorphous state of L-series and crystalline grains in dot structure of spiro-OMeTAD film. The brittleness of spiro-OMeTAD grains will make the film not stable enough. During HRTEM test, sequentially improved membrane quality was observed after using high intensity electron beam for duration test, which is consistent with the sequentially increased T_g as aforementioned. More importantly, it is notable that this pin-hole free and dense film with ultrathin thickness of L-series HTMs will help to suppress the ionic interdiffusion and protect the buried perovskite, which will be discussed in the following section.

All the L-series HTMs exhibit extremely high hydrophobicity. Their water contact angles (θ) are larger than 90°, which is significantly higher than that of the spiro-OMeTAD film (θ = 73.6°, see Fig. S25). Meanwhile, the enlarged water contact angles from L1 to L2 to L3 could be ascribed to the additional aromatic rings of side chains and enlarged fused-rings of main chains.[30, 35] The degradation images of perovskite films in Fig. S26 also suggest that the strong hydrophobicity of the L-series HTMs efficiently protects the perovskite film from the degradation by atmospheric moisture. This result is also consistent with membrane structure judging from TEM images.

Photo-excited energy disorder

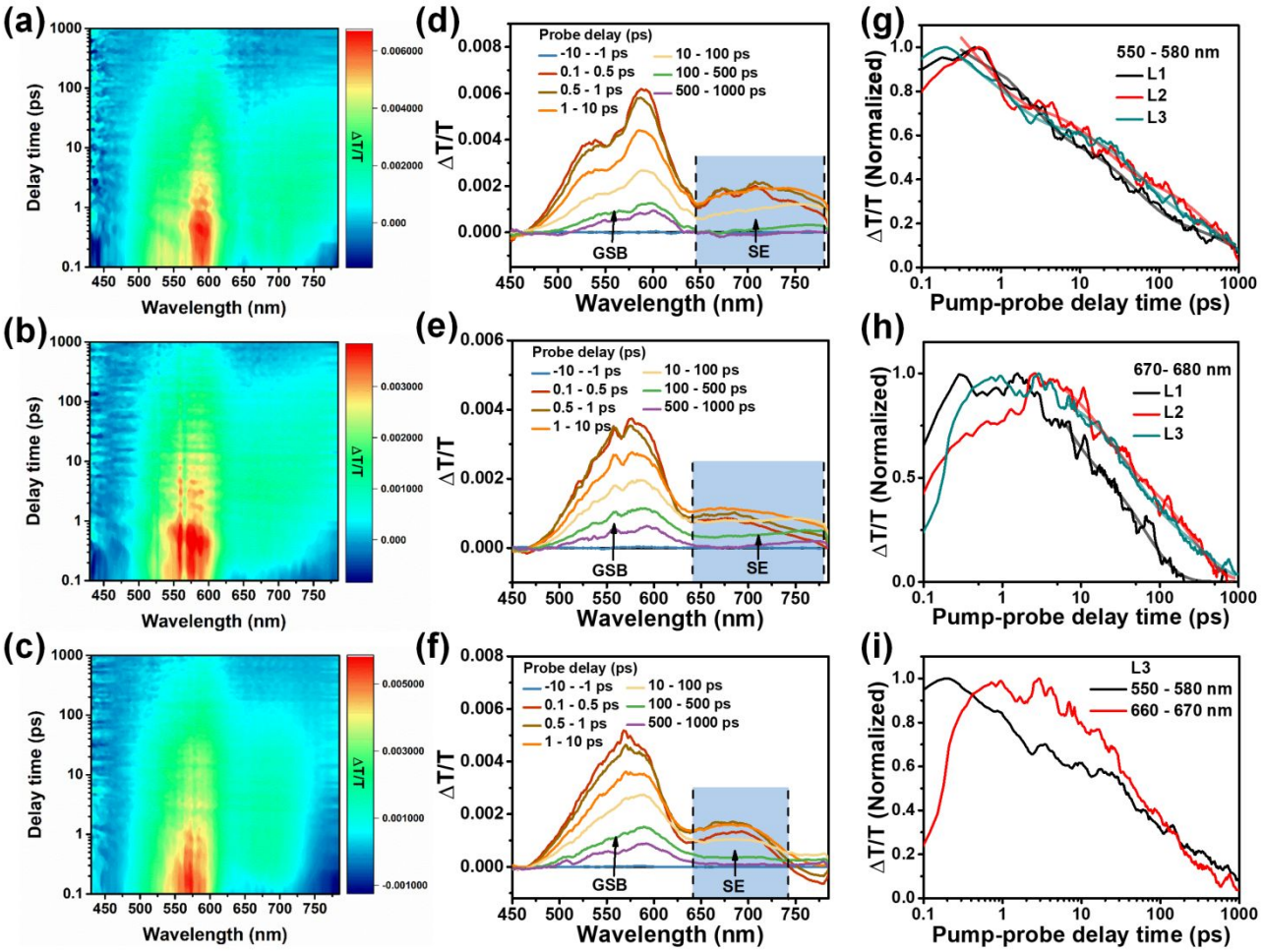

Fig. 4. TAS suggests L-series films have sequentially reduced photoexcited energy disorder. 2D colour plot of TAS of (a) L1, (b) L2, and (c) L3; TAS plots of (d) L1, (e) L2, and (f) L3 HTM films; (g) GSB kinetics at 550-580 nm, and (h) SE kinetics at 660-670 nm; (i) shows the differences in kinetics between GSB and SE. $\tau_{ave} = \sum A_i \cdot \tau_i / \sum A_i$, where A and τ are the fitted amplitudes and the lifetimes of the multi-exponential fitting. The HTM was excited at 400 nm wavelength with an excitation fluence of ~ 5 μJ/cm^2.

To further understand the photo-excited properties of L1-L3 HTMs, the ultrafast transient absorption spectroscopy (TAS) was applied and the sequentially reduced energy disorder was observed. As shown in Figs. 4a-f, all three HTMs exhibit a broad positive signal at 500-650 nm and an additional transient positive signal at 650-720 nm when excited at 400 nm. The feature at 500-650 nm can be assigned to ground state photobleaching (GSB) that coincides with the peak of steady-state absorption spectra (Fig. S27). The positive feature at 650-720 nm coincides with the steady state PL spectrum (Fig. S28), and is assigned to stimulated emission (SE).

The full ground-state recovery of photo-excited HTM films takes over 1 ns. The decay curves were best fit with triexponential functions, indicative of a broad overlap of multiple decay pathways.[52] To compare the GSB decay times, an amplitude average decay time constant of 230, 190, and 250 ps was extracted for L1, L2, and L3, respectively (Fig. 4g). The SE probes the excited state that correlates with the fluorescence in the system. The SE grows in the first few ps as the emissive states are populated. L1 shows a rapid decay that within 100 ps, whereas L2 and L3 takes significantly longer, with L3 having not decayed completely even at

Table 2. Optical, electrochemical, thermal, and charge transport properties of L1, L2 and L3.

	$\lambda_{abs,sol}$ (nm)[a]	$\lambda_{abs,film}$ (nm)	E_g^{opt} (eV)[b]	HOMO (eV)[c]	LUMO (eV)	T_d (°C)	T_g (°C)	μ_h (cm^2 V^{-1} s^{-1})
L1	569	583	1.94	-5.26	-3.32	440	105	2.53×10^{-4}
L2	561	570	1.95	-5.31	-3.36	449	120	3.28×10^{-4}
L3	559	569	1.96	-5.32	-3.36	449	163	3.46×10^{-4}

[a] Measured in CB solution with a concentration; [b] Estimated from the absorption edge in neat film using the equation: $E_g^{opt} = 1240/\lambda_{onset}$ (eV); [c] E_{HOMO}=-(4.8+E_{ox}-0.26) (eV).

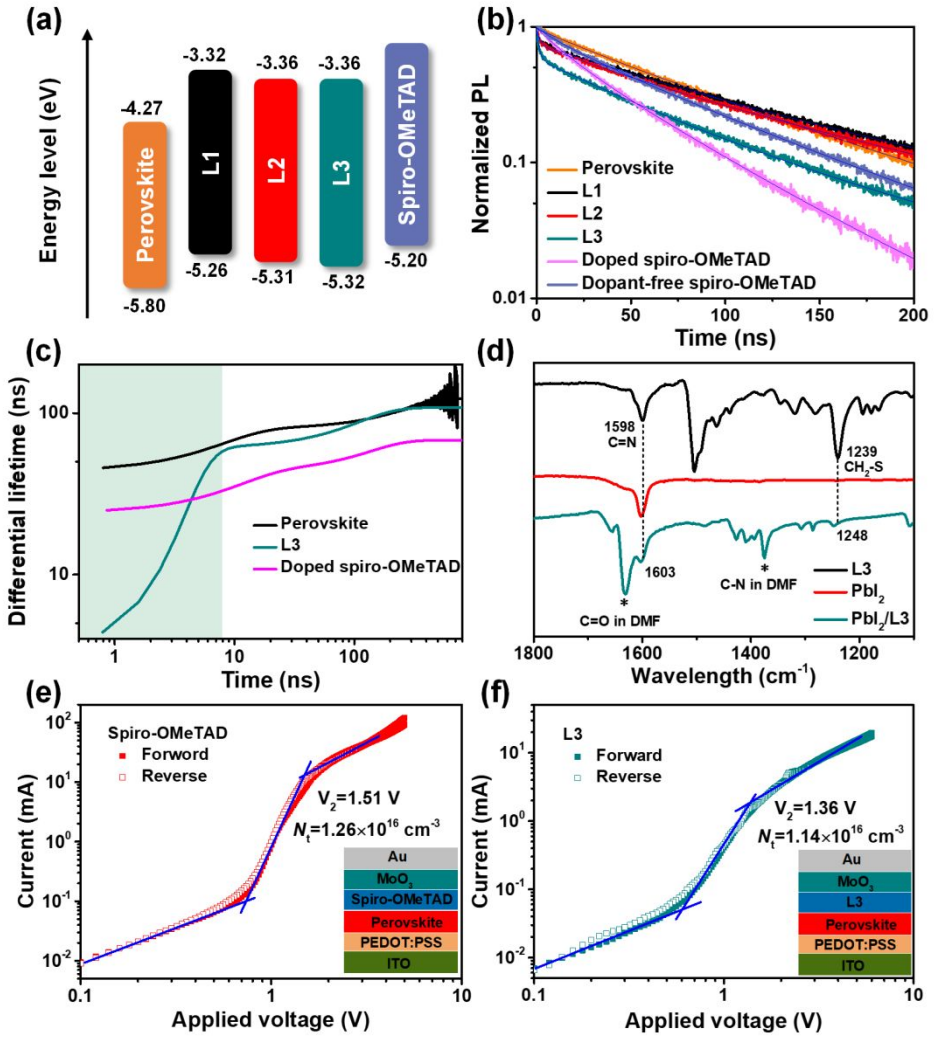

Fig. 5 Charge transfer and passivation effect. (a) Energy level diagram, (b) TRPL and (c) computed differential lifetimes from Fig. 5b for the bare perovskite, L3, and doped spiro-OMeTAD coated perovskites. The shaded areas are a guide marking for charge extraction. (d) FTIR spectra of the powders of L3, PbI_2 and PbI_2/L3 blend. The peak of 1632 cm^{-1} and 1375 cm^{-1} are ascribed to C=O and C-N of DMF, respectively, which form an adduct of PbI_2•xDMF.[60] The forward and reverse SCLC curves of (e, f) hole-only devices.

1 ns (Figs. 4, h and i). The observation of a decay behaviour of the excited state (probed by SE) and the GSB that is independent of each indicates the generation of multiple species following photoexcitation.[52] Interestingly, the extended excited state lifetime of L2 and L3 suggests a reduced recombination rate which is generally regarded as a beneficial quality criterion for electronic materials.

In addition, L1-L3 HTMs exhibit the reduced fold of peaks and a sequentially narrowed GSB and SE width. This is due to better alignment and enhanced π-π stacking as suggested as well from the GIWAXS data and can be indicative of enhanced intermolecular charge transport of L3 HTM (Fig. 2d). This property is not observed by static UV-Vis absorption spectra and PL (Figs. S27 and S28). The narrowing GSB and SE width suggests the reduction of photo-excited energy disorder, which is important for photovoltaics under illumination as well as the photothermal stability under MPP test.

Band alignment and mobility

We in-detail analyse the band alignment. In the film, the main absorption peaks of L1, L2, and L3 are located at 583, 570 and 569 nm (Table 2 and Fig. S27), respectively. Compared with the solution, a red shift of the main peak is observed in the corresponding thin films, which may be attributed to the enhanced intermolecular stacking induced electron delocalization.[53-55] From Tauc plots of L1, L2, and L3 in Fig. S29, the optical band gaps (E_g^{opt}) of L1, L2, and L3 films were determined to be 1.94, 1.95 and 1.96 eV, respectively. The detailed optical and parameters listed in Table 2.

From the oxidation potential of *C-V* curves (Fig. S30), the HOMO energy levels were calculated to be -5.26, -5.31 and -5.32 eV for L1, L2, and L3, respectively.[55] According to the HOMO values from *C-V* curves and the E_g^{opt} from solid film of HTMs, the LUMO levels of L1, L2, and L3 are calculated to be -3.32, -3.36 and 3.36 eV, respectively. The deeper HOMO values of L2 and L3 may better match the VB edge position of the perovskite.[56, 57] The energy level diagram of all three HTMs and the perovskite film are given in Fig. 5a, and one can see that L2 and L3 have a deeper lying HOMO level

and can be expected to provide a better energetic match between the perovskite and the anode interface.

The hole transport behaviour of L1, L2, and L3 films was determined by using the space charge limited current (SCLC) method with a device structure of ITO/ poly(3,4-ethylenedioxythiophene)-poly(styrenesulfonate) (PEDOT:PSS)/HTM/MoO_3/Ag (Fig. S31). All three HTMs exhibited similar hole mobility values of 2.53×10^{-4} cm^2 V^{-1} s^{-1} for L1, 3.28×10^{-4} cm^2 V^{-1} s^{-1} for L2 and 3.46×10^{-4} cm^2 V^{-1} s^{-1} for L3, which are higher than that of the dopant-free spiro-OMeTAD (1.57×10^{-4} cm^2 V^{-1} s^{-1}). Although hole mobility is not very high, but it can extract the holes effectively and block the recombination in ultrathin thickness (~60 nm) in this work judging from their performance aforementioned.

Charge extraction, passivation effect and chemical bonding

The PCE of PSCs with dopant-free spiro-OMeTAD HTM is 15.87%, which is lower than that of L3-PSC, mainly due to low V_{OC} and FF (see Fig. S32 and Table 1). Compared with the PCE of 21.94% for doped spiro-OMeTAD PSC, L3-PSC also exhibits a comparable efficiency of 21.90%, but as well shows a higher and more stable output efficiency at maximum power point (MPP) within 120 s (Figs. S32 and S33). In our case, we do not deposit PEAI on the perovskite surface to passivate surface defects but we find that the photovoltage is acceptable. Therefore, the charge transfer and passivation effect of L-series HTM are further identified. The steady-state photoluminescence (PL) spectra were measured on glass/perovskite/HTM samples (Fig. S34). After covering the perovskite film with HTM, the PL intensity is obviously quenched, especially when it is covered by L3 HTM, indicating that the three HTMs have strong hole extraction and transfer capabilities.[56]

The time resolved PL (TRPL) of the perovskite films with different HTMs were further preformed, as shown in Fig. S35a. It is evident from the magnified spectra in Fig. S35b that the PL decay consists of a fast component followed by a long-lived component in the perovskite films covered with HTMs. The TRPL were fitted with tri-exponential decays, as shown in Fig. S36, and the fitted corresponding parameters are summarized in Table S6. Tri-exponential decays give better fit than traditional bi-exponential decays, which is due probably to the charge extraction/transport (τ_1), radiative recombination (τ_2) and passivation effect events (τ_3), presumably corresponding to the quenching process of photogeneration of free carriers of perovskite through charge transfer (including charge extraction from perovskite to HTL and charge transport in HTL), radiative recombination in the perovskite film, and passivation effects by functional group, respectively. As listed in Table S6, the average lifetimes of L-series perovskite films were incredibly improved compared with bare perovskite film. This indicated the passivation effect of L-series HTM on the perovskite film. Furthermore, differential lifetime was modelled by fitting the TRPL spectra (Fig. 5b) with the equation of $t = -(d\ln(\varphi(t))/dt)^{-1}$,[58, 59] where $\varphi(t)$ is the time-dependent PL photon flux. As shown in Fig. 5c, the processes that reduce the PL counts over time are separable, and the lifetime t is directly readable at each time point.[59]

The perovskite films with L-series HTMs exhibit faster charge extraction process than that of doped spiro-OMeTAD HTM. A readily charge extraction process from the perovskite film to L3 HTM was observed within 10 ns (green region in Figure 5c), which can be mainly ascribed to the extended backbone of the IDTT π-bridge with deep HOMO energy level and high mobility.[44] While the doped spiro-OMeTAD has a faster transport due to its higher mobility. Compared with 21.94% efficiency of the doped spiro-OMeTAD PSCs, L3 PSCs also have a comparable efficiency of 21.9%. This performance is also consistent with TRPL data.

Fourier transform infrared spectroscopy (FTIR) measurement was carried out to confirm chemically-bonded passivation of perovskite surface by L3 HTM. As shown in Fig S37 and Fig. 5d, the CH_2-S peak in thiophene moiety in L3 slightly shifted after mixing with PbI_2, from 1240 cm^{-1} to 1248 cm^{-1}, respectively. The C=N stretch peak in benzothiadiazole moiety of 1598 cm^{-1} also shifted to 1603 cm^{-1}. These results indicate that chemically bonding between PbI_2 and the benzothiadiazole and thiophene moieties of L3 occurred with lone pair electrons. X-ray photoelectron spectroscopy (XPS) measurement was further performed, as shown in Fig. S38. Compared to the bare perovskite film, a shift of the Pb^{2+} 4f towards lower binding energy was observed for the perovskite film covered with L3 HTM, indicating the functional groups in L3 could donate the lone pair electrons to the empty 6p orbital of Pb^{2+} via the coordination interactions and effectively passivate the defects and suppressed the defect-assisted recombination at the interface between the perovskite film and HTMs.[28, 48] The I $3d_{3/2}$ and $3d_{5/2}$ signals for perovskite/L3 to shift to lower binding energy compared to those in the XPS spectrum of bare perovskite film. We believe this shift stems from L3 donating electrons to Pb^{2+}, which perturbs the static interactions between Pb^{2+} and I^- at the interface.[13] A small shift of *N* 1s and *S* 2p also occurs in the perovskite film coated with L3 HTM and the peak of O 1s do not shifts. These results are in good agreement with the FTIR measurement, which demonstrate chemically bonding passivation between PbI_2 and the benzothiadiazole and thiophene moieties of L3 HTM

The trap density was further quantified by the SCLC method. The dark *J-V* curves of hole-only devices with a configuration of ITO/PEDOT:PSS/perovskite/HTM/MoO_3/Ag. We evaluated the trap-state density via the trap-filled limit voltage (V_{TFL}), obtained from $n_t = q\varepsilon\varepsilon_0 V_{TFL}/(qL^2)$,[61-63] where q is the elementary charge, ε relative dielectric constant, ε_0 vacuum permittivity, L thickness of the perovskite film, and V_{TFL} trap-filling limit voltage. As shown in Fig. 5, e and f, V_2 gives the most accurate value for the trap density due to the mixed ionic and electronic nature of perovskites.[63] The trap densities were calculated to be 1.26×10^{16} and 1.14×10^{16} cm^{-3} by V_2 for the devices with doped spiro-OMeTAD and L3 HTL, respectively, with similar values to each other. For the standard spiro-OMeTAD, the dopants can not only enhance the conductivity (Li-salt), but can passivate perovskite film by the pyridine group.[64] For L3 HTL, the low trap states may be attributed to the reduced energy disorder of L3 and passivation effect on the perovskite film.[40] L3 HTL has much thinner thickness (~60 nm) than doped spiro-HTL to block the charge recombination event at the interface, due to close packing, coordination interaction and conformal coverage. Therefore, L3 PSC has similar PV performance to the doped spiro-OMeTAD PSC in our system.

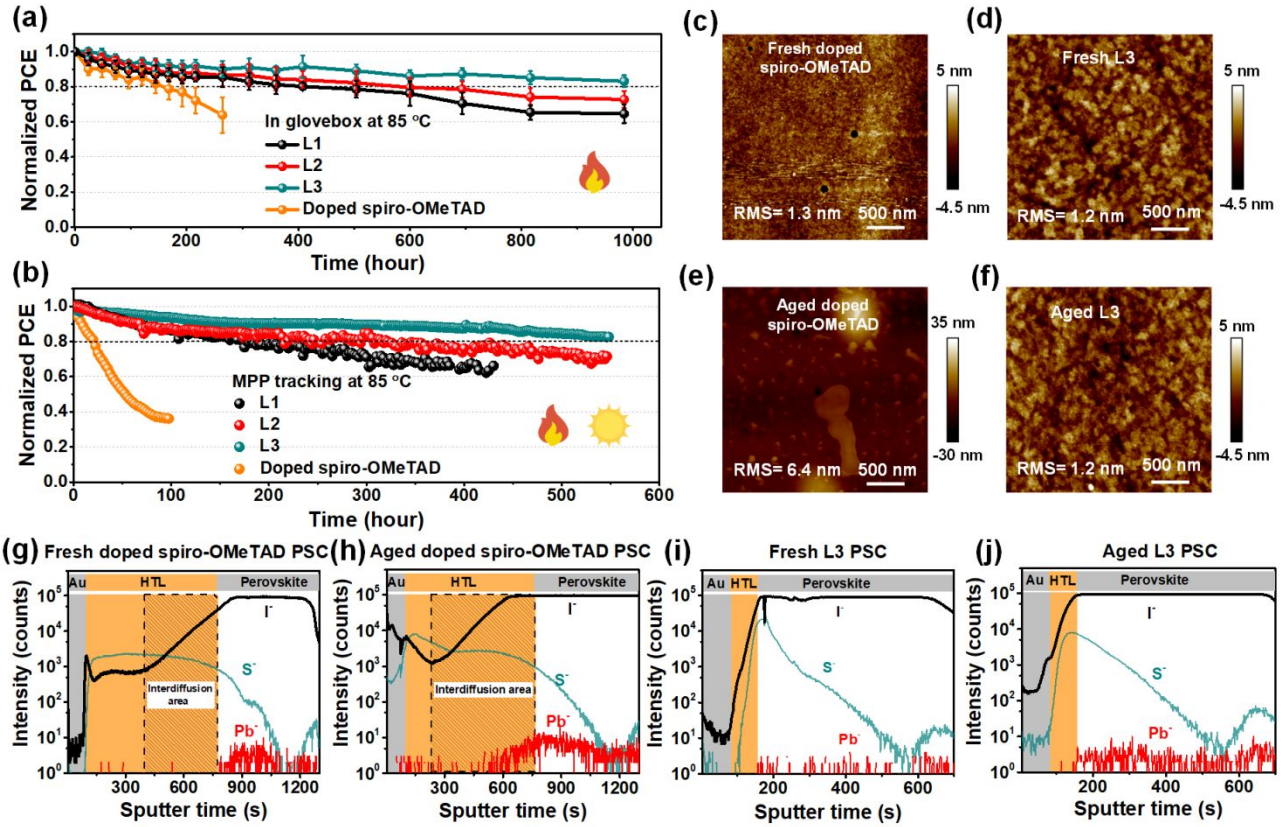

Fig. 6 Long-term stability tests suggest L3 can endure 85°C MPP test**.** (a) 85°C thermal stability, and (b) 85°C MPP tracking stability for unencapsulated doped spiro-OMeTAD and dopant-free L-series PSCs. AFM images of HTMs on ITO substrates, the aging condition is 100°C for 10 hours on the hotplate in N_2-filled glovebox, (c) fresh doped spiro-OMeTAD film, (d) fresh L3 film, (e) aged spiro-OMeTAD film, and (f) aged L3 film. ToF-SIMS of depth profiles of anion distribution within full PSCs: (g) fresh doped spiro-OMeTAD PSC, (h) doped spiro-OMeTAD PSCs with 85°C aging for 10 days in argon, (i) fresh L3 PSC, (j) L3 PSC with 85°C aging for 10 days in argon.

Stability

We have tested the stability of L-series PSCs and control devices with doped spiro-OMeTAD HTM. Firstly, the unencapsulated devices were stored in a glovebox filled with argon under the dark condition. Over 2700 hours, L3-PSC retained 90% of its initial value and the control device had 85% (Fig. S39). This result indicates that dopant free HTM in PSCs can avoid ionic interdiffusion to degrade the perovskite film and prolong the long-term storage stability of PSCs. Secondly, the 85°C thermal stability measurement under argon atmosphere was performed. As shown in Fig. 6a, the PCE of PSCs with doped spiro-OMeTAD HTM quickly decayed to 70% of their initial values within 200 hours, whereas the L3-PSC maintained ~83% of their initial PCE after ~1000 hours. Finally, stability at 85°C and MPP tracking was performed to evaluate the photothermal stability of the unencapsulated devices under white LEDs at one-sun intensity. As shown in Fig. 6b, the L3-PSC could maintain 85% of its initial efficiency after over 500 hours, while the control PSC was dropped rapidly within 100 hours. This is the best photothermal stability of the PSCs with dopant-free organic small molecule HTMs (Fig. 1d and Table S2).

The promising thermal stability of L3-PSCs reveals that dopant-free L3 HTM with a high T_g of 163°C exhibits a more stable molecular configuration than that of doped spiro-OMeTAD HTM with a T_g of ~72°C.[46] From the XRD patterns of perovskite film in Fig. S41, the low PbI_2 peak diffraction and strong (001) perovskite peaks in the aged perovskite film with L3 HTM confirm the improved stability for perovskite covered with L3 HTM. Moreover, as shown in Fig. S41, both the doped spiro-OMeTAD and L3 HTMs-covered perovskite films were found to exhibit red-shifted absorption edges in the UV-vis absorption spectra for aged perovskite film, indicating that the perovskite itself inevitably degrades through the loss of chloride component under heating conditions.[65, 66] This may be one of the reasons for the slightly decreased efficiency of L3-PSC under the 85°C thermal aging test. Although the colour of the perovskite film does not change significantly (see the images in Fig. S42a), degradation spots appeared on the surface of the spiro-OMeTAD film after aging under 85°C for 10 days as shown in Fig. S42b. These degradational spots at the interface between spiro-OMeTAD HTL and metal electrode will further impair the efficiency of the PSCs.

In order to further analyse the influence of the HTM morphology on device efficiency under heating conditions, we used AFM to characterize the morphology of bare HTM before and after heating. As shown in Figs. 6c-f, the morphology of doped spiro-OMeTAD film shows an obvious agglomeration after aging at 100°C for 10 hours accompanied by an increase in surface roughness. On the contrary, negligible changes in the morphology of L3 film could be detected before and after 10 hours aging. Moreover, when the heating time even prolongs to 100 hours, L3 film can still maintain the dense and smooth morphology (Fig. S43), strongly suggesting the excellent thermal stability of L3 HTM.

Furthermore, the ToF-SIMS of depth profiles of iodine anion (I^-) distribution was carried out to analyses ion migration within complete PSCs. As shown in Figs. 6g-j, substantial iodine was detected in spiro-OMeTAD layer for the fresh and aged control device based on doped spiro-OMeTAD due to ionic interdiffusion between Li-salt and iodide ions. The ionic interdiffusion in the fresh control device occurs during the spin-coating process. The additive species can penetrate into perovskite and iodine can diffuse into HTL layer, resulting in iodine gradient area. As shown in Figs. 6g, h, this interdiffusion area was enlarged in spiro-OMeTAD layer after thermal aging process. The iodine migration is the major reason for performance degradation for traditional *n-i-p* PSCs. In contrast, iodine is flatly distributed inside the whole perovskite layer in L3-PSC. After thermal annealing at 85°C for 10 days, the diffusion of I^- ions from the perovskite layer to the Au anion electrode could be significantly suppressed in L3-PSC compared to the control device based on doped spiro-OMeTAD, by a factor of ~100. This again underlines that the dense and conformal film coverage of L3 HTM at 85°C can prevent the iodine migration, leading to ionic fixation and enhanced photothermal stability of L3-PSCs. Therefore, in dopant-free condition, the ionic interdiffusion is greatly suppressed by L3 because of the conformal bonding with perovskite surface.

Conclusions

We reported photothermal stable conventional PSCs with high efficiency based on dopant-free small molecule HTMs with a D-A-D'-A-D configuration. By engineering the IDT π-bridge, the four 4-hexylphenyl side chains and two TT units in IDT π-bridge main chain make L3 HTM possess good film formation quality and proper energy levels, ensuring the efficient charge transport performance. Meanwhile, surface passivation effects by the functional group in HTM also endow the L3 layer with great benefits in charge transport and extraction property at the perovskite/HTM interface with reduced interfacial recombination loss and suppressed ionic interdiffusion. As a result, PSCs with three HTMs (L1, L2 and L3) all showed PCEs more than 20%, especially the PSCs with L3 HTM delivered a champion PCE of 22.61% with an antireflection film. More importantly, due to the high mobility and T_g of L-series HTMs, the dopant-free L3 HTM could avoid the negative effect of additives on perovskite layer and maintain high quality morphology of HTL. As a result, the PSCs with the dopant-free L3 HTM exhibited a great photothermal and operational stability under 85°C, which maintained 83% of initial PCE after ~1000 hours at the dark, and 85% of initial PCE after 500 hours with continuous illumination measured at MPP in the argon-filled glovebox. We demonstrated that conformally bonded ultrathin interface with compact and uniform coverage (~60 nm) to retard iodine migration and protect the buried perovskite. Ultrafast spectroscopy spectra revealed that L-series molecules have sequential reduction of photoexcited energy disorder to illustrate the structure-performance-stability relationship. This work provides a strategy to design high mobility and T_g HTM and shows a promising application prospect of small molecular HTM with the D-A-D'-A-D configuration in conventional *n-i-p* PSCs.

Author Contributions

K.Y.Y. and Y.L. conceived the idea and supervised the overall project. K.Y.Y., Y.L., N.L., C.J.B., L.M.D. and L.G.Y. designed the experiments. Y.L. designed the L1, L2, L3 HTMs. W.Y.Z., Y.H.Z., J.X.H., Q.W. and Y.L. synthesized the L1, L2, L3 HTMs. L.G.Y. fabricated and characterized perovskite thin film and devices. K.C.Z., J.R.W. and H.M.L. helped on the device fabrication and characterization. W.Y.Z., Y.H.Z., J.X.H., R. P.C., W. X. L., Q.W. and Y.L. characterized their structure of HTMs. C.C.S.C. and K.S.W. contributed TRPL and fs-TA measurements and corresponding data analysis. M.C.Q. and X.H.L. carried out the GIWAXs measurements and corresponding data analysis. Z.Z. performed DTF calculation. J.H.Q. helped on ToF-SIMS measurements. K.Y.Y. and L.G.Y. drafted the manuscript and all authors were involved in discussion and revision.

Conflicts of interest

There are no conflicts of interest to declare.

Acknowledgements

This work was in part supported by National Key Research and Development Program of China (2022YFB3803300) and Start-up funds from Central Organization Department and South China University of Technology, as well as funds from the National Natural Science Foundation of China (U2001217) Guangdong Science and Technology Program (Grant Nos: 2020B121201003, 2019ZT08L075, 2019QN01L118), and the Program for Introducing Overseas High-level Talents of Shanxi (Hundred Talents Plan). Y.L. acknowledges funding from the National Natural Science Foundation of China (No. 51973063), the Tip-top Scientific and Technical Innovative Youth Talents of Guangdong Special Support Program (No. 2019TQ05C890), and the 111 Project (No. BP0618009). C.C.S.C. and K.S.W. acknowledge the support from Research Grants Council of Hong Kong (grant number C7035-20G) and William Mong Institute of Nano Science and Technology (grant number WMINST19SC04). N.L. acknowledges the financial support by State Key Lab of Luminescent Materials and Devices, South China University of Technology (Skllmd-2022-03).

References

1. M. Kim, J. Jeong, H. Lu, K. Lee Tae, T. Eickemeyer Felix, Y. Liu, W. Choi In, J. Choi Seung, Y. Jo, H.-B. Kim, S.-I. Mo, Y.-K. Kim, H. Lee, G. An Na, S. Cho, R. Tress Wolfgang, M. Zakeeruddin Shaik, A. Hagfeldt, Y. Kim Jin, M. Grätzel and S. Kim Dong, *Science*, 2022, **375**, 302-306.
2. Z. Li, B. Li, X. Wu, A. Sheppard Stephanie, S. Zhang, D. Gao, J. Long Nicholas and Z. Zhu, *Science*, 2022, **376**, 416-420.
3. X. Zheng, Y. Hou, C. Bao, J. Yin, F. Yuan, Z. Huang, K. Song, J. Liu, J. Troughton, N. Gasparini, C. Zhou, Y. Lin, D.-J. Xue, B. Chen, A. K. Johnston, N. Wei, M. N. Hedhili, M. Wei, A. Y. Alsalloum, P. Maity, B. Turedi, C. Yang, D. Baran, T. D. Anthopoulos, Y. Han, Z.-H. Lu, O. F. Mohammed, F. Gao, E. H. Sargent and O. M. Bakr, *Nat. Energy*, 2020, **5**, 131-140.
4. Y.-H. Lin, N. Sakai, P. Da, J. Wu, H. C. Sansom, A. J. Ramadan, S. Mahesh, J. Liu, R. D. J. Oliver, J. Lim, L. Aspitarte, K. Sharma, P. K. Madhu, A. B. Morales-Vilches, P. K. Nayak, S. Bai, F. Gao, C. R. M. Grovenor, M. B. Johnston, J. G. Labram, J. R. Durrant, J. M.

Ball, B. Wenger, B. Stannowski and H. J. Snaith, *Science*, 2020, **369**, 96.
5. R. Chen, S. Liu, X. Xu, F. Ren, J. Zhou, X. Tian, Z. Yang, X. Guanz, Z. Liu, S. Zhang, Y. Zhang, Y. Wu, L. Han, Y. Qi and W. Chen, *Energy Environ. Sci.*, 2022, **15**, 2567-2580.
6. R. Azmi, E. Ugur, A. Seitkhan, F. Aljamaan, A. S. Subbiah, J. Liu, G. T. Harrison, M. I. Nugraha, M. K. Eswaran, M. Babics, Y. Chen, F. Xu, T. G. Allen, A. U. Rehman, C. L. Wang, T. D. Anthopoulos, U. Schwingenschlogl, M. De Bastiani, E. Aydin and S. De Wolf, *Science*, 2022, **376**, 73-77.
7. J. J. Yoo, G. Seo, M. R. Chua, T. G. Park, Y. Lu, F. Rotermund, Y. K. Kim, C. S. Moon, N. J. Jeon, J. P. Correa-Baena, V. Bulovic, S. S. Shin, M. G. Bawendi and J. Seo, *Nature*, 2021, **590**, 587-593.
8. G. Kim, H. Min, K. S. Lee, D. Y. Lee, S. M. Yoon and S. I. Seok, *Science*, 2020, **370**, 108-112.
9. J. Jeong, M. Kim, J. Seo, H. Lu, P. Ahlawat, A. Mishra, Y. Yang, M. A. Hope, F. T. Eickemeyer, M. Kim, Y. J. Yoon, I. W. Choi, B. P. Darwich, S. J. Choi, Y. Jo, J. H. Lee, B. Walker, S. M. Zakeeruddin, L. Emsley, U. Rothlisberger, A. Hagfeldt, D. S. Kim, M. Gratzel and J. Y. Kim, *Nature*, 2021, **592**, 381-385.
10. Z. Li, C. Xiao, Y. Yang, S. P. Harvey, D. H. Kim, J. A. Christians, M. Yang, P. Schulz, S. U. Nanayakkara, C.-S. Jiang, J. M. Luther, J. J. Berry, M. C. Beard, M. M. Al-Jassim and K. Zhu, *Energy Environ. Sci.*, 2017, **10**, 1234-1242.
11. T. Zhang, F. Wang, H.-B. Kim, I.-W. Choi, C. Wang, E. Cho, R. Konefal, Y. Puttisong, K. Terado, L. Kobera, M. Chen, M. Yang, S. Bai, B. Yang, J. Suo, S.-C. Yang, X. Liu, F. Fu, H. Yoshida, W. M. Chen, J. Brus, V. Coropceanu, A. Hagfeldt, J.-L. Brédas, M. Fahlman, D. S. Kim, Z. Hu and F. Gao, Science, 2022, **377**, 495-501.
12. Z. J. Li, J. Park, H. Park, J. Lee, Y. Kang, T. K. Ahn, B. G. Kim and H. J. Park, *Nano Energy*, 2020, **78**, 105159.
13. B. X. M. Zhao, C. Yao, K. C. Gu, T. R. Liu, Y. Xia and Y. L. Loo, *Energy Environ. Sci.*, 2020, **13**, 4334-4343.
14. X. X. Yin, Z. N. Song, Z. F. Li and W. H. Tang, *Energy Environ.Sci.*, 2020, **13**, 4057-4086.
15. X. L. Sun, X. Y. Yu and Z. A. Li, *ACS Appl. Energy Mater.*, 2020, **3**, 10282-10302.
16. E. Rezaee, X. Liu, Q. Hu, L. Dong, Q. Chen, J.-H. Pan and Z.-X. Xu, *Solar RRL*, 2018, **2**, 1800200.
17. K. Yang, Q. Liao, J. Huang, Z. Zhang, M. Su, Z. Chen, Z. Wu, D. Wang, Z. Lai, H. Y. Woo, Y. Cao, P. Gao and X. Guo, *Angew. Chem. Int. Ed.,* 2022, **61**, e202113749.
18. Z. Zhu, Y. Bai, T. Zhang, Z. Liu, X. Long, Z. Wei, Z. Wang, L. Zhang, J. Wang, F. Yan and S. Yang, *Angew. Chem. Int. Ed.,* 2014, **53**, 12571-12575.
19. N. Arora, M. I. Dar, A. Hinderhofer, N. Pellet, F. Schreiber, S. M. Zakeeruddin and M. Gratzel, *Science*, 2017, **358**, 768-771.
20. Y. Hou, X. Du, S. Scheiner, D. P. McMeekin, Z. Wang, N. Li, M. S. Killian, H. Chen, M. Richter, I. Levchuk, N. Schrenker, E. Spiecker, T. Stubhan, N. A. Luechinger, A. Hirsch, P. Schmuki, H. P. Steinruck, R. H. Fink, M. Halik, H. J. Snaith and C. J. Brabec, *Science*, 2017, **358**, 1192-1197.
21. X. Q. Li, W. J. Chen, S. H. Wang, G. Y. Xu, S. Liu, Y. W. Li and Y. F. Li, *Adv. Funct. Mater.*, 2021, **31**, 2010696.
22. Z. W. Wang, Q. Q. Dong, Y. J. Xia, H. Yu, K. C. Zhang, X. D. Liu, X. Guo, Y. Zhou, M. J. Zhang and B. Song, *Org. Electron.*, 2016, **33**, 142-149.
23. H. Guo, C.-Y. Yang, X. Zhang, A. Motta, K. Feng, Y. Xia, Y. Shi, Z. Wu, K. Yang, J. Chen, Q. Liao, Y. Tang, H. Sun, H. Y. Woo, S. Fabiano, A. Facchetti and X. Guo, *Nature*, 2021, **599**, 67-73.
24. Y. Zhao, T. Heumueller, J. Zhang, J. Luo, O. Kasian, S. Langner, C. Kupfer, B. Liu, Y. Zhong, J. Elia, A. Osvet, J. Wu, C. Liu, Z. Wan, C. Jia, N. Li, J. Hauch and C. J. Brabec, *Nat. Energy*, 2021, **7**, 144-152.
25. Q. Fu, X. Tang, H. Liu, R. Wang, T. Liu, Z. Wu, H. Y. Woo, T. Zhou, X. Wan, Y. Chen and Y. Liu, *J. Am. Chem. Soc.*, 2022, **144**, 9500-9509.
26. Q. Fu, H. Liu, S. Li, T. Zhou, M. Chen, Y. Yang, J. Wang, R. Wang, Y. Chen and Y. Liu, *Angew. Chem. Int. Ed.,* 2022, e202210356.
27. M. J. Jeong, K. M. Yeom, S. J. Kim, E. H. Jung and J. H. Noh, *Energy Environ. Sci.*, 2021, **14**, 2419-2428.
28. T. Niu, W. Zhu, Y. Zhang, Q. Xue, X. Jiao, Z. Wang, Y.-M. Xie, P. Li, R. Chen, F. Huang, Y. Li, H.-L. Yip and Y. Cao, *Joule*, 2021, **5**, 249-269.
29. H. Zhu, Z. Shen, L. Pan, J. Han, F. T. Eickemeyer, Y. Ren, X. Li, S. Wang, H. Liu, X. Dong, S. M. Zakeeruddin, A. Hagfeldt, Y. Liu and M. Grätzel, *ACS Energy Lett.*, 2020, **6**, 208-215.
30. H. Guo, H. Zhang, C. Shen, D. Zhang, S. Liu, Y. Wu and W. H. Zhu, *Angew. Chem. Int. Ed.,* 2021, **60**, 2674-2679.
31. Y.-H. Zhang and Y. Li, *Rare Metals*, 2021, **40**, 2993-3018.
32. M. Jeong, W. Choi In, M. Go Eun, Y. Cho, M. Kim, B. Lee, S. Jeong, Y. Jo, W. Choi Hye, J. Lee, J.-H. Bae, K. Kwak Sang, S. Kim Dong and C. Yang, *Science*, 2020, **369**, 1615-1620.
33. X. Yin, J. Zhou, Z. Song, Z. Dong, Q. Bao, N. Shrestha, S. S. Bista, R. J. Ellingson, Y. Yan and W. Tang, *Adv. Funct. Mater.*, 2019, **29**, 1904300.
34. J. Zhou, X. Yin, Z. Dong, A. Ali, Z. Song, N. Shrestha, S. S. Bista, Q. Bao, R. J. Ellingson, Y. Yan and W. Tang, *Angew. Chem. Int. Ed.*, 2019, **58**, 13717-13721.
35. Y. Wang, W. Chen, L. Wang, B. Tu, T. Chen, B. Liu, K. Yang, C. W. Koh, X. Zhang, H. Sun, G. Chen, X. Feng, H. Y. Woo, A. B. Djurisic, Z. He and X. Guo, *Adv. Mater.*, 2019, **31**, e1902781.
36. Y. Liu, Q. Chen, H.-S. Duan, H. Zhou, Y. Yang, H. Chen, S. Luo, T.-B. Song, L. Dou, Z. Hong and Y. Yang, *J. Mater. Chem. A*, 2015, **3**, 11940-11947.
37. Y. Liu, Z. Hong, Q. Chen, H. Chen, W.-H. Chang, Y. Yang, T.-B. Song and Y. Yang, *Adv. Mater.*, 2016, **28**, 440-446.
38. H. Zhang, Y. Wu, W. Zhang, E. Li, C. Shen, H. Jiang, H. Tian and W.-H. Zhu, *Chem. Sci.*, 2018, **9**, 5919-5928.
39. B. Tu, Y. Wang, W. Chen, B. Liu, X. Feng, Y. Zhu, K. Yang, Z. Zhang, Y. Shi, X. Guo, H. F. Li, Z. Tang, A. B. Djurisic and Z. He, *ACS Appl. Mater. Interfaces*, 2019, **11**, 48556-48563.
40. Q. Cheng, H. Chen, F. Yang, Z. Chen, W. Chen, H. Yang, Y. Shen, X. M. Ou, Y. Wu, Y. Li and Y. Li, *Angew. Chem. Int. Ed.,* 2022, **61**, e202210613.
41. P. Y. Yan, D. B. Yang, H. Q. Wang, S. C. Yang and Z. Y. Ge, Energy Environ. Sci., 2022, 15, 3630-3669.
42. I. McCulloch, R. S. Ashraf, L. Biniek, H. Bronstein, C. Combe, J. E. Donaghey, D. I. James, C. B. Nielsen, B. C. Schroeder and W. Zhang, *Acc. Chem. Res.,* 2012, **45**, 714-722.
43. X. Liu, Q. D. Li, Y. C. Li, X. Gong, S. J. Su and Y. Cao, *J. Mater. Chem. A*, 2014, **2**, 4004-4013.
44. S. Feng, C. Zhang, Y. Liu, Z. Bi, Z. Zhang, X. Xu, W. Ma and Z. Bo, *Adv. Mater.*, 2017, **29**, 1703527.
45. Y. H. Cai, X. L. Zhang, X. N. Xue, D. H. Wei, L. J. Huo and Y. M. Sun, *J. Mater. Chem. C*, 2017, **5**, 7777-7783.
46. T. Malinauskas, D. Tomkute-Luksiene, R. Sens, M. Daskeviciene, R. Send, H. Wonneberger, V. Jankauskas, I. Bruder and V. Getautis, *ACS Appl. Mater. Interfaces*, 2015, **7**, 11107-11116.
47. V. A. Chiykowski, Y. Cao, H. Tan, D. P. Tabor, E. H. Sargent, A. Aspuru-Guzik and C. P. Berlinguette, *Angewandte Chemie International Edition*, 2018, **57**, 1552 9-15533.
48. S. Wang, H. Chen, J. Zhang, G. Xu, W. Chen, R. Xue, M. Zhang, Y. Li and Y. Li, *Adv. Mater.*, 2019, **31**, e1903691.
49. M. Qin, H. Xue, H. Zhang, H. Hu, K. Liu, Y. Li, Z. Qin, J. Ma, H. Zhu, K. Yan, G. Fang, G. Li, U. S. Jeng, G. Brocks, S. Tao and X. Lu, *Adv. Mater.*, 2020, **32**, e2004630.
50. J. Wang, L. Yuan, H. Luo, C. Duan, B. Zhou, Q. Wen and K. Yan, *Chem. Eng. J.*, 2022, **446**, 136968.
51. L. Yuan, H. Luo, J. Wang, Z. Xu, J. Li, Q. Jiang and K. Yan, *J. Mater. Chem. A*, 2021, **9**, 4781-4788.
52. Z. Li, Z. Zhu, C. C. Chueh, S. B. Jo, J. Luo, S. H. Jang and A. K. Jen, *J. Am. Chem. Soc.*, 2016, **138**, 11833-11839.
53. Q. Fan, W. Su, X. Guo, B. Guo, W. Li, Y. Zhang, K. Wang, M. Zhang and Y. Li, *Adv. Energy Mater.*, 2016, **6**, 1600430.

54. R. Wang, L. Lüer, S. Langner, T. Heumueller, K. Forberich, H. Zhang, J. Hauch, N. Li and C. J. Brabec, *ChemSusChem*, 2021, **14**, 3590-3598.
55. L. Yuan, J. Li, Z. W. Wang, P. Huang, K. C. Zhang, Y. Liu, K. Zhu, Z. Li, T. Cao, B. Dong, Y. Zhou, M. Zhou, B. Song and Y. Li, *ACS Appl. Mater. Interfaces*, 2017, **9**, 42961-42968.
56. P. Huang, Q. Chen, K. Zhan g, L. Yuan, Y. Zhou, B. Song and Y. Li, *J. Mater. Chem. A*, 2019, **7**, 6213-6219.
57. Q. Jiang, L. Zhang, H. Wang, X. Yang, J. Meng, H. Liu, Z. Yin, J. Wu, X. Zhang and J. You, *Nat. Energy*, 2016, **2**, 16177.
58. A. Al-Ashouri, E. Köhnen, B. Li, A. Magomedov, H. Hempel, P. Caprioglio, J. A. Márquez, A. B. Morales Vilches, E. Kasparavicius, J. A. Smith, N. Phung, D. Menzel, M. Grischek, L. Kegelmann, D. Skroblin, C. Gollwitzer, T. Malinauskas, M. Jošt, G. Matič, B. Rech, R. Schlatmann, M. Topič, L. Korte, A. Abate, B. Stannowski, D. Neher, M. Stolterfoht, T. Unold, V. Getautis and S. Albrecht, *Science*, 2020, **370**, 1300.
59. B. Krogmeier, F. Staub, D. Grabowski, U. Rau and T. Kirchartz, *Sustain. Energy Fuels*, 2018, **2**, 1027-1034.
60. X. B. Cao, Y. H. Li, F. Fang, X. Cui, Y. W. Yao and J. Q. Wei, *RSC Advances*, 2016, **6**, 70925-70931.
61. Q. Dong, Y. Fang, Y. Shao, P. Mulligan, J. Qiu, L. Cao and J. Huang, *Science*, 2015, **347**, 967-970.
62. D. Shi, V. Adinolfi, R. Comin, M. Yuan, E. Alarousu, A. Buin, Y. Chen, S. Hoogland, A. Rothenberger, K. Katsiev, Y. Losovyj, X. Zhang, P. A. Dowben, O. F. Mohammed, E. H. Sargent and O. M. Bakr, *Science*, 2015, **347**, 519-522.
63. V. M. Le Corre, E. A. Duijnstee, O. El Tambouli, J. M. Ball, H. J. Snaith, J. Lim and L. J. A. Koster, *ACS Energy Lett.*, 2021, **6**, 1087-1094.
64. J. Xie, K. Yan, H. Zhu, G. Li, H. Wang, H. Zhu, P. Hang, S. Zhao, W. Guo, D. Ye, L. Shao, X. Guan, T. Ngai, X. Yu and J. Xu, *Science Bulletin*, 2020, **65**, 1726-1734.
65. H. Yu, F. Wang, F. Xie, W. Li, J. Chen and N. Zhao, *Adv. Funct. Mater.*, 2014, **24**, 7102-7108.
66. C. Li, Q. Guo, H. Zhang, Y. Bai, F. Wang, L. Liu, T. Hayat, A. Alsaedi and Z. Tan, *Nano Energy*, 2017, **40**, 248-257.

Supplementary Materials

Conformally bonded molecular interface retarded iodine migration for durable perovskite solar cells

Ligang Yuan,[1,†] Weiya Zhu,[1,†] Yiheng Zhang,[1] Yuan Li,[1,*] Christopher C. S. Chan,[2] Minchao Qin,[3] Jianhang Qiu,[4] Kaicheng Zhang,[5] Jiaxing Huang,[1] Jiarong Wang,[1] Huiming Luo,[1] Zheng Zhang,[1] Ruipeng Chen,[1] Weixuan Liang,[1] Qi Wei,[1] Kam Sing Wong,[2] Xinhui Lu,[3] Ning Li,[1,*] Christoph J. Brabec,[5, 6] Liming Ding,[7] Keyou Yan[1,*]

[1] School of Environment and Energy, State Key Laboratory of Luminescent Materials and Devices, Institute of Polymer Optoelectronic Materials and Devices, Guangdong Provincial Key Laboratory of Solid Wastes Pollution Control and Recycling, Guangdong Provincial Key Laboratory of Luminescence from Molecular Aggregates, AIE Institute, South China University of Technology, Guangzhou 510000, P. R. China

[2] Department of Physics and William Mong Institute of Nano Science and Technology, The Hong Kong University of Science and Technology, Clearwater Bay, Hong Kong, P. R. China

[3] Department of Physics, The Chinese University of Hong Kong, Shatin 999077, Hong Kong, P. R. China

[4] Shenyang National Laboratory for Materials Science, Institute of Metal Research, Chinese Academy of Sciences, Shenyang, 110016, China

[5] Institute of Materials for Electronics and Energy Technology (i-MEET) Friedrich-Alexander-University Erlangen-Nuremberg Martensstraße 7, Erlangen 91058, Germany

[6] Helmholtz-Institute Erlangen-Nürnberg for Renewable Energy (HI ERN), Forschungszentrum Jülich (FZJ), Erlangen 91058, Germany

[7] Center for Excellence in Nanoscience (CAS), Key Laboratory of Nanosystem and Hierarchical Fabrication (CAS), National Center for Nanoscience and Technology, Beijing 100190 P. R. China

[†] These two authors contributed equally to this work.

*Corresponding author: celiy@scut.edu.cn, ningli2022@scut.edu.cn, kyyan@scut.edu.cn

Materials and Methods

Materials: Methylammonium bromide (MABr, 99.5%), Methylammonium chloride (MACl, 99.5%), Lead iodide (PbI_2, 99.99%), lithium bistrifluoromethane-sulfonimidate (LiTFSI, 99.95%) and 4-tert-butylpyridine (tBP) were purchased from Xi'an polymer light technology Corp. Formamidinium iodide (FAI) and Guanidinium iodide (GAI) were purchased from Greatcell Solar. Ltd. Spiro-OMeTAD (99.86%) purchased from Advanced Election Technology Co., Ltd. The SnO_2 colloid precursor (tin(IV) oxide, 15% in H_2O colloidal dispersion) were acquired from Alfa Aesar.

Isopropanol (IPA, 99.5%), *N,N*-dimethylformamide (DMF, anhydrous, 99.8%), dimethyl sulfoxide (DMSO, anhydrous, 99.8%), chlorobenzene (CB, anhydrous, 99.8%) and acetonitrile (anhydrous, 99.9%) were acquired from Sigma-Aldrich and used as received without further purification. Commercially available reagents and chemicals were purchased from Suzhou Nakai Technology or Energy chemical and used without further purification.

Synthesis for dopant-free HTMs

Synthesis of TPAOMe-BT-Br

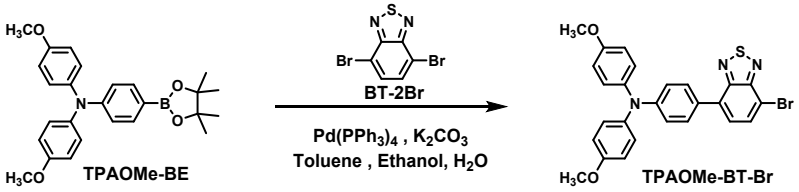

Scheme S1. Synthetic routes of **TPAOMe-BT-Br**.

TPAOMe-BE (3.448 g, 8.00 mmol, purchased from Suzhou Nakai Technology), **BT-2Br** (3.516 g, 12.00 mmol), $Pd(PPh_3)_4$ (30 mg, 0.026 mmol), potassium carbonate (K_2CO_3) aqueous solution (2 mol/L, 20 mL), ethanol (20 mL) and toluene (50 mL) were mixed and stirred under nitrogen atmosphere, and then heated to 100 °C and soaked for 12 h. After the reaction was completed, the mixture was cooled to room temperature and extracted three times with dichloromethane. The crude product was purified by column chromatography (silica gel, petroleum ether/dichloromethane, v/v, 3:1) to afford **TPAOMe-BT-Br** as a red solid compound (3.774 g, 91.0%). **^{1}H NMR (400 MHz, $CDCl_3$) δ 7.88 (d, J = 7.6 Hz, 1H), 7.75 (d, J = 8.5 Hz, 2H), 7.51 (d, J = 7.6 Hz, 1H), 7.13 (d, J = 7.3 Hz, 4H), 7.03 (d, J = 7.5 Hz, 2H), 6.87 (d, J = 8.9 Hz, 4H), 3.81 (s, 6H).**

Synthesis of L1

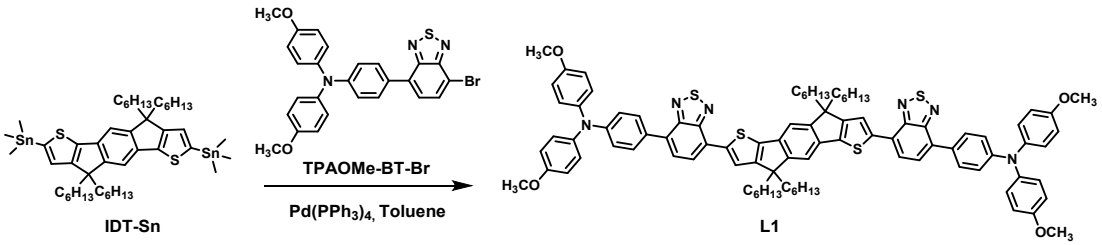

Scheme S2. Synthetic routes of **L1**.

TPAOMe-BT-Br (0.319 g, 0.62 mmol), **IDT-Sn** (0.260 g, 0.28 mmol), $Pd(PPh_3)_4$ (0.013 g, 0.011 mmol) and toluene (15 mL) were mixed and stirred under nitrogen atmosphere, and then heated to 110 °C and soaked for 4 h. After the reaction was completed, the mixture was cooled to room temperature and extracted three times with dichloromethane. The crude product was purified by column chromatography (silica gel, petroleum ether/dichloromethane, v/v, 2:1) to afford **L1** as a black solid compound (0.354 g, 85.5%). **^{1}H NMR (400 MHz, $CDCl_3$) δ 8.06 (s, 2H), 7.97 (d, J = 7.5 Hz, 2H), 7.85 (d, J = 8.6 Hz, 4H), 7.70 (d, J = 7.6 Hz, 2H), 7.39 (s, 2H), 7.15 (d, J = 8.7 Hz, 8H), 7.07 (d, J = 8.5 Hz, 4H), 6.88 (d, J = 8.8 Hz, 8H), 3.82 (s, 12H), 2.14 – 2.06 (m, 4H), 1.96 (t, J = 10.2 Hz, 4H), 1.13 (s, 24H), 0.98 (s, 4H), 0.90 (s, 4H), 0.77 (t, J = 6.6 Hz, 12H). ^{13}C NMR (126 MHz, $CDCl_3$) δ 156.20, 129.70, 127.07, 119.80, 114.79, 113.42, 55.54, 54.23, 39.30, 31.63, 29.78, 24.26, 22.61, 14.05.**

Synthesis of L2

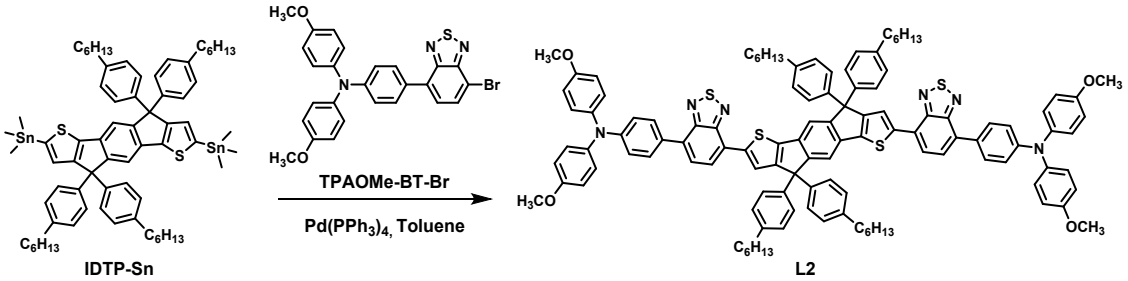

Scheme S3. Synthetic routes of **L2**.

TPAOMe-BT-Br (0.259 g, 0.499 mmol), **IDTP-Sn** (0.280 g, 0.227 mmol, purchased from Suzhou Nakai Technology), $Pd(PPh_3)_4$ (0.010 g, 0.009 mmol) and toluene (15 mL) were mixed and stirred under nitrogen atmosphere, and then heated to 110 °C and soaked for 4 h. After the reaction was completed, the mixture was cooled to room

temperature and extracted three times with dichloromethane. The crude product was purified by column chromatography (silica gel, petroleum ether/dichloromethane, v/v, 2:1) to afford **L2** as a black solid compound (0.366 g, 90.5%). **^{1}H NMR (400 MHz, $CDCl_3$) δ 8.01 (s, 2H), 7.95 – 7.71 (m, 6H), 7.53 (s, 6H), 7.28 (s, 2H), 7.26 – 7.17 (m, 4H), 7.10 (d, J = 8.1 Hz, 14H), 6.88 (s, 12H), 3.82 (s, 12H), 2.60 – 2.54 (m, 8H), 1.59 (p, J = 7.6 Hz, 8H), 1.34 (d, J = 7.6 Hz, 6H), 1.28 (d, J = 14.2 Hz, 18H), 0.86 (t, J = 6.5 Hz, 12H). ^{13}C NMR (126 MHz, $CDCl_3$) δ 141.91, 141.53, 128.42, 128.01, 55.51, 35.61, 31.74, 31.37, 29.18, 22.61, 14.12.**

Synthesis of L3

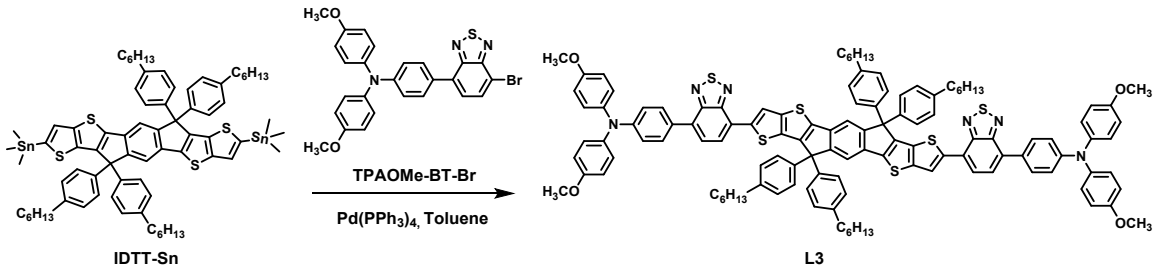

Scheme S4. Synthetic routes of **L3**.

TPAOMe-BT-Br (0.241 g, 0.466 mmol), **IDTT-Sn** (0.285 g, 0.211 mmol, purchased from Suzhou Nakai Technology), $Pd(PPh_3)_4$ (0.010 g, 0.009 mmol) and toluene (15 mL) were mixed and stirred under nitrogen atmosphere, and then heated to 110 °C and soaked for 4 h. After the reaction was completed, the mixture was cooled to room temperature and extracted three times with dichloromethane. The crude product was purified by column chromatography (silica gel, petroleum ether/dichloromethane, v/v, 2:1) to afford **L3** as a black solid compound (0.336 g, 83.8%). **^{1}H NMR (400 MHz, $CDCl_3$) δ 8.54 (s, 2H), 8.09 – 7.79 (m, 6H), 7.56 (s, 6H), 7.28 (s, 2H), 7.28 – 7.27 (m, 2H), 7.25 – 7.10 (m, 12H), 7.04 (s, 8H), 6.92 (s, 10H), 3.87 (s, 12H), 2.61 – 2.55 (m, 8H), 1.62 (d, J = 14.5 Hz, 8H), 1.39 – 1.27 (m, 24H), 0.86 (s, 12H). ^{13}C NMR (126 MHz, $CDCl_3$) δ 141.85, 140.19, 128.55, 128.13, 55.52, 35.63, 31.72, 31.28, 29.20, 22.61, 14.10.**

Fabrication of devices: ITO glass substrates (Advanced Election Technology Co., Ltd.) were cleaned sequentially by sonication in detergent, deionized water, acetone,

ethanol and isopropanol, twice for each liquid and 15 min for each time, followed by ultraviolet-ozone treatment for 30 min. The SnO_2 electron transport layer was coated onto the ITO substrate with diluted SnO_2 nanoparticles solution (2.67%) in ambient air, and then annealed at 150 °C for 30 min. After being cooled to room temperature, the substrate was treated with UV-ozone for 30 min before spin-coating of perovskite solution. The perovskite layer was deposited by a two-step spin coating method; first, 360 mg PbI_2 and 10.2 mg CsI in 600 μL dissolved in mixed solvent (DMF:DMSO (v/v=95:5)) followed by stirring at 70 °C for 4 h, then the PbI_2 solution was spin coated onto the SnO_2 ETL at 2500 rpm for 50 s, during this process, the mixture organic amino solution of FAI:MABr:MACl:GAI (60 mg:6 mg:6 mg:4 mg in 1 mL isopropanol) was adding before the end of 30 s, and then the perovskite film was annealed in at 150 °C for 11 min. For the doped spiro-OMeTAD-based devices, 72.3 mg/mL spiro-OMeTAD with 28.8 μL tBP and 17.5 μL Li-TFSI (520 mg/mL in Acetonitrile) in CB was deposited by spin-coating at 4000 rpm for 30 s. For dopant-free HTM devices, different concentrations in CB solution with different speeds were spin coating on the perovskite film. Finally, MoO_3 blocking layer (6 nm) and metal electrode (80 nm) were eventually deposited by vacuum thermal evaporation (pressure < 2×10^{-4} Pa). The overlapping area between the cathode and anode defined a pixel size of 0.08 cm^{-2}.

HTMs characterizations:

^{1}H-NMR spectra were recorded by DRX-400 spectrometer (400 and 500 MHz ^{1}H-NMR frequency, Bruker Co., Ettlingen, Germany) in $CDCl_3$ at room temperature. ^{13}C NMR spectra were collected using the same instrument at 126 MHz. The mass spectra were recorded on MALDI-TOF/TOF 5800 system (AB SCIEX). Cyclic voltammetry (CV) tests were performed in CH_2Cl_2 solution with 0.1 M tetrabutylammonium hexafluorophosphate (Bu_4NPF_6) as the electrolyte at a scan rate of 50 mV/s, a $Hg/HgCl_2$ (Saturated KCl solution) electrode as the reference electrode, a carbon-glass electrode as the working electrode, a Pt line electrode as the counter electrode

and ferrocene/ferrocenium (Fc/Fc^+) as an internal reference on electrochemistry workstation (CHI660E, China). XPS results were acquired on a photoelectron spectrometer (ESCALAB 250Xi, Thermo Fisher Scientific). Thermogravimetric analysis (TGA) was performed on a thermogravimetric analyzer (TA Instruments) at a scan rate of 20 K/min in the nitrogen atmosphere. Differential scanning calorimetry (DSC) was recorded on a DSC201F2 differential scanning calorimeter under the protection of nitrogen at a heating rate of 10 K/min.

DFT calculation: The neutral and charged molecular geometries are optimized by the DFT method with the Lee-Yang-Parr (B3LYP) hybrid functional and 6-31G(d,p) basis set implemented in the Gaussian 09 package.

Film characterizations measurements:

The absorption spectrum of HTMs and perovskite films were tested using a Cary Series UV-Vis-NIR Spectrophotometer.

Contact angle measurements were conducted on ZJ-7000 with a drop of ultrapure water (0.002 mL). The photographs were taken 1 second after water dripping.

The perovskite film and HTMs surface morphology were characterized by atomic force microscope (AFM, Bruker, Santa Barbara, CA).

Fourier transform infrared spectra were obtained on a CCR-1 instrument (Thermo Nicolet). PbI_2 and L3 are the pure powders. The PbI_2/L3 sample was mixed PbI_2 solution and L3 solution directly, then the powder was dried at 80 °C for eight hours. For the ART FTIR measurements, the perovskite film covered L3 film by spin-coating 1mg/mL L3 CB solution with a speed of 3000 rpm 30s.

The top-view and cross-sectional SEM images of the samples were characterized using a high-resolution scanning electron microscope (Zeiss Merlin). An electron beam accelerated to 5 kV was used with an InLens detector.

Transmission electron microscope (TEM, JEOL JEM-2100 Plus) measurements were performed under 200 kV. We exfoliated the films from the substrates by floating

technique with orthogonal solvent. The substrates with a structure of ITO/PEDOT:PSS/HTM prepared by spin-coating, then deionized water were employed to dissolve the bottom PEDOT:PSS film, leaving behind HTM film on the surface. The films were collected by copper grid for characterization.

The GIWAXS measurements were performed with a Xeuss 2.0 SAXS/WAXS laboratory beam line using a Cu X-ray source (8.05 keV, 1.54 Å) and a Pilatus3R 300K detector. The incidence angle was 0.2º.

Time resolved photoluminescence (TRPL) was performed on encapsulated films of glass substrate/perovskite/HTM. The samples were excited from the top surface with a 640 nm sub-100ps diode laser (Edinburgh Instruments EPL640). The PL was collected and diverted into a monochromator transmitting the peak PL wavelength and collected by a single photon counter to carry out time correlated single photon counting with a Becker and Hickl system. The time resolution is <500 ps.

Transient absorption spectroscopy was carried out on encapsulated pure HTM films to minimize photooxidation and environmental degradation during the measurement. A Ti:Sapphire regenerative laser amplifier (Coherent Legend) provided 800 nm fundamental pulses with pulse width of 100 fs at 1 kHz. Excitation pump pulses at 400 nm was generated by splitting the fundamental pulse into an optical parametric amplifier (Opera Solo). The probe beam is set on a mechanical delay stage and focused onto a YAG crystal to generate a stable supercontinuum for broadband absorption probe. The pump and probe beams are spatially overlapped on the sample surface and the transmission is collected by a spectrometer (Acton SpectraPro 275) equipped with a line array CCD.

Device characterizations measurements:

J–V characteristics of photovoltaic cells were taken using a Keithley 2400 source measurement unit under a simulated AM 1.5G spectrum. With a SS-F5-3A solar

simulator (Enli Technology CO., Ltd.), the light intensity was calibrated by standard KG3 reference silicon solar cells.

The Mott-Schottky plot measurements were measured by an IM6 electrochemical workstation (Zahner Zennium, Germany) at room temperature in ambient conditions. IPCE measurements also were performed on a Zahner system, using a TLS03 light source (300 HZ, 100 counts) at mixed mode.

Mobility and trap state density measurements:

Hole-only devices (ITO/PEDOT:PSS/HTL/MoO_x/Ag) were fabricated to calculate the hole mobility. The dark *J-V* characteristics of the hole-only devices were measured by a Keithley 2400 source.

The mobility of L-series HTLs is extracted by fitting the *J-V* curves by the Mott-Gurney equation of $J = 9\varepsilon_r\varepsilon_0 V^2/(8L^3)$.

The trap state density of perovskite film was determined by the trap-filled limit voltage using the equation of $n_t = 2\varepsilon\varepsilon_0 V_{TFL}/(qL^2)$ with a structure of ITO/PEDOT:PSS/perovskite/HTL/MoO_x/Ag.

Stability measurements: For the long-term storage stability, the unencapsulated PSCs with Ag top electrode were stored at argon filled glovebox under dark condition.

For thermal stability measurement (85°C), Ag electrode was replaced by Au and the PSCs were heated on a hotplate under dark condition, and the temperature was cooled down to room temperature before 30 min of PCE test.

For photo-thermal stability measurement (MPP & 85°C), The illumination was provided by white light-emitting diode lamp in a Lifetime Test equipment (Guangzhou Crysco Equipment Co.Ltd, P3000), and the radiation intensity is adjusted according the J_{SC}, which is equal to the J_{SC} under solar simulator. The temperature of

PSCs was provided an electric resistance heater and control by a temperature controller, and the temperature error is 0.2°C. In this study, our temperature was set to 85°C in argon filled glovebox.

For the XRD and optical images teats for thermal aged perovskite film covered with HTMs, the prepared ITO/SnO_2/perovskite/HTM samples were heated on the hotplate with a temperature of 85°C in argon filled glovebox.

For the AFM and optical microscope image for thermal aged HTM measurements, the 15mg/mL HTMs were spin-coated on the SnO_2/ITO glass substrates and heated on the hotplate with a temperature of 100°C in nitrogen filled glovebox.

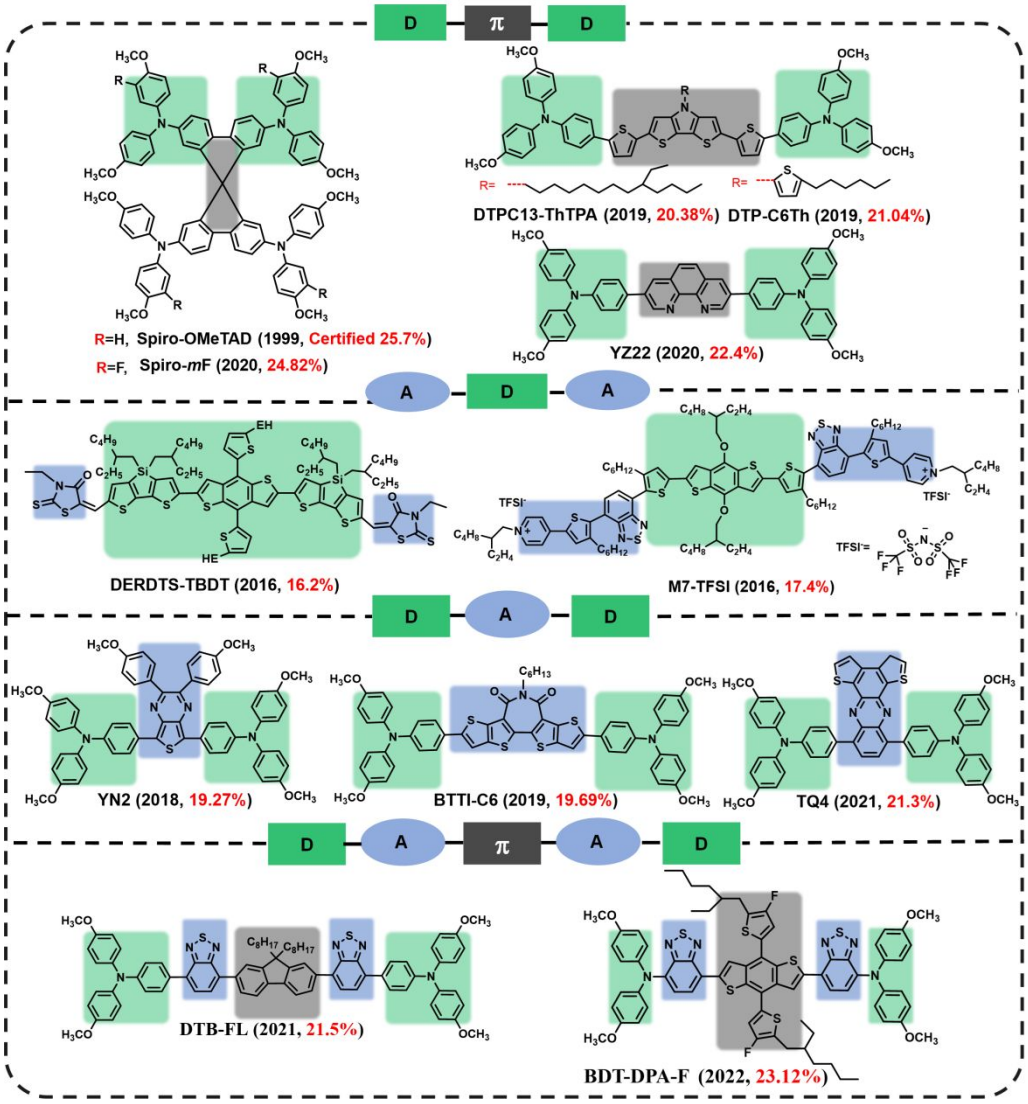

Fig. S1. Some established molecular structures of D-π-D, A-D-A and D-A-D HTMs for PSCs.[1-12]

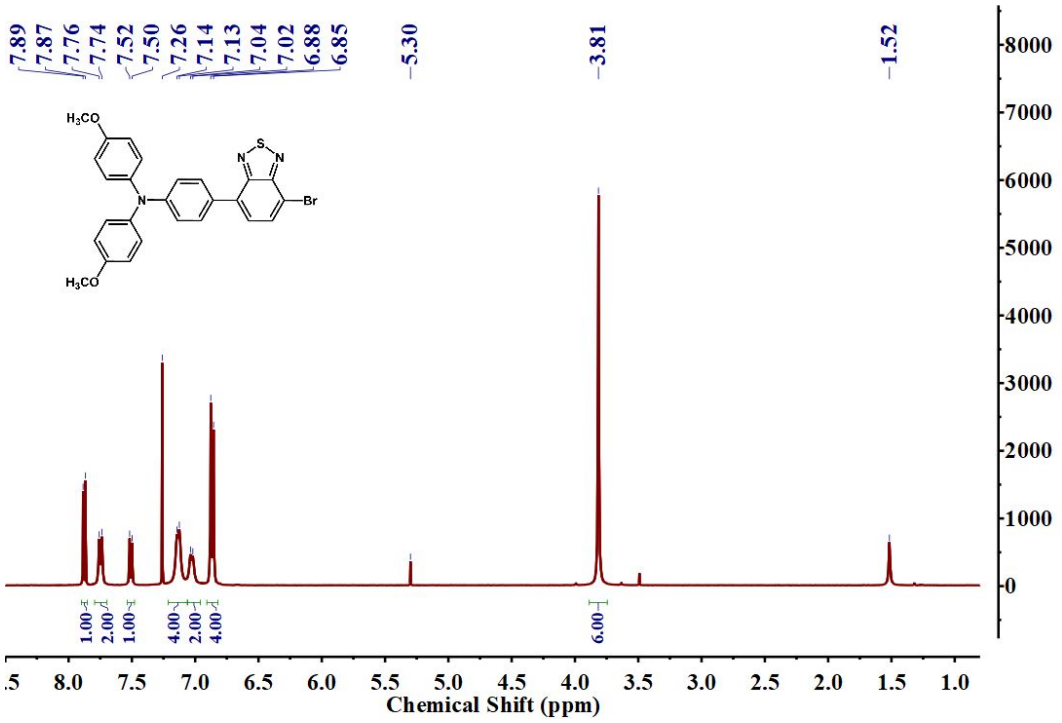

Fig. S2. **^{1}H NMR** spectrum of **TPAOMe-BT-Br**.

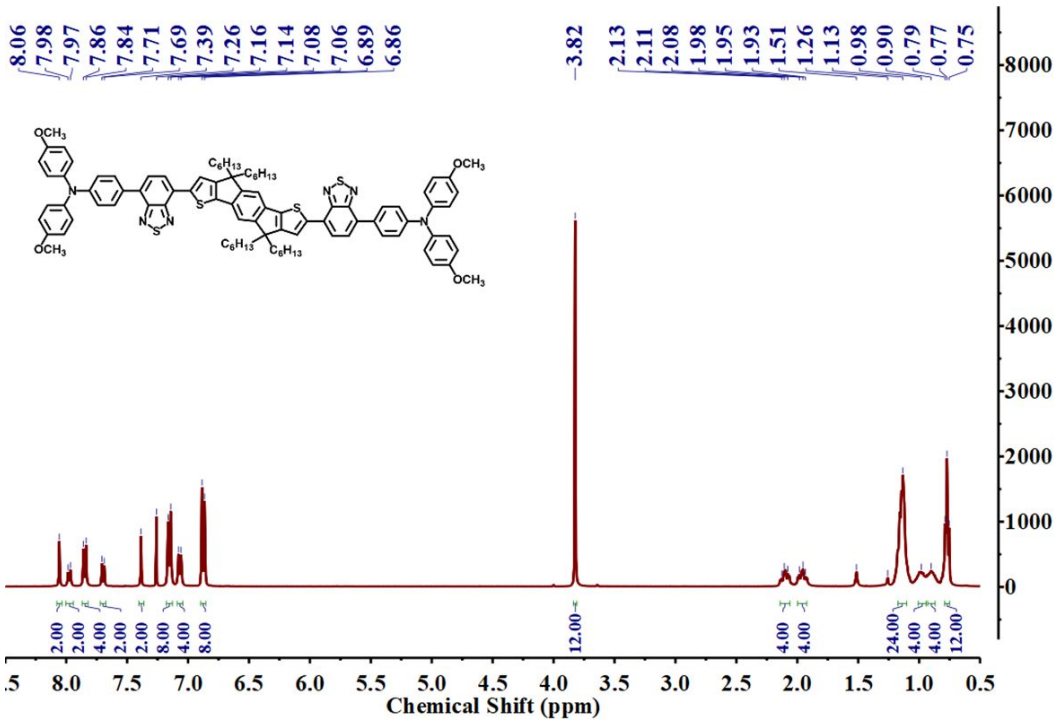

Fig. S3. **^{1}H NMR** spectrum of **L1**.

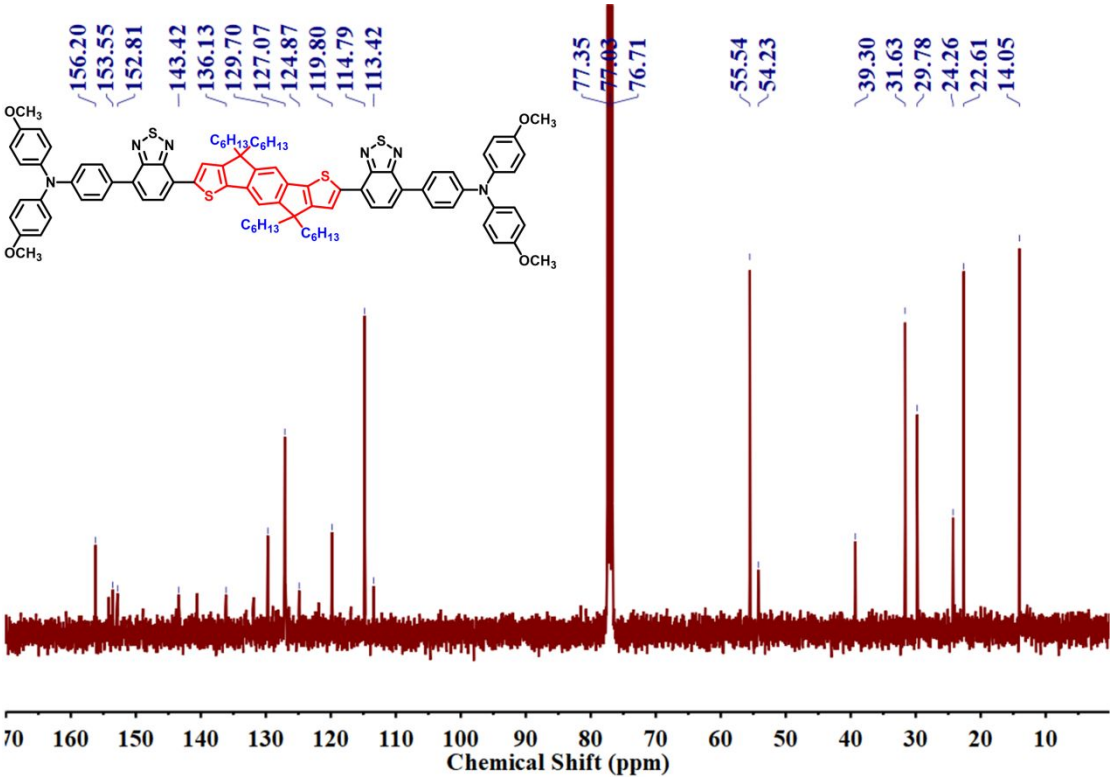

Fig. S4. **^{13}C NMR** spectrum **L1**.

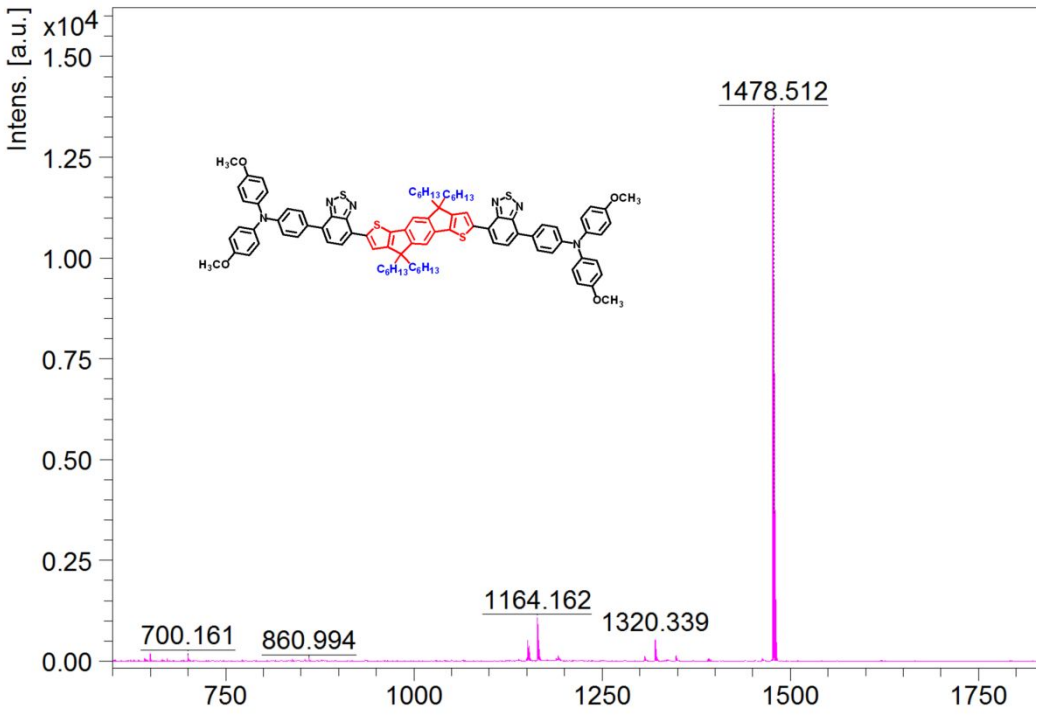

Fig. S5. MALDI-TOF-MS (m/z) spectrometry of **L1**: calcd. for $C_{92}H_{96}N_6O_4S_4$, 1478.06; found: 1478.516.

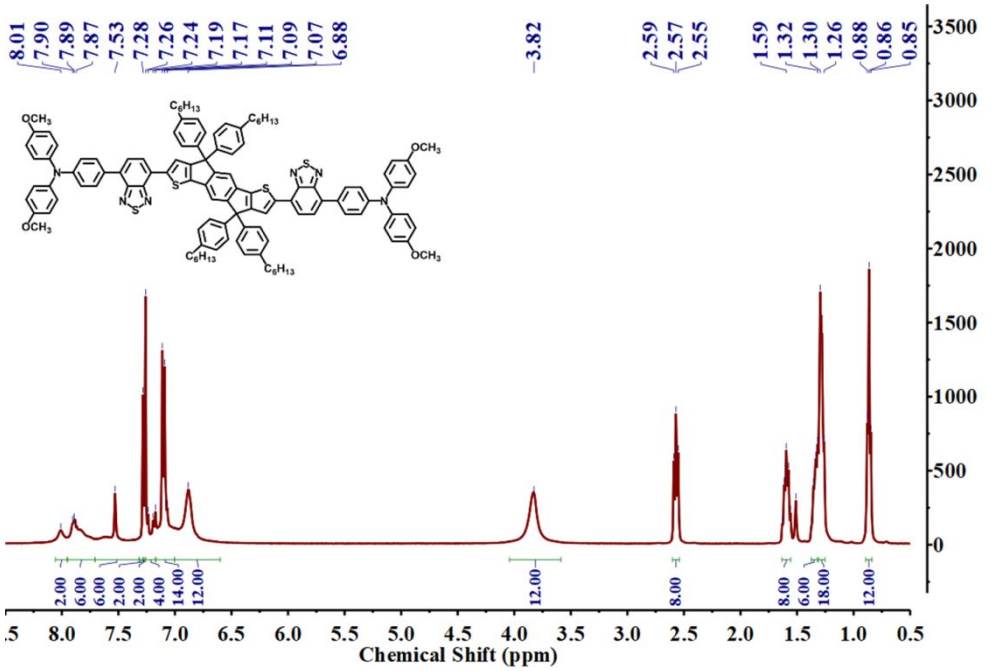

Fig. S6. ^{1}H NMR spectrum of **L2**.

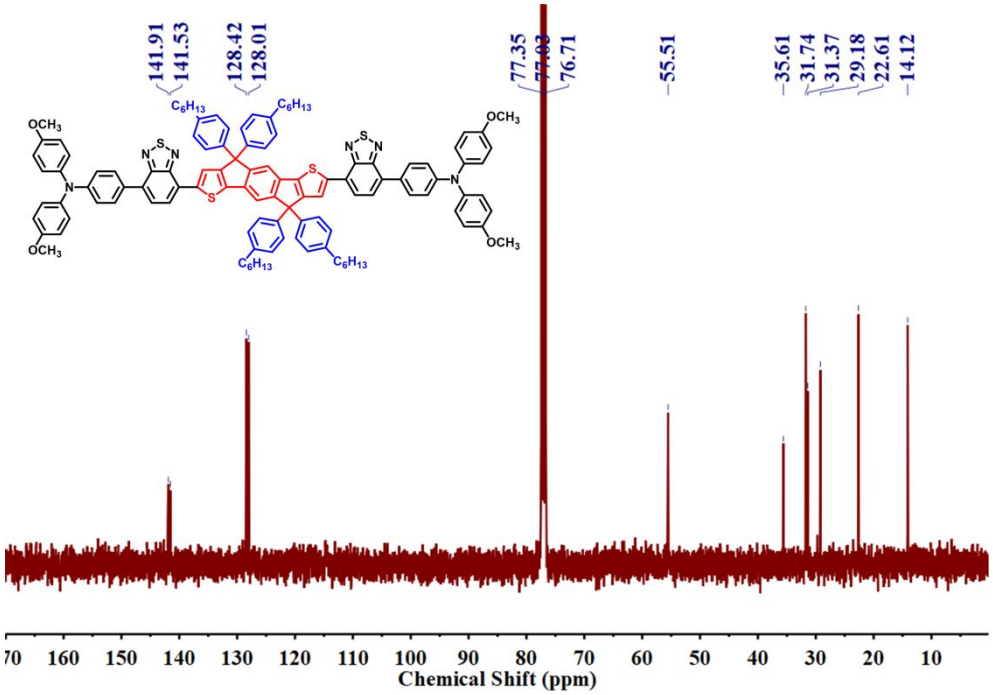

Fig. S7. ^{13}C NMR spectrum **L2**.

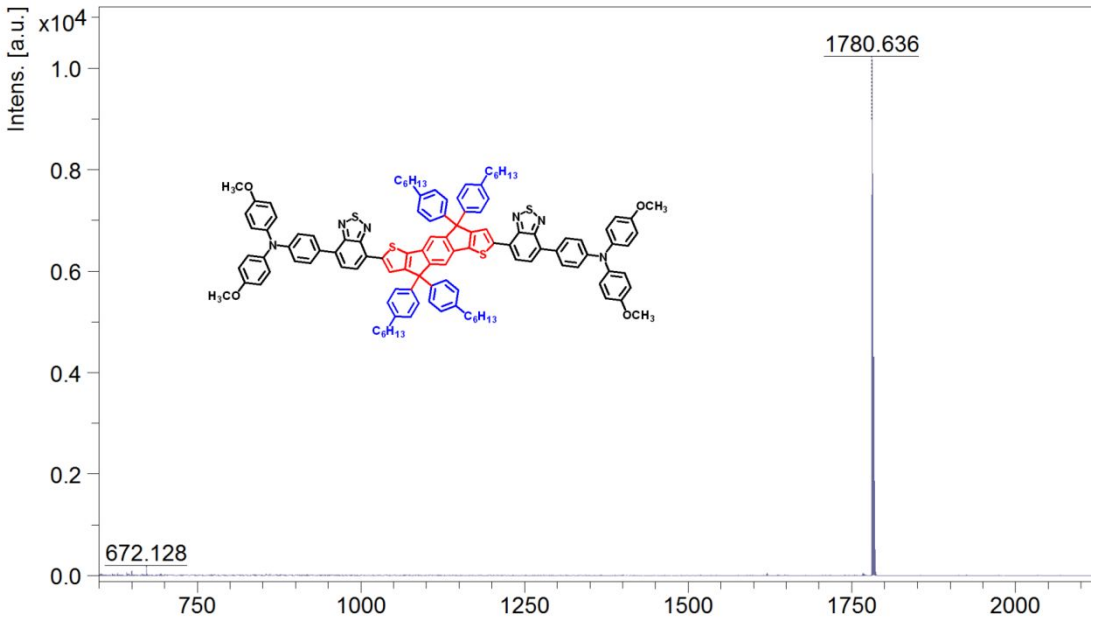

Fig. S8. MALDI-TOF-MS (m/z) spectrometry of **L2**: calcd. for $C_{116}H_{112}N_6O_4S_4$, 1782.45; found: 1780.636.

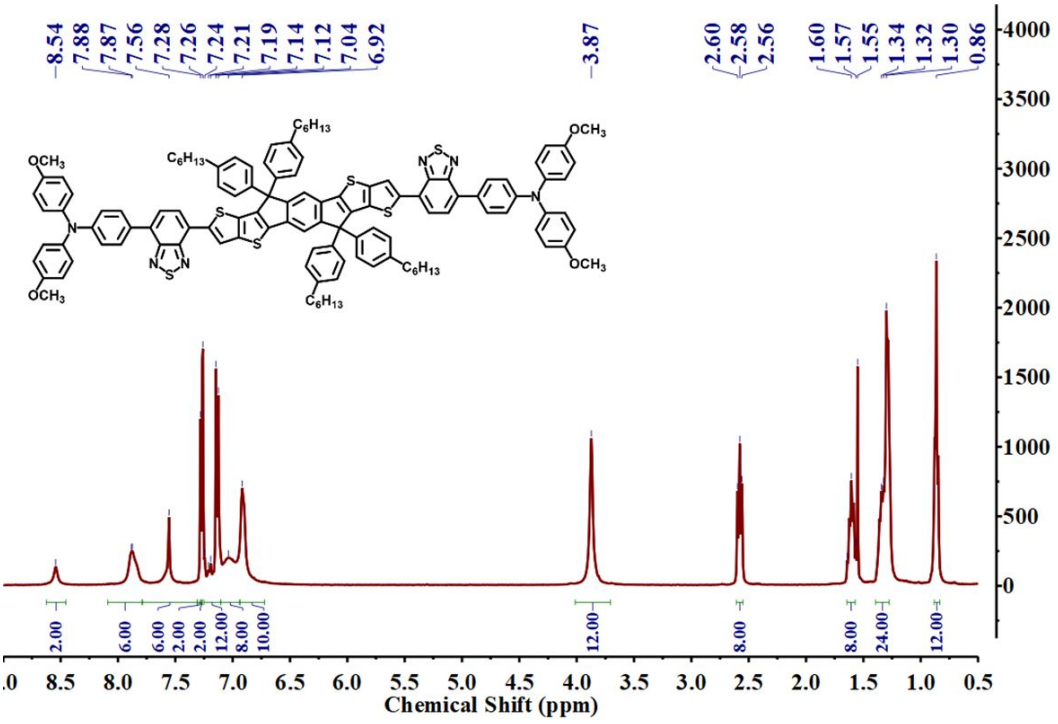

Fig. S9. ^{1}**H NMR** spectrum of **L3**.

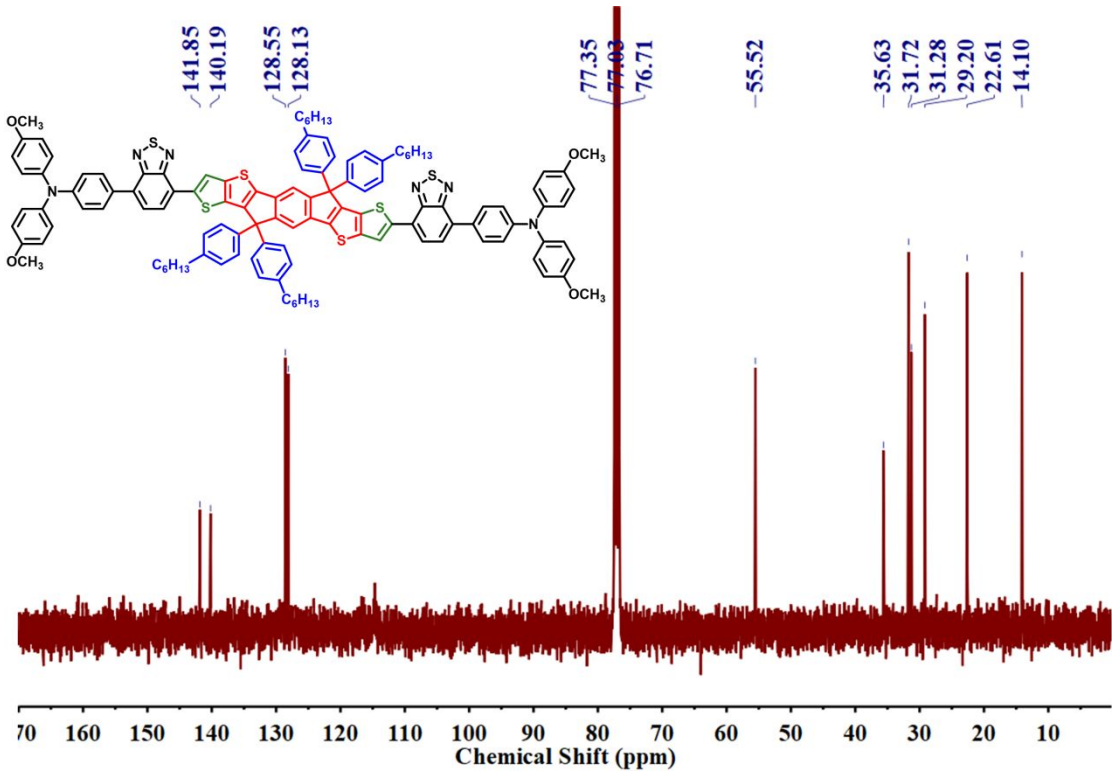

Fig. S10. ^{13}**C NMR** spectrum **L3**.

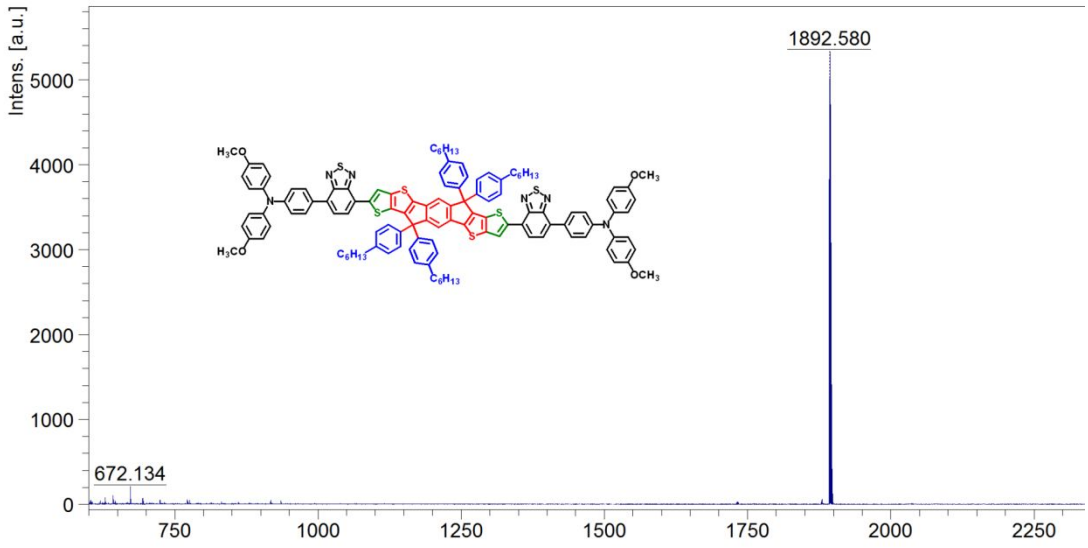

Fig. S11. MALDI-TOF-MS (m/z) spectrometry of **L3**: calcd. for $C_{120}H_{112}N_6O_4S_6$, 1894.61; found: 1892.580.

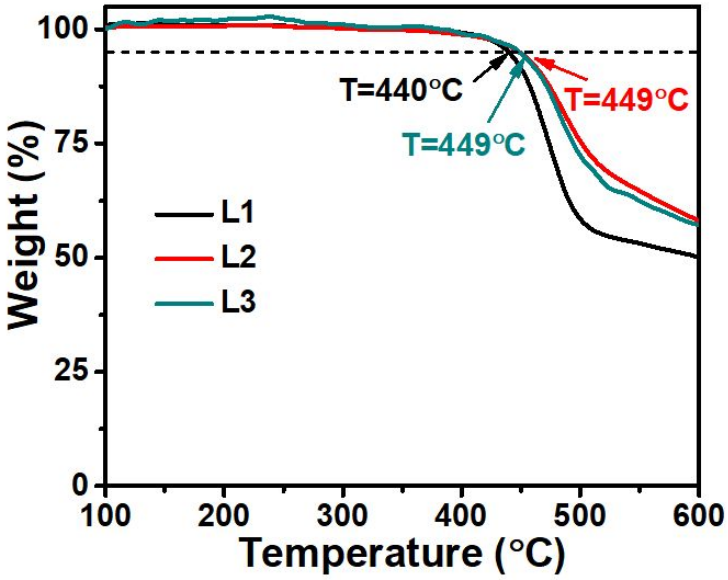

Fig. S12. TGA curves of **L1**, **L2**, and **L3** HTMs. Thermogravimetric analysis (TGA) was performed on a NETZSCH TG 209. Under nitrogen protection, the percentage of sample mass loss was collected at a heating rate of 10 °C/min, and the temperature corresponding to 5% sample mass loss was calculated.

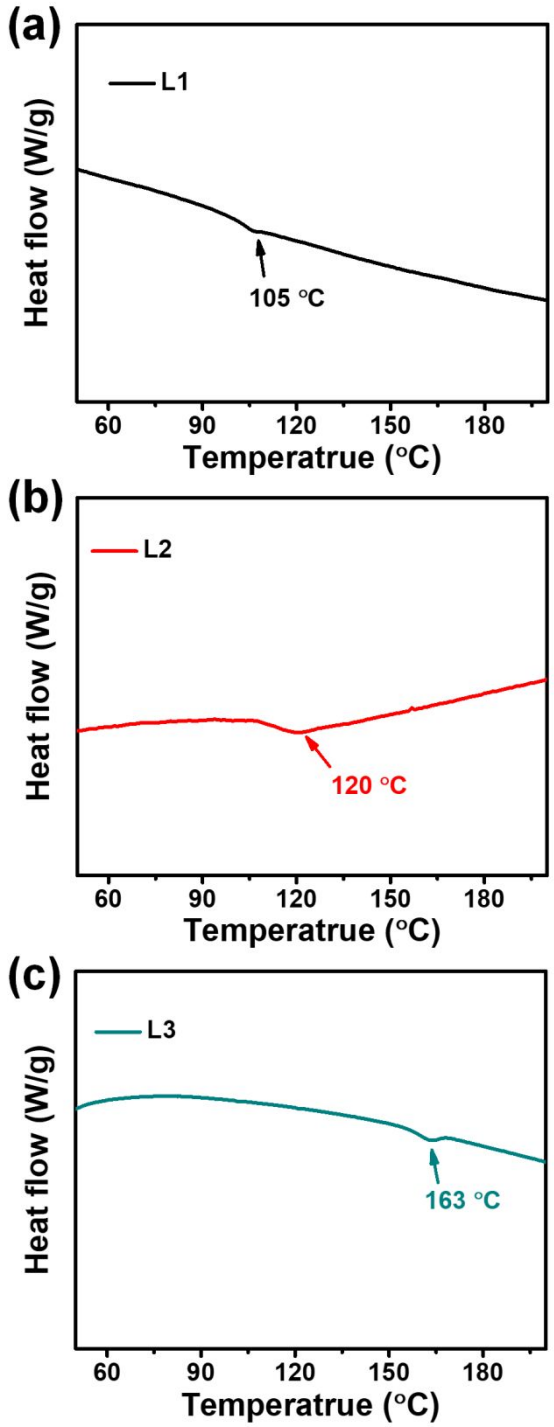

Fig. S13. Differential scanning calorimetry (DSC) curves of (a) **L1**, (b) **L2** and (c) **L3** HTMs. DSC was performed on a Netzsch DSC 200F3 under nitrogen at a heating rate of 10 °C/min to record the heat absorbed or released by the sample, and calculate the melting point of each material. The glass transition temperatures (T_g) of the three molecules are marked in the figure.

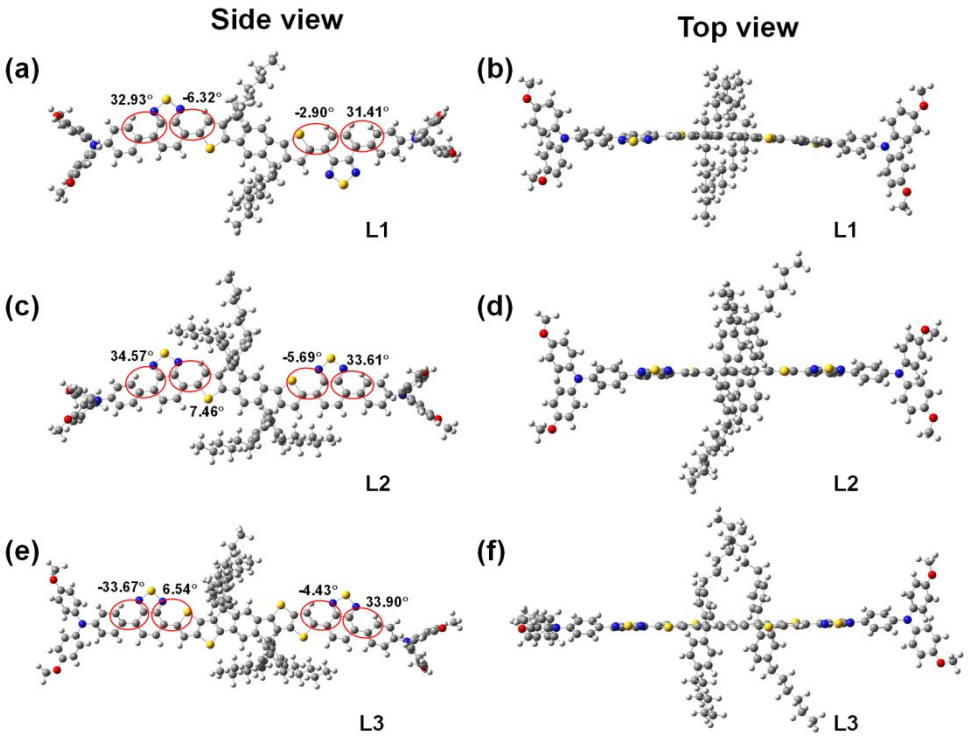

Fig. S14. DFT calculated optimized molecular conformations of **L1**, **L2** and **L3**, respectively. Compared with the **L2**, the torsion angle between the planes of the structural units in the **L3** is smaller, and the shape of **L3** is closer to the plane.

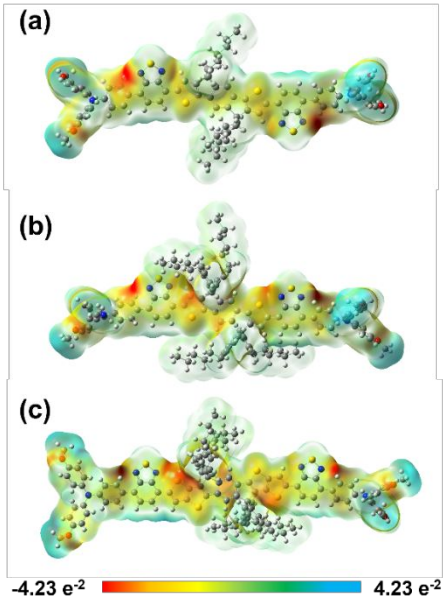

Fig. S15. Electrostatic surface (ESP) potential of (a) **L1**, (b) **L2**, and (c) **L3** molecules. The red and blue colors indicate negative and positive potentials, respectively.

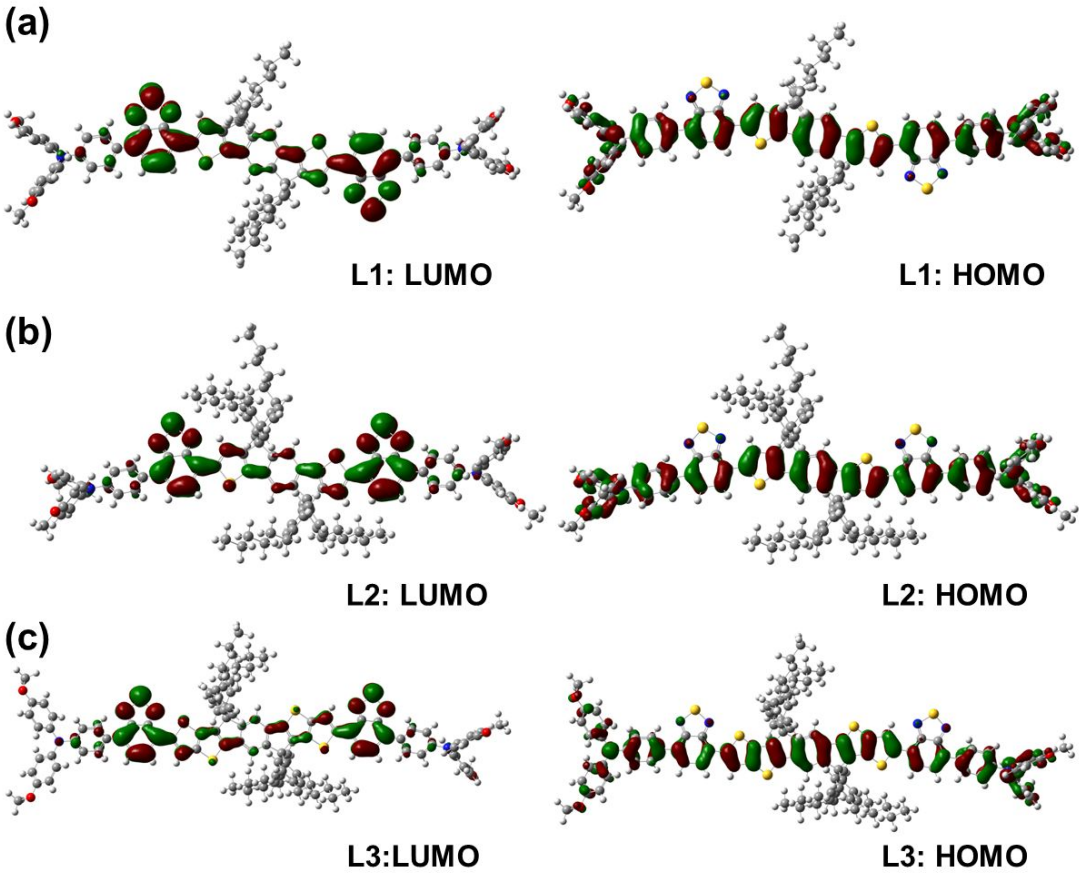

Fig. S16. DFT calculated molecular frontier orbitals of the LUMO and HOMO levels of (a) **L1**, (b) **L2**, and (c) **L3** molecules.

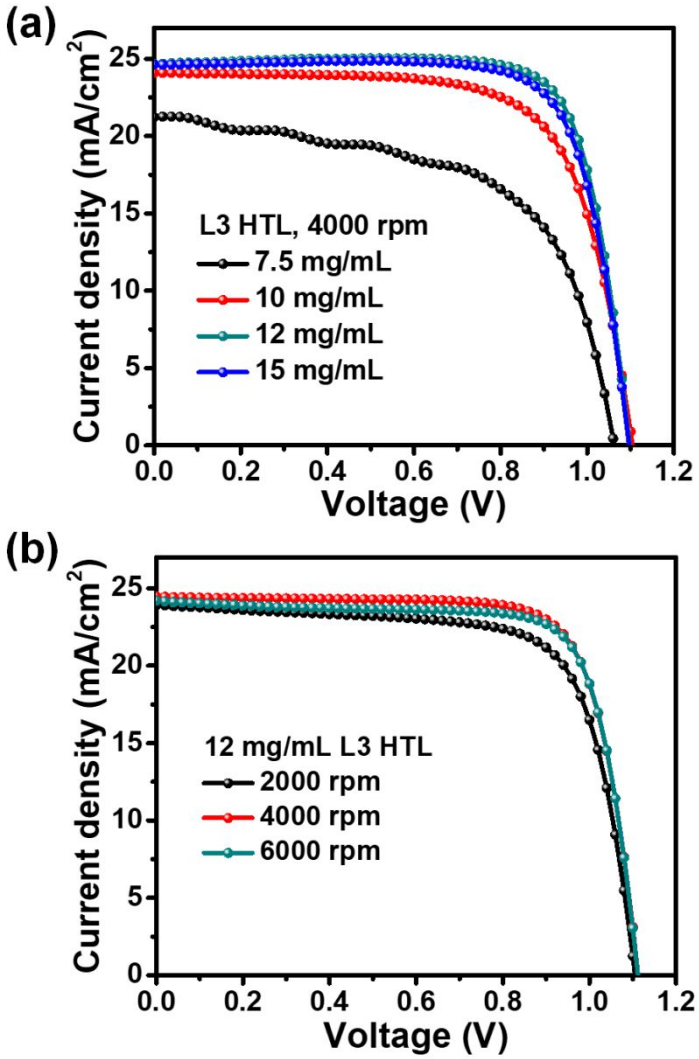

Fig. S17. *J-V* curves of PSCs. (a) different concentration of **L3**, (b) 12 mg/mL **L3** with different speed of spin-coating.

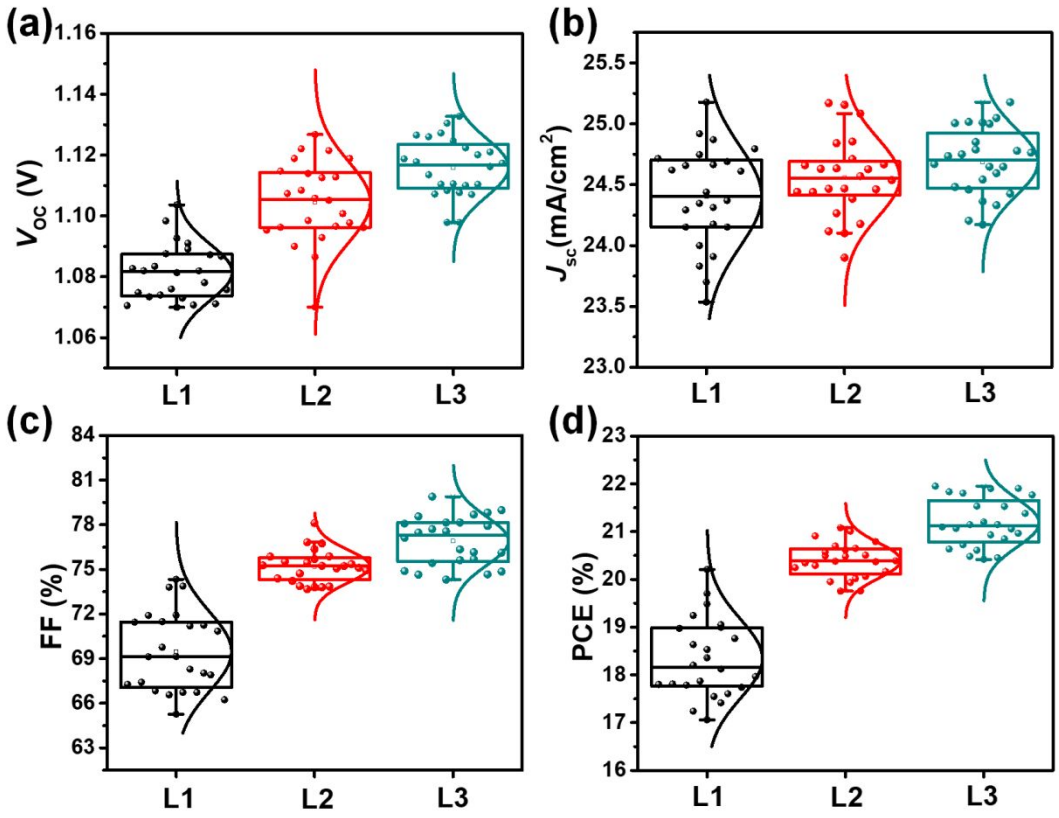

Fig. S18. Histogram of the PSCs with dopant-free HTMs of **L1**, **L2** and **L3**, analyzed from 24 cells. (a) V_{OC}, (b) J_{SC}, (c) FF, and (d) PCE.

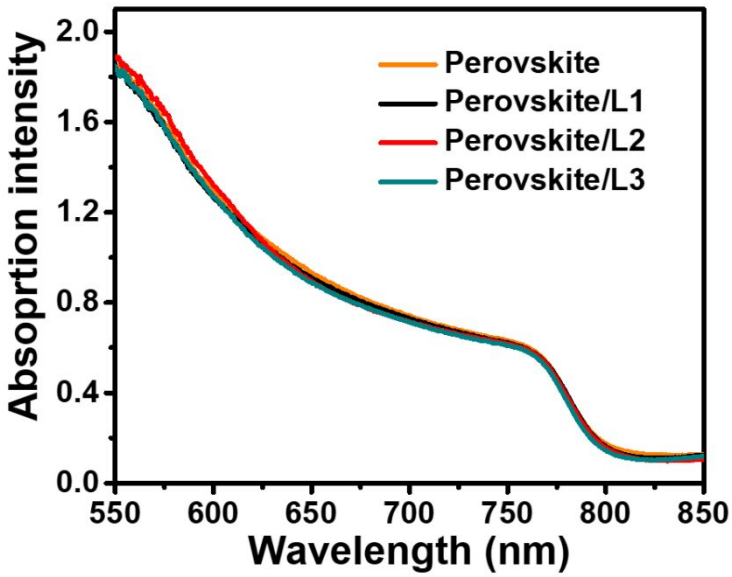

Fig. S19. The absorption spectra of perovskite and perovskite film cover with **L1**, **L2** and **L3** HTL, respectively.

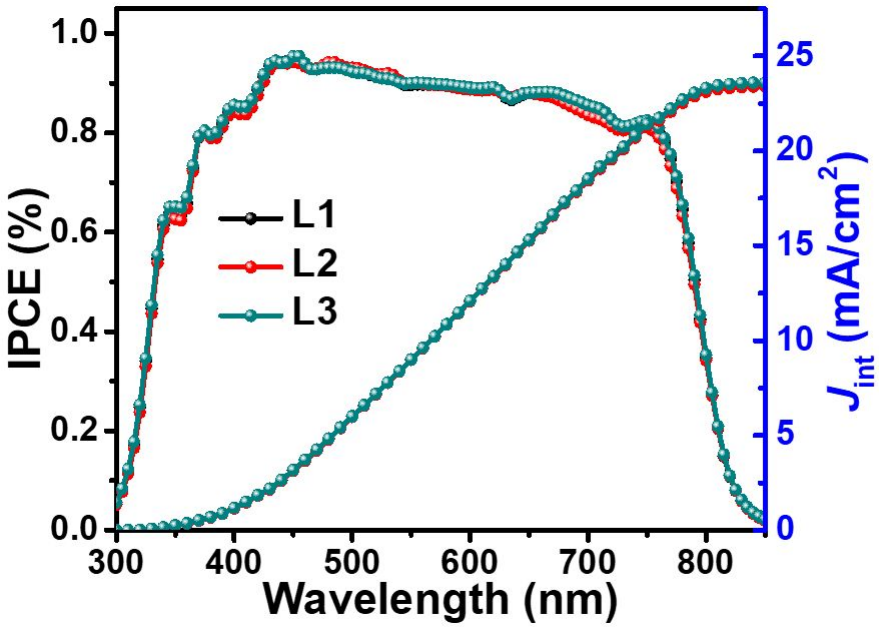

Fig. S20. IPCE curves and integrated J_{SC} of the best PSC with **L1**, **L2**, and **L3**, respectively.

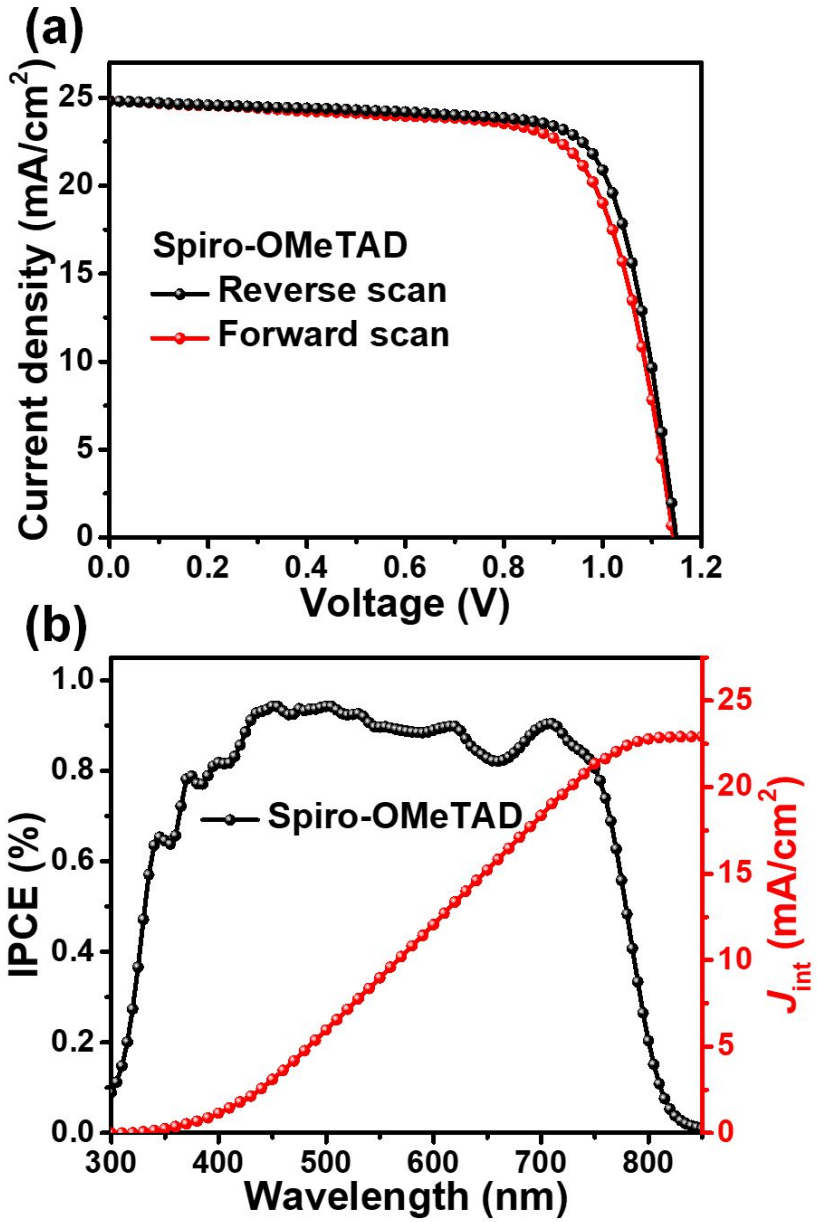

Fig. S21. (a) *J-V* curves and (b) IPCE spectra of PSC with doped **spiro-OMeTAD** HTL

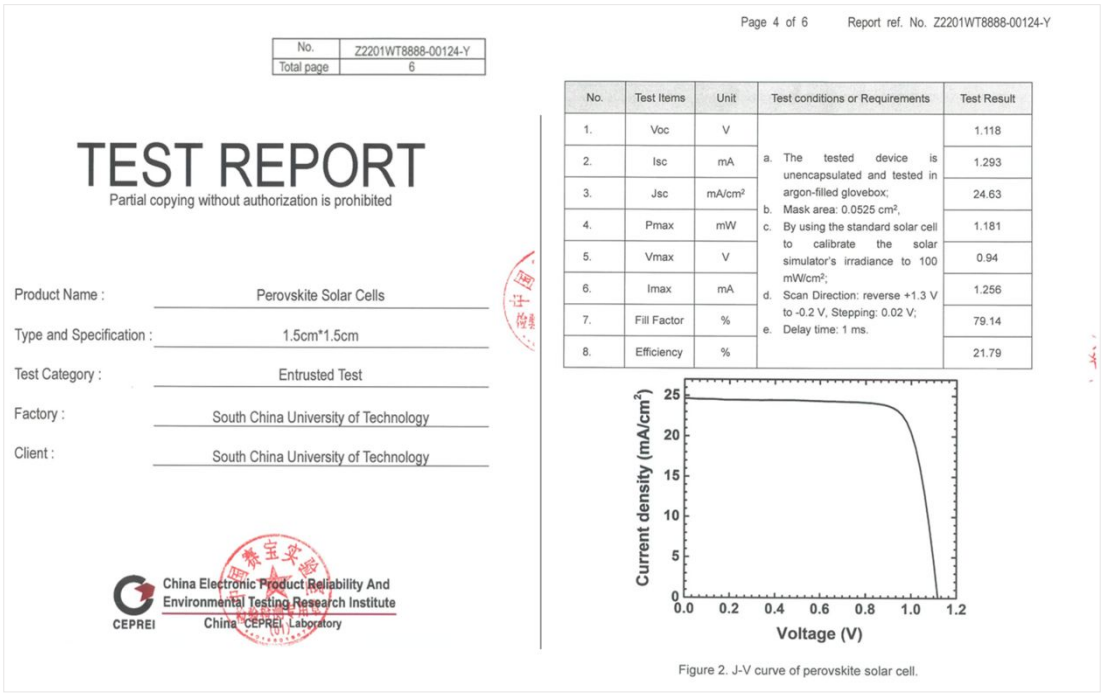

Fig. S22. The certified result of a perovskite solar cell measured by China CEPREI Laboratory. The device achieved V_{OC} of 1.12 V, a J_{SC} of 24.63 mA/cm^2 and an FF of 79.14% and a PCE of 21.79% with a mask area of 0.0525 cm^2.

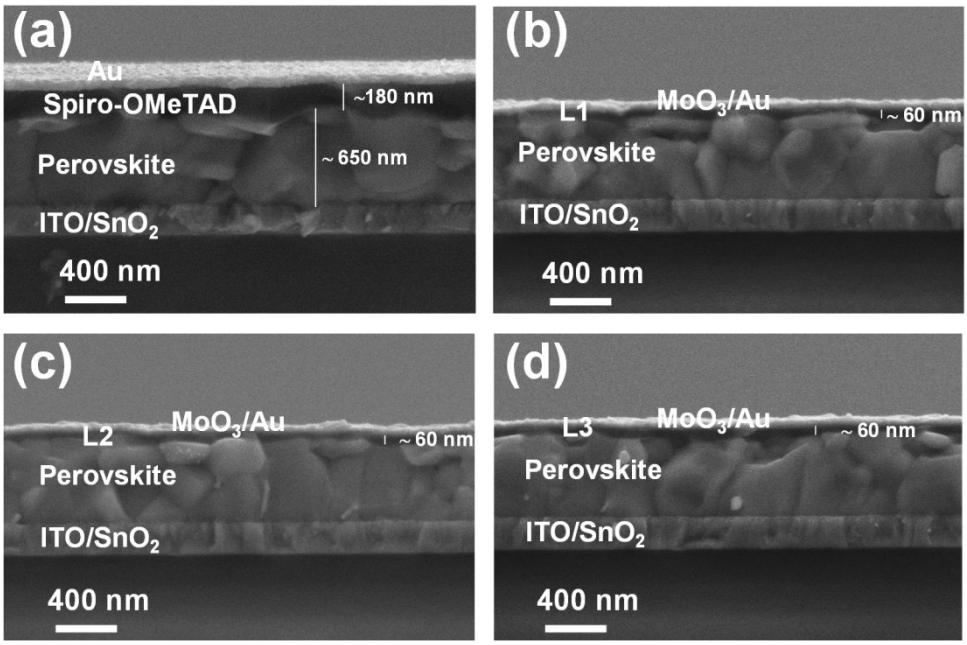

Fig. S23. Across-section SEM images of full PSCs. (a) PSC with doped **spiro-OMeTAD** HTM, (b) PSC with **L1** HTM, (c) PSC with **L2** HTM, and (d) PSC with **L3** HTM.

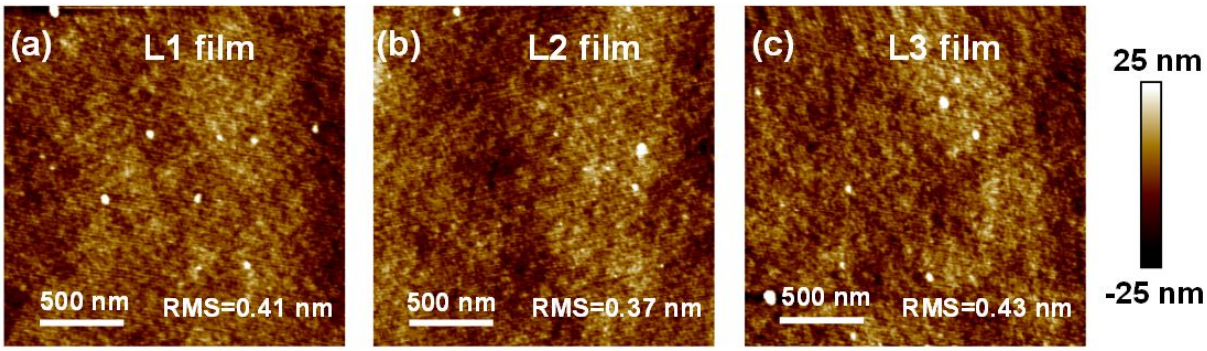

Fig. S24. AFM images of (a) **L1** film, (b) **L2** film and (c) **L3** film. All the HTM films were deposited on silicon wafer substrate.

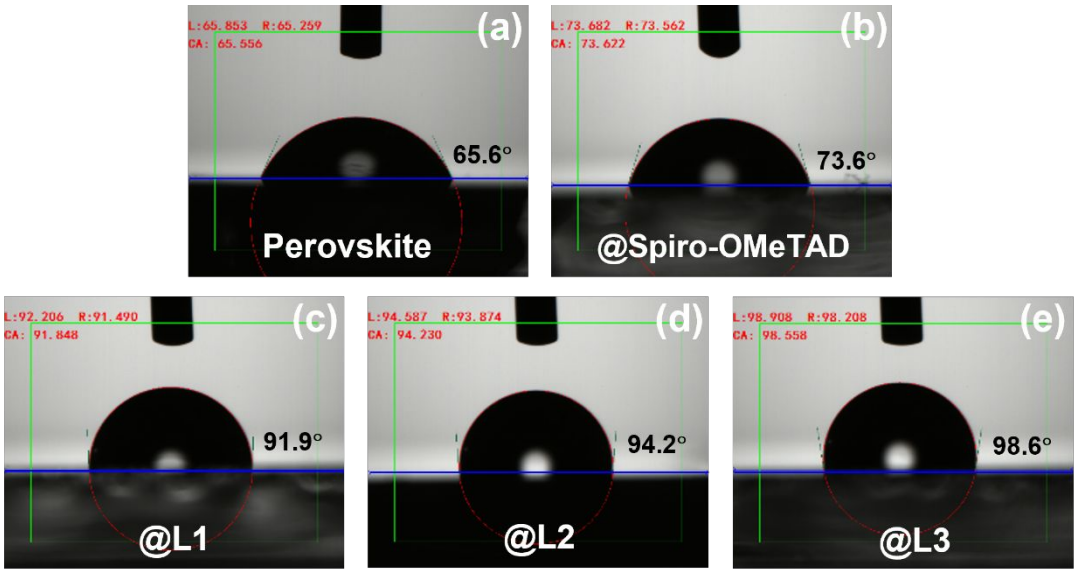

Fig. S25. The images of water contact angle of various surfaces: (a) perovskite film, (b) perovskite film with doped **spiro-OMeTAD** HTL (c) perovskite film with **L1** HTL, (d) perovskite film with **L2** HTL, and (e) perovskite film with **L3** HTL.

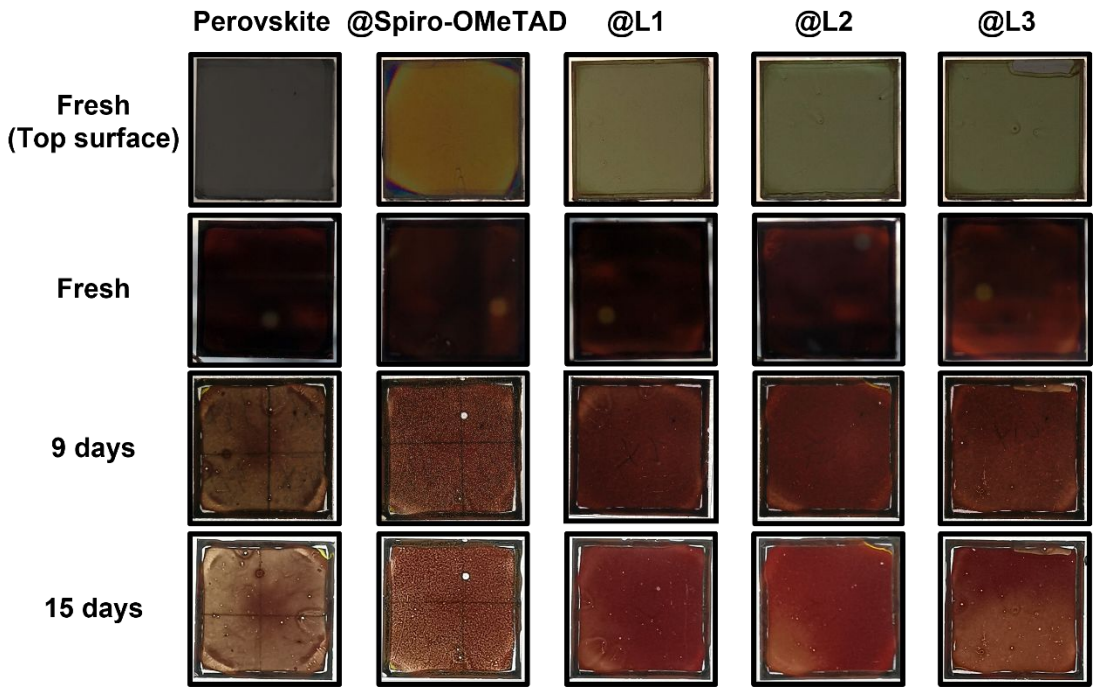

Fig. S26. The degradation images of the perovskite film with different HTL (glass/ITO/SnO_2/perovskite/HTM) under ambient atmosphere with RH=50-60%.

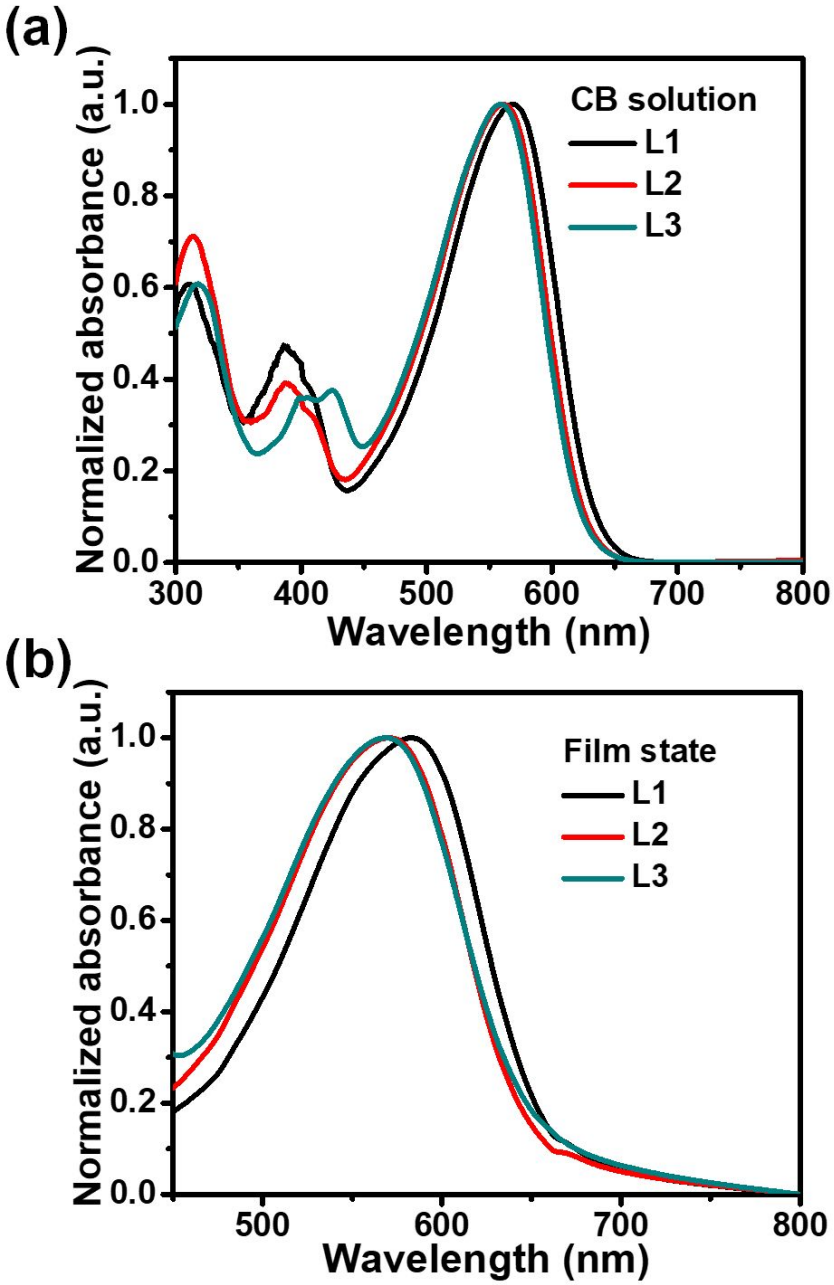

Fig. S27. Normalized UV-Vis absorption spectra of the HTMs in (a) CB solution and (b) film state.

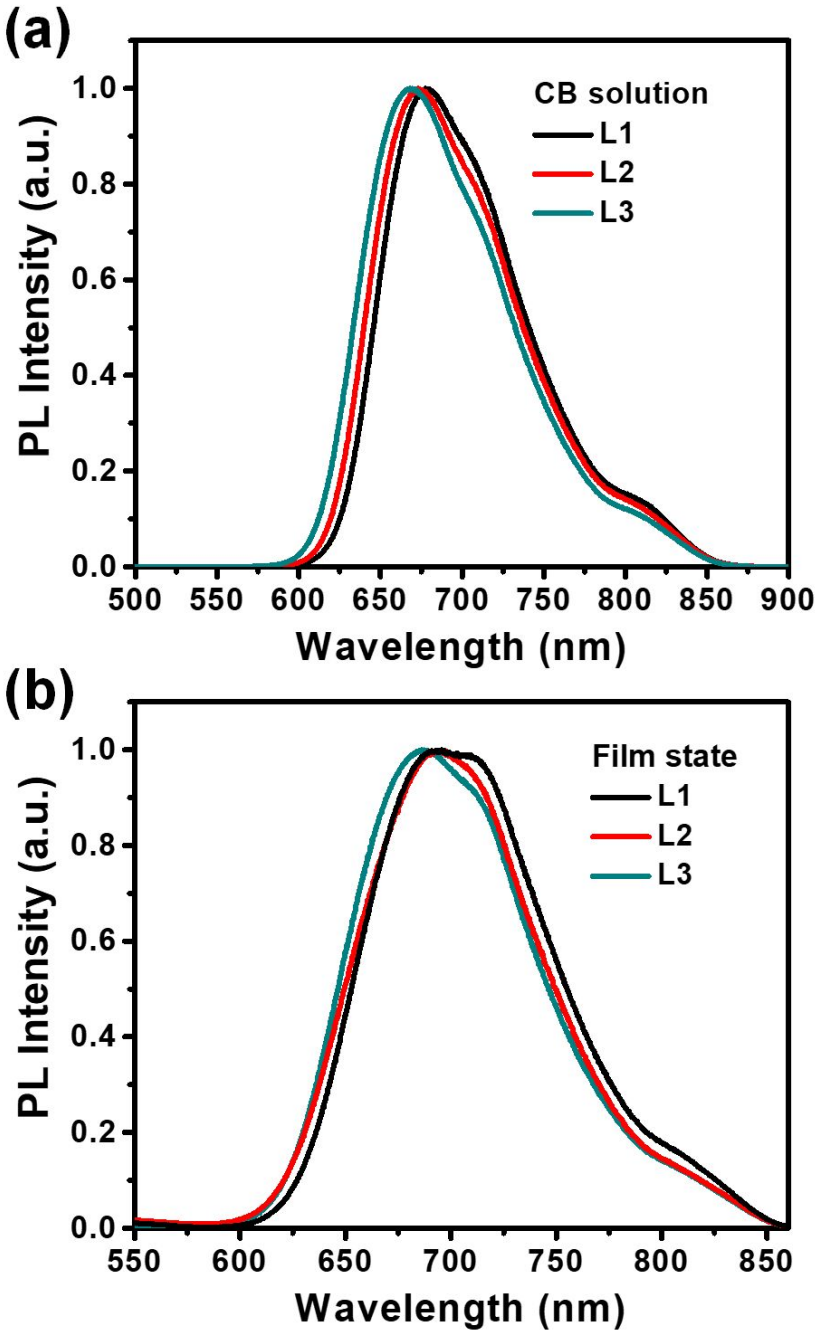

Fig. S28. Steady-state PL of **L1**, **L2** and **L3** HTMs. (a) solution state and (b) film state.

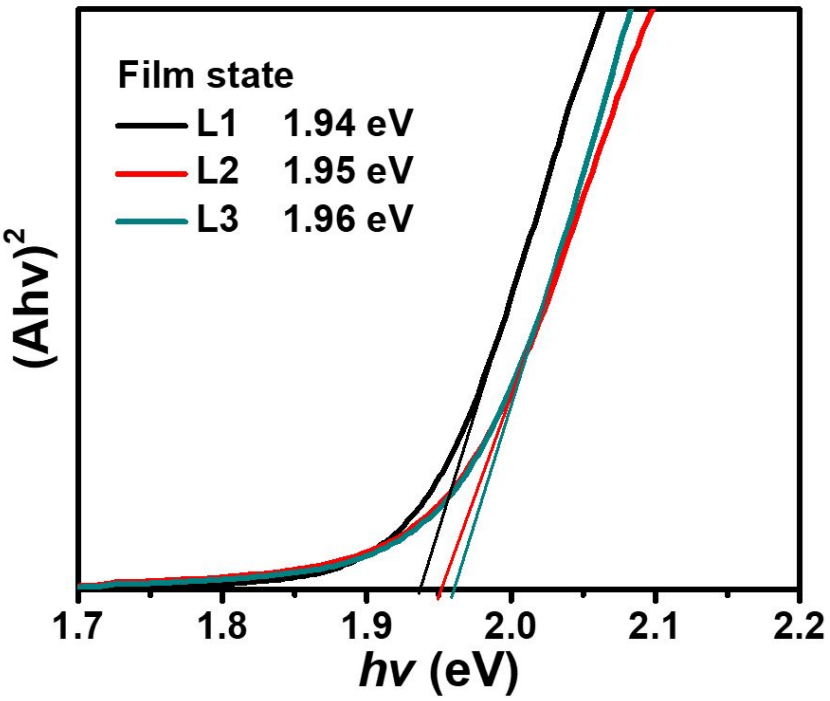

Fig. S29. Tauc plots of **L1**, **L2** and **L3** film.

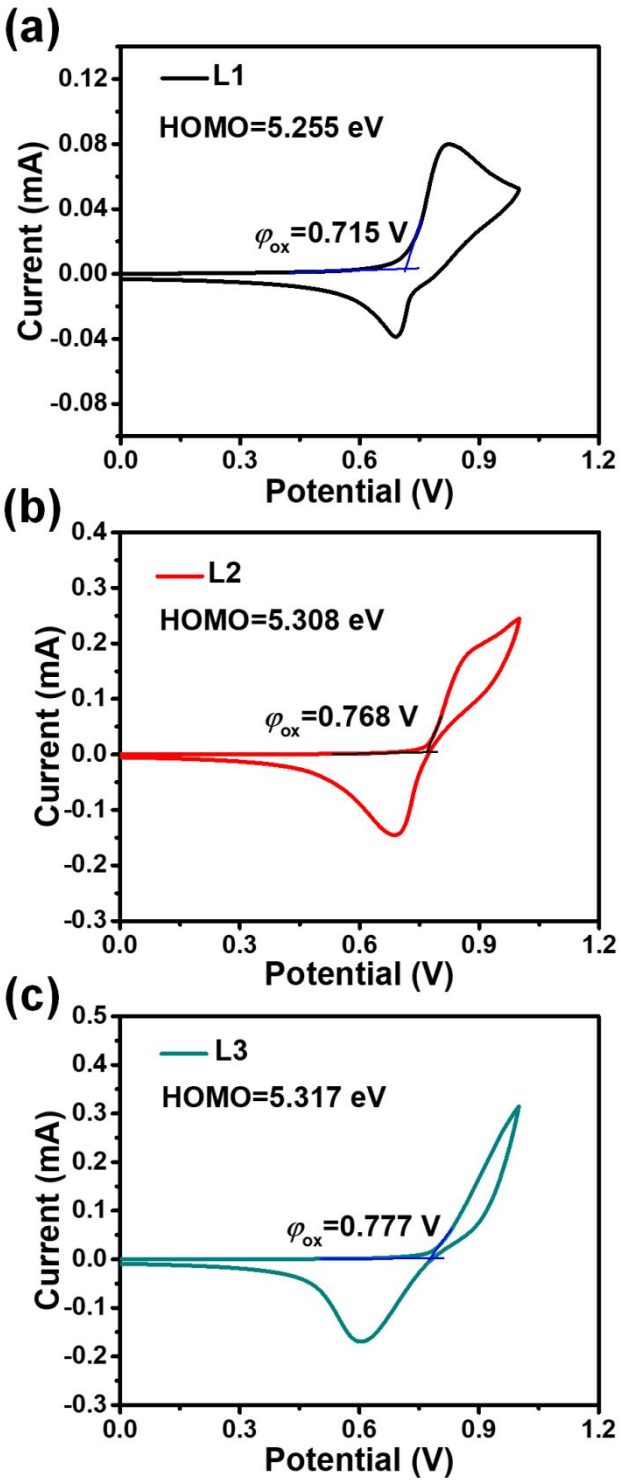

Fig. S30. Cyclic voltammograms of (a) **L1**, (b) **L2** and (c) **L3** film. With the saturated calomel electrode (SCE) as the reference electrode, the energy level of the molecules was calculated according to the equation: E_{HOMO}=-(4.8+E_{ox}-E_f) (eV), where E_{ox} is the initial oxidation potential, E_f is 0.26. The calculated HOMO levels of **L1**, **L2** and **L3** are -5.255, -5.308 and -5.317 eV, respectively.

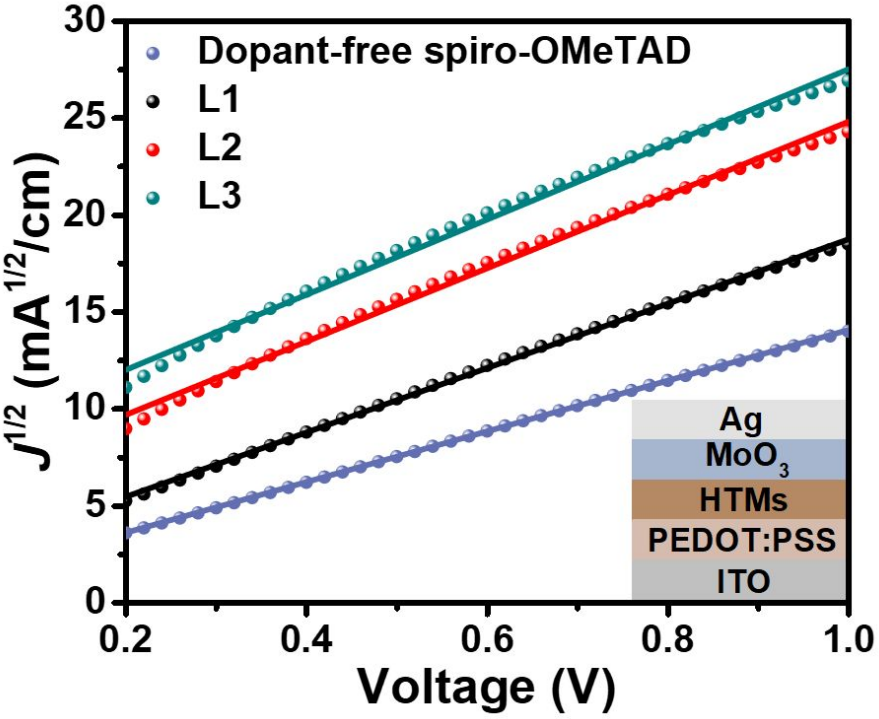

Fig. S31. *J-V* curves of hole-only ITO/PEDOT:PSS/HTM/MoO_3/Ag devices.

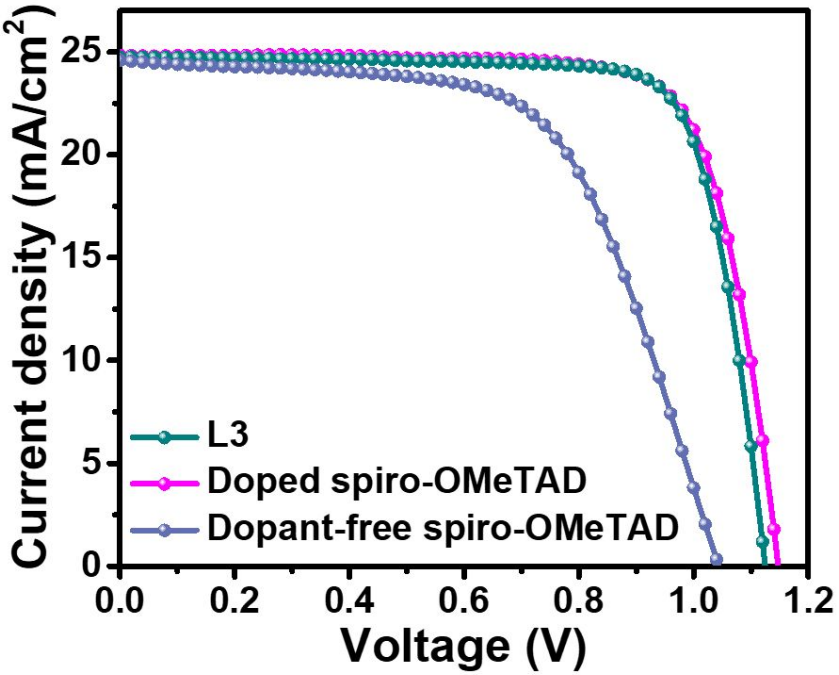

Fig. S32. *J-V* curves of PSCs with doped **spiro-OMeTAD**, dopant-free **spiro-OMeTAD** and **L3** HTM.

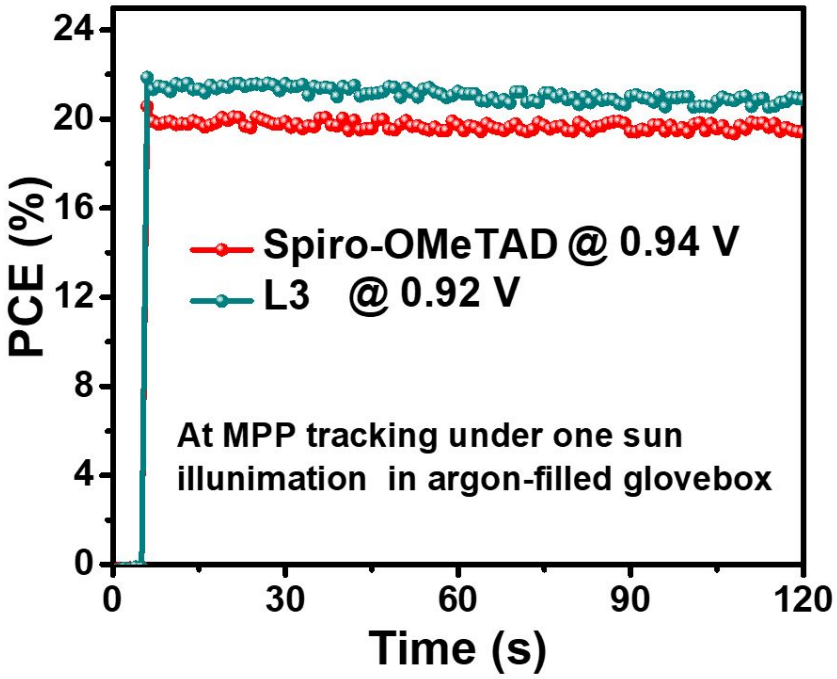

Fig. S33. Stable power output of the best devices with doped **spiro-OMeTAD** and dopant-free **L3** HTL.

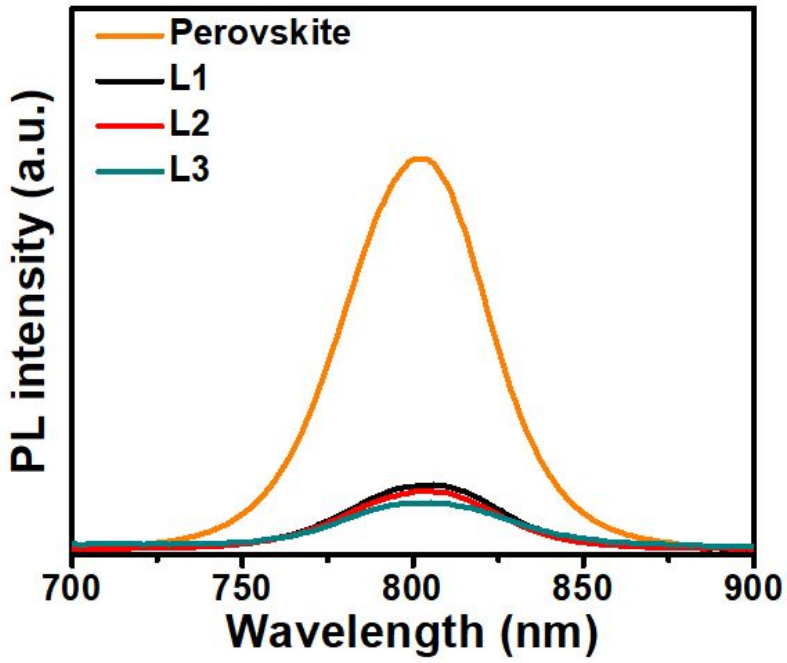

Fig. S34. Steady-state PL of perovskite film and perovskite film covered with **L1**, **L2** and **L3**, respectively.

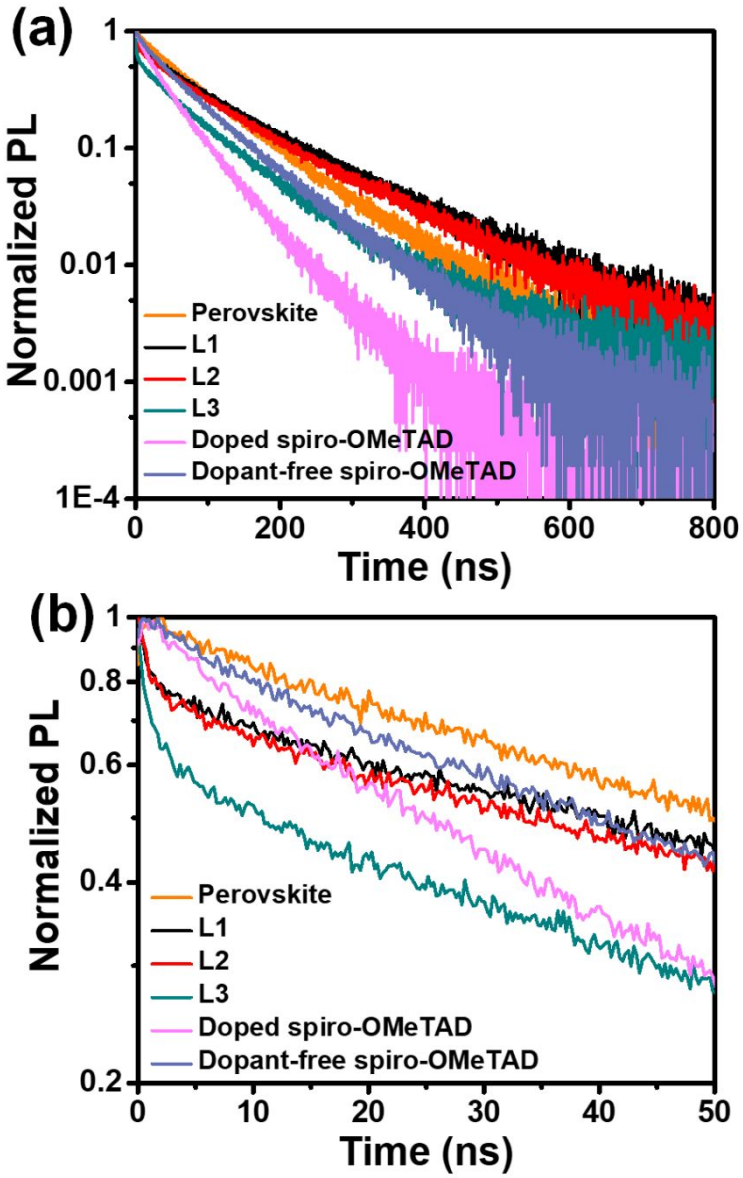

Fig. S35. (a) Time-resolved PL of the perovskite film cover with doped **spiro-OMeTAD**, dopant-free **spiro-OMeTAD** and **L1-3** HTM. (b) Zoom-in to Fig. S36a.

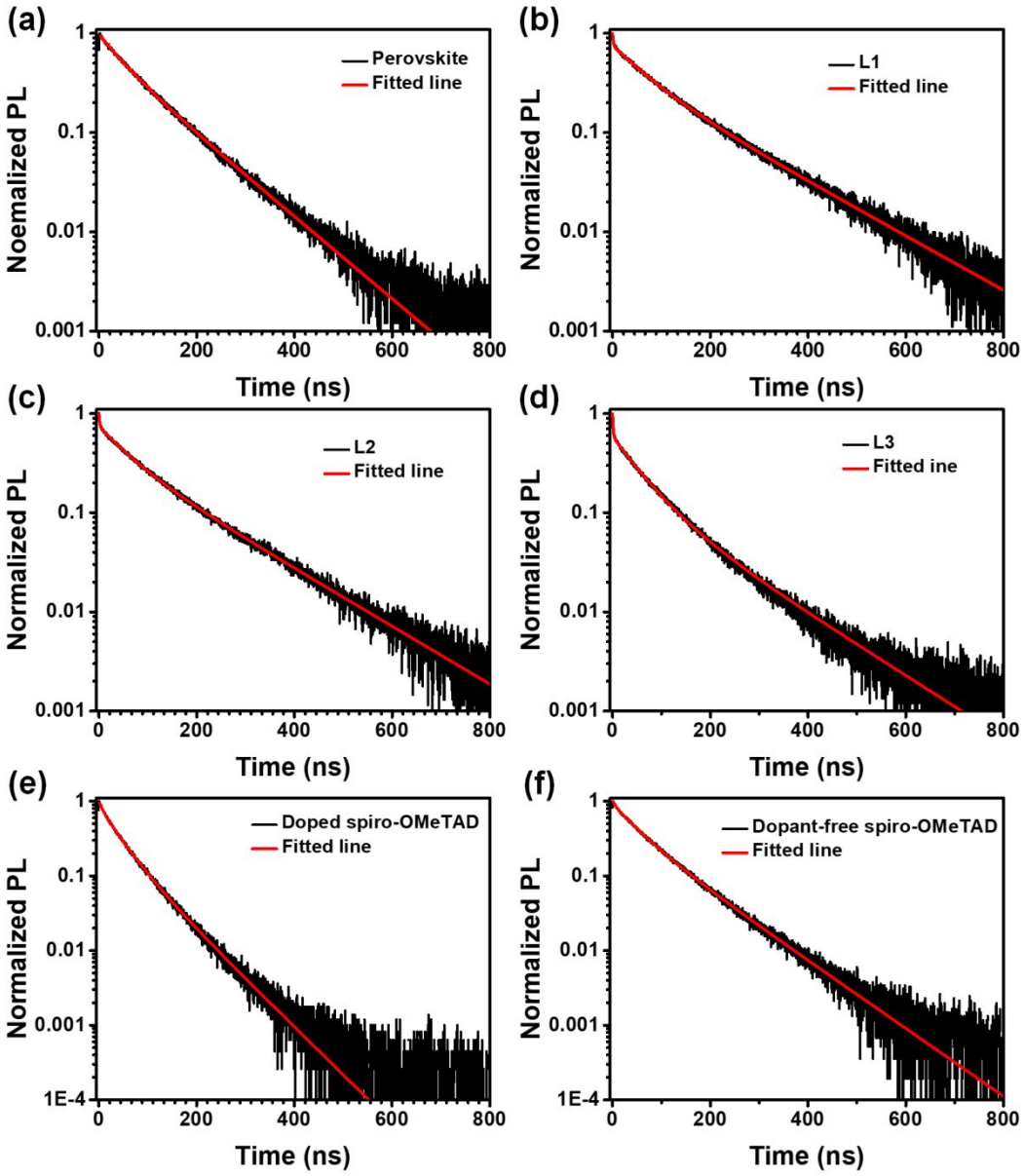

Fig. S36. (a) Time-resolved PL of the perovskite film cover with doped **spiro-OMeTAD**, dopant-free **spiro-OMeTAD** and **L1-3** HTM. (a) bare perovskite film, (b) perovskite film with **L1** HTM, (c) perovskite film with **L2** HTM, (d) perovskite film with **L3** HTM, (e) perovskite film with doped **spiro-OMeTAD** HTM, (f) perovskite film with dopant-free **spiro-OMeTAD** HTM. The corresponding TRPL curves were also fitted by triple-exponential functions (no physical model before, arbitrary choice to better fit the data to help with the differential lifetime evaluation), which includes a fast component (lifetime τ_1, and weight fraction A_1) and an intermediate component (lifetime τ_2, and weight fraction A_2), an slow component (lifetime τ_3, and weight

fraction A_3), presumably corresponding to the quenching process of photogeneration of free carriers of perovskite through charge extraction from the perovskite to the HTLs, radiative recombination in the perovskite film, and passivation effects by functional group, respectively for L-series films. The fit for perovskite film is directly transformed to bi-exponential function due to convergence. The additional decay of spiro-based film may be assigned to trap-mediate recombination.

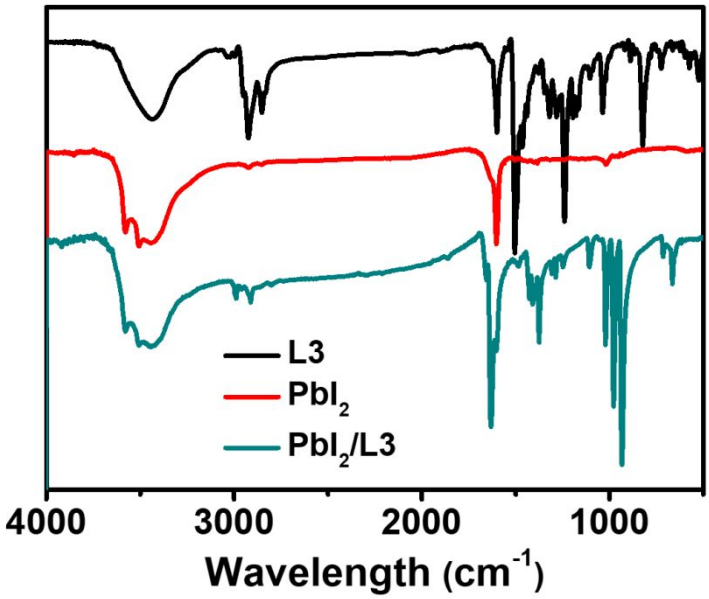

Fig. S37 Full FTIR spectra of the powders of L3, PbI_2 and PbI_2/L3 blend. The PbI_2/L3 sample was mixed PbI_2 solution and L3 solution directly, then the powder was dried at 80 °C for eight hours.

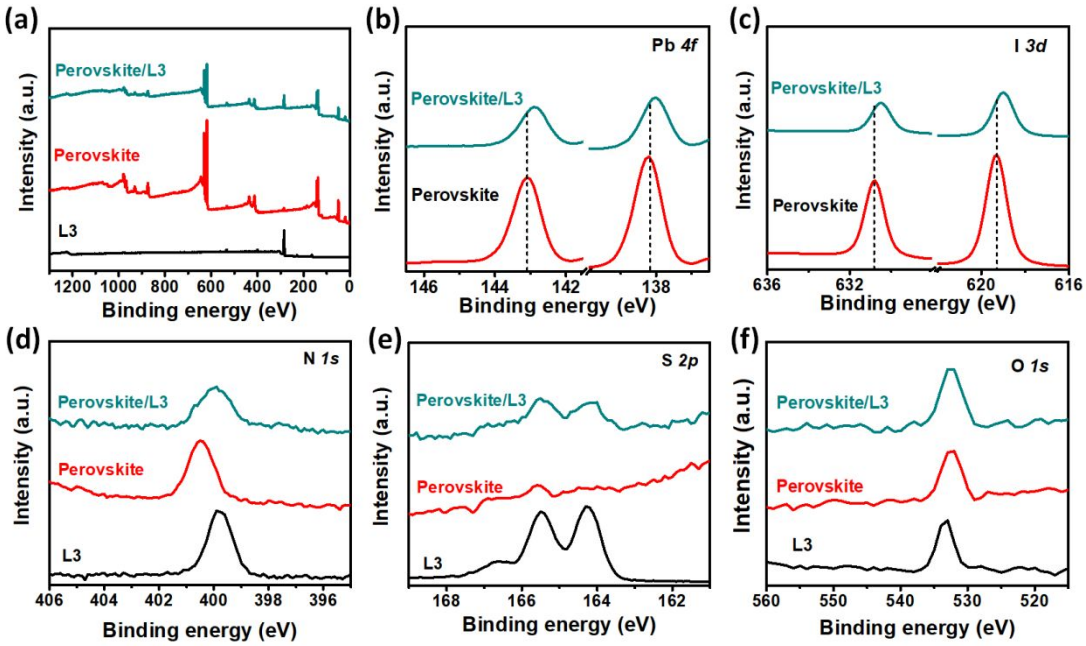

Fig. S38 The XPS spectrum of the perovskite film, L3 film, and perovskite/L3 film. (a) full spectrum, (b) Pb 4f, (c) I 3d (d) N 1s (e) S 2p and (f) O 1s.

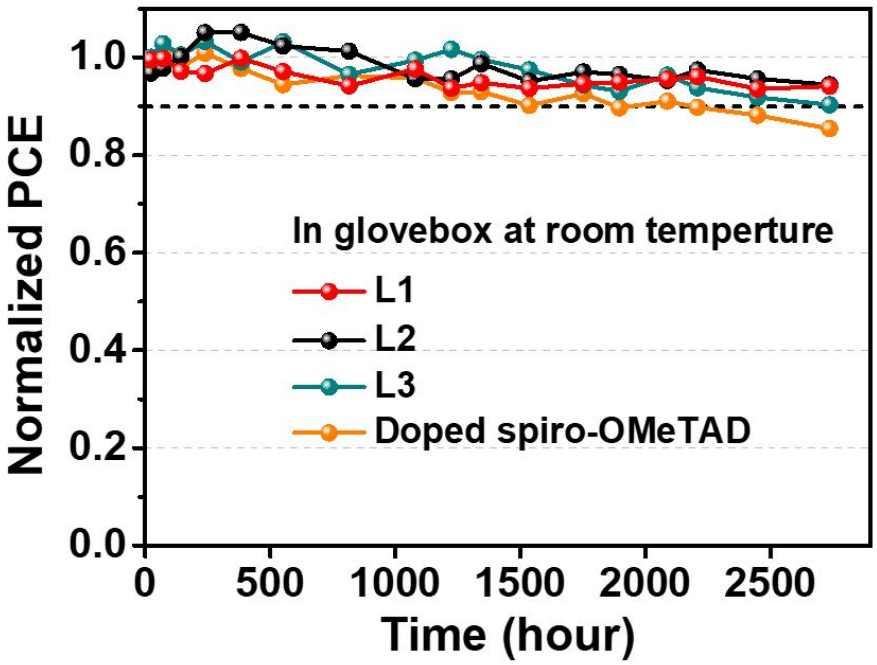

Fig. S39 Long-term stability of unencapsulated control PSC (doped spiro-OMeTAD) and dopant-free L-series PSC stored at argon-filled glovebox.

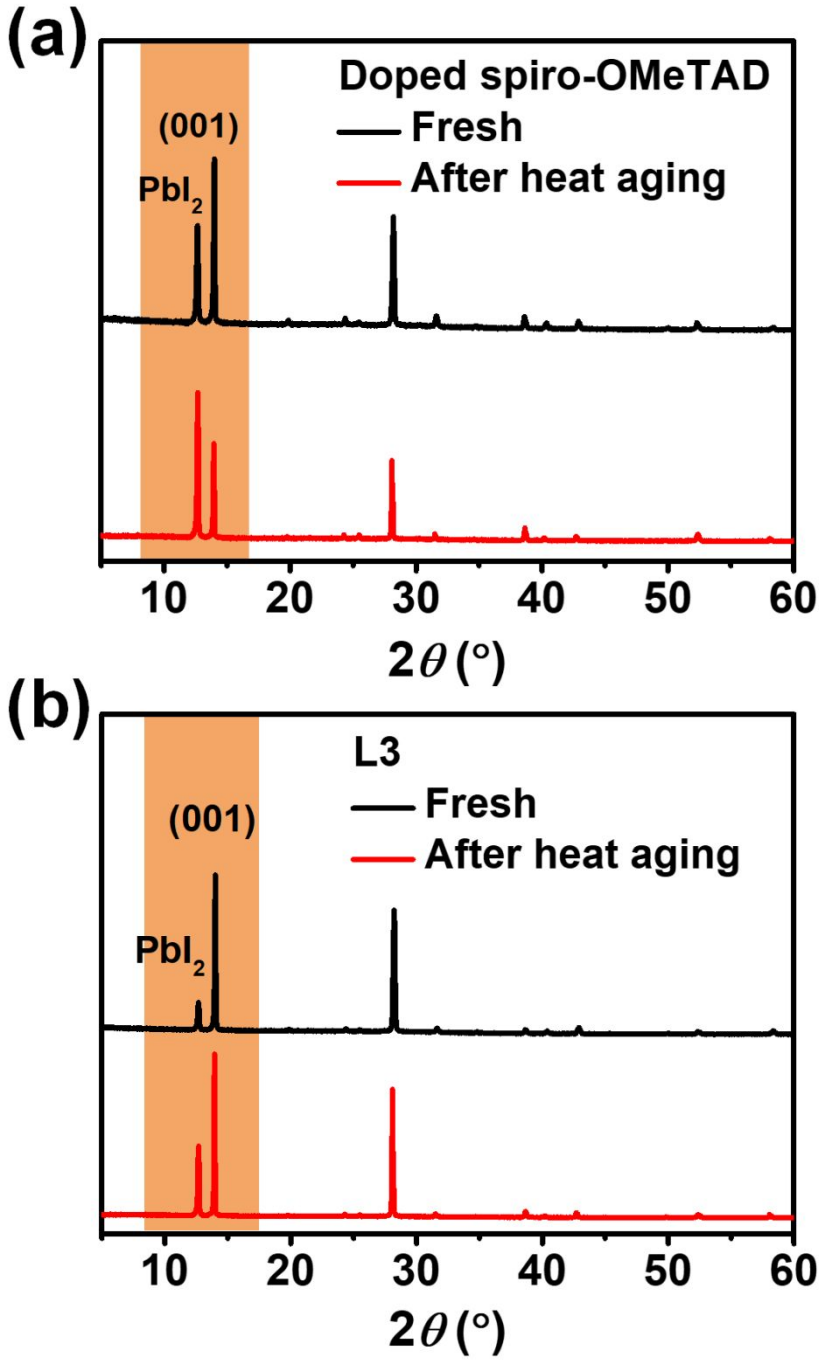

Fig. S40 XRD patterns for doped spiro-OMeTAD perovskite film and L3-perovskite film before and after 85°C aging for 10 days in the argon.

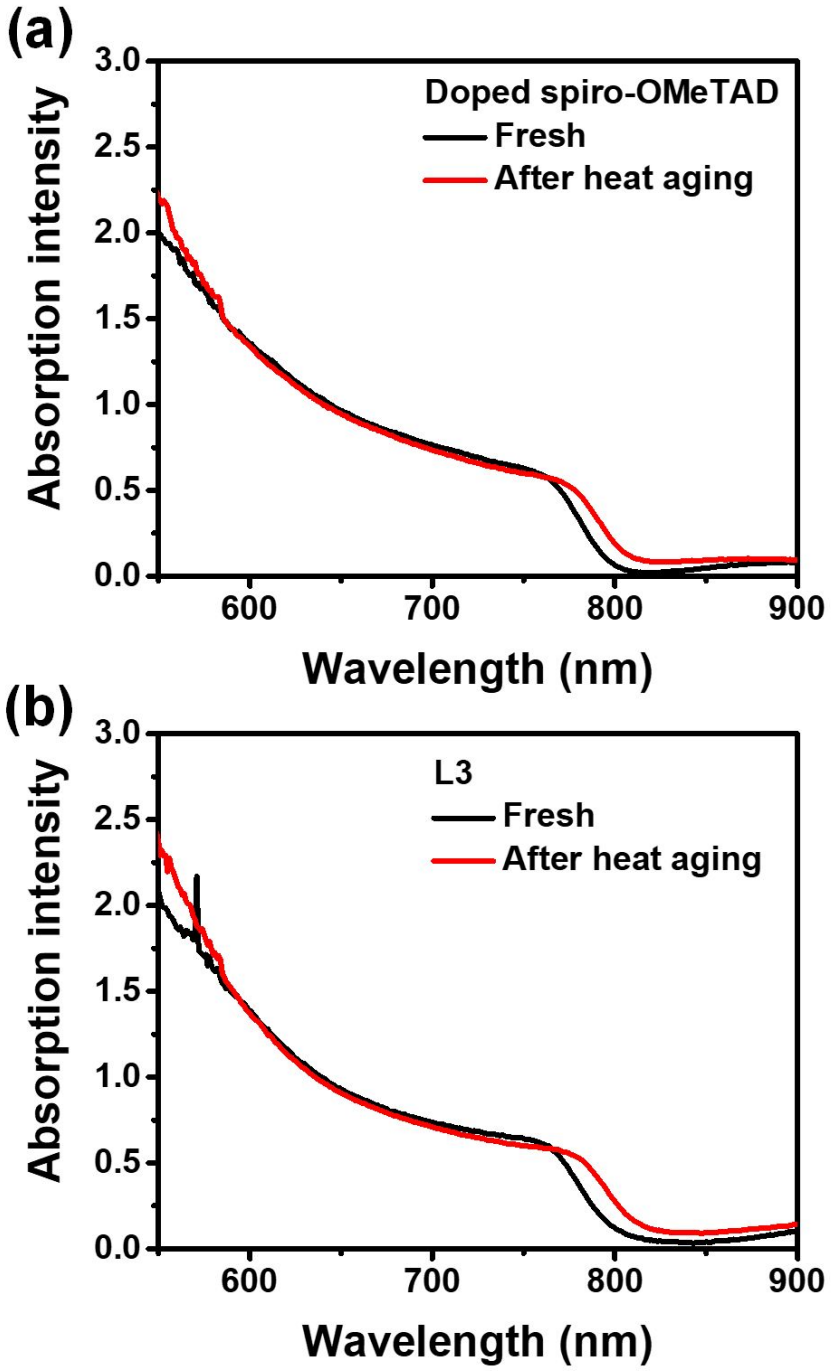

Fig. S41 The absorption spectra of perovskite film coved with doped spiro-OMeTAD and L3 HTL before and after 85°C aging for 10 days in the argon. (a) doped spiro-OMeTAD HTL, (b) L3 HTL.

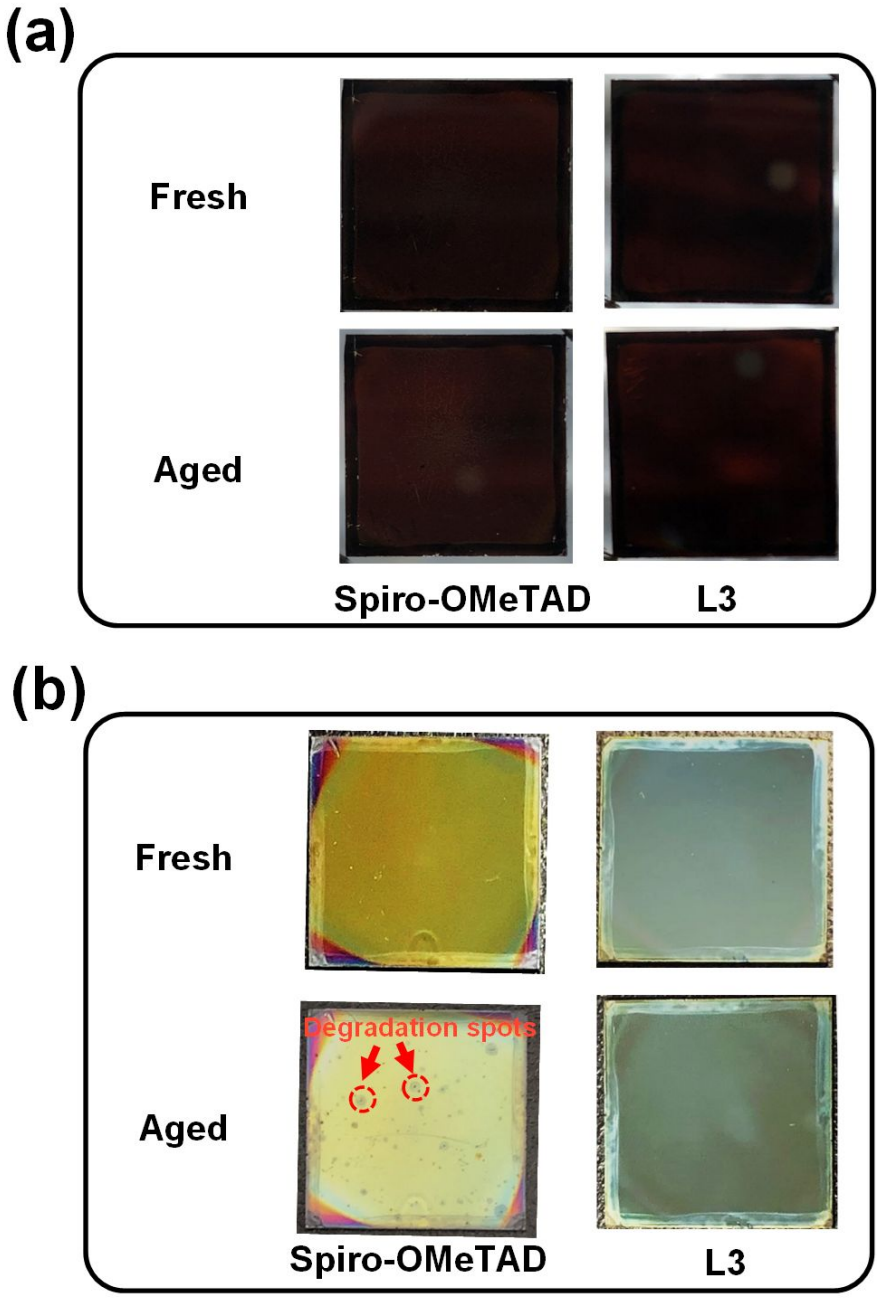

Fig. S42. Photo images for perovskite film with doped spiro-OMeTAD HTL and L3 HTL before and after 85°C aging for 10 days in the argon. (a) glass side, (b) top side.

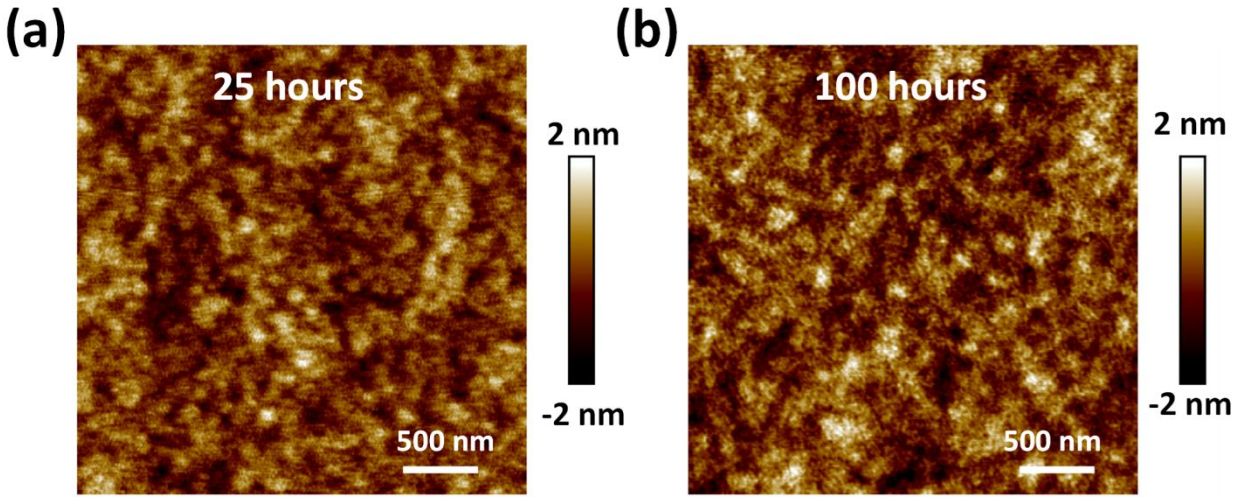

Fig. S43 AFM images of L3 HTMs on ITO substrates, the aging condition is 100°C for (a) 25 hours and (b) 100 hours on the hotplate in N_2-filled glovebox.

Table S1. Summary of thermal stability (at 85°C or MPP tracking at over 70°C) of the state-of-the-art p-i-n and n-i-p PSCs.

Journal	Structure	Stability	Ref.
p-i-n PSCs			
Science	FTO/poly-TPD/$Cs_{0.17}FA_{0.83}Pb(I_{1-x}Br_x)_3$/PCBM/BCP/Cr/Cu	Under full-spectrum sunlight **at 85°C** in ambient air, encapsulated, T_{95}=1200 h.	13
Nat. Energy	ITO/PTAA/perovskite/C_{60}/BCP/Cu	**T=85°C**, T_{90}=1020 h	14
Science	ITO/P3CT-N/$(FAPbI_3)_{0.95}(MAPbBr_3)_{0.05}$/PCBM/$C_{60}$/TPBi/Cu	**T=85°C,** maintained 91.8% for >2200 h.	15
Energy Environ. Sci.	ITO/p-PY/perovskite/PCBM/BCP/Ag	**T=85°C**, maintained over 94% for 500 h, **T=120°C,** maintained over 81% for 200 h.	16
Science	ITO/PTAA/perovskite/C_{60}/BCP/Ag	**Damp heat test (85°C/85%)**, T_{95}>1000 h,	17
Science	ITO/2PACz/3D-perovskite/2D-perovskite/C_{60}/BCP/Ag	**Damp heat test (85°C/85%)**, T_{95}>1200 h.	18
Nature	FTO/NiO/perovskite/PCBM/BCP/Cr/Cr_2O_3/Au	Full spectrum sunlight at **70 to 75°C,** encapsulated, T_{95}=1800 h.	19
n-i-p PSCs			
Joule	FTO/TiO_2/ZrO_2/5AVA$_X$MAPbI$_{1-3}$/carbon	**Damp heat test (85°C/85%**), 1100 h without decay; T=55°C, 9,000 h operational tracking without obvious decay	20
Nat. Energy	FTO/SnO_2/3D:SIG-2D/P3HT/Au	**Damp heat test (85°C/85%),** T_{95}=1056 h	21
Science	ITO/c-TiO_2/TiO_2 nanorods/PMMA:PCBM/$Cs_{0.05}FA_{0.88}MA_{0.07}PbI_{2.56}Br_{0.44}$/PMMA/P3HT:CuPc/Au	**Damp heat test (85°C/85%)**, retained ~95.3% of for >260 h.	22
Science	ITO/SnO_2/3D Perovskite/2D perovskite /spiro-OMeTAD/Au	**T=85°C**, T_{80}=500 h	23
Science	FTO/compact-TiO_2/ mp-TiO_2/perovskite/Spiro-OMeTAD/Au	**T=85°C**, RH=15-25%, T_{80}=1300 h	24

Table S2. Summary of recent developments of doping-free molecule HTMs in *n-i-p* PSCs.

HTM	Perovskite	V_{oc} (V)	J_{sc} (mA/cm^2)	FF (%)	PCE (%)	*Tg* (°C)	Atmosphere	Thermal stability	Publish data	Ref.
Polymer HTMs										
asy-PBTBDT	$Cs_{0.05}FA_{0.81}MA_{0.14}PbI_{2.55}Br_{0.45}$	1.11	22.4	73.2	**18.3**	/		/	2017.08	25
PTEG	Cs-perovskite	1.14	22.5	77.0	**19.8**	/		/	2017.09	26
P3HT	$(FAPbI_3)_{0.95}(MAPbBr_3)_{0.05}$	1.152	24.88	81.4	**23.3**	/		/	2019.03	27
PTB1-C	CsFAMAGA mixed perovskite	1.05	22.37	81.2	**19.06**	/		/	2019.09	28
P3	$MAPbI_3$	1.11	22.8	80.0	**20.3**	/		/	2019.11	29
PBDTT	Cs-perovskite	1.12	23.64	76.67	**20.28**	/		/	2019.12	30
PBTT-T	CsFAMA mixed perovskite	1.14	21.68	76.79	**19.02**	/		/	2020.11	31
alkoxy-PTEG	$Cs_{0.06}FA_{0.78}MA_{0.16}Pb_{0.94}I_{2.4}Br_{0.48}$	23.2	1.14	79.8	**21.2**	/		/	2020.01	32
PBTFO	$Cs_{0.05}(FA_{0.85}MA_{0.15})_{0.95}Pb(I_{0.85}Br_{0.15})_3$	1.21	23.3	75.1	**22.10**	/	N_2	*T*=65°C, unencapsulated, after 500 hours maintains 97%	2020.01	33

PBDT-N20	$(FAPbI_3)_{0.85}(MAPbBr_3)_{0.15}$	1.08	23.4	75.0	18.9	/	Glovebox	*T*=80 °C, after 1500 h maintains over 95%	2020.09	34
PC3	$MAPbI_3$	23.5	1.11	80.0	20.8	/	/	*T*=85°C, under 1 sun illumination after 200 h maintains 70%	2020.09	35
PE10	$FA_{0.85}MA_{0.15}PbI_3$	1.16	24.1	79.8	22.3			T = 85°C, in dark, after 500 h with 45−85% RH maintains 80.5% *T*=85°C, under 1 sun illumination after 240 h maintains 65%	2022.03	36
Ploy-alloy (PM6/PMSe)	$MA_{0.16}FA_{0.84}PbI_3$	1.19	25.07	82.17	24.53		N_2	T = 80 °C, in dark, after 600 h maintains 93%	2022.05	37
PM6	$MA_{0.16}FA_{0.84}PbI_3$	1.19	24.55	82.22	24.04			/	2022.08	38
PFBTI	$Cs_{0.05}FA_{0.95}PbI_3$	1.16	24.6	80.8	23.1			/	2022.10	39
Small molecule HTMs										
2DP-TDB	$FA_{0.85}MA_{0.15}PbI_3$	1.16	24.02	79.57	22.17		N_2	*T*=80°C, unencapsulated, in dark, after 376 h maintains 81%	2021.03	40
Z26	$(FAPbI_3)_{0.85}(MAPbBr_3)_{0.15}$	1.132	23.59	75.0	20.1	98	40% RH	*T*=65°C, unencapsulated, in dark after 120 h maintains ~85%	2017.09	41
TQ2	$MAPbI_3$	1.12	22.55	77.67	19.62	113		/	2018.07	42
TTE-2	$(FAPbI_3)_{0.95}(MAPbBr_3)_{0.05}$	1.11	23.26	77.52	20.04	158		/	2019.01	43
YN3	$(FAPbI_3)_{0.85}(MAPbBr_3)_{0.15}$	1.12	22.43	75	18.84	/		/	2019.02	44
DTPC13-ThTPA	$MA_{0.7}FA_{0.3}PbI_{2.85}Br_{0.15}$	1.135	22.82	78.7	20.38	/		/	2019.07	4
M129	$Cs_{0.05}(FA_{0.83}MA_{0.17})_{0.95}Pb(Br_{0.17}I_{0.83})_3$	1.08	22.50	72.0	17.50	170	N_2	*T*=60 °C, after 72 h maintains 90%	2019.09	45
BTTI-C6	CsFAMA perovskite	1.10	24.00	74.6	19.69	224	N_2	*T*=100 °C, unencapsulated, after 60 h maintains 70%	2019.12	3
DTP-C6Th	$MA_{0.7}FA_{0.3}Pb(I_{0.925}Br_{0.075})_3$	1.157	22.76	79.9	21.04	84.5		/	2019.07	5
YZ22	$Cs_{0.1}FA_{0.9}PbI_3$	1.10	25.1	81.0	22.4	108	Air	*T*=85°C, encapsulated, MPP (1.1 sun) tracking after 60 h maintains 60%	2020.09	7
TQ4	$Cs_{0.05}FA_{0.85}MA_{0.1}Pb(I_{0.97}Br_{0.03})_3$	1.124	23.78	79.0	21.03	131	N_2	*T*=85°C, in dark, after100 h maintains 90%	2020.10	8
DTB-FL	$Cs_{0.05}FA_{0.95}PbI_3$	1.14	23.8	77.4	21.50	87	N_2	*T*=80°C, after 240 h maintains 68%	2020.12	11
MeOTTVT	$Cs_{0.05}FA_{0.85}MA_{0.10}Pb(I_{0.97}Br_{0.03})_3$	1.11	23.89	80.3	21.30	137.1	/	*T*=80°C, in dark, after 220 h maintains 90%	2020.12	46
SFDT-TDM	$Cs_xFA_{1-x}PbI_3$	1.13	24.1	79.5	21.7	/		/	2021.06	47
CB	$MAPbI_3$	1.15	23.60	77.7	21.09			/	2021.08	48
BDT-DPA-F	$FAMAPbI_3$	1.18	24.66	79.57	23.12	/		*T*=85°C, in dark, after 1200 h maintains 80.3%	2022.09	12
L3	(Cs/GA) doped $(FAPbI_3)_{0.95}(MAPbBr_3)_{0.05}$	1.12	25.25	79.84	22.61	163	**Argon**	***T*=85°C, in dark, after 1000 h maintains 83%** ***T*=85°C, MPP tracking after 500 h maintains >85%**	/	This work

Table S3. Summary of device performance of PSCs with L3 HTL fabricated by different concentration at a speed 4000 rpm. The thicknesses of L3 film on ITO glass were determined using by using a Profilometer (Ambios Tech. XP-2).

Concentration	Thickness (nm)	V_{OC} (V)	J_{SC} (mA/cm^2)	FF (%)	PCE (%)
7.5 mg/mL	~33	1.06	21.22	58.77	13.25
10 mg/mL	~45	1.10	24.08	70.02	18.63
12 mg/mL	~54	1.10	24.65	78.15	21.15
15 mg/mL	~61	1.10	24.62	75.87	20.49

Table S4. Summary of device performance of PSCs with L3 HTL fabricated by different speed of spin-coating with a precursor of 12 mg/mL in CB.

12 mg/mL L3 HTL	V_{OC} (V)	J_{SC} (mA/cm^2)	FF (%)	PCE (%)
2K	1.11	23.91	72.11	19.06
4K	1.11	24.48	76.33	20.78
6K	1.11	24.22	76.45	20.57

Table S5. Summary of the performance of PSCs with different HTMs.

HTL	V_{OC} (V)	J_{SC} (mA/cm^2)	FF (%)	PCE (%)
L1	1.08 ± 0.01	24.41± 0.41	69.53 ± 2.61	18.39 ± 0.81
L2	1.10 ± 0.01	24.66 ± 0.32	74.89 ± 1.08	20.37 ± 0.36
L3	1.11 ± 0.01	24.77 ± 0.27	76.42 ± 1.60	21.11 ± 0.49

Table S6. Lifetimes and weighted fractions fitted by triple-exponential functions from the time-resolved PL.

	A_1	τ_1 (ns)	A_2	τ_2 (ns)	A_3	τ_3 (ns)	τ_{avg} (ns)
Pristine	0.34	44.51	0.66	104.91			94.08
L1	0.22	1.60	0.37	63.48	0.41	158.89	133.08
L2	0.24	1.60	0.34	56.55	0.42	149.00	126.68
L3	0.37	1.39	0.45	53.95	0.18	138.81	96
Dopant-free spiro-OMeTAD	0.13	5.66	0.41	46.26	0.46	95.60	79.86
Doped spiro-OMeTAD	0.16	6.59	0.50	34.48	0.34	67.56	52.18

$$\tau_{avg} = \frac{\sum f_i \tau_i^2}{\sum f_i \tau_i}$$

Reference

1. M. Jeong, W. Choi In, M. Go Eun, Y. Cho, M. Kim, B. Lee, S. Jeong, Y. Jo, W. Choi Hye, J. Lee, J.-H. Bae, K. Kwak Sang, S. Kim Dong and C. Yang, *Science*, 2020, **369**, 1615-1620.
2. Y. Liu, Q. Chen, H.-S. Duan, H. Zhou, Y. Yang, H. Chen, S. Luo, T.-B. Song, L. Dou, Z. Hong and Y. Yang, *J. Mater. Chem. A*, 2015, **3**, 11940-11947.
3. B. Tu, Y. Wang, W. Chen, B. Liu, X. Feng, Y. Zhu, K. Yang, Z. Zhang, Y. Shi, X. Guo, H. F. Li, Z. Tang, A. B. Djurisic and Z. He, *ACS Appl. Mater. Interfaces*, 2019, **11**, 48556-48563.
4. J. Zhou, X. Yin, Z. Dong, A. Ali, Z. Song, N. Shrestha, S. S. Bista, Q. Bao, R. J. Ellingson, Y. Yan and W. Tang, *Angew. Chem. Int. Ed.*, 2019, **58**, 13717-13721.
5. X. Yin, J. Zhou, Z. Song, Z. Dong, Q. Bao, N. Shrestha, S. S. Bista, R. J. Ellingson, Y. Yan and W. Tang, *Adv. Funct. Mater.*, 2019, **29**, 1904300.
6. Y. Liu, Z. Hong, Q. Chen, H. Chen, W.-H. Chang, Y. Yang, T.-B. Song and Y. Yang, *Adv. Mater.*, 2016, **28**, 440-446.
7. B. X. M. Zhao, C. Yao, K. C. Gu, T. R. Liu, Y. Xia and Y. L. Loo, *Energy Environ. Sci.*, 2020, **13**, 4334-4343.
8. H. Guo, H. Zhang, C. Shen, D. Zhang, S. Liu, Y. Wu and W. H. Zhu, *Angew. Chem. Int. Ed.*, 2021, **60**, 2674-2679.
9. M. Cheng, K. Aitola, C. Chen, F. Zhang, P. Liu, K. Sveinbjörnsson, Y. Hua, L. Kloo, G. Boschloo and L. Sun, *Nano Energy*, 2016, **30**, 387-397.
10. P. Xu, P. Liu, Y. Li, B. Xu, L. Kloo, L. Sun and Y. Hua, *ACS Appl. Mater. Interfaces*, 2018, **10**, 19697-19703.
11. T. Niu, W. Zhu, Y. Zhang, Q. Xue, X. Jiao, Z. Wang, Y.-M. Xie, P. Li, R. Chen, F. Huang, Y. Li, H.-L. Yip and Y. Cao, *Joule*, 2021, **5**, 249-269.
12. Q. Cheng, H. Chen, F. Yang, Z. Chen, W. Chen, H. Yang, Y. Shen, X. M. Ou, Y. Wu, Y. Li and Y. Li, *Angew. Chem. Int. Ed.*, 2022, **61**, e202210613.
13. Y.-H. Lin, N. Sakai, P. Da, J. Wu, H. C. Sansom, A. J. Ramadan, S. Mahesh, J. Liu, R. D. J. Oliver, J. Lim, L. Aspitarte, K. Sharma, P. K. Madhu, A. B. Morales-Vilches, P. K. Nayak, S. Bai, F. Gao, C. R. M. Grovenor, M. B. Johnston, J. G. Labram, J. R. Durrant, J. M. Ball, B. Wenger, B. Stannowski and H. J. Snaith, *Science*, 2020, **369**, 96.
14. X. Zheng, Y. Hou, C. Bao, J. Yin, F. Yuan, Z. Huang, K. Song, J. Liu, J. Troughton, N. Gasparini, C. Zhou, Y. Lin, D.-J. Xue, B. Chen, A. K. Johnston, N. Wei, M. N. Hedhili, M. Wei, A. Y. Alsalloum, P. Maity, B. Turedi, C. Yang, D. Baran, T. D. Anthopoulos, Y. Han, Z.-H. Lu, O. F. Mohammed, F. Gao, E. H. Sargent and O. M. Bakr, *Nat. Energy*, 2020, **5**, 131-140.
15. X. Li, W. Zhang, X. Guo, C. Lu, J. Wei and J. Fang, *Science*, 2022, **375**, 434-437.
16. R. Chen, S. Liu, X. Xu, F. Ren, J. Zhou, X. Tian, Z. Yang, X. Guanz, Z. Liu, S. Zhang, Y. Zhang, Y. Wu, L. Han, Y. Qi and W. Chen, *Energy Environ. Sci.*, 2022, **15**, 2567-2580.
17. Z. Li, B. Li, X. Wu, A. Sheppard Stephanie, S. Zhang, D. Gao, J. Long Nicholas and Z. Zhu, *Science*, 2022, **376**, 416-420.

18. R. Azmi, E. Ugur, A. Seitkhan, F. Aljamaan, A. S. Subbiah, J. Liu, G. T. Harrison, M. I. Nugraha, M. K. Eswaran, M. Babics, Y. Chen, F. Xu, T. G. Allen, A. U. Rehman, C. L. Wang, T. D. Anthopoulos, U. Schwingenschlogl, M. De Bastiani, E. Aydin and S. De Wolf, *Science*, 2022, **376**, 73-77.
19. S. Bai, P. Da, C. Li, Z. Wang, Z. Yuan, F. Fu, M. Kawecki, X. Liu, N. Sakai, J. T.-W. Wang, S. Huettner, S. Buecheler, M. Fahlman, F. Gao and H. J. Snaith, *Nature*, 2019, **571**, 245-250.
20. A. Mei, Y. Sheng, Y. Ming, Y. Hu, Y. Rong, W. Zhang, S. Luo, G. Na, C. Tian, X. Hou, Y. Xiong, Z. Zhang, S. Liu, S. Uchida, T.-W. Kim, Y. Yuan, L. Zhang, Y. Zhou and H. Han, *Joule*, 2020, **4**, 2646-2660.
21. Y.-W. Jang, S. Lee, K. M. Yeom, K. Jeong, K. Choi, M. Choi and J. H. Noh, *Nat. Energy*, 2021, **6**, 63-71.
22. J. Peng, D. Walter, Y. Ren, M. Tebyetekerwa, Y. Wu, T. Duong, Q. Lin, J. Li, T. Lu, M. A. Mahmud, O. L. C. Lem, S. Zhao, W. Liu, Y. Liu, H. Shen, L. Li, F. Kremer, H. T. Nguyen, D.-Y. Choi, K. J. Weber, K. R. Catchpole and T. P. White, *Science*, 2021, **371**, 390.
23. T. Bu, J. Li, H. Li, C. Tian, J. Su, G. Tong, L. K. Ono, C. Wang, Z. Lin, N. Chai, X.-L. Zhang, J. Chang, J. Lu, J. Zhong, W. Huang, Y. Qi, Y.-B. Cheng and F. Huang, *Science*, 2021, **372**, 1327.
24. G. Kim, H. Min, K. S. Lee, D. Y. Lee, S. M. Yoon and S. I. Seok, *Science*, 2020, **370**, 108-112.
25. J. Lee, M. Malekshahi Byranvand, G. Kang, S. Y. Son, S. Song, G. W. Kim and T. Park, *J. Am. Chem. Soc.*, 2017, **139**, 12175-12181.
26. G.-W. Kim, J. Lee, G. Kang, T. Kim and T. Park, *Adv. Energy Mater.*, 2018, **8**, 1701935.
27. E. H. Jung, N. J. Jeon, E. Y. Park, C. S. Moon, T. J. Shin, T. Y. Yang, J. H. Noh and J. Seo, *Nature*, 2019, **567**, 511-515.
28. F. Qi, X. Deng, X. Wu, L. J. Huo, Y. Q. Xiao, X. H. Lu, Z. L. Zhu and A. K. Y. Jen, *Adv. Energy Mater.*, 2019, **9**, 1902600.
29. F. Zhang, Z. Yao, Y. Guo, Y. Li, J. Bergstrand, C. J. Brett, B. Cai, A. Hajian, Y. Guo, X. Yang, J. M. Gardner, J. Widengren, S. V. Roth, L. Kloo and L. Sun, *J. Am. Chem. Soc.*, 2019, **141**, 19700-19707.
30. G. You, Q. Zhuang, L. Wang, X. Lin, D. Zou, Z. Lin, H. Zhen, W. Zhuang and Q. Ling, *Adva. Energy Mater.*, 2019, **10**, 1903146.
31. L. Wang, Q. Zhuang, G. You, X. Lin, K. Li, Z. Lin, H. Zhen and Q. Ling, *ACS Appl. Energy Mater.*, 2020, **3**, 12475-12483.
32. J. Lee, G. W. Kim, M. Kim, S. A. Park and T. Park, *Adv. Energy Mater.*, 2020, **10**, 1902662.
33. Z. J. Li, J. Park, H. Park, J. Lee, Y. Kang, T. K. Ahn, B. G. Kim and H. J. Park, *Nano Energy*, 2020, **78**, 105159.
34. X. Q. Jiang, X. Liu, J. F. Zhang, S. Ahmad, D. D. Tu, W. Qin, T. G. Jiu, S. P. Pang, X. Guo and C. Li, *J. Mater. Chem. A*, 2020, **8**, 21036-21043.
35. Z. Yao, F. Zhang, Y. Guo, H. Wu, L. He, Z. Liu, B. Cai, Y. Guo, C. J. Brett, Y. Li, C. V. Srambickal, X. Yang, G. Chen, J. Widengren, D. Liu, J. M. Gardner, L. Kloo

and L. Sun, *J. Am. Chem. Soc.*, 2020, **142**, 17681-17692.
36. Z. Yao, F. Zhang, L. He, X. Bi, Y. Guo, Y. Guo, L. Wang, X. Wan, Y. Chen and L. Sun, *Angew. Chem. Int. Ed.*, 2022, **61**, e202201847.
37. Q. Fu, X. Tang, H. Liu, R. Wang, T. Liu, Z. Wu, H. Y. Woo, T. Zhou, X. Wan, Y. Chen and Y. Liu, *J. Am. Chem. Soc.*, 2022, **144**, 9500-9509.
38. Q. Fu, H. Liu, S. Li, T. Zhou, M. Chen, Y. Yang, J. Wang, R. Wang, Y. Chen and Y. Liu, *Angew. Chem. Int. Ed.*, 2022, **n/a**, e202210356.
39. Y. Bai, Z. Zhou, Q. Xue, C. Liu, N. Li, H. Tang, J. Zhang, X. Xia, J. Zhang, X. Lu, C. J. Brabec and F. Huang, *Adv. Mater.*, 2022, 2110587.
40. Q. Fu, Z. Y. Xu, X. C. Tang, T. T. Liu, X. Y. Dong, X. D. Zhang, N. Zheng, Z. Q. Xie and Y. S. Liu, *Acs Energy Lett.*, 2021, **6**, 1521-1532.
41. F. Zhang, Z. Q. Wang, H. W. Zhu, N. Pellet, J. S. Luo, C. Y. Yi, X. C. Liu, H. L. Liu, S. R. Wang, X. G. Li, Y. Xiao, S. M. Zakeeruddin, D. Q. Bi and M. Gratzel, *Nano Energy*, 2017, **41**, 469-475.
42. H. Zhang, Y. Wu, W. Zhang, E. Li, C. Shen, H. Jiang, H. Tian and W.-H. Zhu, *Chem. Sci.*, 2018, **9**, 5919-5928.
43. C. Shen, Y. Wu, H. Zhang, E. Li, W. Zhang, X. Xu, W. Wu, H. Tian and W. H. Zhu, *Angew. Chem. Int. Ed.*, 2019, **58**, 3784-3789.
44. D. Zhang, P. Xu, T. Wu, Y. Ou, X. Yang, A. Sun, B. Cui, H. Sun and Y. Hua, *J. Mater. Chem. A*, 2019, **7**, 5221-5226.
45. J. Wang, H. Zhang, B. Wu, Z. Wang, Z. Sun, S. Xue, Y. Wu, A. Hagfeldt and M. Liang, *Angew. Chem. Int. Ed.*, 2019, **58**, 15721-15725.
46. H. Zhu, Z. Shen, L. Pan, J. Han, F. T. Eickemeyer, Y. Ren, X. Li, S. Wang, H. Liu, X. Dong, S. M. Zakeeruddin, A. Hagfeldt, Y. Liu and M. Grätzel, *ACS Energy Lett.*, 2020, **6**, 208-215.
47. J. Wang, X. Wu, Y. Z. Liu, T. Qin, K. C. Zhang, N. Li, J. Zhao, R. Q. Ye, Z. X. Fan, Z. G. Chi and Z. L. Zhu, *Adva. Energy Mater.*, 2021, **11**, 2100967.
48. K.-M. Lee, W.-H. Chiu, Y.-H. Tsai, C.-S. Wang, Y.-T. Tao and Y.-D. Lin, *Chem. Eng. J.*, 2022, **427**, 131609.